HIGH RESOLUTION MEASUREMENTS OF THE SUNYAEV-ZEL'DOVICH EFFECT IN GALAXY CLUSTERS AT 90 GHZ

Alexander H. Young

A DISSERTATION

in

Physics and Astronomy

Presented to the Faculties of the University of Pennsylvania

in Partial Fulfillment of the Requirements for the degree of Doctor of Philosophy

2014

Supervisor of Dissertation

Mark Devlin, Professor, Physics and Astronomy

Graduate Group Chairperson

Marija Drndic, Professor, Physics and Astronomy

Dissertation Committee:

James Aguirre, Assistant Professor, Physics and Astronomy

Gary Bernstein, Professor, Physics and Astronomy

Robert Thornton, Associate Professor, Physics

Philip Nelson, Professor, Physics and Astronomy

Acknowledgements

I would like to thank the multitude of people who have made my graduate career and dissertation research possible. First and foremost, I would like to thank my advisor, Mark Devlin, for his guidance and for maintaining a fun and productive research group that I am glad to have been a part of. He has provided me the opportunity to develop a broad range of technical and analytical skills that have enabled me to grow into a successful and independent researcher. Mark has a talent for determining the path of least resistance toward any particular goal, and I have learned from him how to be efficient and thorough in my research. MUSTANG-1.5 would never have become a reality if Mark hadn't continued driving the project forward despite the obstacles we faced along the way.

I have been fortunate to work with many great people on the MUSTANG project. Simon Dicker has proven a great mentor throughout my graduate career and made the many long days spent working on the cryostat enjoyable. He has taught me a great deal about instrumentation and analysis as well as provided me the opportunity to take a leading role in many projects as we developed MUSTANG-1.5. I would like to thank Brian Mason for providing constant support in carrying out MUSTANG observations, analyzing the data, and interpreting the results. Phil Korngut introduced me to the MUSTANG instrument, science, and observing. His enthusiasm and extensive knowledgebase made my transition to a new field smooth and enjoyable. I had fun leading many overnight observations with Charles Romero and I am grateful for all his help in analyzing the MUSTANG data and in writing software to make the data reduction more efficient. I would also like to thank all of the collaborators who have contributed to meaningful discussions and provided support to the MUS-

TANG project including Craig Sarazin, Jack Sayers, Jon Sievers, Nick Battaglia, James Aguirre, Kent Irwin, Hannes Hubmayr, Sherry Cho, and Jeff McMahon.

I owe a great debt to the amazing postdocs I have worked with during my career. I would like to thank Tony Mroczkowski and Erik Reese for guiding me in my research, helping me put together successful proposals, and facilitating my involvement in the SZE community. I was fortunate to attend a great many conferences and workshops that I would not have even known existed without them. Developing and implementing the microwave multiplexing electronics with Justus Brevik was a great experience. Without his efforts to design and build the signal processing firmware and software we would not be ready to read out detectors right now.

I would like to thank all the folks at NRAO for helping to make MUSTANG-1.5 happen and providing a comfortable and enjoyable environment during the times I spent at Green Bank. The GBT operators Barry Sharp, Greg Monk, Donna Stricklin, and Dave Curry provided timely assistance with all issues I encountered during the many late-night observing sessions. I am grateful to Dennis Egan, Jeff Cromer, Mike Hedrick, Steve White, Mike Stennes, Dave Woody, Mark Whitehead, Paul Marganian, John Ford, Marty Bloss, Pam Ford, Melinda Mello. I would like to acknowledge NRAO for supporting my graduate research for two years through the Student Observing Support program.

I am grateful to everyone I have worked with in the cosmology group at UPenn over the past five years. I enjoyed the many trips to Picnic and Starbucks with Ben Schmitt, Bob Thornton, and Elio Angile. Ben's energy and enthusiasm has made for many great discussions about science and life in general. Jeff Klein has answered every question I have thrown his way and has helped me troubleshoot many of the problems I have encountered in the lab.

I would like to thank Jennifer Lynch who has been a great companion throughout our five years of graduate school together. I am truly grateful for her love and support. Finally, I would like to thank my parents and my brother who have been a constant positive influence in my life. They have encouraged me in my scientific career every step of the way. This thesis is dedicated to them.

ABSTRACT

HIGH RESOLUTION MEASUREMENTS OF THE SUNYAEV-ZEL'DOVICH EFFECT IN GALAXY CLUSTERS AT 90 GHZ

Alexander H. Young

Mark J. Devlin

The MUltiplexed SQUID/TES Array at Ninety GHz (MUSTANG) is a 64-pixel array of transition-edge sensor (TES) bolometers built at the University of Pennsylvania (UPenn) for the Green Bank Telescope (GBT) in collaboration with a number of universities and government agencies such as NASA-GSFC, NRAO, and NIST. MUSTANG carried out observations between 2008 and 2013 and will soon be replaced by a new receiver (MUSTANG-1.5). MUSTANG-1.5 is a 223-pixel array of feedhorn-coupled polarimeters, which are read out with a novel microwave SQUID multiplexer. MUSTANG-1.5 offers many advantages over MUSTANG including more stable cryogenics, a larger field of view ($\sim 5.5'$ compared to $42''$ for MUSTANG), and a significant improvement in sensitivity. These capabilities enable a far more comprehensive observing program.

MUSTANG is aimed at measuring the distortion in the Cosmic Microwave Background (CMB) spectrum that arises due to the Sunyaev-Zel'dovich Effect (SZE). The SZE is the inverse Compton-scattering of CMB photons as they pass through the dense plasma in clusters of galaxies. The SZE is a nearly redshift-independent, com-

plementary probe of the ICM to X-ray emission and combined analyses of both data sets provide a better understanding of astrophysical phenomena such as shocks, cold fronts, and Active Galactic Nucleus (AGN) outbursts. Understanding how substructure, especially in merging clusters, affects the scaling between SZE flux and total cluster mass is essential to placing tight constraints on cosmological parameters with SZE surveys.

In this thesis, I present some of the last ever observations carried out by MUSTANG, which are centered on two massive galaxy clusters, MACS J0647.7+7015 and MACS J1206.2-0847. I discuss a model-fitting technique that has been used to quantitatively compare MUSTANG and lower resolution SZE data from Bolocam to study ICM pressure profiles. I report on the design, commissioning, and current status of MUSTANG-1.5 including the detectors, cryogenics, optics, and the microwave multiplexing readout electronics. Finally, I present early characterization of the cryogenics and readout electronics as the instrument nears deployment-readiness and discuss plans for the early science program.

Contents

List of Tables

List of Figures

Chapter 1

Introduction

Once thought to be relaxed, spherical, systems in hydrostatic equilibrium, clusters of galaxies exhibit a wide range of phenomena that make them astrophysical laboratories for some of the most energetic events in the Universe since the Big Bang [Sarazin 2002]. To the extent that their dark matter to baryonic ratio approaches the universal value, clusters serve almost as miniature universes in which both cosmology and astrophysics can be studied. The complex processes discovered in clusters include shocks and cold fronts [Markevitch & Vikhlinin 2007], ripples and sound waves [Fabian et al. 2006], cavities produced from AGN feedback [McNamara & Nulsen 2007], and sloshing of the intracluster medium (ICM) within a cluster's gravitational potential (e.g., ZuHone et al. 2010).

In this thesis, I describe the MUSTANG and MUSTANG-1.5 projects, which aim to measure the Sunyaev-Zel'dovich Effect (SZE) in galaxy clusters with unprecedented angular resolution. MUSTANG completed observations of twelve clusters from the Cluster Lensing And Supernova survey with Hubble (CLASH) sample in order to

carry out a multi-wavelength analysis of the CLASH clusters and investigate their dynamical states. With MUSTANG-1.5 we aim to observe a statistically significant sample of hundreds of clusters in order to assess the impact of astrophysical phenomena on cosmological parameters derived from clusters.

In this introduction, I give a brief overview of the standard model of cosmology and the Cosmic Microwave Background (CMB). I describe the basic properties of galaxy clusters the origin of the SZE. Finally, I discuss the ways in which galaxy clusters can be used to determine cosmological parameters and why high-resolution SZE measurements are crucial for precision cosmology using clusters.

1.1 The Standard Cosmological Model

In the Big Bang model of cosmology, originally developed by Georges Lemaitre in 1931 [Lemaître 1931], the early universe expands from an initial extremely hot and dense state. This was first evidenced by the linear velocity-distance relationship measured by Edwin Hubble in 1929 [Hubble 1929]. Hubble measured light emitted by nearby galaxies and determined that their apparent velocity with respect to Earth increased with distance according to $v = H_0 d$, where H_0 is referred to as the Hubble constant. It is logical to assume that objects moving away from each other today were closer together in the past and at very early times the Universe was likely in a dense state before the Big Bang event initiated the expansion.

According to the Cosmological Principle, the Universe is homogeneous and isotropic. In 1922, several years prior to Hubble's discovery, Alexander Friedmann had applied Einstein's general theory of relativity to derive a set of equations govern-

ing the expansion of a Universe filled with a perfect fluid [Friedmann 1922]. These "Friedmann equations" are given by

$$\left(\frac{\dot{a}}{a}\right)^2 = \frac{8\pi G\rho}{3} - \frac{kc^2}{a^2}, \tag{1.1}$$

$$\frac{\ddot{a}}{a} = -\frac{4\pi G}{3}\left(\rho + \frac{3P}{c^2}\right), \tag{1.2}$$

where $a = 1/(1+z)$ is a "scale factor" describing the relative size of the Universe as it expands, G is Newton's gravitational constant, k is related to the curvature of space (taken to be zero for flat geometry), ρc^2 is the energy density, and c is the speed of light in a vacuum. The redshift z provides a measurement of how much the Universe has expanded with $z = 0$ representing today and $z = 1$ representing a time when the Universe was half its current size. In Friedmann's second equation, P is the pressure. The quantity $\dot{a}/a$ is typically given as the evolving Hubble parameter H.

The primary goal of modern cosmology is to describe the initial conditions and evolution of the Universe in a single standard model, analogous to, but not to be confused with, the highly successful standard model of particle physics. The ΛCDM model has done so far a good job so far of describing observations with only six parameters, and there are numerous ongoing scientific endeavors to discover conflicts with or extensions to this paradigm. In ΛCDM, the energy content of the Universe is comprised of radiation ρ_R, matter ρ_m, and the so-called "dark energy" ρ_Λ. We can then rewrite equation 1.1 as

$$\left(\frac{H}{H_0}\right)^2 = \Omega_R(1+z)^4 + \Omega_M(1+z)^3 + \Omega_k(1+z)^2 + \Omega_\Lambda, \tag{1.3}$$

where $\Omega_X = \rho_X/\rho_c$ and $\rho_c = 3H^2/(8\pi G)$ is the critical density for a geometrically flat Universe. H_0 is the present day value of the Hubble constant, measured to be ~ 68 km s^{-1} Mpc^{-1} [Planck Collaboration et al. 2013a].

For a Universe filled with a perfect fluid, the equation of state is

$$P = w\rho c^2, \tag{1.4}$$

where w is a constant. Under the dust approximation, matter consists of stationary particles with no pressure, which yields $w = 0$. The pressure due to a uniform field of radiation is $P = \rho c^2/3 \rightarrow w = 1/3$. The detection of the accelerated expansion of the Universe by measurements of distant type Ia supernova [Perlmutter et al. 1999] requires a dominant energy density component with negative pressure since, by Equation 1.2, $\ddot{a} > 0$ implies $\rho < -3P$ (or $w < -1/3$). Using the Friedmann equations and conservation of energy for a cosmological constant that does not depend on the scale factor, it is straightforward to determine that $P = -\rho$, or $w = -1$. Therefore, dark energy, in the form of a cosmological constant, would explain the accelerated expansion of the Universe. Some alternatives and extensions to ΛCDM suggest that dark energy may have $w \neq 1$ or that w evolves with time. Currently, observations find that $w = -1.084 \pm 0.063$ [Hinshaw et al. 2013] and do not yet rule out the alternative models for dark energy. Future observations aimed at placing tighter constraints on w will be crucial to better understanding the nature and evolution of dark energy.

An extension to ΛCDM known as inflation states that the Big Bang was immediately followed by a period of rapid expansion [Guth 1981]. Inflation explains many of the puzzling characteristics of the CMB, for instance the so-called "horizon

problem" where thermal equilibrium appears to exist between regions of space that should have been unable to come into causal contact. This rapid expansion converts quantum fluctuations into gravitational potential perturbations, which are imprinted on the temperature distribution, as seen in the CMB, and in the density distribution, as traced by the large scale structures such as galaxy clusters that we see today.

1.2 The Cosmic Microwave Background

The CMB, was first predicted by Ralph Alpher and Robert Herman in 1948 [Alpher & Herman 1948] and later discovered serendipitously by Arno Penzias and Robert Wilson in the 1960s [Penzias & Wilson 1965]. The origin of the CMB can be traced back to the epoch of recombination, approximately 380,000 years after the Big Bang. At this time, the Universe comprised a hot plasma of particles, including electrons, protons, and neutrons, and light, all in thermal equilibrium. When the Universe expanded and cooled to a temperature of approximately 3,000 K, positively charged ions were able to capture electrons and form electrically neutral atoms such as hydrogen and helium. The matter and light content of the Universe effectively decoupled and the photons were now able to propagate freely. Today, we see these photons arrive at Earth with a nearly perfect blackbody spectrum

$$B_\nu(T) = 2\frac{\nu^2}{c^2}\frac{h\nu}{e^{h\nu/k_\mathrm{B}T} - 1}, \tag{1.5}$$

as shown in Figure 1.1. From this spectrum we know the CMB to be in thermal equilibrium with $T \sim 2.725$ K and peak emission in the microwave at $\nu \sim 160$ GHz.

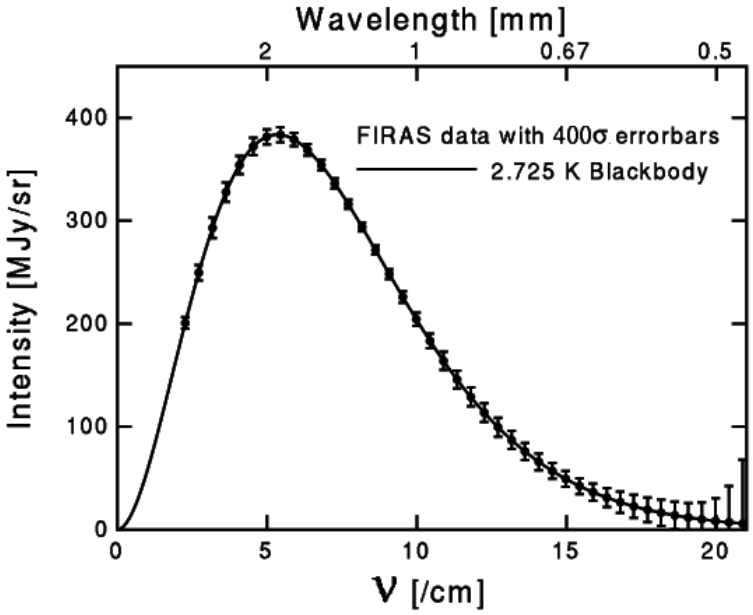

Figure 1.1: Measurement of the 2.73 K CMB spectrum from COBE FIRAS shown with 400σ error bars. Image source: www.astro.ucla.edu/∼wright/spectrum.gif.

The time at which CMB photons first began to freely propagate is often referred to as the "surface of last scattering".

In the early 1990s, observations with the COBE satellite measured precisely the perfect blackbody spectrum of the CMB and revealed tiny spatial temperature fluctuations ($\Delta T/T \approx 10^{-5}$) not accounted for by the intrinsic dipole anisotropy due to the motion of the Earth with respect to the CMB rest frame, instrumental errors, or foreground contaminants [Mather et al. 1990; Smoot et al. 1992]. This signature of higher-order CMB anisotropy, predicted by inflationary cosmology, provides a powerful probe of the early universe.

In the more than two decades that have followed, measurements of the CMB temperature anisotropy, and more recently polarization anisotropy, continue to improve our understanding the geometry, initial conditions, and evolution of the Universe [e.g.,

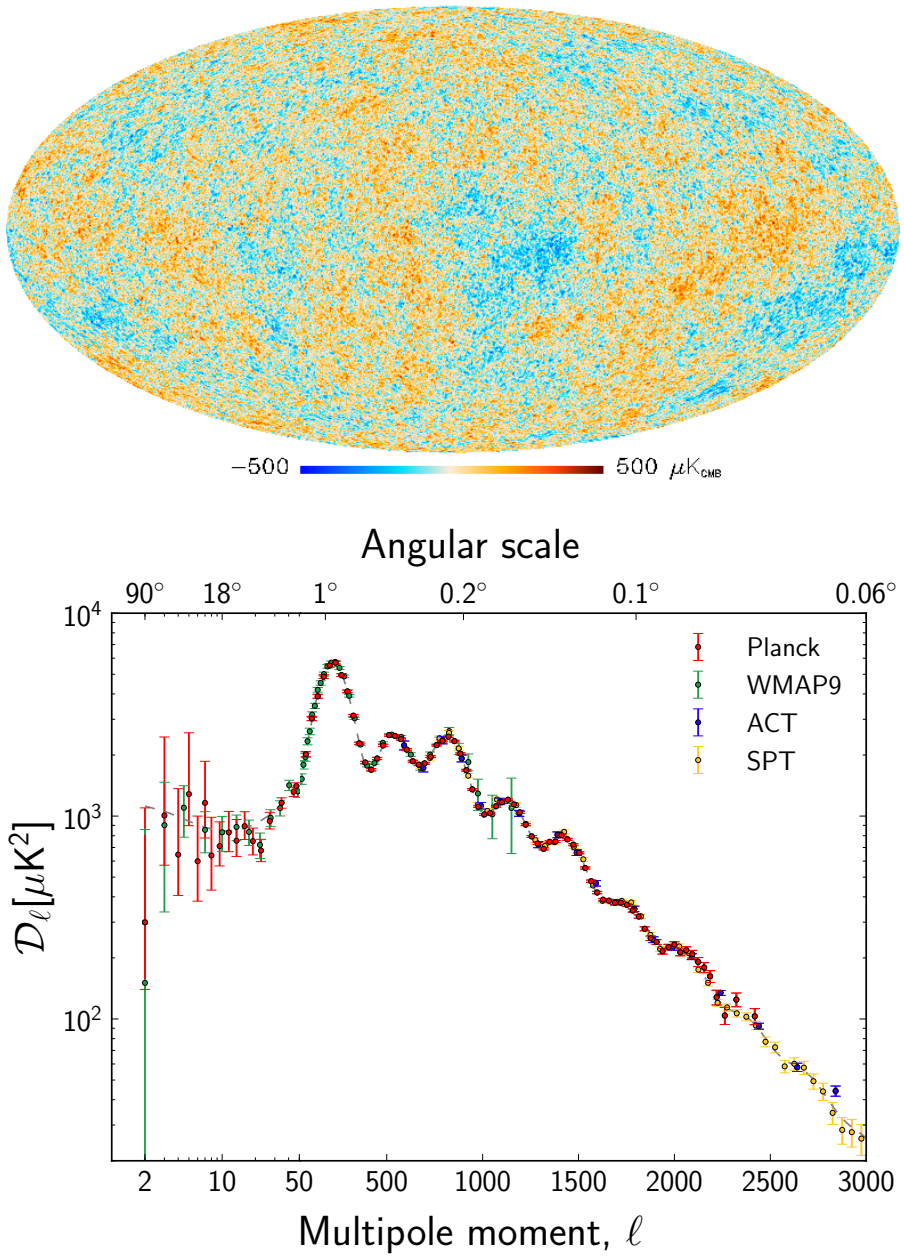

Figure 1.2: *Planck* all-sky temperature map of the CMB (top) and associated angular power spectrum, including complementary measurements by *WMAP*, ACT, and SPT (bottom). Figures taken from Planck Collaboration et al. 2013a.

Brown et al. 2009; Komatsu et al. 2011; Reichardt et al. 2012; Sievers et al. 2013; Ade et al. 2014]. The highest resolution (to date) all-sky temperature map of the CMB from the *Planck* satellite is shown in Figure 1.2. Typical models of inflationary cosmology follow Gaussian statistics and can thus be fully characterized by their angular power spectrum. The CMB power spectrum from the *Planck* observations is shown at the bottom of Figure 1.2 with complementary measurements covering additional angular scales from the Wilkinson Microwave Anisotropy Probe (*WMAP*), Atacama Cosmology Telescope (ACT), and South Pole Telescope (SPT).

On large angular scales (low ℓ modes) the CMB is dominated by temperature fluctuations that are modulated by acoustic oscillations within the plasma at the surface of last scattering. Additional fluctuations are predicted to exist due to gravitational waves produced during inflation. On smaller angular scales ($\ell \gtrsim 3000$), the CMB is imprinted with secondary anisotropies associated with intervening structures as the photons propagate to us from the surface of last scattering. These include scattering effects between CMB photons and energetic free electrons, gravitational lensing effects from large scale structures, and polarization due to the reionization of the Universe [Aghanim et al. 2008]. We can use precise measurements of these secondary anisotropies to probe the evolution of structure in Universe as well as deduce the primary CMB signal at these high ℓ modes.

1.3 Galaxy Clusters

The temperature fluctuations in the CMB trace density fluctuations in the Universe at the time of recombination. As the Universe evolved, these density pertur-

bations collapsed under gravity to form large gravitational potential wells. Within these dense concentrations of matter, individual galaxies ($M \sim 10^{11}\ M_{\odot}$), galaxy groups ($M \sim 10^{13}\ M_{\odot}$), and eventually galaxy clusters ($M \gtrsim 10^{14}$) were formed (see Chapter 2).

Clusters of galaxies are the largest gravitationally bound systems in the Universe and encompass volumes great enough to be considered representative samples of the Universe at large. Clusters are comprised primarily of dark matter (85%), diffuse hot plasma known as the intra-cluster medium (ICM) (12%), as well as stars and galaxies (3%). The high dark matter to baryonic matter ratio in clusters provides strong evidence that we live in a dark matter dominated Universe. In addition to the cosmological information inferred from these objects, clusters also serve as rich astrophysical laboratories. The diverse matter content of clusters provides a wide range of observables across the EM spectrum from synchrotron radiation at radio wavelengths to thermal bremsstrahlung emission in X-ray bands.

Figure 1.3 shows a composite image of the cluster MACS J0025.4-1222[1]. The optical image from the Hubble Space Telescope (HST) shows the galaxy population in the cluster as well as foreground and background stars and galaxies. Some of the background galaxies are gravitationally lensed by the intervening massive cluster. This provides an indirect measurement of the cluster mass distribution, which is overlaid in blue. The X-ray measurement of the ICM from the *Chandra* X-ray satellite is shown in red. There is an obvious offset between the ICM contained within the cluster core and the galaxy and dark matter content to the east and west. This is

[1]Typically clusters are named based on the survey in which they were detected and their location in equatorial coordinates. For instance, MACS J0025.4-1222 was detected during the MAssive Cluster Survey [Ebeling et al. 2001] and is roughly located at RA = 00h25m29s , DEC = -12°22′37″

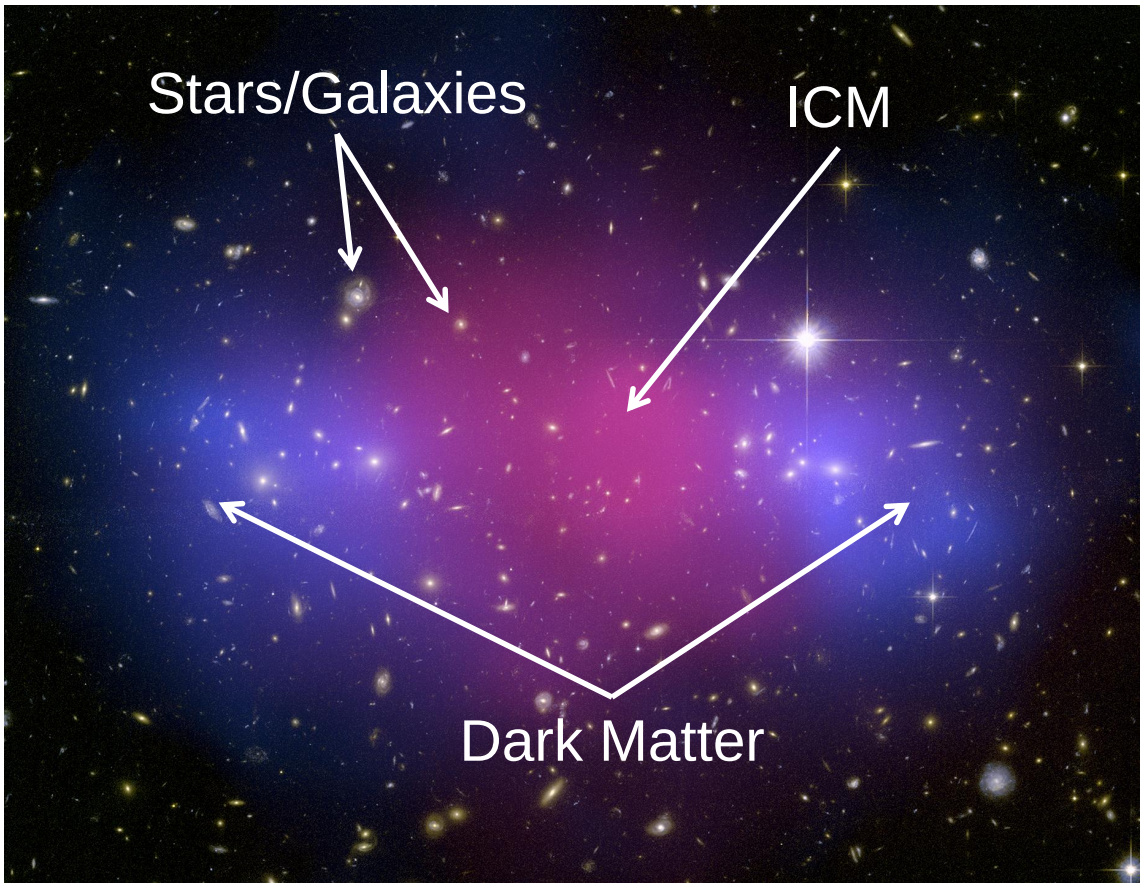

Figure 1.3: Composite image of galaxy cluster MACS J0025.4-1222. The optical data from HST are overlaid with the ICM imaged by *Chandra* (red) and the dark matter distribution (blue) inferred from gravitational lensing.

because this particular system is undergoing a merger event where two galaxy groups or subclusters are colliding. The dark matter and galaxy populations are collisionless and pass through each other unhindered. The ICM, however, is a collisional fluid and the gas from a merging subcluster will lag behind the dark matter due to ram pressure from the plasma.

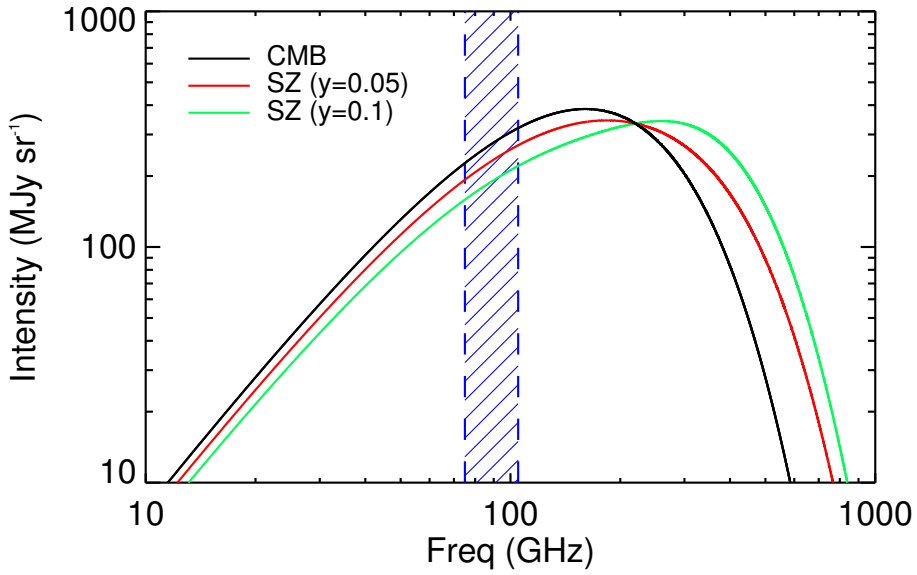

Figure 1.4: The CMB spectrum (black) with distortions due to the SZE, from two clusters of different mass. The red curve corresponds to a cluster with a peak SZE surface brightness ($\Delta I_{SZE} \propto y$) twice that of the green curve. Both clusters are approximately 1000 times brighter (in the SZE) than a typical cluster. Within the MUSTANG observing band, given by the blue hashed region, the SZE manifests as a decrement in the expected CMB intensity.

1.4 The Sunyaev-Zel'dovich Effect

The interaction between photons from the CMB and the ICM in galaxy clusters gives rise to the Sunyaev-Zel'dovich Effect (SZE). The SZE occurs when CMB photons inverse Compton scatter off energetic electrons [Sunyaev & Zel'dovich 1972] in the $T_e \sim 10^7$ K ICM. Given a typical electron density $n_{\rm e} = 10^{-3}$ cm^{-3} and effective line of sight depth $\ell = 5$ Mpc, the electron optical depth $\tau_e = \int n_e \sigma_T d\ell \approx 0.01$. Therefore, the ICM in a typical cluster will only scatter $\sim 1\%$ of CMB photons via the SZE, which is a small but measurable effect.

The magnitude of the distortion in the CMB due to the SZE is proportional to the Compton-y parameter

$$\Delta I_{SZE} \propto y \equiv \int P_e d\ell, \tag{1.6}$$

where P_e is the ICM pressure. Figure 1.4 shows the predicted distortion in the CMB spectrum due to two intervening clusters, respectively. These clusters are chosen to have y approximately 1000 times higher than in a typical cluster in order to enhance the effect for illustration. I discuss the SZE formalism in more detail in §2.2.2.

In addition to the thermal SZE described above, there is an additional distortion in the CMB spectrum due to bulk motion of a cluster along the line of sight, referred to as the kinetic SZE (kSZE). The kSZE is given by [Carlstrom et al. 2002]

$$\frac{\Delta T_{kSZE}}{T_{CMB}} = -\tau_e \left(\frac{v_z}{c}\right) \tag{1.7}$$

where v_z is the peculiar velocity of the cluster along the line of sight. The kSZE is a much smaller effect than the thermal SZE, except at the thermal SZE null at $\sim$ 218 GHz, and has only recently been detected, first by a statistical analysis of stacked cluster observations [Hand et al. 2012], and potentially directly detected by Bolocam [Mroczkowski 2011; Sayers et al. 2013a] observations of MACS J0717.5+3745, which was an analysis initially motivated by MUSTANG observations. Since the kinetic SZE is not the primary focus of this work, I will use SZE when referring to the thermal effect only, and denote the kinetic effect separately as kSZE.

1.5 Cosmology from Clusters

Surveys of the SZE are currently being carried out by such instruments as ACT [Niemack et al. 2010], SPT [Reichardt et al. 2013], and (until 2013) the *Planck* satellite [Planck Collaboration et al. 2013b] to locate galaxy clusters across large regions of the sky and to relatively high redshifts $z > 1$. The evolution of the cluster mass function, which describes the number of clusters of a certain mass as a function of redshift, is strongly dependent on cosmological parameters such as σ_8 and w (see Chapter 2). Therefore, cluster catalogs spanning a wide range of masses and redshifts have the potential to tightly constrain cosmological parameters. However, these studies rely on the accurate determination of the relations between observables, such as the integrated SZE flux, and the total mass of clusters.

Astrophysical processes in clusters can contribute significant scatter to the observable-mass relationships, discussed further in §2.3. In particular, major and minor mergers can drive clusters out of the assumed state of hydrostatic equilibrium and bias inferred mass estimates. High-resolution imaging with X-ray and SZE instruments such as MUSTANG can reveal merging events and help determine the extent to which cluster observables are biased by the associated astrophysical phenomena.

Most recent observations of the ICM, especially at higher redshifts, have focused on inner parts of clusters (R $\lesssim$ few Mpc), primarily due to lack of observing sensitivity and angular resolution in the lower density regions of the clusters at large radii. Accurate measurements of the physical properties of the ICM in cluster outskirts can provide a better understanding of large-scale structure formation and place tighter

constraints on cosmological parameters such as the baryon mass fraction Ω_b and Ω_m. We expect MUSTANG-1.5 to measure the ICM at high-resolution out to the virial radius of a large number of clusters, which is discussed in Chapter 7.

The spatial fluctuations of the SZE as a function of angular scale, or the SZE power spectrum, is a very sensitive function of cosmological parameters controlling the growth of large scale structures, in particular σ_8 and Ω_m. Measurements of the total CMB power spectrum with ground-based instruments such as ACT and SPT probe the high ℓ modes ($\ell \sim 1000$) where the SZE dominates over the primary CMB. After making assumptions for the systematic uncertainties due to contributions from radio sources, thermal dust emission, the Cosmic Infrared Background (CIB), and the kSZE, the SZE power spectrum can be extracted from the total CMB power spectrum. The amplitude of the SZE spectrum determined in this way was found to be $\sim 2\sigma$ lower than expected [Reichardt et al. 2012; Sievers et al. 2013]. However, the SZE power spectrum at small angular scales depends strongly (at the tens of percent level) on cluster physics [Shaw et al. 2010; Battaglia et al. 2012], therefore a better understanding of astrophysical processes in clusters may lead to improved cosmological constraints.

For more details on cosmological parameters constraints derived from observations of galaxy clusters see the recent review by Allen et al. 2011.

1.6 Thesis Organization

In Chapter 2, I discuss the formation and evolution of galaxy clusters and our current understanding of the ICM properties. In Chapter 3, I give an overview of the

MUSTANG instrument on the Green Bank Telescope. In Chapter 4, I present the 2010-2013 MUSTANG observations of the CLASH clusters and the multi-wavelength analysis described in Young et al. [2014, *in prep.*]. In Chapters 5 and 6, I introduce the next generation instrument MUSTANG-1.5, constructed at UPenn and expected to achieve first light in the coming fall. I focus primarily on my work to implement the novel microwave multiplexing readout electronics, developed in a collaboration with NIST and NRAO. Finally, I discuss proposed observing programs for MUSTANG-1.5 and the expected scientific capabilities of the new instrument in Chapter 7.

Chapter 2

Galaxy Clusters

Clusters are massive ($M \gtrsim 10^{14}\ M_{\odot}$) mostly spherical structures comprised of thousands of individual galaxies, diffuse plasma, and, most of all, dark matter. They generally extend several Mpc in diameter and contain a ratio between baryonic and dark matter mass ($f_b = (M_{\rm gas} + M_{\rm galaxy})/M_{\rm tot} \approx 13\%$) that is within 20% of the universal value ($f_b \approx$17%) [Komatsu et al. 2011; Gonzalez et al. 2013]. Clusters are therefore expected to represent a fair sampling of the matter content of the Universe, and their formation and evolution will provide a sensitive probe of cosmology [e.g., Allen et al. 2011].

Additionally, cluster assembly is governed by violent mergers of smaller mass groups and galaxies, many of which can dissipate energies $\gtrsim 10^{63}$ ergs [Sarazin 2002], which makes them unique laboratories for studying astrophysical phenomena. Some of these astrophysical observations include shocks and cold fronts [Markevitch & Vikhlinin 2007], ripples and sound waves [Fabian et al. 2006], cavities produced from active galactic nuclei (AGN) feedback [McNamara & Nulsen 2007], and sloshing

of the ICM within a cluster's dark matter potential. (e.g., ZuHone et al. 2010). In this chapter, I introduce basic details of galaxy clusters including the hierarchical formation paradigm, physical properties, observables, and the mass proxies important for using clusters for precision cosmology. I provide a general overview of these topics in order to motivate the construction of MUSTANG-1.5 and the early science program.

2.1 Cluster Formation

The matter content of the Universe is understood to be composed of $\sim 80\%$ dark matter and $\sim 20\%$ baryons [Hinshaw et al. 2013]. Following inflation and recombination, the Universe was patterned with a uniform and isotropic Gaussian random field of density perturbations, which collapsed under gravity to form a cosmic web of local overdensities and filaments (Figure 2.1; Springel et al. 2005). In the standard hierarchical model, galaxies begin to form under gravitational collapse in the potential wells of the overdense regions. The galaxies are pulled by gravity along the large-scale filaments and merge with other galaxies to form groups. These groups merge to form clusters, typically within dark matter halos at intersections of the filaments. For a recent review on cluster formation and evolution see Kravtsov & Borgani [2012].

The process of mass assembly within a typical cluster, is shown in Figure 2.2. Major and minor mergers occur throughout the formation history of the cluster and continue to occur in many clusters today. In the absence of recent merger activity, clusters are expected to relax into a state of hydrostatic equilibrium (HSE) where gravitational collapse is balanced by pressure support from the ICM [Sarazin 2002].

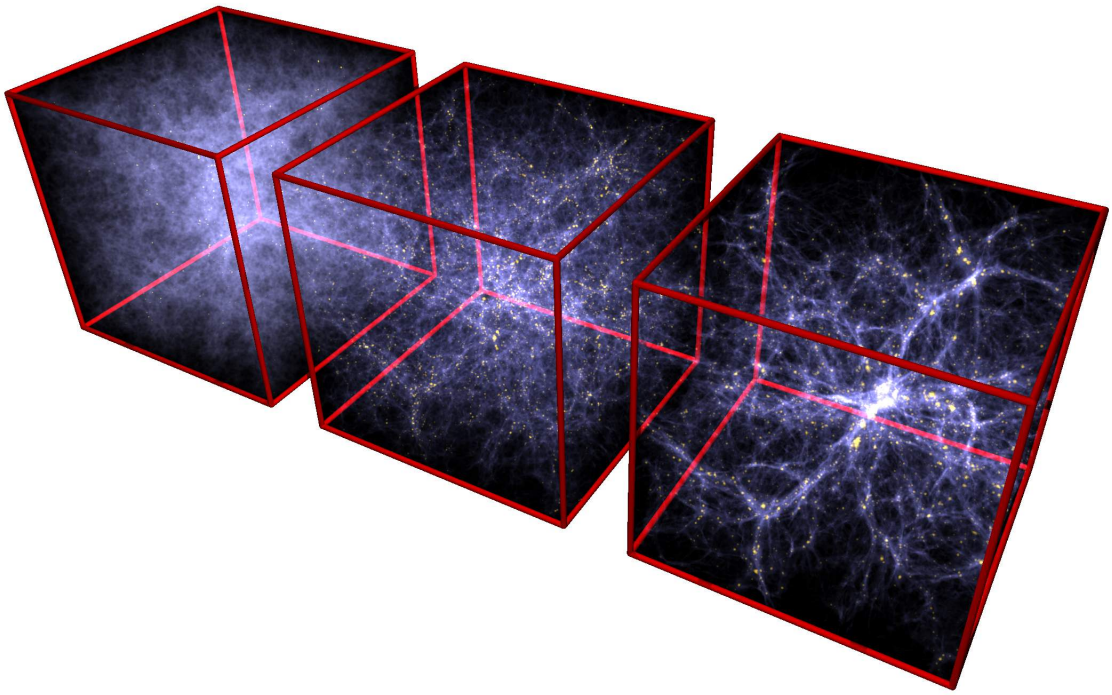

Figure 2.1: The Millennium Simulation [Springel et al. 2005], tracing the evolution of the dark matter distribution in the Universe. The initial density distribution is inferred from fluctuations in the CMB. The box size is 100 h^{-1}Mpc on a side and the boxes represent $z = 6$, $z = 2$, and $z = 0$, respectively, from left to right. As the Universe evolves, overdense regions of dark matter collapse to form an intricate web of filaments.

Assuming spherical symmetry, HSE is given by

$$\frac{dP}{dr} = -\frac{GM(< r)}{r^2}\rho, \tag{2.1}$$

where P is the gas pressure, G is the gravitational constant, $M(< r)$ is the mass enclosed within radius r, and ρ is the gas density.

Under the assumption of HSE (Equation 2.1) the cluster mass can readily be determined from observable properties of the ICM. However, deviations from HSE,

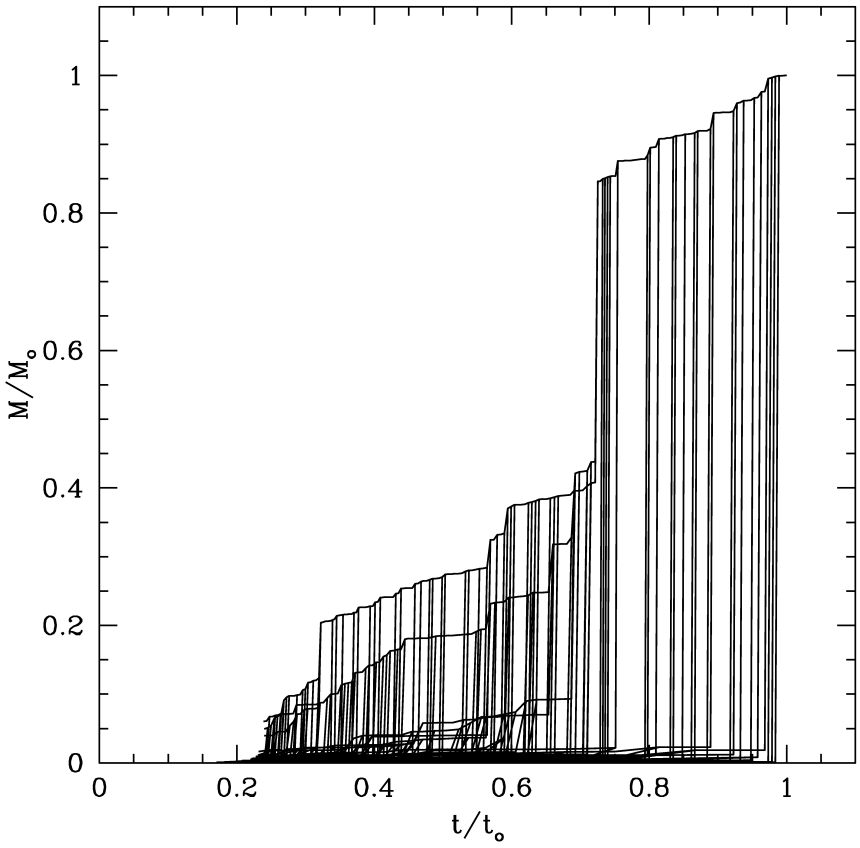

Figure 2.2: Merger tree illustrating the mass assembly history of a 10^{15} $M_{\odot}$ cluster predicted by N-body simulations. Vertical lines indicate when major and minor mergers occured. Figure taken from Randall et al. [2002].

such as those caused by merging activity, will impact the relationship between these quantities. Understanding the extent to which these scaling relations are biased by cluster dynamics is important for cosmological studies using clusters, as I discuss further in §2.3.

2.2 Cluster Properties

Cluster observables span the EM spectrum. X-ray and millimeter-wave SZE observations measure the physical properties of the ICM, such as density and temperature. Radio observations have discovered diffuse synchrotron emission in many galaxy clusters, typically associated with merger-induced shock fronts, turbulence, or AGN activity [e.g., van Weeren et al. 2011; Cassano et al. 2012]. Optical imaging reveals the individual galaxy population and provides measurements of gravitational lensing to constrain the cluster mass distribution. Figure 2.3 shows a variety of phenomena revealed by a composite image of the triply merging cluster MACS J0717.5+3745.

2.2.1 X-ray

The ICM is composed of free particles and ions in kinetic equilibrium with particle velocities described by a Maxwell-Boltzmann distribution

$$f(v) = \sqrt{\frac{2}{\pi}\left(\frac{m}{k_{\rm B}T}\right)^3} v^2 e^{-mv^2/2k_{\rm B}T}, \tag{2.2}$$

where $f(v)$ is the probability of finding a particle with velocity v, m is the particle mass, and T is the plasma temperature. In X-ray wavebands, the majority of the

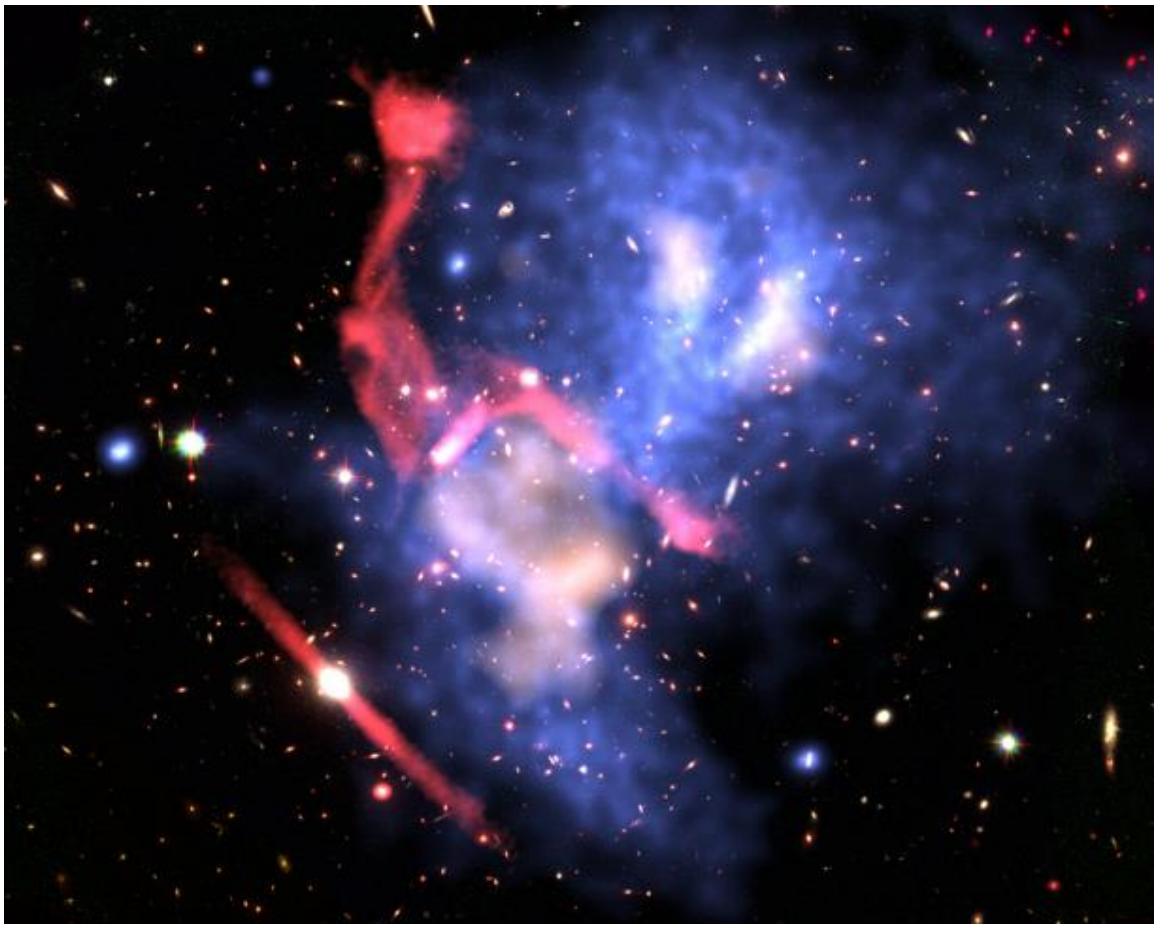

Figure 2.3: Composite image of MACS J0717.5+3745, a complex merger of at least three clusters at $z = 0.55$. The HST optical image is overlaid with X-ray surface brightness measured by *Chandra* (blue), 610 MHz radio observation from GMRT (red), and MUSTANG high-resolution SZE image (white). The X-ray data traces thermal emission in the ICM, while the SZE reveals non-thermal pressure structure in the hot plasma. Radio emission in the form of a relic likely points to shock-driven electrons interacting with strong magnetic fields. Figure courtesy of Reinout van Weeren.

emission in a $T \gtrsim 10^7$ K ICM comes from thermal Bremsstrahlung (or free-free) radiation produced when electrons are deflected by ions in the plasma. The emissivity ϵ_ν from this emission mechanism at frequency ν is given by [Sarazin 2002]

$$\epsilon_\nu \propto n_{\rm e} T^{-1/2} e^{-h\nu/k_{\rm B}T} \sum_i Z_i^2 n_i g_{ff}, \tag{2.3}$$

where $n_{\rm e}$ is the electron density, and the sum is given over all ions i with atomic numbers Z_i and densities n_i. The Gaunt factor g_{ff} is a correction factor applied to account for quantum mechanical effects.

The X-ray surface brightness (in units of counts cm^{-2} s^{-1} sr^{-1}) is

$$S_X = \frac{1}{4\pi(1+z)^3} \int {n_{\rm e}}^2 \Lambda_{ee}(T_{\rm e}, Z) d\ell, \tag{2.4}$$

where $\Lambda_{ee}(T_{\rm e}, Z) = \epsilon_\nu / {n_{\rm e}}^2$ is referred to as the X-ray cooling function. The X-ray surface brightness is strongly dependent on density and scales with temperature approximately as $T^{-1/2}$.

In addition to thermal Bremsstrahlung emission, line emission is also present and becomes dominant at lower plasma temperatures. Line emission depends on the density and abundance of the element responsible for the line as well as the plasma temperature. It can be shown that the line emission and continuum emission both scale as the square of density and the ratio between the two can be used to determine the temperature and heavy metal abundances of the ICM [Sarazin 2002].

Thus, X-ray observations represent a powerful probe of the physical properties of the ICM. The combination of high resolution continuum and spectroscopy provided

by the *Chandra* X-ray observatory has opened a new window into studies of cluster observations, and led to numerous discoveries of astrophysical phenomena in the ICM such as AGN bubbles and pressure ripples in the ICM, shocks, and cold fronts [e.g., Fabian et al. 2006; Markevitch & Vikhlinin 2007; McNamara & Nulsen 2007]. It is important to note, however, that X-ray emissivity falls off steeply with redshift $S_X \propto (1+z)^{-4}$ (Equation 2.4, in energy units) and most X-ray observations have been limited to relatively nearby clusters. Additionally, the strong dependence on density makes it difficult to image the outskirts of clusters where the ICM density is low.

2.2.2 SZE

In recent years, the SZE has been demonstrated as a powerful complementary probe of the ICM to X-ray observations. The SZE scales with ICM pressure integrated along the line of sight [Sunyaev & Zel'dovich 1972], specifically

$$\frac{\Delta I_{\rm SZE}}{I_0} = g(\nu, T_{\rm e})y, \tag{2.5}$$

where the primary CMB surface brightness normalization is $I_0 = 2(k_{\rm B}T_{\rm CMB})^3(hc)^{-2} = 2.7033 \times\ 10^8$ Jy sr^{-1}.[1] The function $g(\nu, T_{\rm e})$ describes the frequency dependence of the thermal SZE [Carlstrom et al. 2002] and includes the relativistic corrections of Itoh et al. [1998] and Itoh & Nozawa [2004]. Making the standard assumption that the ICM behaves as an ideal gas where $P_e = n_{\rm e}k_{\rm B}T_{\rm e}$ and using Equation 1.6, y can

[1]Radio astronomers often represent flux in units of Janskies where 1 Jy= 10^{-26} W/($m^2\sqrt{\rm Hz}$)

be written as

$$y = \frac{\sigma_{\rm T}}{m_{\rm e}c^2} \int n_{\rm e} k_{\rm B} T_{\rm e}\, d\ell, \tag{2.6}$$

where $\sigma_{\rm T}$ is the Thomson cross section, $m_{\rm e}c^2$ is the electron rest energy, and the integration is along the line of sight ℓ.

For SZE observations, it is useful to define the cylindrically integrated Compton-y within an aperture $\theta = R/D_A$

$$Y_{\rm cyl}(R) = Y_{\rm SZ} D_A^2 = D_A^2 \int y d\Omega, \tag{2.7}$$

where D_A is the angular diameter distance of the cluster and Ω is the solid angle of the integration. The spherically integrated Compton-y, which can be inferred from $Y_{\rm cyl}$, under the assumption of spherical symmetry, is given by

$$Y_{\rm sph}(R) = 4\pi \frac{\sigma_{\rm T}}{m_{\rm e}c^2} \int_0^R P_e(r) r^2 dr. \tag{2.8}$$

Following Mroczkowski [2011], $P_{\rm gas}(r) = (1 + 1/\mu_e) P_e(r)$, where $\mu_e \approx 1.17$ is the typical mean particle weight per electron for the ICM, and the thermal energy for an ideal gas is

$$E_{\rm th}(r) = \frac{3}{2} \int_0^R P_{\rm gas}(r) 4\pi r^2 dr. \tag{2.9}$$

Combining Equations 2.8 and 2.9, $Y_{\rm sph}$ is shown to directly trace thermal energy according to

$$Y_{\rm sph}(R) = \frac{2\sigma_{\rm T} E_{\rm th}(R)}{3(1 + 1/\mu_e) m_{\rm e}c^2}. \tag{2.10}$$

Then by the virial relation, assuming HSE and accounting for non-zero surface

pressure

$$2E_{\rm th}(R) - 3P_{\rm gas}(R)V = -U_g(R) \tag{2.11}$$

$$= 4\pi G \int_0^R M_{\rm tot}(r)\rho_{\rm gas}(r) r dr \propto Y_{\rm sph}(R), \tag{2.12}$$

where U_g is the gravitational energy for a spherical volume of gas with density $\rho_{\rm gas}$. Thus, for spherically symmetric clusters in HSE, $Y_{\rm sph}$ (and by extension $Y_{\rm SZ}$) is shown to be a direct tracer of cluster mass [see Mroczkowski 2011].

2.2.3 Optical and Gravitational Lensing

Optical (and near-IR) observations measure the galaxy population of clusters. Measurements of the richness, defined as the number of galaxies within a specified volume, luminosity, and velocity dispersion can provide constraints on the mass and dynamical state of the cluster.

Direct mass measurements can be obtained from optical observations of gravitational lensing. Gravitational lensing arises when light from a background object is bent due to gravity by a massive intervening object (the lens) before propagating to the observer. Typically there are two categories of lensing - strong and weak, characterized by the way in which the phenomenon manifests. Strong lensing measures individual background objects that appear either as multiple images or bright distortions in the shape of arcs (Figure 2.4). Weak lensing on the other hand measures the slight distortions in the shapes of a large sample of background objects. Both strong and weak lensing provide a means to infer the total mass of the lens.

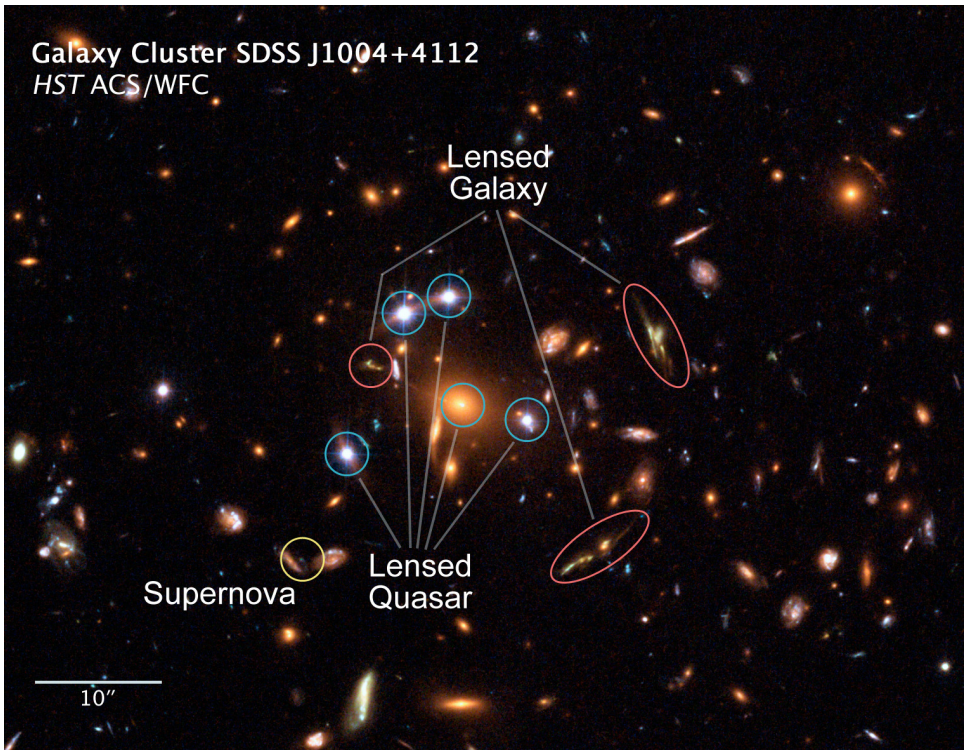

Figure 2.4: Observed gravitational lensing of background objects by intervening galaxy cluster SDSS J1004+4122. Multiple images of a background quasar and distorted lensing arcs of a background galaxy are clearly detected. Image credt: ESA, NASA, K. Sharon (Tel Aviv University) and E. Ofek (Caltech).

With the high resolution and sensitivity provided by the HST, lensing has become a powerful tool for measuring the total mass of $z \sim 0.5$ galaxy clusters. In fact, gravitational lensing measurements of the Bullet Cluster [Markevitch et al. 2002] provide some of the strongest evidence for the existence of collisionless dark matter.

2.2.4 Radio

Non-thermal components of the ICM, such as diffuse synchrotron emission in radio wavebands, play an important role in understanding the underlying plasma

astrophysics and cluster evolution. These radio sources are typically categorized as radio relics or radio halos based on their geometry and location within the host cluster. All clusters with radio halos are undergoing merger processes, but not all merging clusters host halos and this dichotomy has yet to be fully understood [Feretti et al. 2012].

Radio relics, such as the one revealed by the GMRT in Figure 2.3, are typically associated with shock fronts driven by cluster mergers, but the primary mechanisms by which radio halo and relics form are still debated [e.g., Brunetti et al. 2001; Keshet 2010]. As tracers of cluster mergers, these radio sources are useful in determining the dynamical state of clusters and therefore provide a better understanding the potential sources of scatter in the observable-mass scaling relations.

In addition to diffuse radio emission such as relics and halos, many clusters harbor radio-loud galaxies in the central brightest cluster galaxy (BCG). These AGN are understood to be associated with powerful jets of radiation emitted due to accretion of gas onto a supermassive black hole in the BCG. AGN are characterized as having steep spectral indices $\alpha > 0.7$ where $S_\nu \propto \nu^{-\alpha}$ and S_ν is the flux at frequency ν.[2] Therefore, AGN that are bright (tens of mJy) at low frequencies ($\nu < 1.4$ GHz), tend to be much fainter at higher frequencies where the SZE spectrum peaks, but they can still contribute significantly to the SZE flux measurements [see, e.g., Gralla et al. 2013].

[2]Sometimes α is defined as having the opposite sign such that $S_\nu \propto \nu^{\alpha}$.

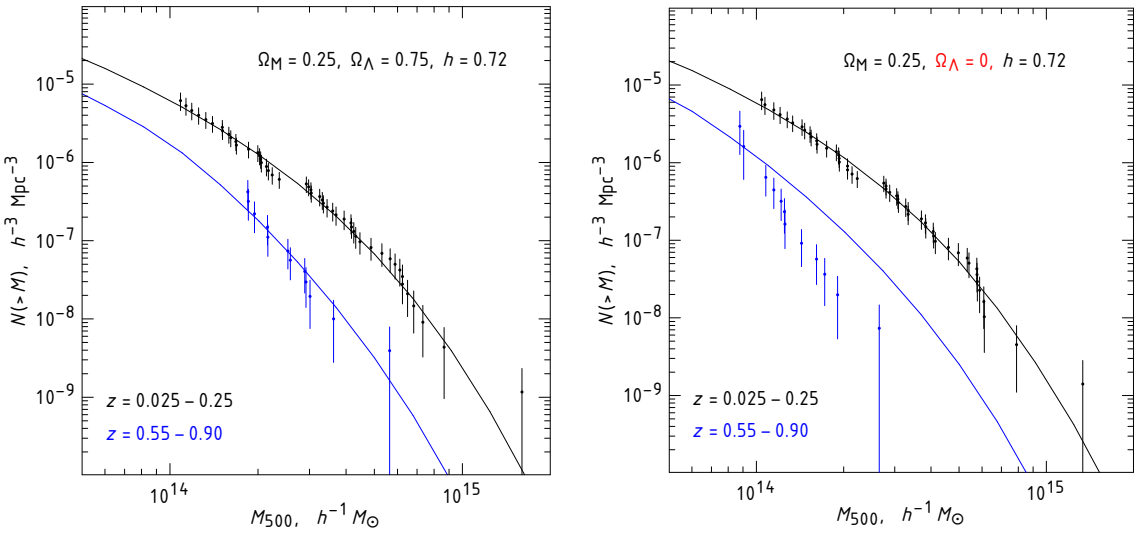

Figure 2.5: Cluster mass function in two different redshift bins for a cosmology with a cosmological constant (left) and without (right). The data do not match the model prediction for the $\Omega_\Lambda = 0$ cosmology. Figure taken from Vikhlinin et al. [2009].

2.3 Cluster Scaling Relations

As tracers of the evolution of large scale structure in the Universe, clusters represent an important cosmological probe. However, a better understanding of cluster astrophysics leading to accurate mass calibrations and low-scatter mass proxies will be essential to unlocking the full potential of clusters as tools for precision cosmology [Allen et al. 2011].

2.3.1 The Mass Function

The cluster mass function dN/dm given by Press & Schechter [1974] describes the number density of clusters as a function of their mass assuming that clusters form from the collapse of density fluctuations above a certain critical overdensity. The

evolution of the cluster mass function as a function of redshift can be written as

$$\frac{d^2N}{dzdm} = \left(\frac{dN}{dm}\right)\left(\frac{dV}{dz}\right), \tag{2.13}$$

where dV/dz describes the expansion history of the Universe. Since dV/dz depends on dark energy and dN/dm is sensitive to σ_8, measures of the cluster abundance are strongly dependent on cosmology. Figure 2.5, taken from Vikhlinin et al. [2009], shows the predicted mass function for two different cosmologies. It is clear that the data agree better for a Universe with a cosmological constant Ω_Λ than without. In order to constrain these cosmological parameters tightly, it is important to determine the mass accurately.

2.3.2 Scaling Relations

The total mass of a galaxy cluster can be directly determined from gravitational lensing, provided lensed background objects are visible and accurately measured. Achieving sufficient signal-to-noise to measure the mass in clusters spanning a wide range of masses and redshifts would be prohibitively expensive. However, observables that show a characteristic scaling with cluster mass and are easier to measure, such as X-ray luminosity or SZE flux, can be used to infer individual cluster masses with lower observational costs. Typically, in order to cover large regions of the sky, instrumental resolution is sacrificed for field of view and small-scale features from cluster astrophysical phenomena are not resolved. Physical processes often lead to departures from these observable-mass scaling relations. The MUSTANG program discussed in this thesis centers primarily on high-resolution measurements of clusters in order to

determine the extent to which these relations are affected by cluster physics.

Clusters forming primarily under gravitational collapse of collisionless particles are self-similar objects predicted to exhibit power-law scaling between cluster properties and total mass [Kaiser 1986]. Self-similarity means that clusters are identical when scaled by their mass. It is useful to define a convention R_Δ, which is defined as the radius at which the mean interior mass density of a cluster is Δ times the critical density of the Universe at the redshift of the cluster, such that $M_\Delta = (4\pi/3)\Delta\rho_c R_\Delta^3$. R_{500} is typically chosen to represent the radial extent of a cluster.

Some popular X-ray, SZE, and optical scaling relations include [e.g., Giodini et al. 2013]

$$L_X \propto E_z^{7/3} M_{\rm tot}^{4/3}$$

$$M_{\rm tot} \propto E_z^{-2/5} Y_X^{3/5}$$

$$Y_{\rm SZ} D_A^2 \propto E_z^{2/3} f_{\rm gas} M_{\rm tot}^{5/3}$$

$$M_{\rm vir} \propto \sigma_v^2 R_{\rm vir},$$

where L_X is the X-ray luminosity, $E_z = H(z)/H_0$, $M_{\rm tot}$ is the total cluster mass, $Y_X = M_{\rm gas} k_{\rm B} T_X$, $f_{\rm gas}$ is the gas fraction $M_{\rm gas}/M_{\rm tot}$, $M_{\rm vir}$ is the virial mass, σ_v is the global velocity dispersion, and $R_{\rm vir}$ is the virial radius. These scaling relations assume HSE, spherical symmetry, and dynamical equilibrium.

In the past decade, significant progress has been made to understand the sources of departures from the simple power-law scaling between cluster mass and observables. The left panel of Figure 2.6 shows the scaling between integrated Compton-y and the

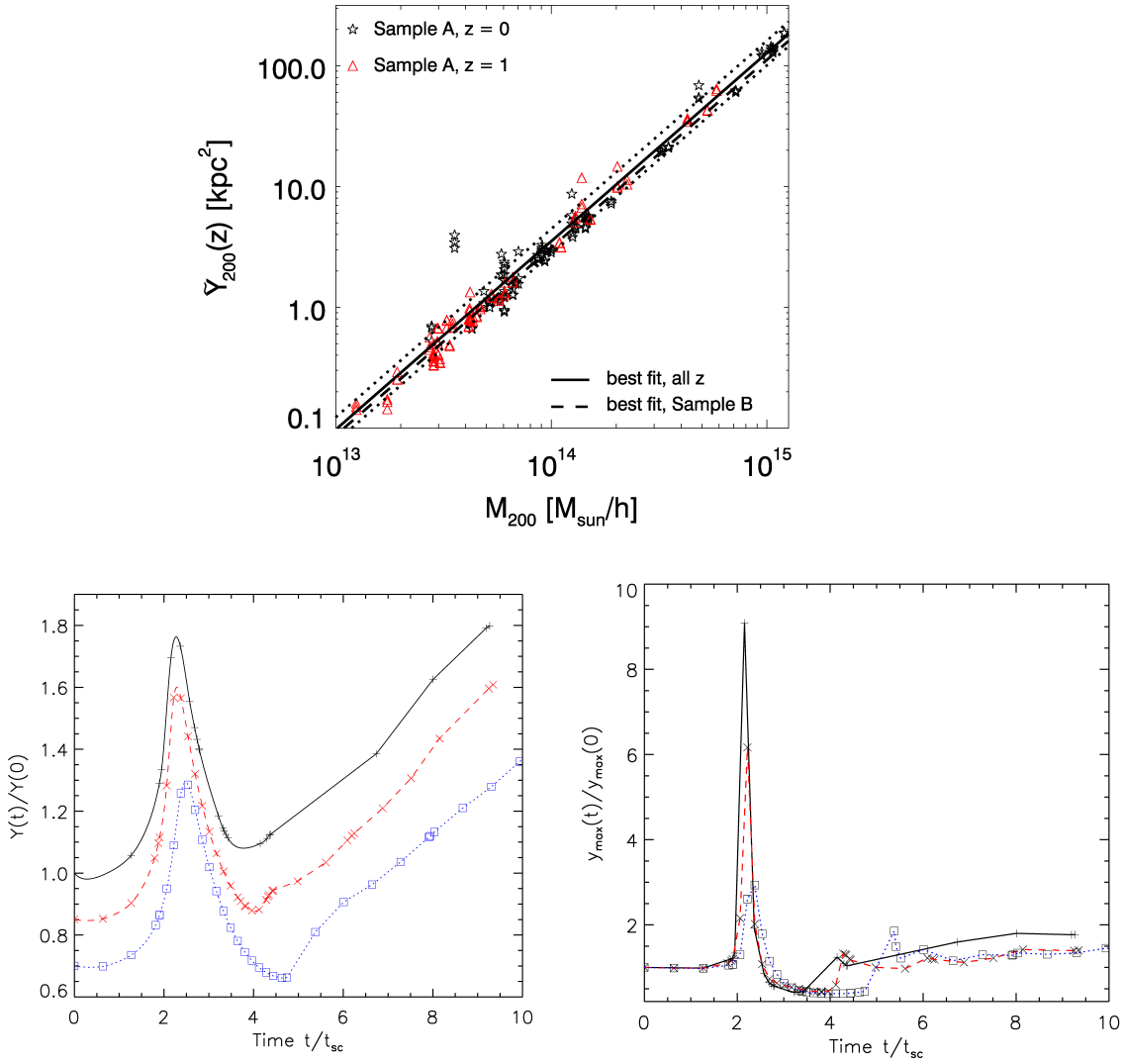

Figure 2.6: **Top:** Integrated Compton-y scaling relations from a simulated sample of clusters in a variety of dynamical states. The outliers correspond to clusters undergoing major mergers. This panel was taken from Krause et al. [2012]. **Bottom:** Integrated Compton-y (left) and peak y measured in simulated major mergers with three different impact parameters (differentiated by color). The curves have been arbitrarily offset for visualization purposes. The integrated Y is on average suppressed during the merger. The peak y is boosted strongly during the merger, but only for a short period of time before reaching a relatively stable value. The bottom panels were taken from Wik et al. [2008].

true cluster mass from a simulated cluster sample, taken from Krause et al. [2012]. The strong positive outliers correspond to major mergers included in the simulation. The right panels of Figure 2.6 show the boost in integrated and peak Compton-y, respectively, from a simulated 1:1 mass ratio major merger, taken from Wik et al. [2008]. Therefore, if the dynamical state and morphology of the cluster environment is neglected or unknown, the ICM observables may be skewed such that the inferred cluster mass differs significantly from the true value.

2.4 Cluster Profiles

The dark matter distribution in clusters is predicted by high-resolution numerical N-body simulations [Navarro et al. 1997] to follow a power law with slope that increases with radius, given by

$$\frac{\rho(r)}{\rho_c} = \delta_s \left[\left(\frac{r}{r_s} \right) \left(1 + \frac{r}{r_s} \right)^2 \right]^{-1}, \tag{2.14}$$

where δ_s is a characteristic scale density and r_s is a scale radius. Equation 2.14 is referred to as the Navarro-Frenk-White (NFW) profile. Since the gas pressure distribution is expected to follow the dark matter distribution, Nagai et al. [2007] adopt a generalized NFW (gNFW) pressure profile

$$\tilde{P}(X) = \frac{P_0}{(C_{500}X)^\gamma [1 + (C_{500}X)^\alpha]^{(\beta-\gamma)/\alpha}}, \tag{2.15}$$

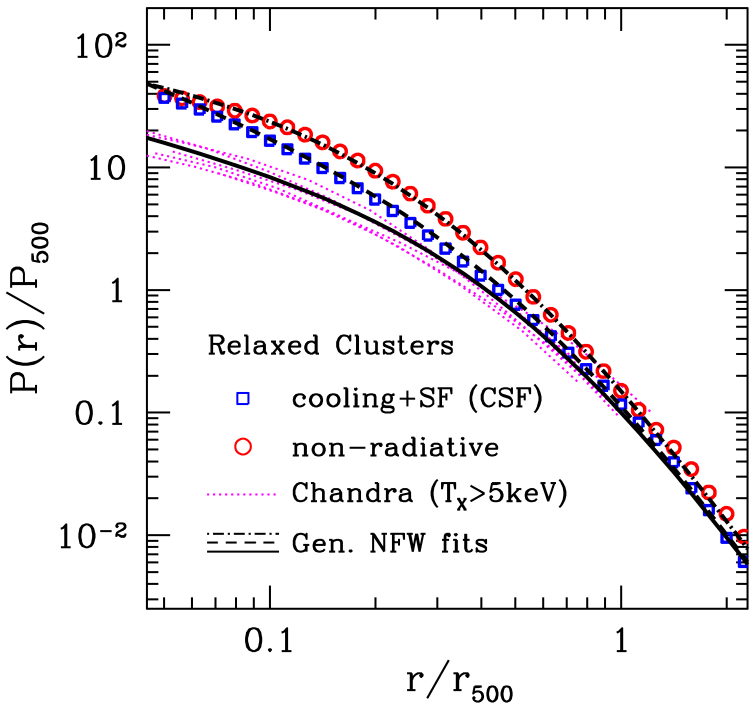

Figure 2.7: Generalized NFW profiles fit to simulated clusters and clusters observed by *Chandra*. The simulations that include processes such as radiative cooling and star formation, reproduce the gNFW ICM profile from observations better than the non-radiative simulations. Figure taken from Nagai et al. [2007].

where $X = R/R_{500}$, C_{500} is the concentration parameter, often given in terms of the scale radius R_s ($C_{500} = R_{500}/R_s$), P_0 is the normalization factor, γ is the inner slope ($r << R_s$), α is the intermediate slope ($r \sim R_s$), and β is the outer slope ($r >> R_s$). Nagai et al. [2007] find that the gNFW profile accurately describes pressure profiles in the simulated relaxed clusters as well as those measured by *Chandra* (Figure 2.7). In Chapter 4, a joint analysis of MUSTANG and Bolocam data is carried out to determine best-fit gNFW parameters for two potentially unrelaxed clusters.

2.5 Cluster Physics

In this chapter I have emphasized the importance of understanding the physical processes in the ICM in order to make cosmological inferences from clusters. As large scale cluster surveys continue to probe higher in redshift and lower in mass, where deep follow-up observations may be too costly or time-consuming, it becomes all the more important to understand the nature of departures from the simple observable-mass scaling relationships upon which these studies will rely. Mergers are perhaps the strongest source of deviations from HSE, and are often revealed by the presence of shocks and cold fronts. The sharp contrast in pressure across a shock provides an attractive target for high resolution SZE imaging aimed at determining the dynamical state of these complicated systems. Therefore, I will give a summary of these phenomena here and point the reader to Markevitch & Vikhlinin [2007] for a comprehensive review.

2.5.1 Shocks and Cold Fronts

As groups and subclusters fall into the gravitational potential wells in regions of high mass concentration (§2.1) they collide with kinetic energies in excess of 10^{65} ergs, a large fraction of which is dissipated in the form of shocks and turbulence in the ICM [Markevitch & Vikhlinin 2007]. Shocks can accelerate ultrarelativistic electrons producing diffuse synchrotron emission as these particles encounter magnetic fields in the ICM. Cold fronts are often produced at the boundaries of both the subcluster and the disturbed cluster core [Markevitch 2010].

A prime example of an energetic cluster merger is the system 1E0657-56, com-

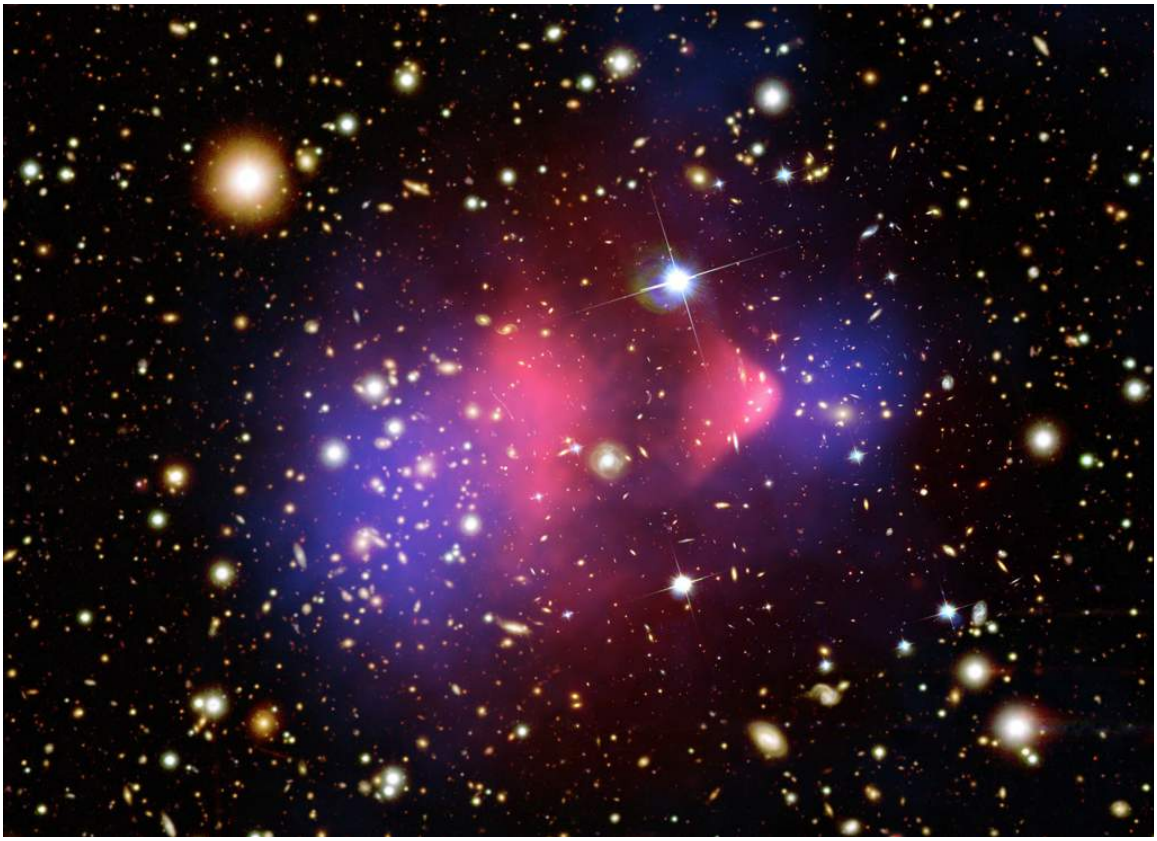

Figure 2.8: Composite image of the Bullet Cluster. The optical image from HST is overlaid with the X-ray surface brightness (red) and the dark matter distribution (blue). The separation between these components is due to the drag force acting on the collisional ICM, while the collisionless dark matter passes through unhindered. Image Credit: M. Markevitch et. al.; D. Clowe et al.; NASA/CXC/CfA; ESO WFI; STScI; U. Arizona.

monly referred to as the "Bullet Cluster". Figure 2.8 shows the composite image comprised of the X-ray surface brightness (red), mass distribution from weak lensing (blue), and galaxy population from optical imaging (color map). During this merger, the ICM from the subcluster (the bullet) is held back by ram pressure while the dark matter and galaxies continue to propagate westward[3]. As the cold dense subcluster passes through the massive cluster core at greater than the sound speed, it generates a prominent shock front followed (to the east) by a cold front at the tip of the bullet.

Figure 2.9 shows the thermodynamic properties of the ICM during a merger. The X-ray surface brightness and ICM density behaves similarly for both shocks and cold fronts, but the temperature and pressure behave quite differently. For cold fronts, the pressure is continuous with the temperature lower on the high density side and higher on the low density side. Shocks feature a sharp discontinuity in pressure, and the opposite trend in temperature. These characteristics are reflected in the right panel of Figure 2.9, which shows the cold front at $r \sim 12''$ and the shock front at $r \sim 45''$.

[3]Note: Astronomical maps display the sky as viewed from below and therefore East and West will appear reversed compared to a street map that is displayed as viewed from above.

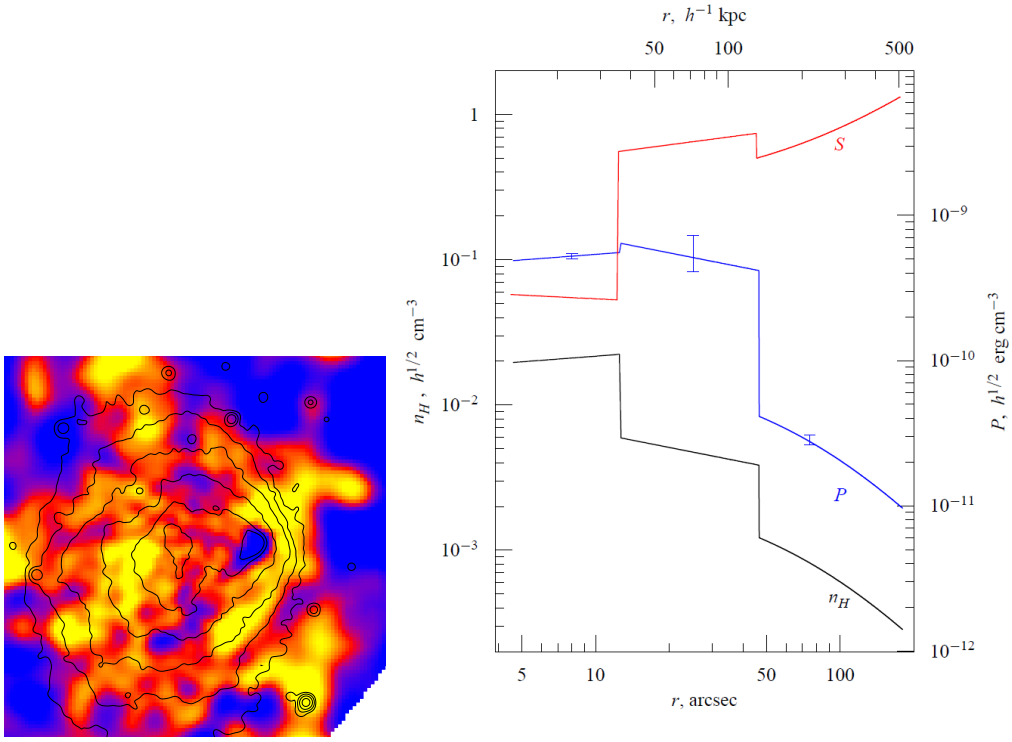

Figure 2.9: **Left:** Temperature map of the Bullet Cluster with X-ray surface brightness contours overlaid. The blue regions are $T < 6$ keV and the yellow regions have $T > 20$ keV. **Right:** Density, pressure, and entropy $S = Tn^{-2/3}$ profiles across the bullet and shock regions. The front edge of the cold dense bullet is bounded by a cold front, identified by continuous pressure and sharp discontinuity in density and X-ray surface brightness. West of the cold front there is a region of hot gas followed by both a density and pressure jump, as expected for a shock front. These figures were taken from Markevitch [2010].

Chapter 3

MUSTANG Instrument

MUSTANG was constructed between 2005 and 2007 in a collaboration between several institutions including primarily The University of Pennsylvania (UPenn), The National Radio Astronomy Observatory (NRAO), NASA Goddard Space Flight Center (GSFC), and The National Institute of Standards and Technology (NIST). The receiver is shown in Figure 3.1 and consists of a vacuum vessel (or cryostat), re-imaging optics, a closed-cycle refrigeration system, and a 64-pixel detector array. In this chapter, I describe the primary components of the instrument, characterize the cryogenic performance following several observing seasons, and present measurements of a 100-pixel detector array fabricated by NIST in 2010 for testing in MUSTANG. A summary of the MUSTANG specifications is given in Table 3.1.

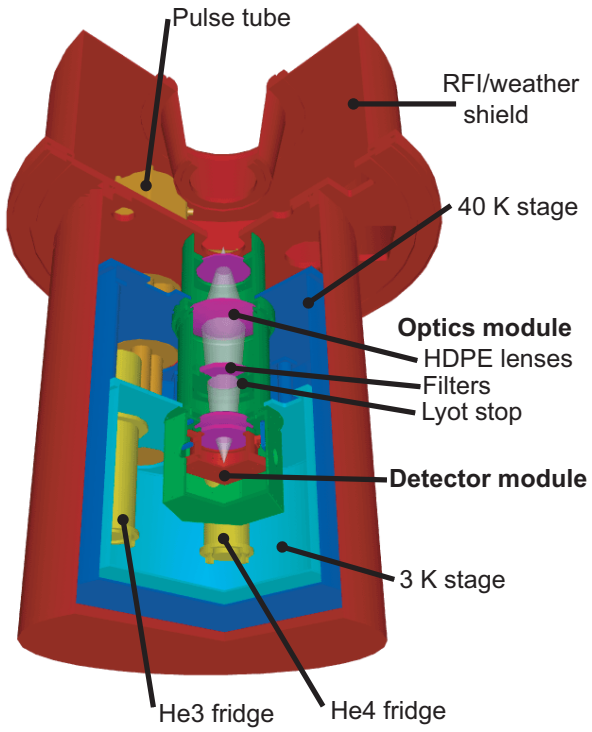

Figure 3.1: A cross-section of MUSTANG, taken from Dicker et al. [2008].

$N_{\rm det}$	64
T_c	490 mK
$T_{\rm bath}$	300 mK
G	372 pW/K
τ	5 ms
$P_{\rm sat}$	42 pW
NEP_G (theory)	6×10^{-17} W/$\sqrt{\rm Hz}$
NEP_G (measured)	1.6×10^{-16} W/$\sqrt{\rm Hz}$
NEP_γ	1.3×10^{-16} W/$\sqrt{\rm Hz}$
$P_{\rm inst}$	5 pW
RMS Noise $4.25' \times 4.25'$	201 μJy/beam$\sqrt{\rm hr}$

Table 3.1: Technical specifications of MUSTANG, including the total number of detectors ($N_{\rm det}$), TES transition temperature (T_c), thermal bath temperature ($T_{\rm bath}$), thermal conductance between the bath and TES (G), typical thermal time constant ($\tau = C/G$), saturation power ($P_{\rm sat}$), predicted and measured phonon noise (NEP_G), photon noise during typical weather conditions (NEP_γ), and the RMS noise level reached in a one hour observation (ignoring overhead) of a $4.25' \times 4.25'$ region.

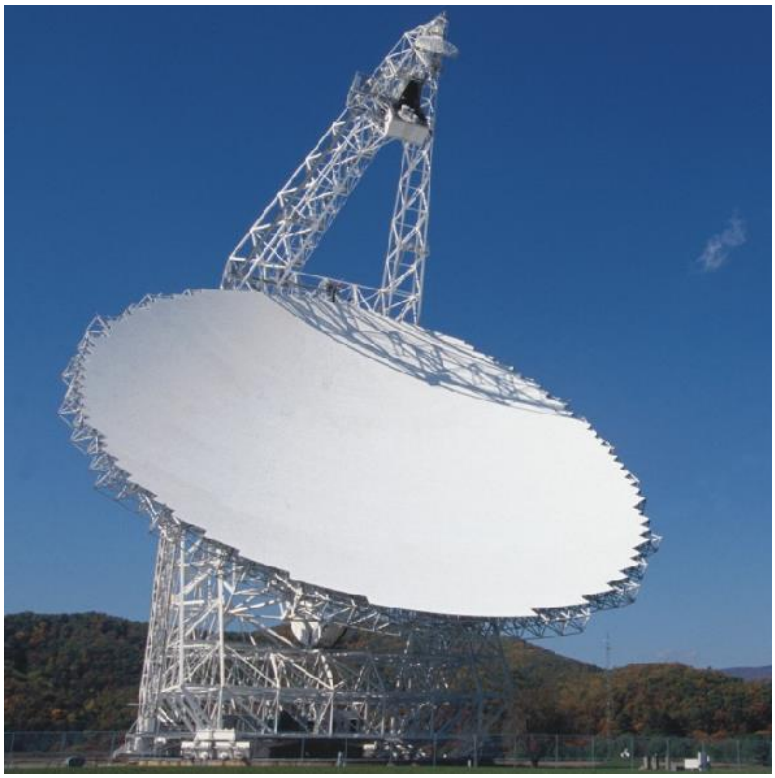

Figure 3.2: The 100-meter Green Bank Telescope located in Green Bank, WV, USA.

3.1 The Green Bank Telescope

The Green Bank Telescope (GBT; Figure 3.2) is a 100-meter diameter off-axis Gregorian telescope in Green Bank, West Virginia. The primary mirror consists of 2004 panels mounted with actuators on each corner. This "active" surface can be adjusted to correct for deformations due to gravity as the telescope slews to different elevations. The predicted correction factors are based on the median elevation within a particular scan, the physical structure of the GBT, and measurements from an Out-Of-Focus Holography (OOF) technique [Nikolic et al. 2007]. The corrected surface shape is typically accurate to $\sigma_s \sim 240\mu$m, which according to the Ruze Formula

[Ruze 1966] provides a surface efficiency of $\exp(-(4\pi\sigma_s/\lambda)^2) = 44\%$ at 90 GHz.

The receiver cabin is located at the Gregorian Focus of the telescope and houses up to eight different receivers, any of which can be rotated into focus by the GBT operator. MUSTANG is the first GBT receiver fielded in the highest frequency band, from 81-99 GHz. The other GBT receivers span nearly three orders of magnitude in frequency down to the VHF-band ($\sim$ 100 MHz), which enables a wide variety of science capabilities including studies of pulsar timing (e.g., Ransom et al. [2014]), galaxy formation and evolution (e.g., Lockman et al. [2012]), and astrophysical phenomena in galaxy clusters Mason et al. [e.g., 2010]; Korngut et al. [e.g., 2011]; Mroczkowski et al. [e.g., 2012]). The combination of angular resolution and sensitivity provided by the GBT at radio and microwave frequencies is unparalleled.

3.2 Detectors

The MUSTANG detector package (Figure 3.3) was fabricated at GSFC and contains an 8×8 array of Transition-Edge Sensor (TES) bolometers. TESs are operated in the narrow temperature region between superconducting and normal resistance states (Figure 3.4). The center of the transition is defined as the critical temperature T_c and the slope of the transition is given by $\alpha \equiv (T/R)dR/dT$. In this region, a small increase in temperature of the TES will yield a relatively large increase in resistance, and, with appropriate readout electronics, a measurable current. Below I briefly describe the principles behind a TES as they apply to the MUSTANG instrument.

A TES bolometer consists of a superconducting film coupled to an absorbing membrane (Figure 3.5). The TES is weakly coupled to a thermal bath at temperature T_b

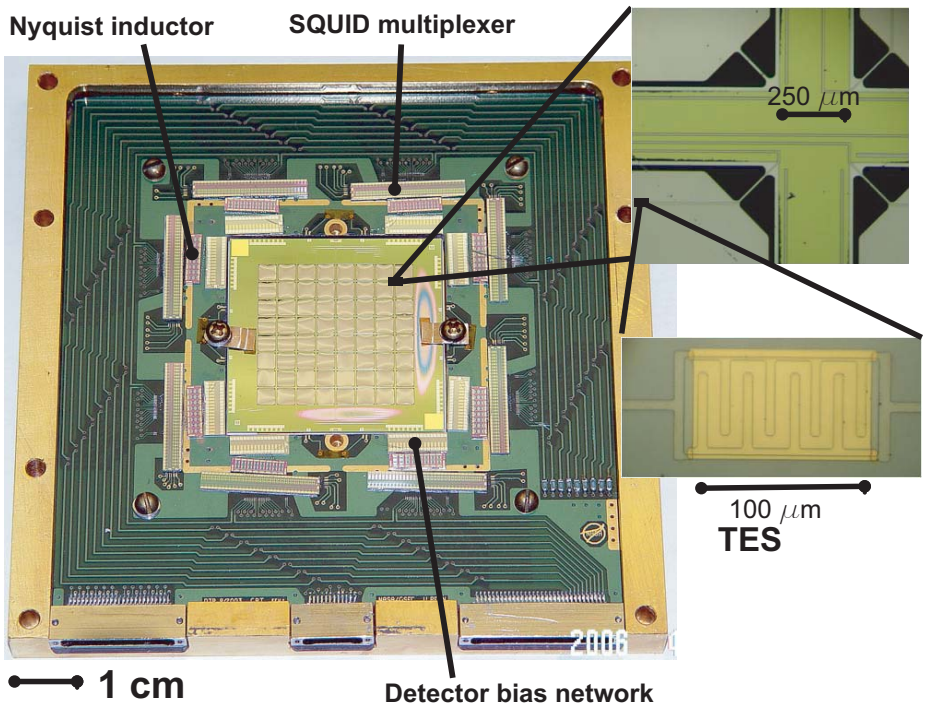

Figure 3.3: The MUSTANG detector array including the multiplexing chip and readout electronics. The enlarged view of the detector corners in the upper right shows the 10 μm legs that support the TES membranes. A close-up of the TES is also shown. Figure from Dicker et al. [2008]

through a thermal conductance $G \equiv dP/dT$. Incident optical power $P_{\rm opt}$ absorbed by the TES membrane will increase the TES temperature and therefore resistance $R_{\rm TES}$. At fixed bias voltage $V_{\rm bias}$, the Joule power ($P_{\rm Joule} = V_{\rm bias}^2/R_{\rm TES}$) will then decrease. This negative electrothermal feedback allows the TES to self-regulate in temperature and ensures that the total power on the bolometer ($P_{\rm opt} + P_{\rm Joule}$) remains constant [Irwin & Hilton 2005]. Therefore changes in the TES current will directly trace changes in the incident optical power. By measuring the change in current through the TES, one can then determine the optical power absorbed by the bolometer. A method for

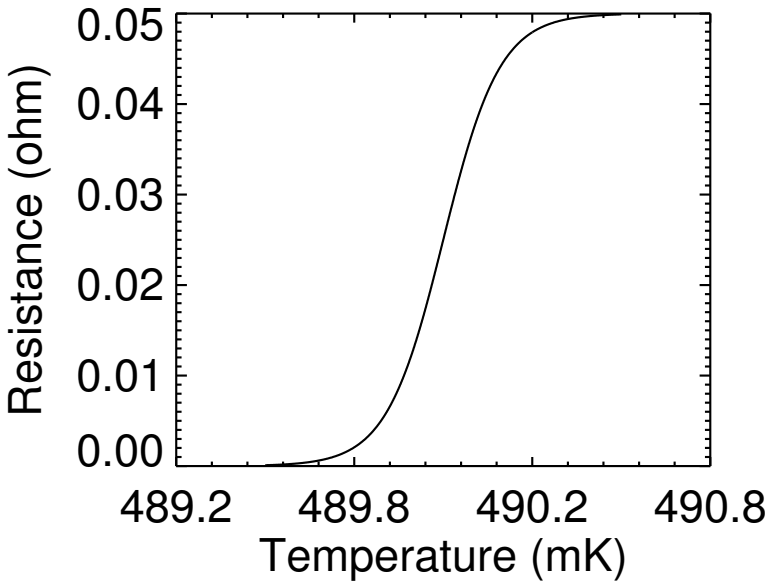

Figure 3.4: Normal-superconducting transition for a TES with $T_c = 490$ mK, $\alpha = 2000$, and $R_N = 50$ mΩ.

reading out a TES with a Superconducting QUantum Interference Device (SQUID) is described in §3.4.

The TES response is governed primarily by both a thermal and an electrical differential equation [Irwin & Hilton 2005]. Neglecting additional power contributions due to noise, the thermal differential equation is given by

$$C\frac{dT}{dt} = P_{\rm Joule} + P_{\rm opt} - P_{\rm bath}, \tag{3.1}$$

where C is the heat capacity of the bolometer, T is the TES temperature, and $P_{\rm bath}$ is the power flowing to the thermal bath from the substrate. In steady state, where

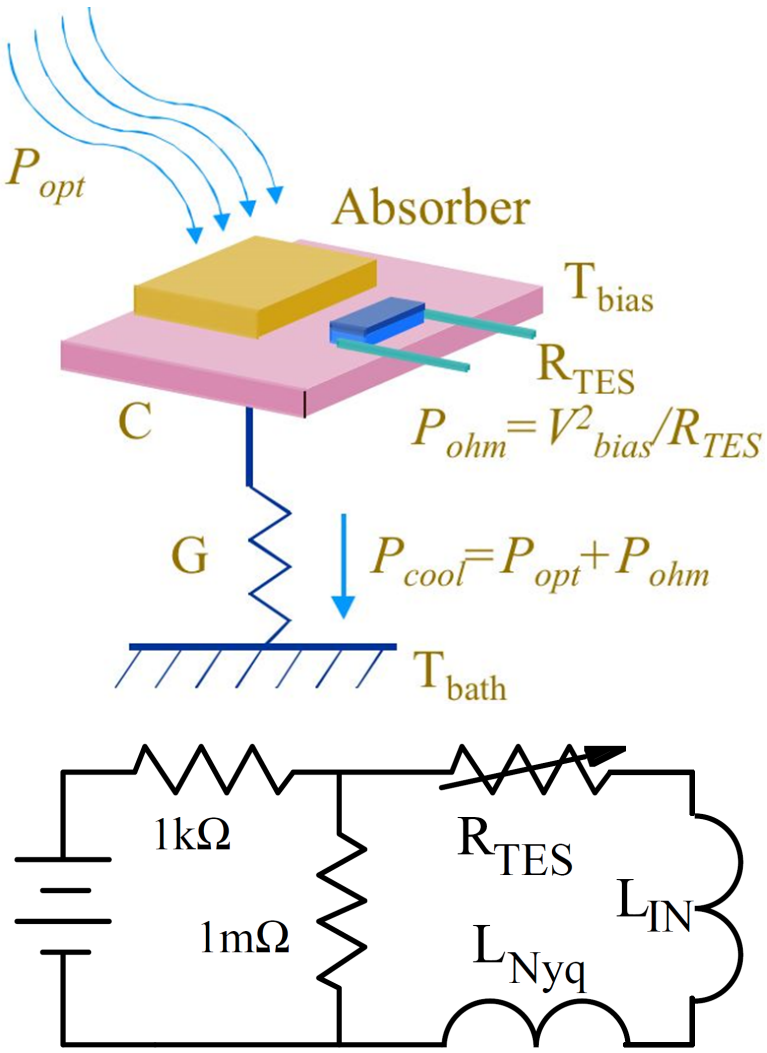

Figure 3.5: A TES bolometer. **Top:** Incident power is absorbed by a Bismuth coated membrane and heats a TES sensor. As the TES temperature changes the resistance changes. By measuring the change in current through the TES one can determine the amount of power deposited on the bolometer. Figure courtesy of Dominic Benford (NASA-GSFC). **Bottom:** A TES bias circuit. Current through a shunt resistor (1 mΩ here) in parallel with the TES provides a constant voltage bias. An input inductor generates a change in magnetic flux proportional to the change in current through the TES. A Nyquist inductor is sometimes used to filter out high frequency noise that would otherwise alias into the signal band. Figure taken from Benford et al. [2000].

the input power balances the power flowing to the thermal bath,

$$K(T^N - T_b^N) = P_{\rm opt} + P_{\rm Joule}, \tag{3.2}$$

where $K = G(T^{N-1})/N$ and N is a constant determined by the nature of the link between the bolometer and the thermal bath. For the MUSTANG bolometers $N \approx 2.8$. The electrical differential equation is

$$L\frac{dI_{\rm TES}}{dt} = V_{\rm bias} - I_{\rm TES}R_L - I_{\rm TES}R_{\rm TES}, \tag{3.3}$$

where L is the inductance, $I_{\rm TES}$ is the current through the TES, $V_{\rm bias}$ is the bias voltage, R_L is the shunt resistance $R_{\rm SH}$ plus any parasitic resistance $R_{\rm PAR}$, and $R_{\rm TES}$ is the resistance of the TES, which is a function of both temperature and current.

The TES response is characterized by an intrinsic thermal time constant $\tau = C/G$ determined by the heat capacity of the bolometer and coupling to the thermal bath. The electrothermal feedback mechanism provides an effective response time $\tau_{\rm eff}$, given by

$$\tau_{eff} = \frac{\tau}{(\alpha P_{\rm Joule}/GT) + 1}. \tag{3.4}$$

Since α is positive for TES bolometers, the TES effective time constant is typically much faster than for semi-conducting bolometers, which have a negative α.

For astronomical observing, it is important to tune C and G, and thereby $\tau_{\rm eff}$, appropriately based on the signal bandwidth. Increasing G will yield detectors with faster response times, but with higher intrinsic noise, as described in §3.3. For astronomical observing, the bolometers must respond quickly enough to measure a

signal as a source passes through a beam. The slew speed of the GBT for a typical MUSTANG scan is ~ 1 arcminute/s, which corresponds to a beam crossing time of ~ 170 ms. The MUSTANG detector time constants are on the order of milliseconds and therefore sufficiently fast for GBT observing.

3.3 Noise

It is often convenient to express all sources of noise in terms of the Noise Equivalent Power (NEP), which is the equivalent optical power that provides a signal-to-noise ratio of 1 in 1 Hz bandwidth. For MUSTANG the dominant sources of noise are photon noise, which is the fundamental noise limit due to the random arrival of photons across the astronomical beam, and phonon noise, which is determined by physical characteristics of the detectors and the coupling to the thermal bath.

3.3.1 Photon Noise

The intensity of light entering the telescope is subject to the random arrival of the individual photons within the telescope beam. The following calculations are based on GBT Memo 280[1] and primarily follow Sayers [2008]. For MUSTANG the primary emission sources are the atmosphere, the ground (from $\sim 2\%$ optical spillover of the primary mirror [Dicker & Devlin 2005]), and the internal components in the instrument itself. The optical loading from the instrument itself and emission from the ground is $P_{\rm inst} \approx 5$ pW.

Photon noise can be broken into two limiting terms based on the number of

[1]See www.gb.nrao.edu/∼bmason/pubs.html

photons in a particular mode

$$N_\gamma \propto (e^{h\nu/k_\mathrm{B}T} - 1)^{-1}. \tag{3.5}$$

If the number of photons is small ($h\nu << k_\mathrm{B}T$) then they will obey Poisson statistics. If the number of photons is large ($h\nu >> k_\mathrm{B}T$) they behave as bosons and bunch together. MUSTANG receives thermal emission from sources between 4 K ($k_\mathrm{B}T \sim 10^{-22}$ J) and 300 K ($k_\mathrm{B}T \sim 10^{-21}$ J). At 90 GHz, $h\nu \sim 10^{-22}$ J, so we need to include both limiting terms in our calculation of the photon noise, given by

$$NEP_\gamma^2 = NEP_\mathrm{Poisson}^2 + NEP_\mathrm{Bose}^2. \tag{3.6}$$

Then, assuming the optical power P_opt is uniform across the band, then according to Sayers [2008]

$$NEP_\gamma^2 = 2h\nu P_\mathrm{opt} + \frac{2P_\mathrm{opt}^2}{\Delta\nu}, \tag{3.7}$$

where $P_\mathrm{opt} = P_\mathrm{atm} + P_\mathrm{inst}$. We define $P_\mathrm{atm} = A\eta\epsilon k_\mathrm{B}T\Delta\nu$ for an atmosphere A airmasses deep[2], with emissivity ϵ, optical efficiency between source and detector η, and bandpass $\Delta\nu$. For MUSTANG, during acceptable weather conditions at the GBT, $\epsilon \sim 0.15$, and $\eta \sim 50\%$, and $T \sim 265$ K. At observation angles of 45° ($A = 1.4$), and with the 18 GHz bandpass, this gives $P_\mathrm{atm} \approx 4.5$ pW. Therefore, according to Equation 3.7 we expect $NEP_\gamma \approx 1.3 \times 10^{16}$.

If the dominant source of noise in an instrument is photon noise it is said to

[2]At lower pointing elevations the telescope is looking through more atmosphere, typically measured in airmasses A such that $A = \sec(z)$, where z is observing angle with respect to the zenith.

have achieved background-limited performance (BLIP) and no further reduction in instrumental noise will improve signal-to-noise. NEP_γ is often given as $NEP_{\rm BLIP}$.

3.3.2 Phonon Noise

Fluctuations in the measured signals also arise due to the thermal energy carriers, or phonons, between the detector and the thermal bath. This phonon noise (or G-Noise) NEP_G is given by [e.g., Mather 1982]

$$NEP_G^2 = 4k_{\rm B}T_c^2 G F_{link}, \tag{3.8}$$

where $F_{\rm link} = (1/2)(1 + (T_b/T_c)^{N-1})$. The power flowing to the thermal bath $P_{\rm bath}$ is

$$P_{\rm bath}(T) = \frac{G}{NT^{N-1}}\left(T^N - T_b^N\right). \tag{3.9}$$

The detector will be maintained at its equilibrium temperature by strong electrothermal feedback when the total power dissipated ($P_{\rm opt} + P_{\rm Joule}$) is less than $P_{\rm bath}(T_c)$. We write this power $P_{\rm sat}$ as

$$P_{\rm sat} = P_{\rm bath}(T_c) = \frac{GT_c}{N}\left(1 - \left(\frac{T_b}{T_c}\right)^N\right). \tag{3.10}$$

In order to achieve background-limited sensitivity ($NEP_G < NEP_\gamma$) it is important therefore to construct bolometers with values for G and T_c that minimize NEP_G, given by Equation 3.8, but provide a saturation power that is sufficiently high for the expected optical loading during observing. For MUSTANG, the poorest

weather conditions under which we would collect data correspond to ~ 12 pW optical load. Taking into account a safe margin for error, $P_{\rm sat} = 25$ pW and T_c 450 mK were chosen as target values. For $T_b = 300$ mK, this corresponds to $G = 229$ pW/K and a theoretical $NEP_G = 4.4 \times 10^{-17}$ W/$\sqrt{\rm Hz}$. However, after manufacturing we measured the bolometers to have $P_{sat} = 42$ pW and $G \sim 372$ pW/K, which yields $NEP_G \approx 6 \times 10^{-17}$. The sensor NEP was directly measured from detector power spectra and determined to be $\sim 1.6 \times 10^{-16}$ W/$\sqrt{\rm Hz}$ at 10 Hz, which far exceeds our estimates and pushes MUSTANG into a detector-limited performance regime [Dicker et al. 2008].

3.3.3 NIST Test 100-pixel Array

In late 2010, we commissioned a new 10×10 TES array from NIST (Figure 3.6) to try for lower detector NEPs and saturation powers.

Several test TES pixels were characterized in the lab in order to determine the optimal design for the 100-pixel array. Plots of the TES current as a function of applied bias voltage, referred to as I–V curves, are shown in Figure 3.7. We measured the time constants of the TESs by applying a square wave to the detector bias lines (see Figure 3.8). The optimal TES design was found to be one with 50% of the SiN membrane etched away, providing a time constant $\tau \approx 11$ ms and saturation power $P_{\rm sat} = 40$ pW.

We received the 100-pixel array, which was constructed using the etched SiN design, during a maintenance period in December 2010. The measured I–V curves showed large variations in transition temperatures among detectors within the same

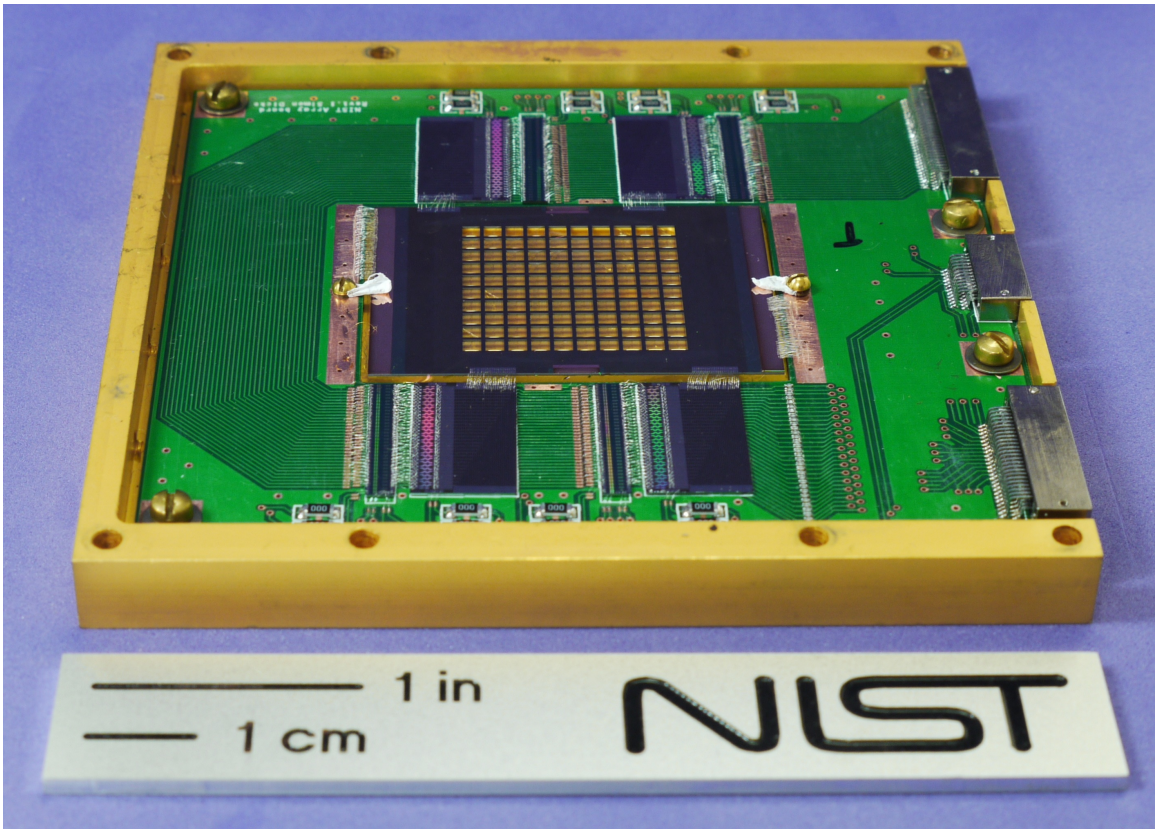

Figure 3.6: The 10 × 10 array fabricated by NIST for use in MUSTANG.

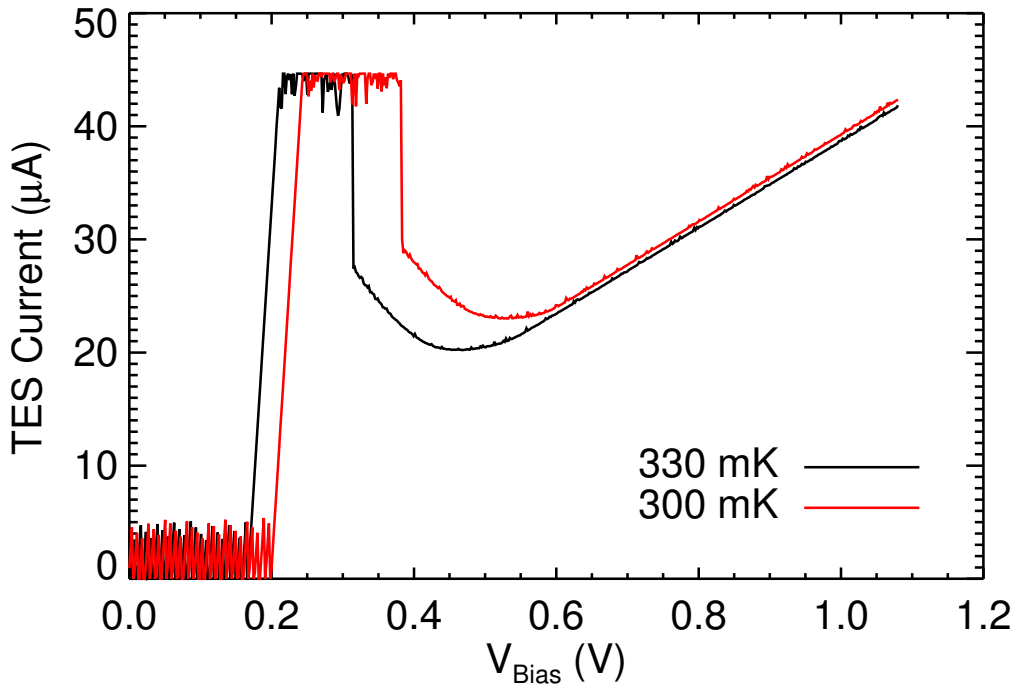

Figure 3.7: Measured I–V curve at two different bath temperatures for a test pixel with 50% SiN absorber removed by etching. T_c is determined in advanced by measuring current as a function of bath temperature for a fixed bias voltage. The I–V curves at measured at varying bath temperatures provides P_J as a function of T_b at the assumed T_c. Then using one can determine the G and N values from fits to Equation 3.2.

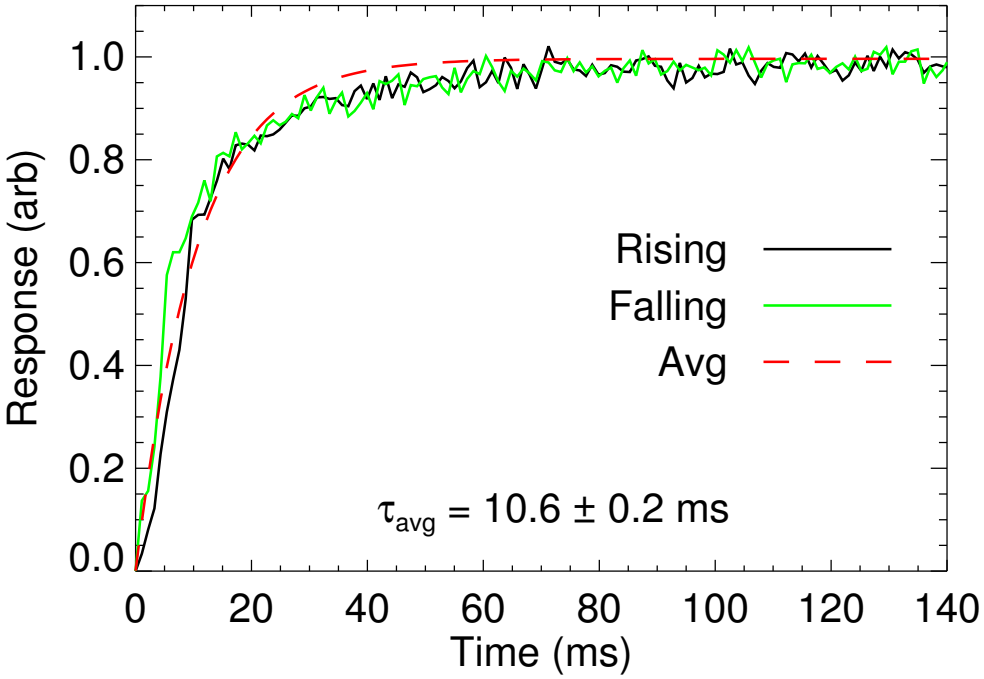

Figure 3.8: TES response to a 0.5 Hz square wave for rising (black) and falling (green) regions of the input waveform, averaged over several periods. The falling response curve has been flipped and normalized such that it can be more easily compared by eye to the rising response curve. The best fit average time constant for this particular pixel was found to be 10.6 ± 0.2 ms.

column (Figure 3.9). Since a single TES bias is shared within each column (described further in §3.4), this would greatly reduce the overall number of responsive detectors during normal operations. We also found the time constants to be considerably slower on average than that of the test pixel. Lastly, we measured the white noise level to be almost twice as high as the original 8×8 array. Therefore, we deployed MUSTANG with the proven GSFC array for subsequent observing seasons.

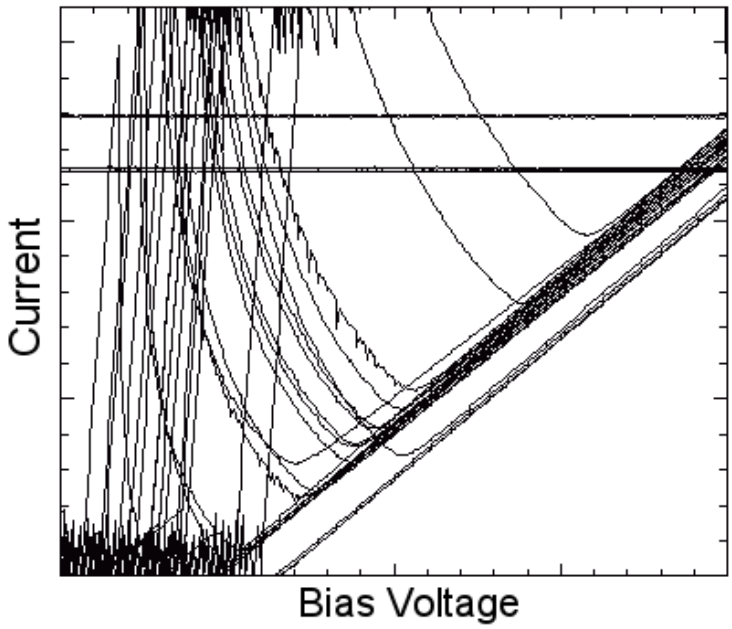

Figure 3.9: I–V curves for column 1 of the 10×10 NIST array. Since the bias voltage is shared by each of the rows, there are very few pixels in this column that will be on the transition for a given bias. The other columns in the array showed similar scatter in T_c.

3.4 Time-Division Multiplexing Readout

Time-Division Multiplexing (TDM) is a technique used in many large scale TES arrays including the polarization sensitive receiver on the Atacama Cosmology Telescope (ACTPol; Niemack et al. [2010]), the balloon-borne CMB polarimeter SPIDER [Filippini et al. 2010], and the BICEP2 telescope [Ogburn et al. 2010]. In an array with many tens to thousands of detectors, reading out individual detectors would require a prohibitive number of wires. Instead pixels are grouped into logical columns and rows (not necessarily based on the physical geometry of the array) and read out sequentially.

A schematic of the MUSTANG SQUID readout circuit is shown in Figure 3.10.

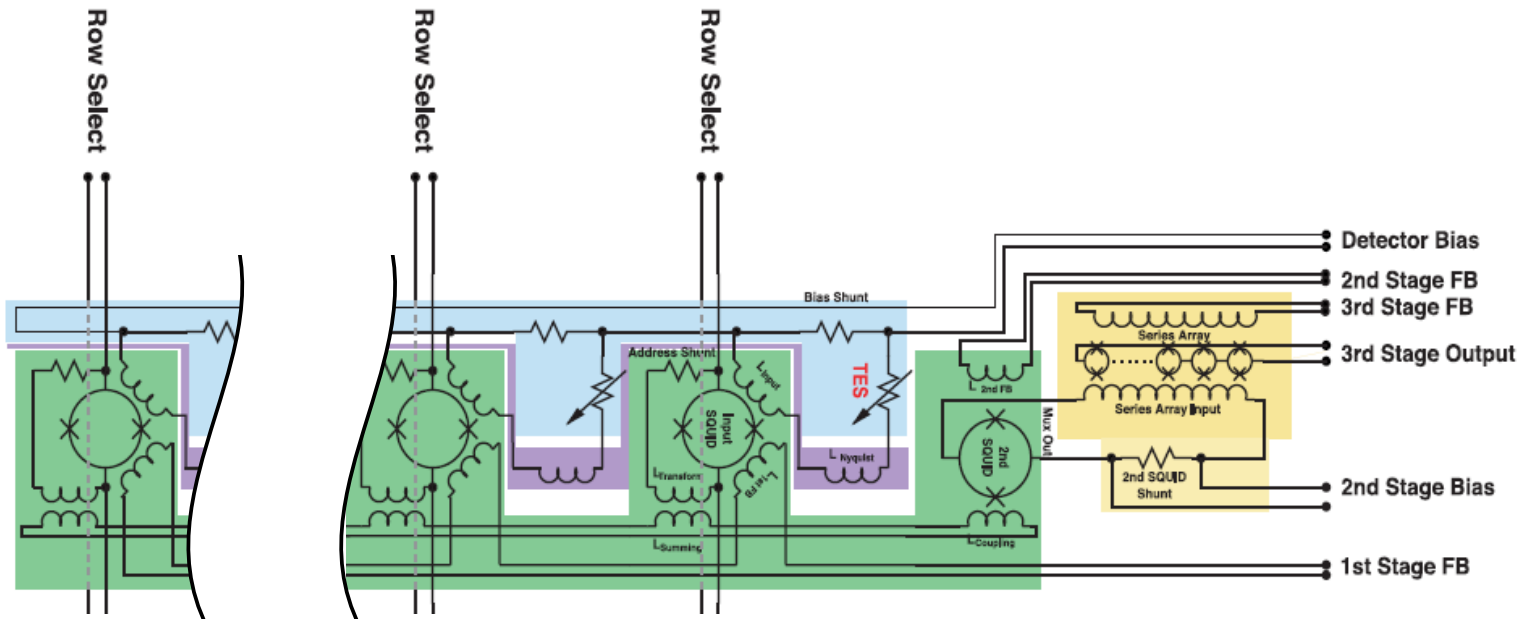

Figure 3.10: A schematic of one column in the MUSTANG TDM. The green shaded region indicates the multiplexer circuit, blue indicates the TES circuit, purple is a nyquist inductor chip intended to prevent high-frequency noise from aliasing into the readout, and yellow is the "series array" module containing the 3rd stage SQUID amplifier array. Figure adapted from Benford et al. [2003].

The TES circuit in MUSTANG is inductively coupled to a SQUID amplifier which acts essentially as an extremely sensitive magnetometer. A change in TES current will generate magnetic flux through the SQUID, which will induce a change in current through the SQUID. Each SQUID has two inputs, a bias voltage and a magnetic flux offset. The bias voltage for each SQUID is set such that the SQUID operates at the steep, linear region of its sinusoidal response. The flux offset, or feedback flux, is automatically adjusted by the warm readout electronics to keep the SQUID at the optimal operating point. The voltage necessary to generate this feedback flux, which traces the power incident on the bolometer, is recorded by the warm readout electronics.

The MUSTANG 64-pixel array is divided into 8 columns and 8 rows. Each pixel is coupled to a 1^{st} stage SQUID (SQ1) and each row of SQ1s shares a common bias voltage. The SQ1s in a column share a common feedback flux and are inductively coupled to a summing circuit, which is in turn coupled to a 2^{nd} stage SQUID (SQ2). At any given time, voltage bias is applied to only one row of SQ1s and the rest of the rows are set to zero. Therefore, although each SQ2 measures the combined flux from all SQ1s in a column, only one SQ1 in that column will be active at a time and the rest of the SQ1s will be superconducting. By activating each row sequentially, every pixel can be read out individually. The SQ2s are inductively coupled to a series of SQUIDs (SQ3s), which provide a final stage of amplification before the output is routed to the room temperature electronics.

3.5 Cryogenics

The MUSTANG array is cooled to 300 mK with a combination of Pulse Tube (PT) cryocooler, ^{4}He adsorption refrigerator, and ^{3}He adsorption refrigerator. The PT provides continuous cooling with thermal stages at 40 K and 3 K. The adsorption fridges are closed vessels containing a volume of activated charcoal charged with ^{4}He or ^{3}He, at least one condensation stage, and an evaporation pot. A schematic of the cryogenics is shown in Figure 3.11. A cryogenic cycle consists of heating and then cooling the charcoal, which will provide base temperatures of 700 mK (for ^{4}He) and 300 mK (for ^{3}He).

The cycling procedure is as follows. At low temperatures ($\sim$ 3 K) the helium is completely adsorbed by the charcoal. A gas-gap heat switch controls the thermal link between the charcoal and the 3 K plate in the cryostat. At the start of the cycle, the charcoal is heated to release the helium, which will then condense on the 3 K stage and drip into the evaporation pot. When the evaporator cools to a pre-determined trigger temperature, at which point most of the helium is believed to have condensed, the charcoal heater is turned off and the heat switch is turned on. The charcoal now begins to cool and adsorbs the helium as it evaporates. This "pumping" reduces the temperature of the helium to the base temperatures mentioned above. The ^{3}He fridge is nearly identical to the ^{4}He fridge except that the primary condensing stage is coupled to the ^{4}He evaporator at 700 mK. When all of the ^{3}He evaporates, a new cycle must begin. A typical cycle for MUSTANG lasts more than 12 hours, which exceeds the maximum duration of an observing session.

The performance of the cryogenics depends strongly on the behavior of the PT, the

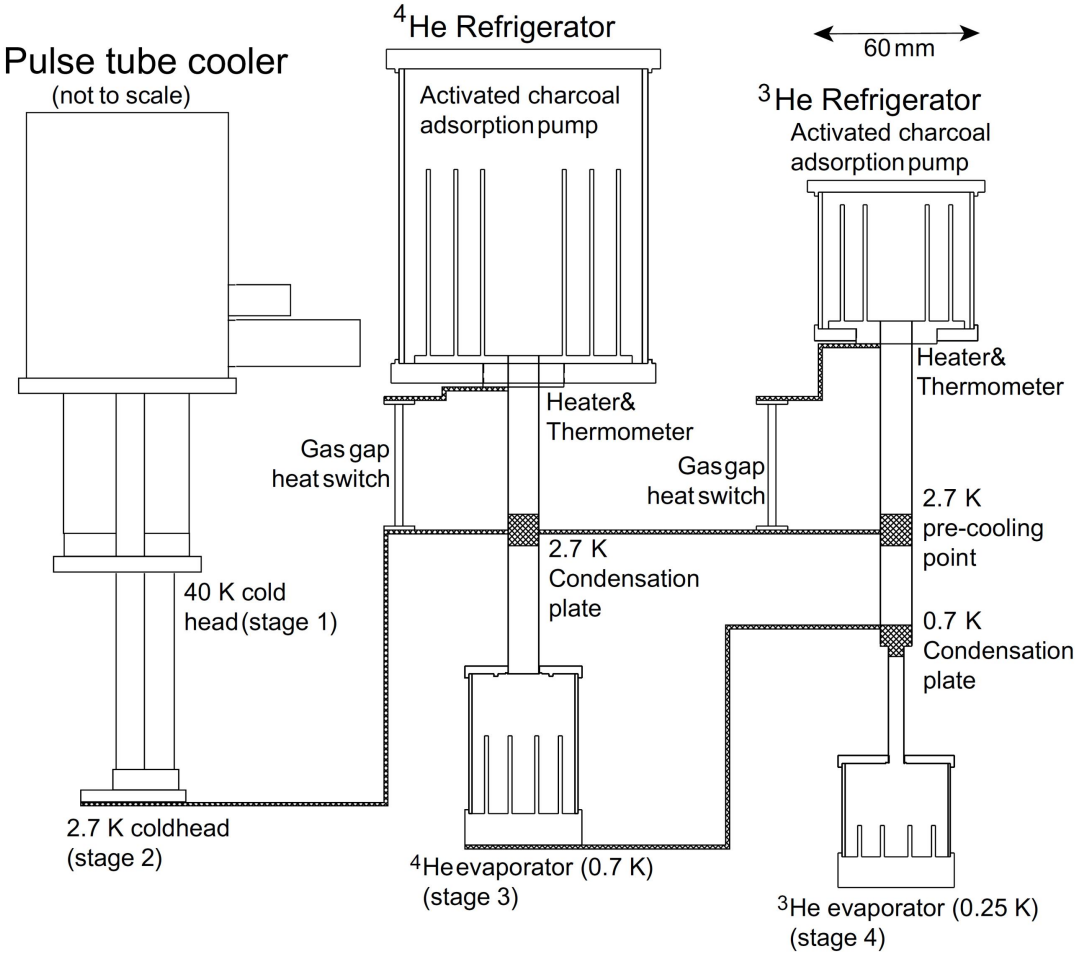

Figure 3.11: The closed-cycle refrigeration used for MUSTANG. The PT provides a 3 K stage for condensing ^{4}He and pre-condensing ^{3}He. The ^{4}He fridge provides a 700 mK condensing stage for the ^{3}He fridge. Figure from Devlin et al. [2004].

capacity of the fridges, and the parasitic load within the cryostat. Thermal stages are connected by heat straps made from Oxygen-Free High-Conductivity (OFHC) copper, which has very high thermal conductivity. Annealing these heat straps has been shown to greatly improve performance.

Chapter 4

MUSTANG Observations

Since 2008, MUSTANG has carried out hundreds of hours of observations. These include observations of AGN jets in M87 and Hydra A [Cotton et al. 2009], star formation in the Orion Nebula [Dicker et al. 2009], and high-resolution SZE images of more than a dozen galaxy clusters [Mason et al. 2010; Korngut et al. 2011; Young et al. 2014, *in prep.*; C. Romero et al. 2014, *in prep.*]. MUSTANG strongly confirmed (> 13-σ) the presence of merger activity in RX J1347.5-1145 [Mason et al. 2010; Korngut et al. 2011] hinted at by observations with the Nobeyama 45 m telescope [Komatsu et al. 2001]. More recently, Bolocam observations supported by MUSTANG provided evidence for the first detection of the kSZE in a single cluster [Mroczkowski et al. 2012; Sayers et al. 2013b].

In this chapter, I begin with a brief overview of the map making and calibration of the MUSTANG data. I then discuss the recent MUSTANG observations and scientific results, in particular those focused on the CLASH cluster sample. I summarize in general terms the multi-wavelength analysis carried out in Mroczkowski et al. [2012]

and Young et al. [2014, *in prep.*]. I then describe a map-domain joint fitting algorithm used in Young et al. [2014, *in prep.*] to fit gNFW profiles to both Bolocam and MUSTANG data. Finally, I present the results from the multi-wavelength analysis of MACS J0647.7+7015 and MACS J1206.2-0847.

4.1 MUSTANG Map Making

MUSTANG has two independent software pipelines, based in Interactive Data Language (IDL), for producing maps from time-ordered data (TOD), also referred to as timestreams. The first,***multimakemap***, is described in Korngut et al. [2011]. The second is a recently developed pipeline called ***mustangmap***, which uses different filtering techniques and an iterative algorithm that is less susceptible to contamination from bad data.

For a detailed description of the map making procedures that have been used with MUSTANG see Mason et al. [2010]; Korngut et al. [2011]; Korngut [2011]. Both pipelines employ a per-pixel high-pass filter to remove low frequency noise from the individual timestreams. Noise from the atmospheric emission is on large angular scales and can be removed by subtracting a common mode template from the timestreams. This template is constructed from the mean or median value across all live detectors for each sample. The subtraction is usually done iteratively to mask out detectors that are revealed to be excessively noisy after the first pass, which in turn provides a more accurate common mode template.

While the common mode subtraction is crucial to recover faint signals behind the bright atmosphere, it will also remove any astronomical signals of interest on angular

scales larger than the instantaneous field of view of the array. For MUSTANG the field of view is $\sim 42''$ and the common mode subtraction typically removes 90-95% of the bulk SZE flux from a typical cluster. This means that the primary strength of MUSTANG comes from the high angular resolution and the ability to image substructure associated with cluster astrophysical phenomena.

4.2 Flat Fielding and Absolute Calibration

Prior to generating a map, we determine the relative gains of each detector to account for variations in sensitivity across the array. Several times during an observing session a "CAL" scan is executed. During the CAL, the telescope slews off source and an optical load is applied by flashing an internal calibrator lamp with a slow ~ 1 Hz square wave. The signal is applied uniformly across the array so this allows us to determine the relative gain of each detector and convert the data from raw counts from the Digital-to-Analog Converter (DAC) to units of CALs. This also allows us to mask out the detectors that are optically unresponsive prior to map-making.

In order to convert the data from CALs into physical units such as Janskys, we observe two classes of calibrators during an observing session. At least once per session, we scan a primary calibrator, typically a small (unresolved) planet such as Uranus, for which the absolute flux is well-constrained at 90 GHz. Immediately after the primary calibrator scan, we observe a secondary calibrator, which is a bright compact source (typically a distant quasar) located near the science target. This allows us to determine the absolute flux of the secondary calibrator, which we expect to remain stable during a particular observing session.

Since the secondary calibrator remains close to the science target, we can scan it frequently throughout the night. This allows us to take into account any changes in optical sensitivity such as that due to weather or variations in pointing elevation. For every scan of the secondary calibrator we also repeat the "CAL" scan so that the conversion from DAC counts to Janskys is robust. As a bonus, the compact source provides a measurement of the telescope point spread function (PSF), which tells us when the telescope needs to be re-focused.

4.3 CLASH

The most recent MUSTANG scientific objective has been to follow-up all accessible clusters from the CLASH sample. The 25 clusters in CLASH have comprehensive multi-wavelength coverage, including deep 16-band HST imaging, and X-ray observations with *Chandra* and XMM-*Newton*. Bolocam at the Caltech Submillimeter Observatory (CSO) leads the CLASH SZE imaging efforts at 1.1 and 2.1 mm to measure pressure profiles in higher redshift systems than previously determined by X-ray observations [Sayers et al. 2013a]. Recently, using the optical, lensing, and X-ray measurements from the CLASH program, Bolocam provided new constraints on the scaling relations between SZE flux and cluster mass in $z \sim 0.5$ systems [Czakon et al. 2014]. For a detailed overview of the full CLASH science program see Postman et al. [2012].

MUSTANG brings to CLASH the high-resolution SZE imaging to detect substructure, and constrain ICM properties in the cluster cores. Bolocam and MUSTANG cover complementary angular scales since the MUSTANG FOV is roughly the same

Cluster	Centroid (J2000) R.A.	Dec.	z	Obs. Time (hrs)	Ref
Abell 209	01:31:53.1	−13:36:48	0.206	23	5
MACS J0329-0211	03:29:41.5	−02:11:46	0.450	25	5
MACS J0429-0253	04:29:36.0	−02:53:06	0.399	24	5
MACS J0647+7015	06:47:50.5	+70:14:53	0.591	26	4,5
MACS J0717+3745	07:17:32.1	+37:45:21	0.546	35	3,5
MACS J0744+3927	07:44:52.3	+39:27:27	0.698	12	2,5
Abell 611	08:00:56.8	+36:03:26	0.288	25	5
MACS J1115+0129	11:15:51.9	+01:29:55	0.355	25	5
MACS J1149+2223	11:49:35.4	+22:24:04	0.544	25	5
Abell 1423	11:57:17.4	+33:36:40	0.213	5	5
MACS J1206-0847	12:06:12.5	−08:48:07	0.439	25	4,5
CLJ1226+3332	12:26:57.9	+33:32:49	0.888	10	2,5
MACS J1311-0310	13:11:01.7	−03:10:51	0.451	21	5
RXJ1347-1145	13:47:30.8	−11:45:09	0.451	6	1,2,5
MACS J1423+2404	14:23:47.9	+24:04:43	0.545	22	5
Abell 383	02:48:03.3	−03:31:46	0.188	—	—
MACS J0416-2403	04:16:08.8	−24:04:14	0.420	—	—
RXJ1532+3021	15:32:53.8	+30:20:59	0.363	—	—
MACS J1720+3536	17:20:16.7	+35:36:23	0.387	—	—
Abell 2261	17:22:27.0	+32:07:58	0.224	—	—
MACS J1931-2635	19:31:49.6	−26:34:34	0.352	—	—
MACS J2129-0741	21:29:25.7	−07:41:31	0.589	—	—
RXJ2129+0005	21:29:39.7	+00:05:18	0.235	—	—
MS2137-2353	21:40:15.1	−23:39:40	0.313	—	—
RXJ2248-4431	22:48:44.8	−44:31:45	0.348	—	—

Table 4.1: Summary of MUSTANG CLASH observations. The columns give the name, X-ray centroid coordinates, redshift, total observing time (including 40-50% overhead for tuning and calibration), and reference publication. References are 1) Mason et al. [2010], 2) Korngut et al. [2011], 3) Mroczkowski et al. [2012], 4) Young et al. [2014, *in prep.*], 5) C. Romero et al. [2014, *in prep.*]. See Sayers et al. [2013a] for redshift references. Several clusters were not observed either due to scheduling constraints or because the systems were inaccessible to Green Bank during the September-April MUSTANG observing season and not targeted in the first place.

width as the $1'$ Bolocam beam. Therefore a joint analysis of Bolocam and MUSTANG data should provide a better understanding of the SZE flux on scales from $\sim 9''$ to $\sim 8'$. Coupled with the deep X-ray and HST observations, the dynamical and thermodynamical states of each CLASH cluster will be well constrained.

A summary of the MUSTANG CLASH observations is given in Table 4.1. Of the 25 clusters in the sample, MUSTANG observed 15 of them, six did not receive observing time, and four were excluded as MUSTANG targets because they are at declinations $< 20°$.

4.4 X-ray Derived Maps

Combined analysis of X-ray and SZE data has already proven to be a useful technique for characterizing the substructure in the MUSTANG maps [e.g., Korngut et al. 2011; Mroczkowski et al. 2012]. With the deep *Chandra* imaging and spectroscopy available for each CLASH cluster we were able to produce reliable X-ray derived SZE flux maps to compare directly to the MUSTANG images. This procedure relies on accurate temperature information and a measurement of the integrated SZE flux on large angular scales. The procedure is as follows.

Assuming the temperature is constant along the line of sight, we can rewrite Equation 2.4 as

$$n_{\rm e} \approx \sqrt{\frac{4\pi(1+z)^3 S_X}{\Lambda_{ee}(T_{\rm e}, Z)\ell}}, \tag{4.1}$$

where S_X is in units of photons cm^2 s^{-1} sr^{-1}. We approximate Equation 2.6 as $y \approx \sigma_{\rm T}/(m_{\rm e}c^2) n_{\rm e} k_{\rm B} T_{\rm e} \ell$ and use Equation 4.1 to derive from the X-ray data a "pseudo"-

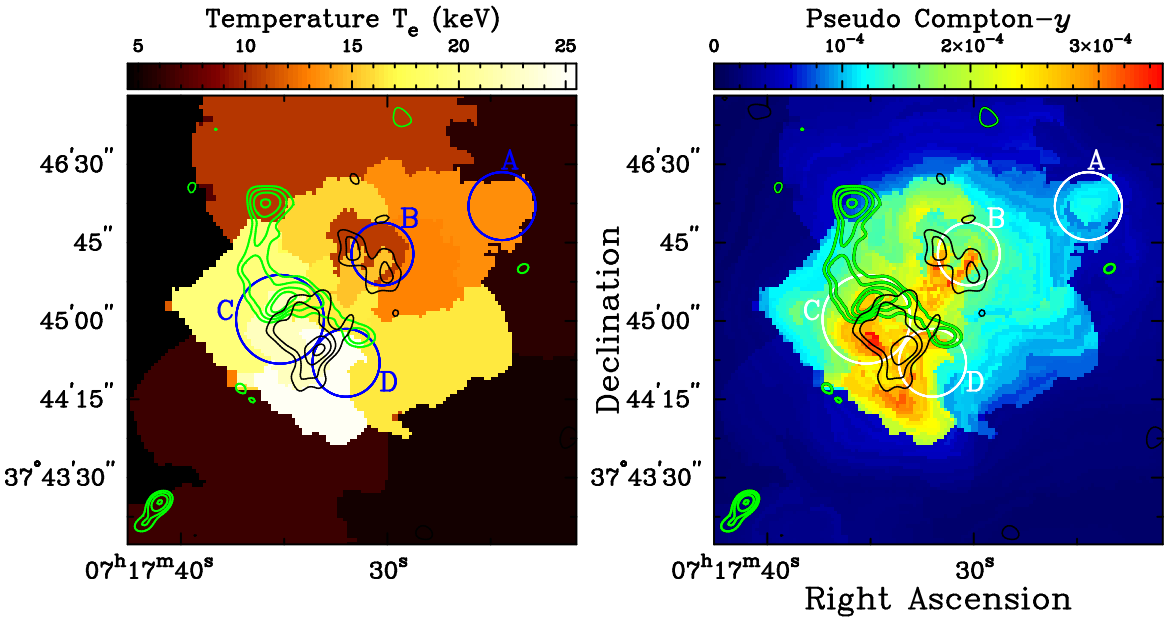

Figure 4.1: X-ray derived temperature (left) and pseudo-y (right) maps from *Chandra* observations of MACS J0717.5+3745. Optically identified sub-clusters from Ma et al. [2009] are circled. MUSTANG SZE contours are overlaid in black and radio contours from GMRT observations are overlaid in green. MUSTANG detects pressure substructure coincident with the hot gas near the disturbed main core as well as a separate feature associated with sub-cluster B. For further details on the morphological interpretation of these images see Mroczkowski et al. [2012].

Compton-y value, or pseudo-y, so-called because ℓ is not constrained by the X-ray data alone,

$$y = \frac{\sigma_{\rm T} k_{\rm B} T_{\rm e}}{m_{\rm e} c^2} \sqrt{\frac{4\pi (1+z)^3 S_{\rm X} \ell}{\Lambda_{ee}(T_{\rm e}, Z)}}. \tag{4.2}$$

We use a measurement of the integrated Compton-y ($Y_{\rm SZ} D_A^2 = \int y d\Omega$) within $R < 1'$ from an SZE instrument such as Bolocam or the Sunyaev-Zel'dovich Array (SZA)[1] to infer ℓ and normalize the X-ray pseudo-y map accordingly. This assumes that ℓ is constant azimuthally, which turns out to be a reasonable approximation for typical cluster density profiles [see Mroczkowski et al. 2012].

[1] http://astro.uchicago.edu/sza

In Mroczkowski et al. [2012], a temperature map is constructed by dividing the image into regions according to the surface brightness distribution and a chosen signal-to-noise (S/N) threshold. This technique uses the *contbin* algorithm from Sanders [2006] to select these regions. Within each bin, the temperature $k_{\rm B}T_{\rm e}$ and metallicity Z are extracted from spectral fits to X-ray data in the $0.7 - 7.0$ keV energy range. Equation 4.2 can then be used to determine y for each map bin. Figure 4.1, taken from Mroczkowski et al. [2012], shows X-ray derived maps produced following this procedure.

In the absence of deep X-ray spectroscopy or reliable spectral fits, we adopt an isothermal temperature distribution with average $k_{\rm B}T_{\rm e}$ and Z values reported in the literature for a particular target. In Young et al. [2014, *in prep.*], we find this to be a reasonable assumption given the relatively flat azimuthal temperature profiles reported in the ACCEPT database [Cavagnolo et al. 2009].

Once we have the temperature and Λ_{ee} maps, and we have determined ℓ from complementary SZE data, we can construct the pseudo-y map. It is then straightforward to produce a pseudo-SZE map according to Equation 2.5.

4.5 Multi-Wavelength Analysis of MACS J0647 and MACS J1206

In this section, I present the analysis and results from observations of MACS J0647.7+7015 and MACS J1206.2-0847 as reported in Young et al. [2014, *in prep.*]. The X-ray measured physical properties of MACS J0647.7+7015 and MACS J1206.2-

Cluster	R_{500} (Mpc)	P_{500} (10^{-3}keV cm^{-3})	M_{500} ($10^{14}M_{\odot}$)	$k_{\rm B}T$ (keV)	Y_{500} (10^{-10})
MACS J0647.7	1.26 ± 0.06	9.23 ± 2.57	10.9 ± 1.6	11.5 ± 1.1	1.7 ± 0.5
MACS J1206.2	1.61 ± 0.08	10.59 ± 3.07	19.2 ± 3.0	10.7 ± 1.3	5.5 ± 1.6

Table 4.2: X-ray derived physical properties for MACS J0647.7+7015 and MACS J1206.2-0847. These values are taken from calculations in Mantz et al. [2010]; Sayers et al. [2013a].

0847 from Mantz et al. [2010]; Sayers et al. [2013a] are summarized in Table 4.2. In this work, we fit a set of gNFW pressure profiles [Nagai et al. 2007], including the specific case of the "universal pressure profile" [Arnaud et al. 2010, hereafter A10], to deprojected average pressure profiles from Bolocam measurements of MACS J0647.7+7015 and MACS J1206.2-0847. The best-fit models are projected into 2D Compton-y maps and then fit to the MUSTANG data according to the procedure outlined in §4.5.4.

4.5.1 MUSTANG Observing Strategy and Data Reduction

The MUSTANG observations of MACS J0647.7+7015 and MACS J1206.2-0847 largely follow the procedure described in Mason et al. [2010] and Korngut et al. [2011]. We direct the telescope in a Lissajous daisy scan pattern to modulate the astronomical signal to higher frequencies above the significant low frequency noise. We choose seven pointing centers surrounding the cluster core, which provides relatively uniform coverage in the central $1'$ and increasing noise toward the edges of the map.

During observations, nearby bright compact quasars were mapped roughly every 30 minutes to track changes in the beam profile including drifts in telescope gain and pointing offsets. Typically, if a substantial change in the beam profile was found,

we re-focused the active surface using OOF [Nikolic et al. 2007]. We used JVAS 0721+7120 for MACS J0647.7+7015 and JVAS 1229+0203 for MACS J1206.2-0847 to determine these gains and focusing corrections. Fluxes of the planets we used for primary calibration were calculated based on brightness temperatures from WMAP observations [Weiland et al. 2011]. The absolute flux of the data is calibrated to an accuracy of $\sim 10\%$.

The MUSTANG data are reduced using the ***mustangmap*** pipeline discussed in §4.1. The bolometric timestreams are high-pass filtered by subtracting a high order polynomial determined by the scan speed of the telescope. For a typical 300 s scan, and $40''$/s scan speed, we choose a $\sim 100^{\text{th}}$-order polynomial. In order to remove atmospheric noise on large angular scales, we subtract the mean measurement from all detectors for each sample in time. This also removes astronomical signals on angular scales larger than the instantaneous FOV of the instrument ($\approx 42''= 255$ kpc at $z = 0.5$).

Within each timestream, we assign a weight w to each detector based on the standard deviation of the measurement ($w = 1/\sigma^2$). To produce a "signal map", the timestreams are binned into $1'' \times 1''$ spatial pixels. Weights are binned in the same way to produce a "weight map". We smooth both of these maps with the MUSTANG point spread function (PSF) and multiply the signal map by the square root of the weight map to generate a map in units of S/N - the "SNR map".

We generate an independent "noise map" by flipping the sign of measurements from every other scan and binning the data into a grid with the same pixel size as the signal map. As we do for the signal map, we use the pixel weights to convert

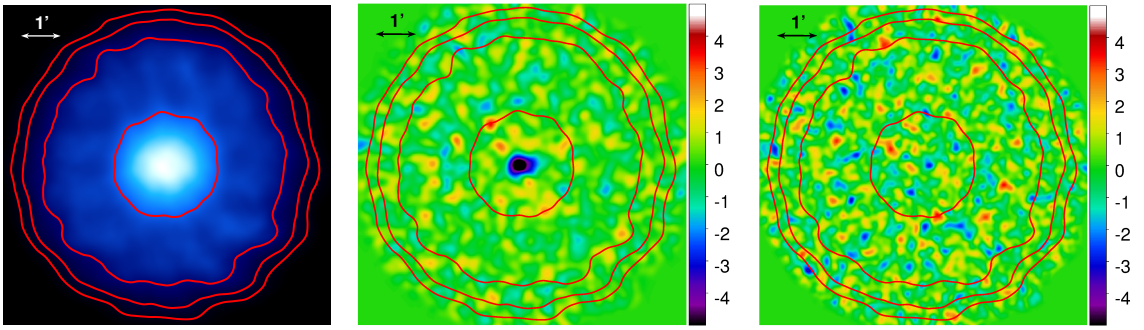

Figure 4.2: Example weight (left), SNR (middle), and noise SNR (right) maps for MACS J0647.7+7015. The red contours for the weight map correspond to descending steps of peak weight divided by 2^n for n=[1,2,...,5]. Therefore at the highest contour the pixel weights have dropped by a factor of 2, implying that the noise has increased by a factor of $\sqrt{2}$. The SNR map and noise SNR map have been scaled down by a factor $\sigma_N = 1.3$ as explained in the text.

the noise map to units of S/N, referred to as a "noise SNR map". We define a scale factor σ_N as the standard deviation of the noise SNR map. For a Gaussian noise distribution, $\sigma_N = 1$. We can therefore use σ_N as a normalization factor to ensure that the calculated S/N values are realistic. Typically, we find $\sigma_N \approx 1.5$, which means either that the gain-flipped maps are likely over-estimating the noise or the weight maps are under-estimating the noise. We expect this to be a systematic effect, however, so scaling by σ_N should provide a reasonable correction. Since $\sigma_N > 1$ we are generally erring on the conservative side with the reported S/N values.

Figure 4.2 shows the weight, SNR, and noise SNR maps for MACS J0647.7+7015. For reference, we overlay contours from the weight map where each descending step measures a factor of 2 decrease in weight, or $\sqrt{2}$ increase in noise.

4.5.2 Bolocam

Bolocam is a 119-pixel bolometer array at the Caltech Submillimeter Observatory (CSO) capable of operating at 1.1 and 2.1 mm, with resolutions of 31″ and 58″, respectively, and an instantaneous FOV of 8′. For more details on the Bolocam instrument see Haig et al. [2004].

Bolocam has mapped to high significance the SZE decrement at 2-mm in 45 X-ray selected clusters, referred to as the Bolocam X-ray/SZ (BoXSZ) sample [Sayers et al. 2013a, hereafter S13], which encompasses all 25 CLASH clusters, including MACS J0647.7+7015 and MACS J1206.2-0847.

4.5.3 Bolocam Derived Models

Bolocam measurements of the SZE on large angular scales provide constraints on ICM pressure profiles and the scaling relation between SZE flux and cluster mass [Czakon et al. 2014, S13]. The Bolocam gNFW profiles are derived following the fitting procedure in S13, which I summarize briefly below.

First, the Bolocam data are reduced, calibrated, and binned into a 2D map according to the procedure in Sayers et al. [2011]. The data are converted to pressure using Equation 2.5 assuming an isothermal temperature distribution with the spectroscopic X-ray temperature given in Table 4.2. Then the data deprojected into a 3D pressure profile by fitting the 2D data to a 2D power law pressure profile processed with the Bolocam transfer function and PSF. Once we have the deprojected pressure profile for a specific cluster, we can fit a parametrized pressure profile such as a gNFW given by Equation 2.15 (see S13).

4.5.4 Map-Domain Model-Fitting

While MUSTANG provides high-resolution imaging, the angular transfer function falls off steeply beyond the instrument FOV. Bolocam has lower resolution, but a larger field of view and therefore is sensitive to the bulk SZE signal on larger angular scales (beyond $\sim 10'$). A combined Bolocam+MUSTANG model-fitting approach will allow us to place better constraints on the ICM characteristics over the full range of angular scales provided by both instruments. The procedure I discuss here represents the first step towards the robust joint-fitting procedure from C. Romero et al. [2014, *in prep.*].

We begin by constructing a model map in units of Jy/beam smoothed to MUSTANG resolution. We simulate an observation of the model by injecting noise from real observations and then processing the mock observation through the MUSTANG map making pipeline. By subtracting the injected noise from the output map we obtain a filtered model map without residual noise.

To fit the filtered model maps to the data in the map domain we use the general linear least squares fitting approach from *Numerical Recipes* [Press et al. 1992], outlined briefly below.

We construct an $N \times M$ design matrix $\mathbf{A}$, where each element A_{ij} corresponds to a model component (e.g., a point source or gNFW model) X_j evaluated at map pixel x_i. We allow for each model component a single free parameter, a scalar amplitude, a_j. We call the M-length vector of amplitudes $\overrightarrow{a}$ and define a model vector,

$$\overrightarrow{d}_{mod} = \mathbf{A}\overrightarrow{a}.$$

The goodness of fit statistic, χ^2, is given by

$$\chi^2 = (\overrightarrow{d} - \overrightarrow{d}_{mod})^T \mathbf{N}^{-1} (\overrightarrow{d} - \overrightarrow{d}_{mod}),$$

where $\overrightarrow{d}$ represents the measured values of each map pixel and $\mathbf{N}$ is the noise covariance matrix, where

$$N_{ij} = < n_i n_j > - < n_i >< n_j > .$$

Here, $\overrightarrow{n}$ is taken to be pixel values of a noise map, and the covariance matrix is calculated using the ensemble average over statistically identical noise realizations. Given that our detector noise is dominated by phonon noise (Chapter 3), the pixel noise is largely uncorrelated, so we therefore take the noise covariance matrix $\mathbf{N}$ to be diagonal. The best-fit amplitudes, corresponding to the minimum χ^2, are then

$$\overrightarrow{a} = (\mathbf{A}^T \mathbf{N}^{-1} \mathbf{A})^{-1} \mathbf{A}^T \mathbf{N}^{-1} \overrightarrow{d}.$$

The parameter uncertainties $\sigma^2(a_k)$ are given by the diagonal elements of the parameter covariance matrix $(\mathbf{A}^T \mathbf{N}^{-1} \mathbf{A})^{-1}$.

We perform the fits over a region within $1'$ of the cluster centers. This scale is chosen to match the MUSTANG angular transfer function and we find that the results do not change significantly for larger regions. Given the $1'' \times 1''$ map pixels, this yields roughly $\pi(60)^2 = 11,310$ degrees of freedom, minus the number of model components we include in each fit. The probability to exceed χ^2 (PTE), which represents the likelihood that the data are described by a particular model rather than random chance, is calculated using the IDL routine *mpchitest*.

Model	P_0	C_{500}	γ	α	β
S13 Ensemble	4.29	1.18	0.67	0.86	3.67
S13 Cool-core	0.65	1.18	1.37	2.79	3.51
S13 Distrubed	17.3	1.18	0.02	0.90	5.22
A10 Ensemble	8.40	1.18	0.31	1.05	5.49
A10 Cool-core	3.25	1.13	0.77	1.22	5.49
A10 Disturbed	3.20	1.08	0.38	1.41	5.49
MACS J0647 G9	0.54	0.29	0.90	1.05	5.49
MACS J1206 G7	1.13	0.41	0.70	1.05	5.49

Table 4.3: Best-fit gNFW models from S13 and A10, as well as the best-fit MUSTANG+Bolocam models presented in this work. For the ellipsoidal models in the last two rows, C_{500} is computed from the average of the major and minor axes.

4.5.5 ICM Pressure Profiles

For this work, our primary goal is to bridge the angular scales covered by both Bolocam and MUSTANG in order to accurately model the ICM pressure profile from the cluster core to the outskirts. The pressure of the ICM in clusters from the A10 and S13 samples is well described by the gNFW profile given in Equation 2.15. The gNFW model parameters for the respective ensemble S13 and A10 samples, in addition to subsets defined according to cluster morphology, are given in Table 4.3. Also shown are the best-fit MUSTANG+Bolocam parameters for MACS J0647.7+7015 and MACS J1206.2-0847. Pressure profiles for each of these models, scaled based on P_{500}, R_{500}, and z given in Table 4.2, are displayed in Figure 4.3. The solid lines correspond to the A10 sample, while the dashed lines signify the S13 sample. The diamonds show the X-ray derived values presented in the Archive of Chandra Cluster Entropy Profile Tables (ACCEPT) database [Cavagnolo et al. 2009]. Also included

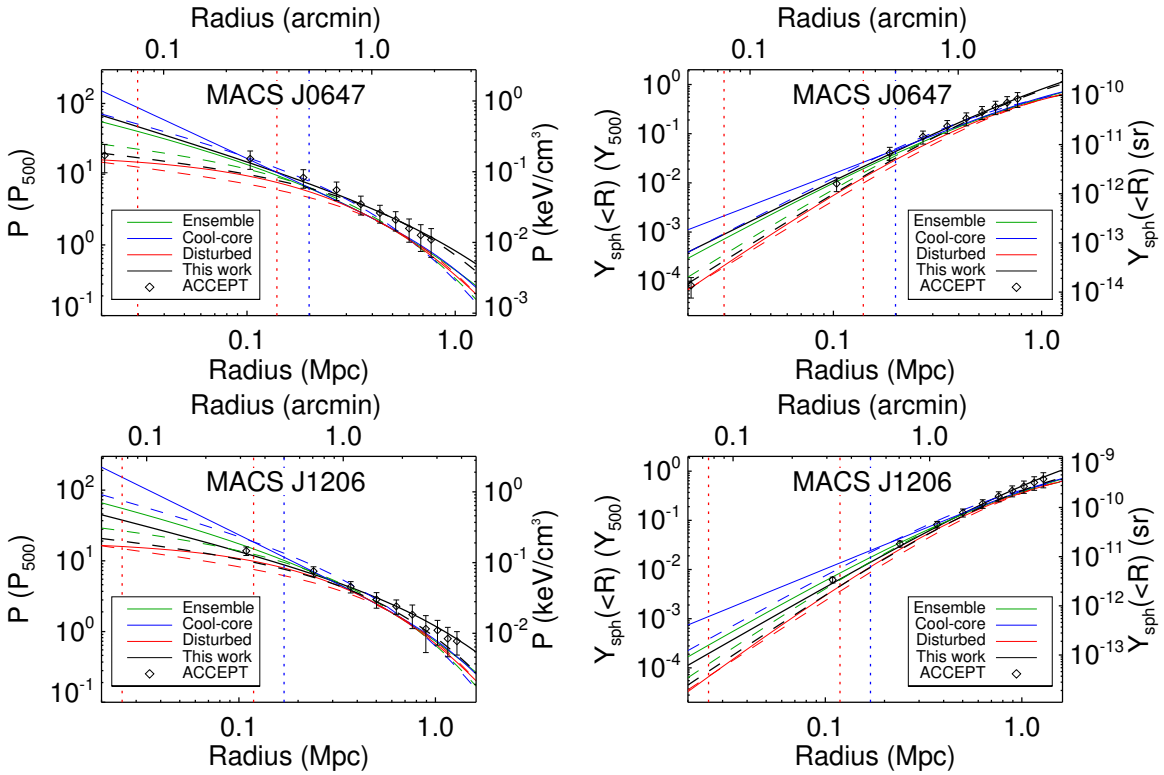

Figure 4.3: Pressure (left) and integrated Compton-y (right) profiles for MACS J0647.7+7015 (upper) and MACS J1206.2-0847 (lower). Solid lines refer to the A10 sample of X-ray selected clusters, while dashed lines correspond to the S13 sample including all of the CLASH clusters. For A10 and S13, respectively, "ensemble" refers to the entire cluster sample and profiles from the subsets of cool-core and disturbed morphologies are separately shown. The X-ray derived pressure measurements from the ACCEPT database are plotted as diamonds. The best-fit MUSTANG+Bolocam model presented is shown as the solid black line in each plot. The vertical dotted lines surround the radial dynamic range (resolution to FOV) covered by MUSTANG (red) and Bolocam (blue). The integrated Compton-y profiles were computed according to Equations 4.3 and 4.4.

are plots of the spherically integrated Compton-y, $Y_{\rm sph}(< R)$, given in A10 by

$$Y_{\rm sph}(< R) = \frac{4\pi\sigma_{\rm T}}{m_{\rm e}c^2}\int_0^R P(r)r^2dr. \tag{4.3}$$

$Y_{\rm sph}$ is given in units of Y_{500}, as in A10, where

$$Y_{500} = \frac{\sigma_{\rm T}}{m_{\rm e}c^2}\frac{4\pi}{3}R_{500}^3P_{500}. \tag{4.4}$$

For the combined analysis of MACS J0647.7+7015 and MACS J1206.2-0847, we start by fitting a set of parametrized gNFW pressure profiles to the Bolocam data as described above. For each profile, α and β are fixed to the A10 universal values of 1.05 and 5.49, respectively. The normalization P_0, centroid, and scale radius $R_s = R_{500}/C_{500}$ are allowed to float. Each profile is assigned a fixed γ value spanning 0 to 1.5. We choose a grid over γ values because we expect MUSTANG to be the most sensitive to the inner slope of the ICM profile. The best-fit pressure profiles for each γ value are shown in Figure 4.4. For convenience the integrated Compton-y profiles for each cluster are also shown.

Each of the Bolocam-best-fit 3D profiles are projected onto a 2D map and compared to the MUSTANG data as described in §4.5.4. We can then determine the values for γ, P_0, and C_{500} that best describe both the MUSTANG and Bolocam data.

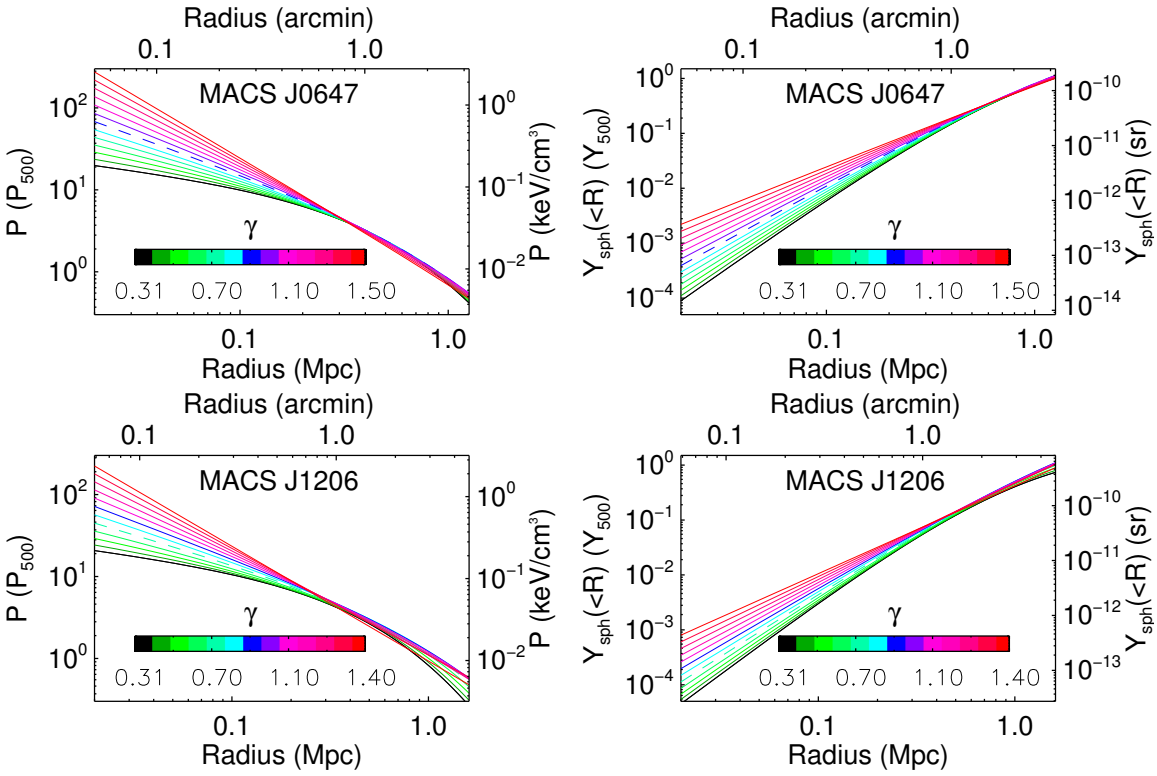

Figure 4.4: Pressure (left) and spherically integrated Compton-y (right) profiles generated from fits of generalized NFW models to Bolocam measurements of MACS J0647.7+7015 and MACS J1206.2-0847. Each profile represents the gNFW that best fits the Bolocam data given a fixed value of γ, differentiated by color as shown. In general, Bolocam has the largest constraining power on scales of $\sim 1'$ for pressure and $\sim 2'$ for integrated Compton-y. The dashed lines correspond to the best fit MUSTANG+Bolocam models from this work.

4.6 MACSJ0647.7+7015

MACS J0647.7+7015, discovered during the Massive Cluster Survey (MACS), is a seemingly relaxed massive system at $z = 0.591$, but contains two central cD galaxies, which may indicate ongoing merger activity [Mann & Ebeling 2012]. Figure 4.5 shows a composite image of MACS J0647.7+7015 including optical, lensing, and X-ray images. MUSTANG contours in steps of 1-σ beginning at 3-σ are overlaid in white. The mass distribution from strong lensing analysis [Zitrin et al. 2011] appears to be doubly peaked and elongated in the E-W direction. The X-ray emission measured by *Chandra* shows similar elongation as does the SZE flux measured by MUSTANG.

The MUSTANG map of MACS J0647.7+7015 is shown in Figure 4.6. The peak SZE flux is $-121 \pm 16\,\mu$Jy/beam. The decrement (> 3-σ) is primarily elongated with a width $\approx 20''$. The total SZE flux measured by MUSTANG, within the region with > 3-σ significance of the decrement, $S_{90} = -535 \pm 38\,\mu$Jy.

The X-ray derived pseudo-SZE template derived according to Equation 4.2 and smoothed to the MUSTANG resolution is shown in Figure 4.7. The X-ray contours are overlaid in black while contours from the Bolocam SZE measurement are overlaid in red. Normalizing the integrated pseudo Compton-y based on the Bolocam flux measurement yields an effective depth $\ell = 1.44$ Mpc.

4.6.1 Model Fits

Following the procedure outlined in Section 4.5.4, we determine the thermal SZE model that best simultaneously describes the MUSTANG and Bolocam data to be

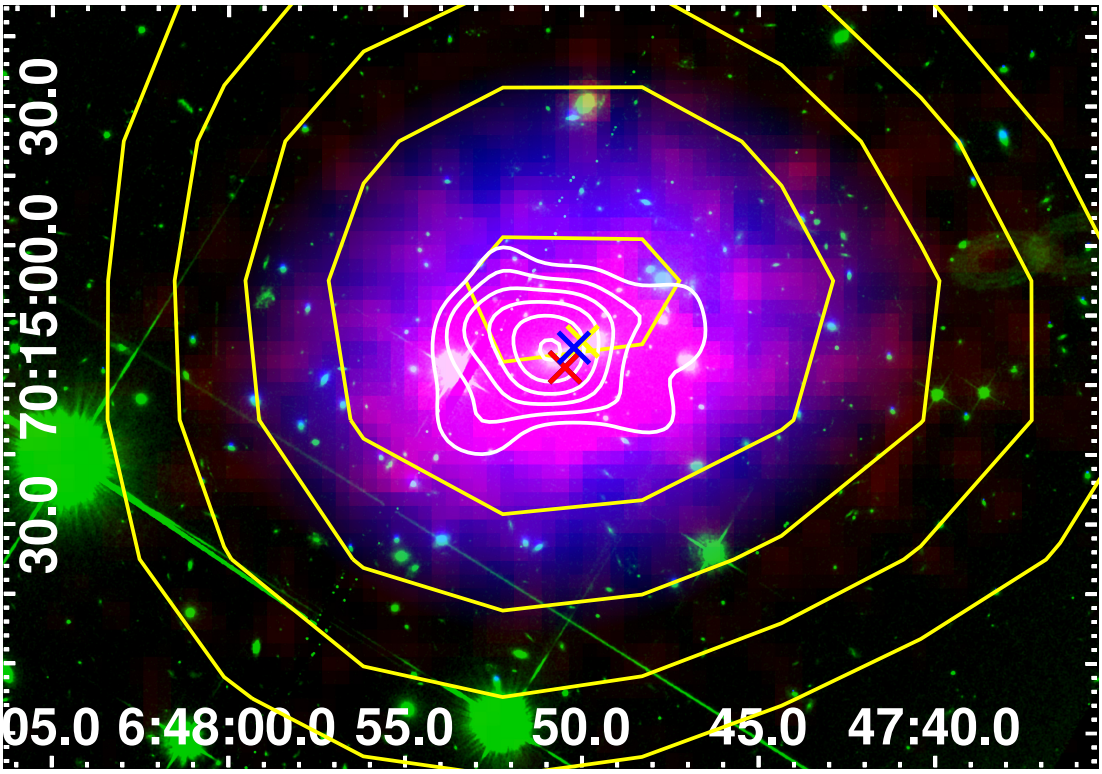

Figure 4.5: Composite image of MACS J0647.7+7015. Green is HST, blue is the total mass distribution derived from gravitational lensing, and red is X-ray surface brightness measured by *Chandra*. MUSTANG S/N contours are overlaid in white and Bolocam contours (arbitrary units) are overlaid in yellow. Although the Bolocam peak is located slightly north of the cluster center, there is good agreement in general between the X-ray, SZE, and lensing mass distributions. Crosses denote the centroid for the X-ray surface brightness (red), BCGs (blue), and Bolocam SZE (yellow). MACS J0647.7+7015 exhibits an elliptical morphology with two distinct cD galaxies, which may indicate merger activity, but otherwise appears to be relaxed.

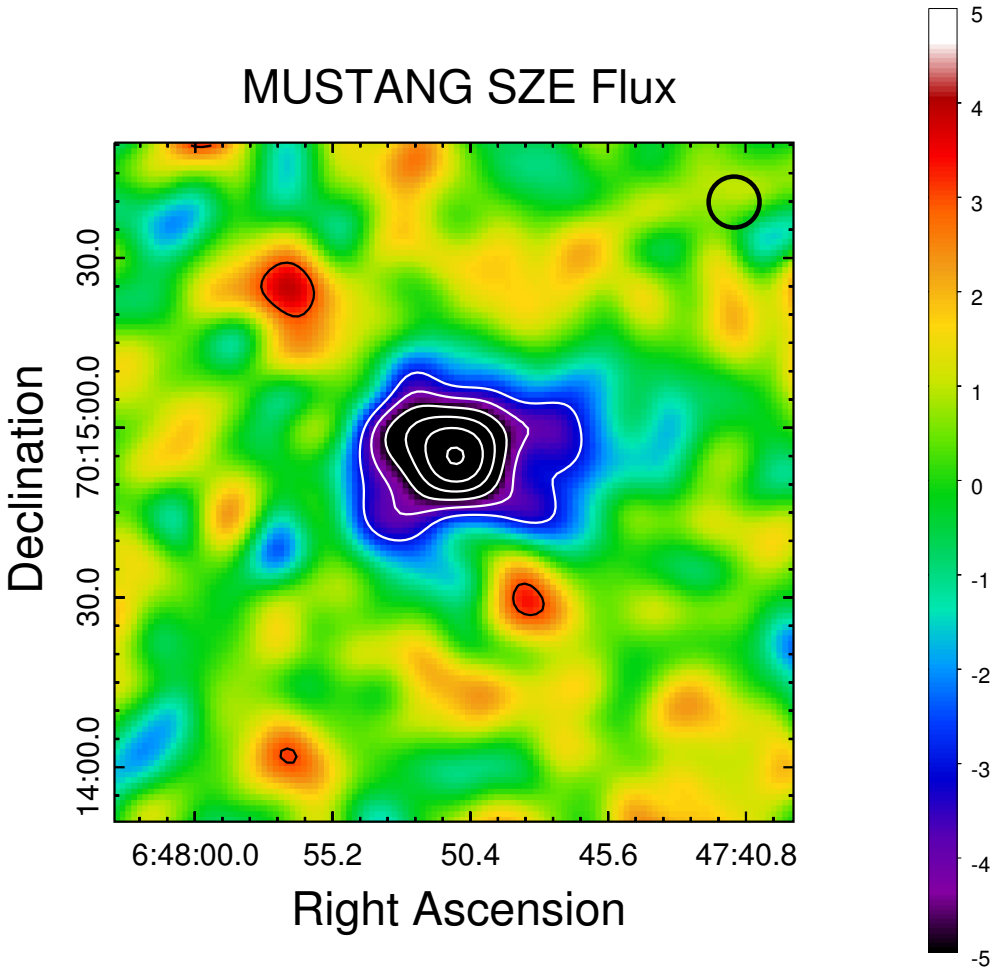

Figure 4.6: MUSTANG SZE S/N map of MACS J0647.7+7015 smoothed with the 9″ beam represented by the black circle in the upper right. Contours are shown in increments of $1-\sigma$ beginning at $3-\sigma$ for SZE decrement (white) and positive flux (black).

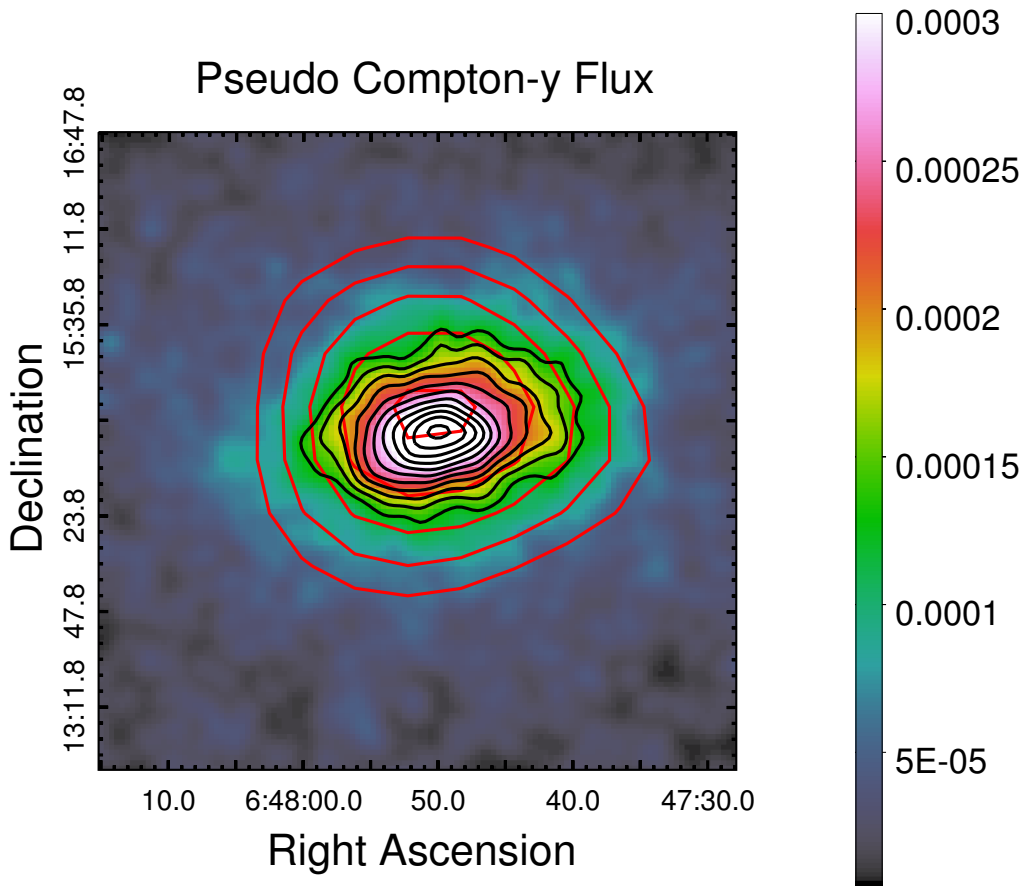

Figure 4.7: MACS J0647.7+7015 X-ray derived Compton-y map assuming an isothermal temperature of 11.5 keV and effective depth $\ell = 1.44$ Mpc. The contours are shown for X-ray (black) and Bolocam data (red) in increments of 2.6×10^{-5} beginning at 1.3×10^{-4}.

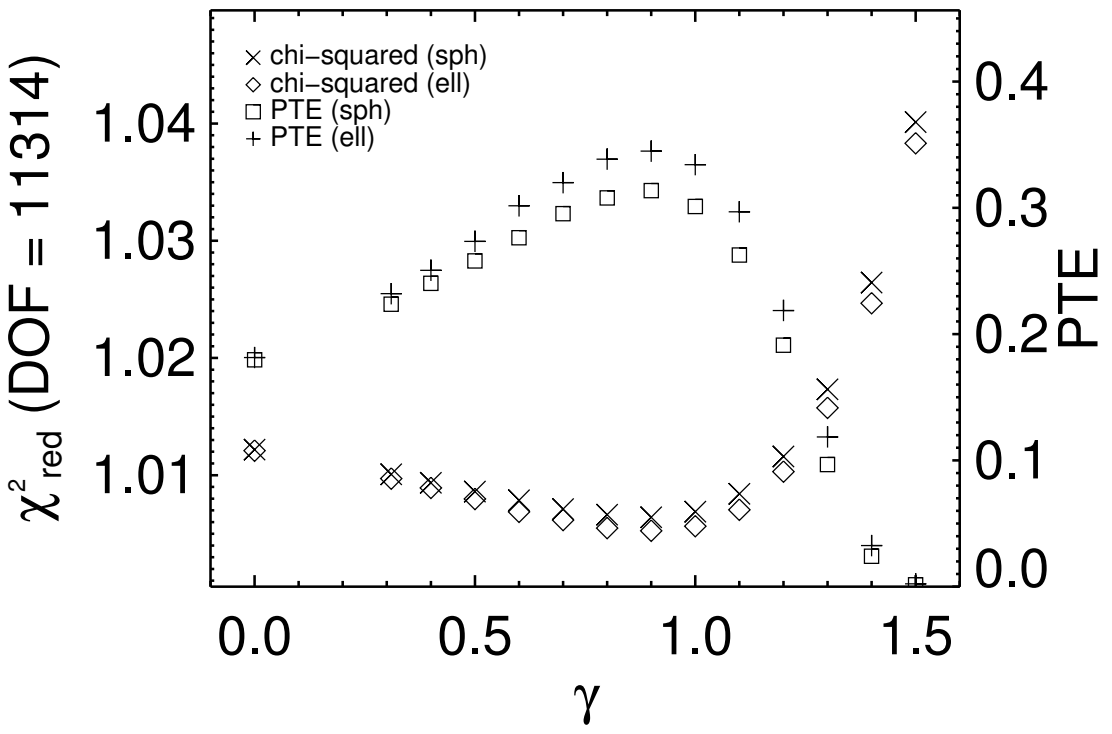

Figure 4.8: Goodness of fit parameters from the comparison between MUSTANG data and the Bolocam-derived models for MACS J0647.7+7015. We determine the best-fit model to be an elliptical gNFW($\gamma = 0.90$), with χ^2_{red}/DOF= 11374/11314 and PTE=0.34.

an ellipsoidal gNFW profile with

$$[P_0, C_{500}, \gamma, \alpha, \beta] = [0.54, 0.29, 0.90, 1.05, 5.49], \tag{4.5}$$

hereafter referred to as the $\gamma = 0.9$, or G9, model. Figure 4.8 shows the calculated $\chi^2_{\rm red}$ and PTE as a function of γ.

The X-ray pseudo-SZE and G9 model for MACS J0647.7+7015, after being filtered through the MUSTANG pipeline, are shown in Figure 4.9. Also shown are the azimuthally averaged radial profiles. The X-ray flux is concentrated on smaller scales

and passes through the MUSTANG pipeline with less attenuation compared to the gNFW models, which have shallower profiles extending to larger radii. The filtered G9 flux peak is offset slightly north of the X-ray peak. The radially averaged profiles from the filtered maps agree fairly consistently between all three data sets.

4.6.2 Discussion

In MACS J0647.7+7015, we find good agreement between the MUSTANG high-resolution SZE image and the X-ray and Bolocam measurements. The SZE appears to be elliptical and rotated only slightly compared to the position angle of the X-ray and lensing distributions.

The compact positive source to the NE in Figure 4.6 appears to be significant ($> 3\sigma$) even after accounting for the lower observing coverage outside the cluster core. In computing the significances we have assumed that the MUSTANG map-domain noise follows a Gaussian distribution within a $2'$ radius, which we verified by inspecting the histogram of the noise map for MACS J0647.7+7015. However, we find no counterparts for these sources in any other data set. High resolution radio observations were not obtained for MACS J0647.7+7015 so spectral coverage close to 90 GHz is limited. We take jackknives of the data, split into four equal integration times, and the source appears in each segment, which is unlikely for a spurious noise feature. Therefore, it is possible that this is a yet unidentified object such as a lensed high-z dusty galaxies or shallow spectrum AGN, which may be confirmed by future high resolution radio observations closer in frequency to 90 GHz.

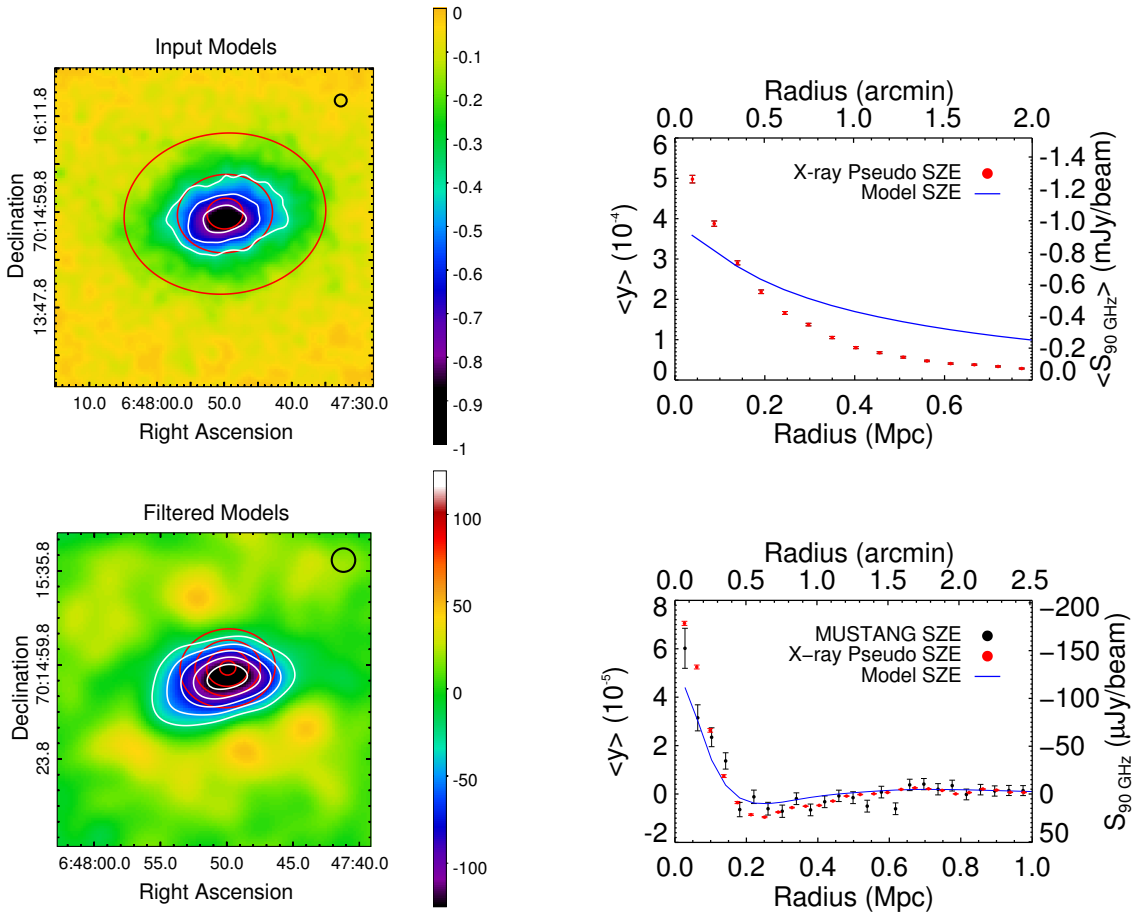

Figure 4.9: MACS J0647.7+7015 pseudo SZE map derived from *Chandra* X-ray data (left, white contours) with red contours representing the elliptical gNFW($\gamma = 0.9$), or G9, model from this work, both smoothed to the MUSTANG resolution. Azimuthally averaged profiles are shown on the right. **Top row:** Models before applying the MUSTANG transfer function. Contours are overlaid in units of -200 μJy/beam starting at -400 μJy/beam. **Bottom row:** Models after applying the MUSTANG transfer function. All contours are overlaid in units of -50 μJy/beam starting at -50 μJy/beam. Aside from the central ~ 0.1 Mpc where the X-ray and SZE flux are sharply peaked, the radially averaged flux from MUSTANG, shown in the lower right, closely follows both the G9 model and the X-ray pseudo SZE flux.

4.7 MACSJ1206.2-0847

MACS J1206.2-0847 is a generally relaxed system at $z = 0.439$ that has been studied extensively in X-ray, lensing, SZE, and optical (e.g., Ebeling et al. 2001, 2009; Umetsu et al. 2012; S13). A composite image with the multi-wavelength data is shown in Figure 4.10.

Ebeling et al. [2009] report a giant gravitational arc 20″ west of the BCG and a 15″ long excess of X-ray emission in the direction of the arc. Gilmour et al. [2009] classify MACS J1206.2-0847 as visually relaxed, however the high velocity dispersion hints at potential merger activity along the line of sight.

The MUSTANG SZE map of MACS J1206.2-0847 is shown in Figure 4.11. The majority of the SZE decrement extends to the northeast and is contaminated by positive emission from the central AGN.

The X-ray surface brightness and derived 90 GHz SZE Flux are shown in Figure 4.12. The Bolocam normalization of the pseudo SZE map yields an effective depth $\ell = 2.02$ Mpc.

4.7.1 Central AGN

The BCG in MACS J1206.2-0847 harbors a radio-loud AGN which is detected by MUSTANG with a slightly extended elliptical morphology. Using the low frequency ($\nu < 1.4$ GHz) flux measurements reported in the SPECFIND V2.0 catalog [Vollmer et al. 2010], we calculate the spectral index $\alpha = -1.26 \pm 0.1$ with abscissa $\beta = 6.2 \pm 0.2$.[2]

[2] $\log(S(\nu)) = \alpha \log(\nu) + \beta$

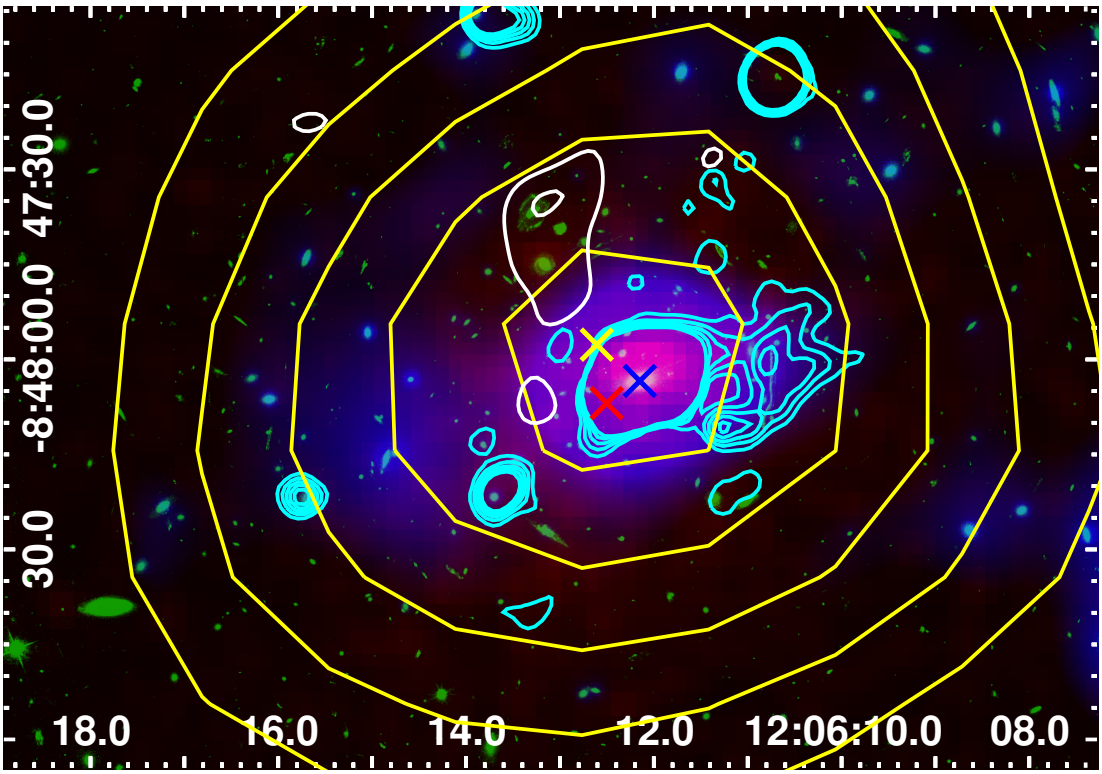

Figure 4.10: Composite image of MACS J1206.2-0847. Green is HST, blue is the total mass distribution derived from gravitational lensing, and red is X-ray surface brightness measured by *Chandra*. MUSTANG S/N contours are overlaid in white and Bolocam contours (arbitrary units) are overlaid in yellow. The crosses denote the centroids from the Bolocam data (yellow), the diffuse X-ray distribution (red), and the BCG (blue). The offsets between these centroids could be indicative of a disturbed cluster morphology (see Mann & Ebeling [2012]).

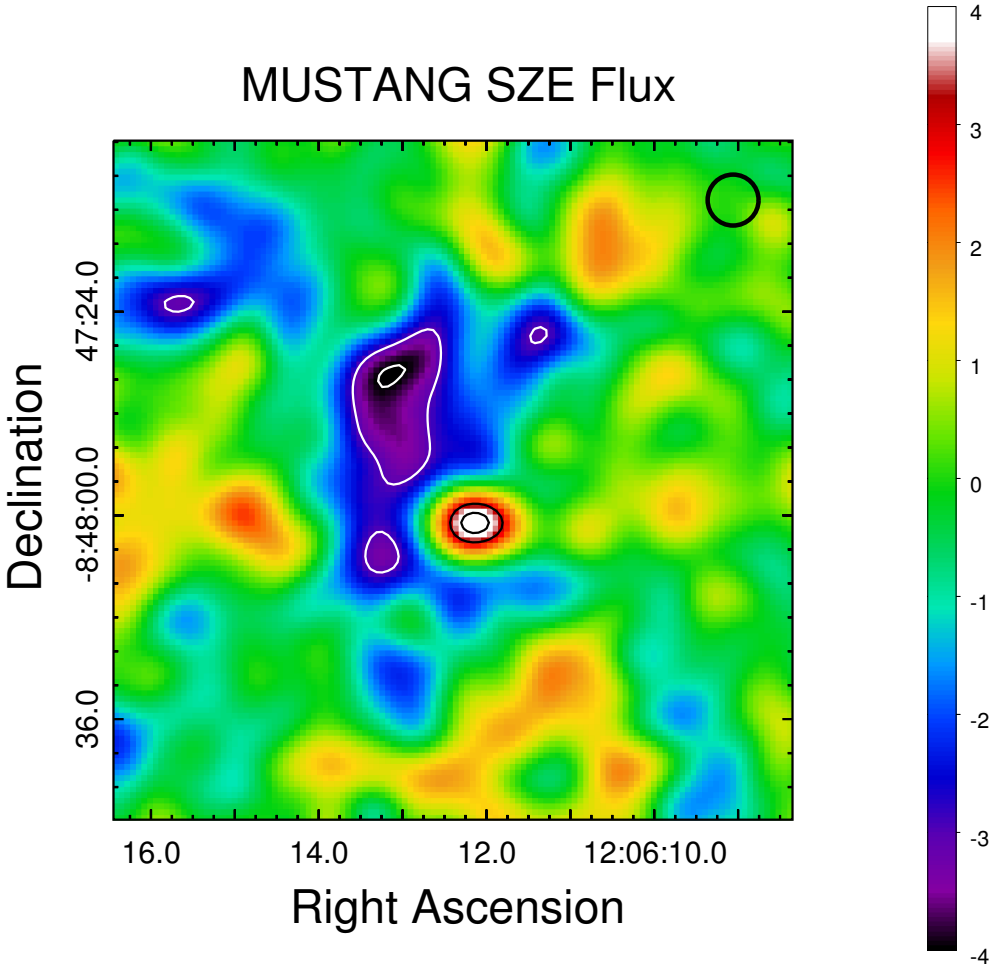

Figure 4.11: MUSTANG S/N map of MACS J1206.2-0847. Black (white) contours are positive (negative) S/N = [3, 4]. The 9″ MUSTANG beam is drawn as a black circle in the upper right. Emission at 90 GHz from the central AGN is clearly detected at > 4-σ. While most of the SZE decrement is presumably washed out by the point source, there appears to be significant SZE flux detected to the northeast

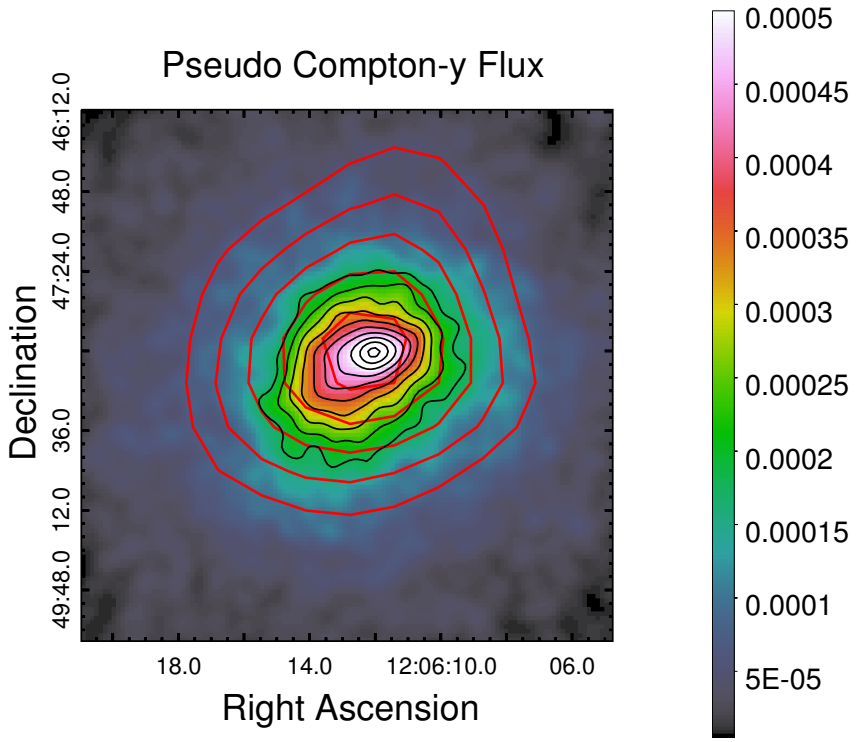

Figure 4.12: MACS J1206.2-0847 X-ray derived Compton-y map assuming an isothermal temperature of 10.7 keV and effective depth $\ell = 2.02$ Mpc. The contours, in increments of 0.25×10^{-4} beginning at 1.7×10^{-4}, are X-ray (black) and Bolocam data (red).

Model	S_{90} (μJy)	α	β
SPECFIND	879 ± 253	-1.26 ± 0.09	6.19 ± 0.24
A10	674 ± 61	-1.32 ± 0.05	6.34 ± 0.25
G7	765 ± 61	-1.28 ± 0.05	6.25 ± 0.24
Null	584 ± 61	-1.35 ± 0.05	6.45 ± 0.25

Table 4.4: Point source fluxes derived from joint fits with bulk SZE models. The first row is the prediction at 90 GHz extrapolated from measurements at lower frequencies given in the SPECFIND catalog [Vollmer 2009]. The A10 model refers to the ensemble parameters given in Table 4.3. The G7 model is the best-fit MUSTANG+Bolocam model from this work, a gNFW with $\gamma = 0.7$. The "null" model assumes there is no SZE decrement coincident with the point source. This represents a lower limit on the flux at 90 GHz and and therefore the steepest (most negative) likely spectral index.

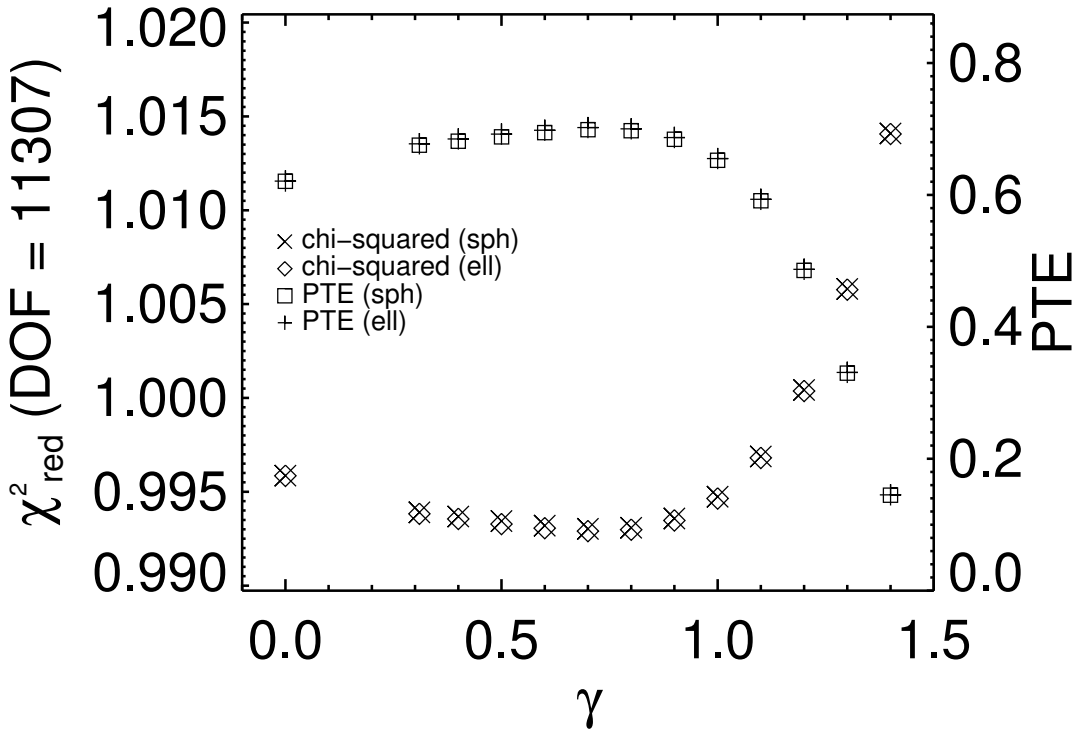

Figure 4.13: Goodness of fit parameters from the comparison between MUSTANG data and the Bolocam-derived models for MACS J1206.2-0847. We determine the best-fit model to be an elliptical gNFW ($\gamma = 0.70$), for which we calculate χ^2_{red}/DOF= 11227/11307 and PTE=0.70.

4.7.2 Model Fits

Using the archival radio data from NVSS we construct a compact source model and allow the amplitude to float in the joint fits with bulk SZE models, in order to account for the degeneracy between the co-spatial positive emission and SZE decrement. The values of the SZE flux at 90 GHz (S_{90}), α, and β for three combinations of models are given in Table 4.4. Null refers to the source flux assuming there is no SZE signal present, and represents a lower limit on S_{90} and upper limit on α.

Figure 4.13 shows the goodness of fit statistics for the gNFW + point source

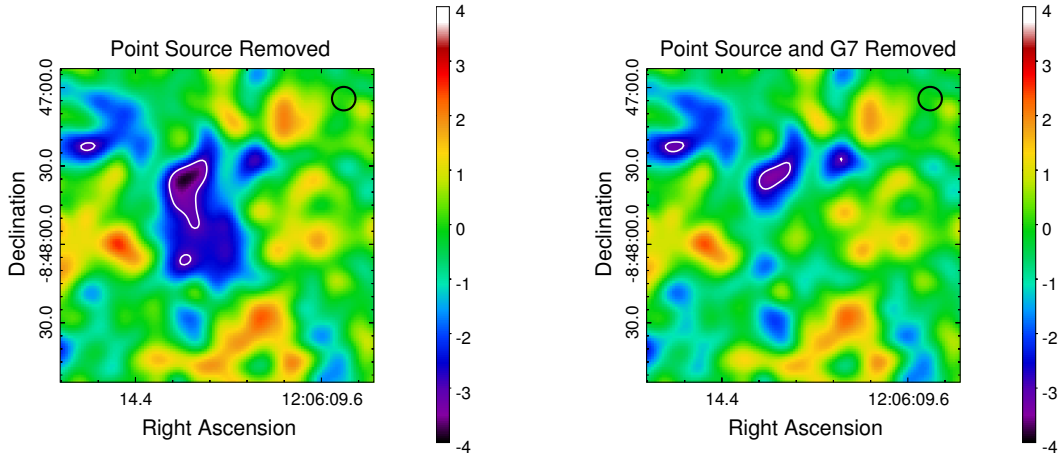

Figure 4.14: MUSTANG S/N map of MACS J1206.2-0847 with a point source model subtracted (left), and additionally the G7 ($\gamma = 0.7$) model subtracted (right). Contours are overlaid at 1-σ intervals starting at 3-σ. There is a residual flux $S_{90} = -236 \pm 15$ μJy in the region with $>$ 3-σ significance not accounted for by the G7 model.

model fitting. With χ^2_{red}= 0.993 and PTE = 0.70, the best fit model appears to be an elliptical gNFW with

$$[P_0, C_{500}, \gamma, \alpha, \beta] = [1.13, 0.41, 0.70, 1.05, 5.49], \tag{4.6}$$

hereafter G7. After subtracting the point source and G7 model, we find a 3-σ residual feature in MACS J1206.2-0847 (see Figure 4.14). The 3-σ contour encompasses a 73 arcsecond^2 (2 kpc^2) region with an integrated flux of 61 ± 21 μJy (see Table 4.5). Using Equation 2.5 we calculate the integrated Compton-y, $Y_{\rm SZ} D_A^2 = 7.3 \times 10^{-7}$ Mpc^2.

The initial and filtered G7 and pseudo-SZE models are shown in Figure 4.15. The Bolocam model is much more extended than the X-ray and is subsequently filtered the most by the MUSTANG transfer function. The pseudo-SZE model shows a much higher peak after filtering, but diminishes rapidly with radius.

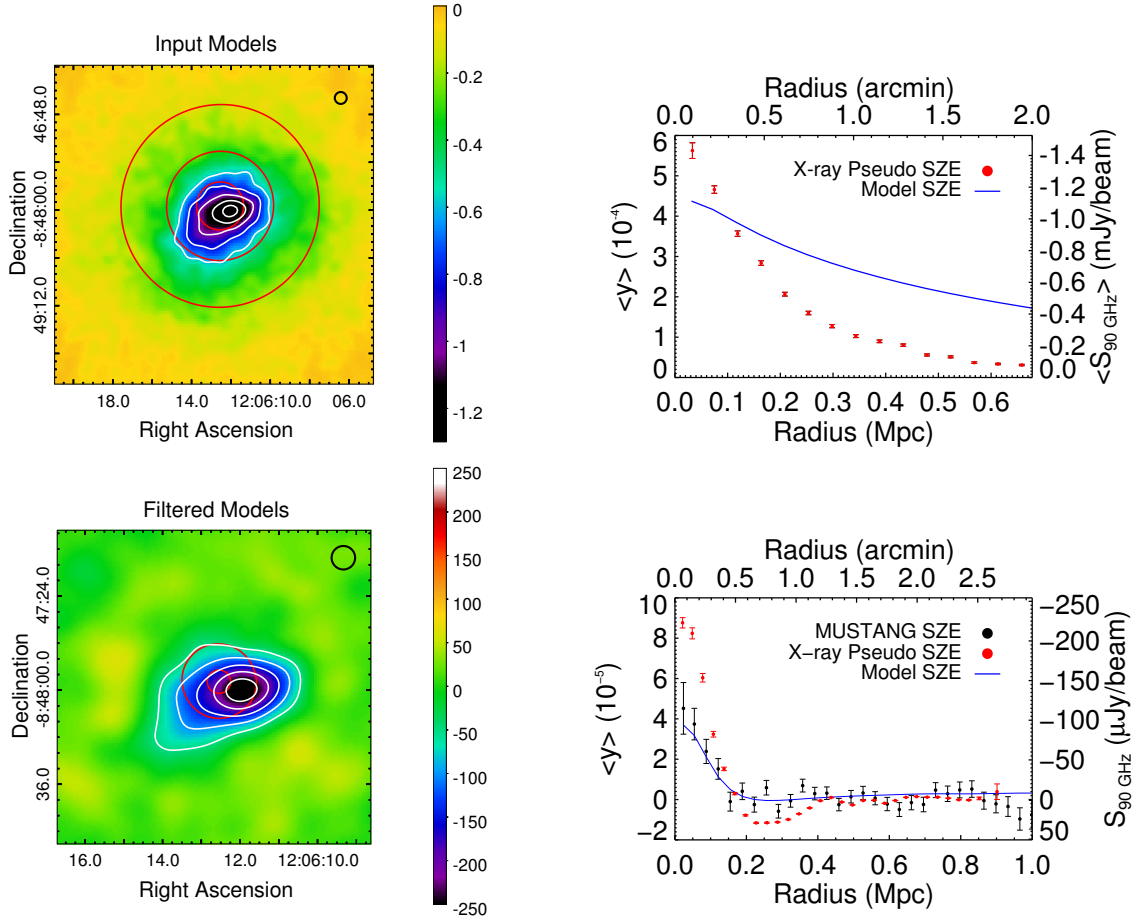

Figure 4.15: Pre- and post-processed models for MACS J1206.2-0847, each smoothed to the MUSTANG PSF given by the black circles in the maps. **Upper left:** Pseudo-SZE map derived from *Chandra* X-ray data (color image, white contours), with contours from the G7 model overlaid in red. Both sets of contours are overlaid in steps of -200 μJy/beam starting at -600 μJy/beam. **Upper right:** Radially averaged profiles corresponding to the pseudo-SZE map and the G7 model, starting from the X-ray centroid. **Bottom left:** Pseudo-SZE map and G7 model after applying MUSTANG transfer function. Contours are overlaid in units of -25 μJy/beam starting at -75 μJy/beam. **Bottom right:** Radially averaged profiles for the filtered maps including the MUSTANG data. The X-ray flux shows a sharper peak compared to the Bolocam and MUSTANG data, which could be a result of the way in which the pseudo-y map was normalized.

Components Subtracted	S_{90} (μJy)	$Y_{SZ}D_A^2$ (10^{-8} Mpc^2)	M_{500} (10^{13} $M_\odot$)	L_X (10^{43} erg s^{-1})
Point source	-193 ± 36	32 ± 6	2.6 ± 1.0	3.0 ± 1.7
Point source, G7	-61 ± 21	9.5 ± 3.3	1.3 ± 0.7	2.0 ± 1.3

Table 4.5: MACS J1206.2-0847 Integrated SZE Flux Estimates and Mass Lower Limits. M_{500} and L_X are derived from the A10 $Y_{SZ}-M_{500}$ and $M_{500}-L_X$ scaling relations. Here we use the $-765\,\mu$Jy point source model from §4.7.1.

4.7.3 Discussion

The joint Bolocam+MUSTANG G7 model for MACS J1206.2-0847 provides a good fit to the MUSTANG data when including a point source model. There is relatively minor variation in the PTE values reported in Figure 4.13 between $\gamma = 0.3$ and $\gamma = 0.8$ so γ is not tightly constrained for this system. This is likely due to the strong degeneracy between the gNFW parameters, which is not accounted for in this analysis. For instance, increasing γ will have nearly the same effect as increasing the normalization factor P_0 while decreasing the scale radius R_s. The joint-fitting approach in C. Romero et al. [2014, *in prep.*] will address this problem by covering a larger parameter space and accounting for both SZE data sets simultaneously.

The MUSTANG observation of MACS J1206.2-0847 reveals a > 4-σ SZE decrement to the NE. After removing the model component that best fits both MUSTANG and Bolocam, there is a > 3-σ excess. This signal does not appear to have a counterpart in the X-ray surface brightness image, nor is there a diffuse radio feature in GMRT observations (private communication) that would point to an energetic merger event. When comparing the MUSTANG map to the optical image and the weak lensing mass reconstruction from Umetsu et al. [2012] we do however see some

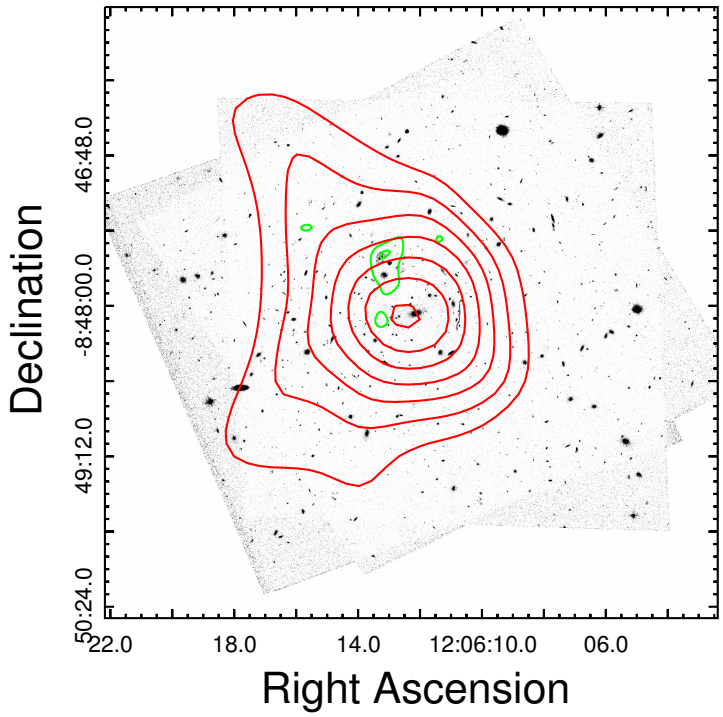

Figure 4.16: Optical image from HST (greyscale) overlaid with the weak lensing mass distribution (red) from Umetsu et al. 2012 and the MUSTANG S/N contours (green). In addition to the E-W elongation noted in previous observations, there is an elongation to the NE. This suggests that the MUSTANG SZE detection may correlate with real structure such as an infalling galaxy group.

evidence that this source may be attributed to a filamentary structure to the N-NE (see Figure 4.16).

The optical image of MACS J1206.2-0847 from a single HST band is shown in Figure 4.16 with the weak lensing mass from Umetsu et al. [2012] overlaid in red contours and the MUSTANG SZE flux overlaid in the green contours. The SE elongation follows a filamentary structure that has been noted in Umetsu et al. [2012]. Additionally, there appears to be an elongation in the mass distribution to the NE, in

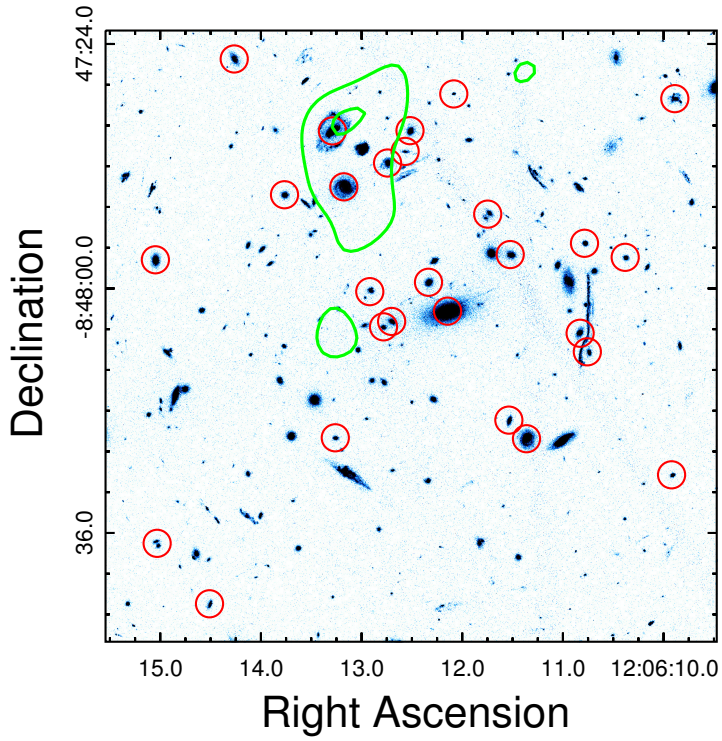

Figure 4.17: Optical image from HST (greyscale) with cluster member galaxies circled in red. The MUSTANG S/N contours are overlaid in green. We define cluster members to have spectroscopic redshifts [Biviano et al. 2013] with $|z_{clus} - z_{mem}| \leq 0.02$ ($R_{los} \lesssim 7$ Mpc).

the direction of the feature detected by MUSTANG. The lower resolution SZE image from Bolocam finds a centroid in the same direction (Figure 4.10). The MUSTANG feature coincides with several cluster member galaxies (Figure 4.17), which we suggest may constitute an in-falling group with X-ray luminosity below the detection limit of the *Chandra* observation.

With this scenario in mind, we use the SZE flux measurement to explore the physical properties such a group would likely have in order to remain below the X-ray detection threshold. The lower limits, in which we assume MUSTANG de-

tects all of the SZE flux associated with the group, are $M_{500} = 1.3 \times 10^{13}\ M_{\odot}$ and $L_X = 7.99 \times 10^{43}$ erg s^{-1}. In this calculation we have assumed the $Y - M$ and $Y - L_X$ scaling relations given in A10. We note that $Y_{\rm SZ} D_A^2 = 9.53 \times 10^{-8}$ Mpc^2 is outside the parameter space covered by the A10 and Czakon et al. [2014] samples and the error bars reflect the significant extrapolation.

At the location of the MUSTANG residual feature, the exposure-corrected $0.1 - 2.4$ keV *Chandra* image yields an X-ray flux of $3.0 - 5.0 \times 10^{-14}$ erg s^{-1} cm^{-2}. This provides an upper limit of the soft 0.1-2.4 keV X-ray luminosity $L_X < 2.2 - 3.5 \times 10^{43}$ erg s^{-1} for an infalling subcluster either below the X-ray detection threshold or masked by the main cluster emission. Using the Malmquist Bias corrected $L_X - M_{500}$ scaling relations of Pratt et al. [2009], which are consistent with the $Y - M$ and $Y - L_X$ scaling relations in A10, we find that the region selected by MUSTANG is consistent with an infalling subcluster with $M_{500} < 6.2 - 8.4 \times 10^{13}\ M_{\odot}$, which agrees with the mass estimated from the MUSTANG SZE flux above. We note that an X-ray bright compact source, coincident with a spiral galaxy in the optical imaging (Figures 4.10 and 4.17), is located at the southern tip of the region selected by MUSTANG at > 4-σ, which could be the BCG of a putative infalling group. While the faint MUSTANG SZE detection does not unambiguously confirm a dynamical event such as a group merging with the main cluster, it does hint at a potential departure from hydrostatic equilibrium. Additionally, the centroid of the diffuse X-ray emission appears significantly offset from the BCG (Figure 4.10), which suggests some degree of merging activity in the cluster [Mann & Ebeling 2012].

Chapter 5

MUSTANG-1.5 Instrument

MUSTANG-1.5 is the next generation receiver constructed to replace MUSTANG [Dicker et al. 2014]. The focal plane consists of 223 feedhorn-coupled TES polarimeters, read out with novel microwave multiplexing electronics (Chapter 6). With MUSTANG-1.5 we address several of the limitations of MUSTANG including detector sensitivity, spatial dynamic range, and cryogenic stability. In this chapter, I discuss the design, construction, and laboratory characterization of the new receiver. Figure 5.1 shows a 3D model and exterior photograph of the MUSTANG-1.5 instrument.

5.1 Detectors

The MUSTANG-1.5 detectors are polarization sensitive TES bolometers fabricated by NIST (see Figure 5.2). The detector design is based on the detectors used in recent CMB polarization experiments such as ABS [Essinger-Hileman et al. 2010] and

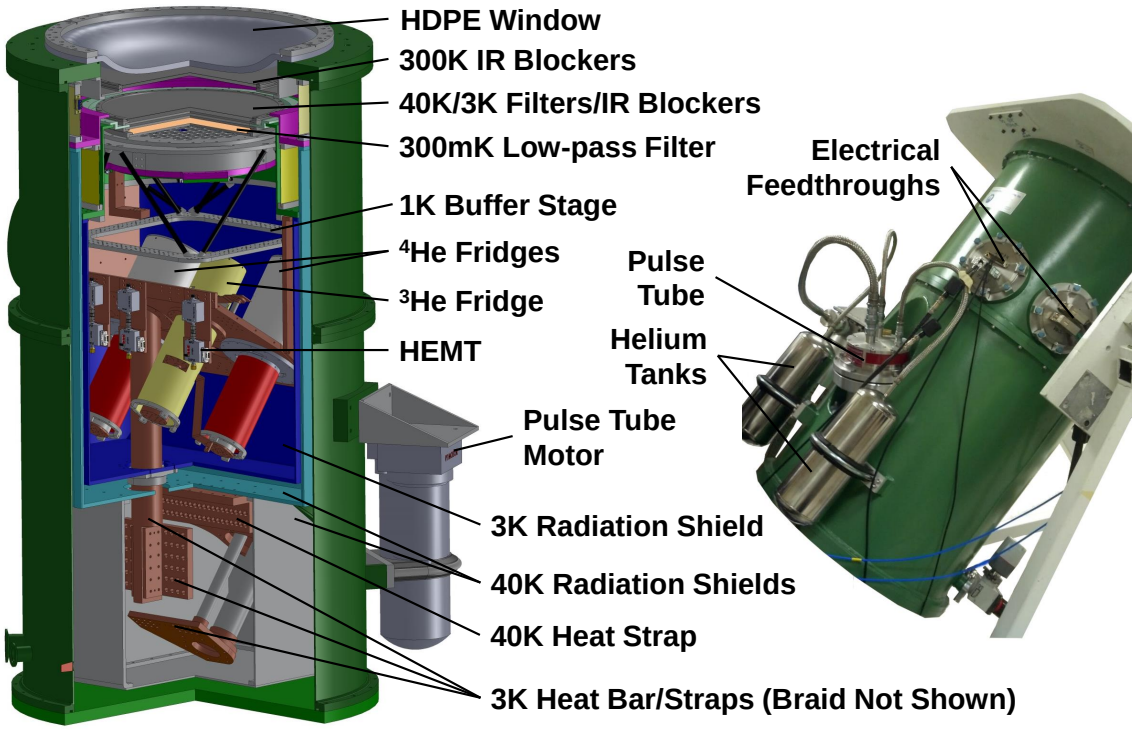

Figure 5.1: Cross-section view and photograph of the MUSTANG-1.5 receiver. Externally, the pulse tube (PT) is connected to a motor and two helium reservoirs with flexible hoses. The motor is connected to a water-cooled Cryomech compressor (not shown). Internally, the 1st stage of the PT is connected to a 40 K thermal radiation shield through flexible copper braid (not shown). The 2nd stage is connected to a long copper bar with flexible copper braid. The ^{3}He and ^{4}He fridges are mounted to a copper structure, which also holds the HEMT amplifiers. Radiation shielding at 40 K and 3 K surround most of the internal components to block thermal radiation emitted by the vacuum can at room temperature.

ACTPol [Niemack et al. 2010]. Incident radiation is coupled to the detector by a feed-horn and separated into orthogonal polarizations by a broadband planar orthomode transducer (OMT) [e.g., McMahon et al. 2009]. The power travels from the OMT down a coplanar waveguide (CPW) to microstrip transition, then to a TES island (one for each polarization) where it is dissipated by a length of lossy gold meander. A choke between the waveguide and the OMT prevents radiation from leaking out and coupling to nearby detectors. The TES membranes are thicker and much smaller than those used in MUSTANG and we therefore expect them to be significantly less sensitive to vibrations.

The third TES island on each bolometer is not optically coupled and can be used to measure the dark electrical noise. Additionally, each TES island contains a heater which can be used to monitor changes in detector sensitivity. Due to limitations in the PCB manufacturing process, we are only able to fit traces leading to heaters in a

$N_{\rm det}$	223 (64)
T_c	490 mK
$T_{\rm bath}$	300 mK
G	331 pW/K
$P_{\rm sat}$	45 pW
NEP_G (theory)	5.5×10^{-17} W/$\sqrt{\rm Hz}$
NEP_γ	1.6×10^{-16} W/$\sqrt{\rm Hz}$
$P_{\rm inst}$	5 pW
RMS Noise $4.25' \times 4.25'$	21 (40) μJy/beam$\sqrt{\rm hr}$

Table 5.1: Technical specifications of MUSTANG-1.5, including the total number of detectors ($N_{\rm det}$), TES transition temperature (T_c), thermal bath temperature ($T_{\rm bath}$), thermal conductance between the bath and TES (G), targeted saturation power ($P_{\rm sat}$), predicted phonon noise (NEP_G), photon noise during typical weather conditions (NEP_γ), and the RMS noise level reached in a one hour observation (ignoring overhead) of a $4.25' \times 4.25'$ region. The values in parentheses correspond to the 64-detector configuration of MUSTANG-1.5.

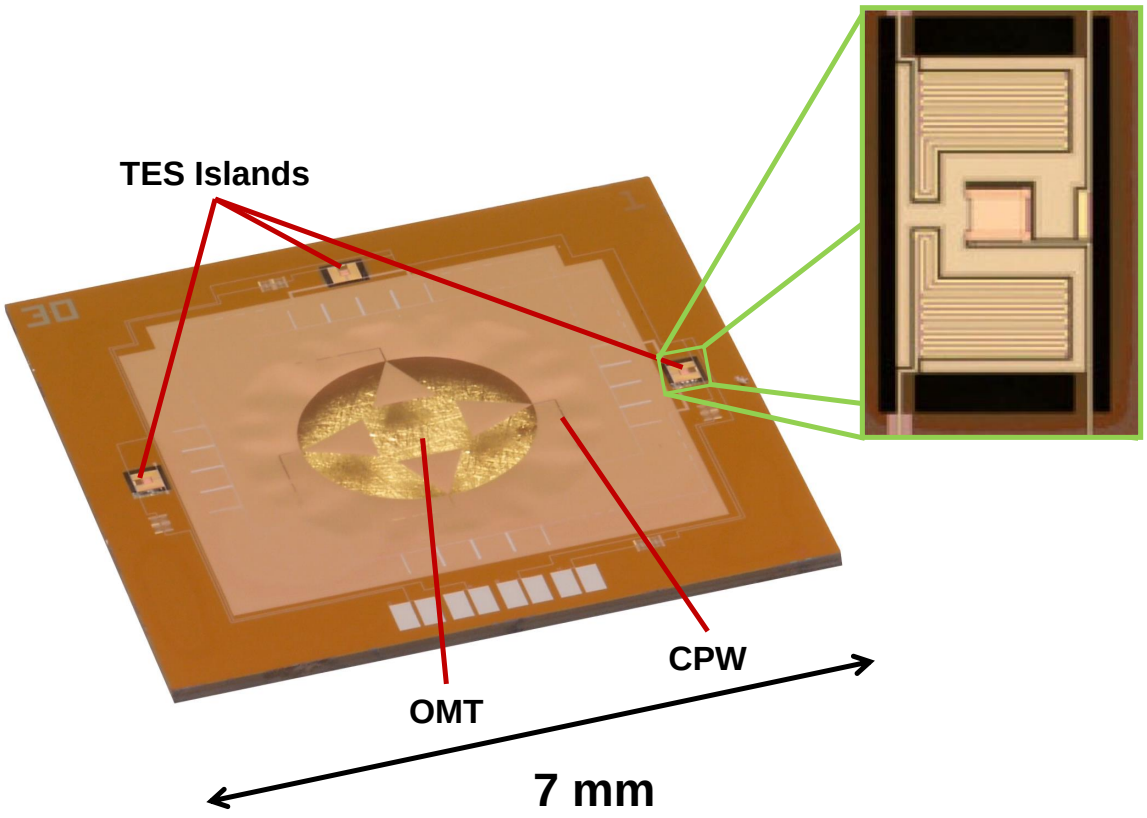

Figure 5.2: A MUSTANG-1.5 90 GHz detector prototype fabricated by NIST. The final MUSTANG-1.5 detectors will be circular. The OMT is made up of four triangular segments, which couple incident radiation, from two orthogonal polarizations, to the CPW leading to the TES islands where the power is dissipated via lossy gold meanders. A close-up of an individual TES from Grace et al. [2014] is shown to the right.

few detectors modules and none of the dark TESs are connected. However, we expect the TES noise to be below the photon limit so there is little need for reading out the dark TESs in the first place. We use an external optical calibration source to monitor detector sensitivity so the heater lines are not strictly necessary either.

Given a range of typical weather conditions at the GBT, we compare the total noise $NEP_{\rm Tot}$ with the photon noise NEP_{γ} in order to determine the optimal target

Saturation Power	NEP_G 10^{-17} W/$\sqrt{\text{Hz}}$	Best Weather 45°	Good Weather 45°	Moderate Weather 30°
10 pW	2.7	1.04*	1.01*	1.00*
15 pW	3.3	1.06	1.03*	1.00*
20 pW	3.8	1.09	1.05	1.01*
29 pW	4.6	1.14	1.07	1.01
45 pW	5.7	1.20	1.10	1.02

Table 5.2: $NEP_{\text{Tot}}/NEP_{\gamma}$ for a wide range of weather conditions, TES saturation powers, and observing angles. The asterisks denote weather conditions for which the atmospheric loading exceeds the saturation power of the TES, rendering it no longer sensitive. T_c is taken to be 490 mK and T_b = 300 mK. The photon noise for best ($\epsilon = 0.05$) to moderate ($\epsilon = 0.3$) weather conditions ranges from $8.9 - 29.2 \times 10^{-17}$ W/$\sqrt{\text{Hz}}$. We find that a 45 pW saturation power provides photon-limited sensitivity and robust performance under the full range of targeted operating conditions. Table adapted from Dicker et al. [2014].

saturation power (Table 5.2). The values marked with an asterisk correspond to cases for which the atmospheric loading exceeds the saturation power and the detector would cease to function. In order to provide dependable performance over a wide range of expected weather conditions and observing elevations, we choose a saturation power of 45 pW.

The TESs on each detector are connected to gold bond pads through superconducting aluminum traces. Wire bonds carry the TES bias, and in some cases electrical heater power, from the pixels to matching bond pads on a duroid[1] circuit board (see Figure 5.3). The superconducting aluminum traces lead to four positions where the MUX chips, each used to readout 16 dual-pol detectors, will be mounted. Due to manufacturing limitations we were unable to space traces close enough together to populate every feedhorn. Since the initial MUSTANG-1.5 deployment will consist of at most 64 detectors the sparsely-populated PCB is adequate for now. Technical chal-

[1] www.rogerscorp.com

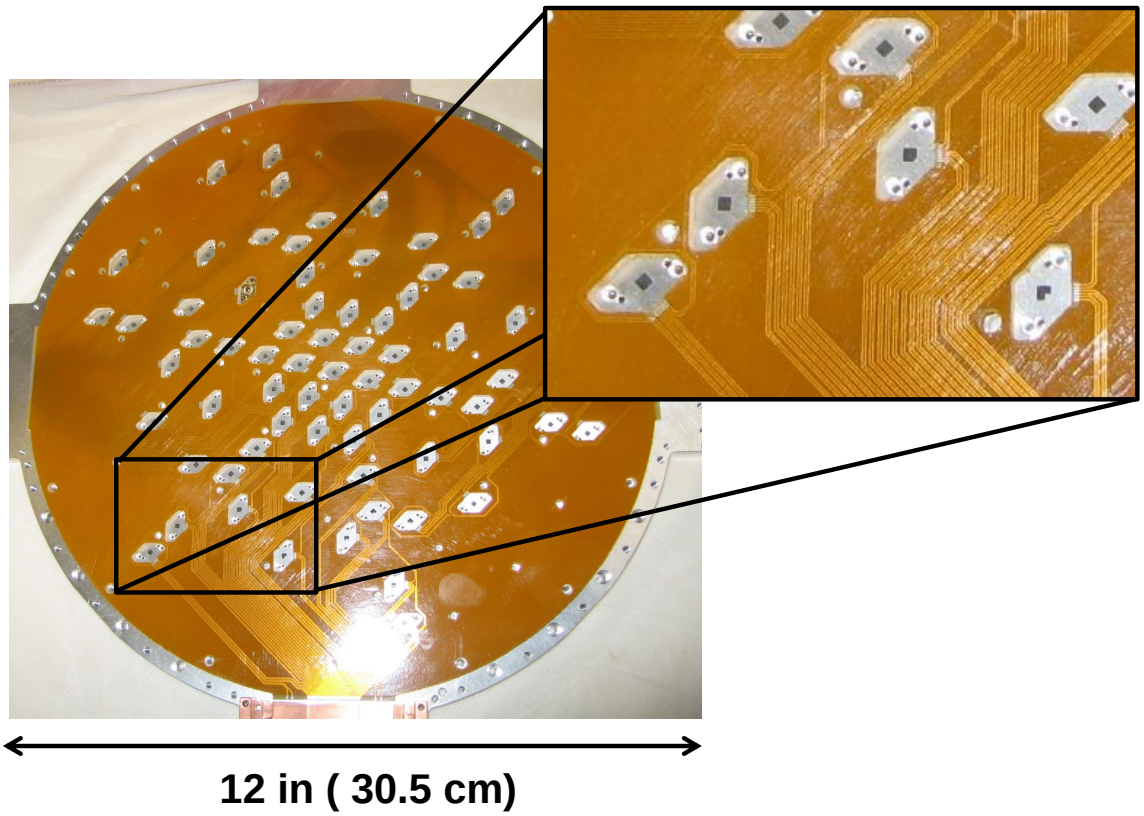

Figure 5.3: The MUSTANG-1.5 detector PCB overlaid on the square waveguide plate. Aluminum traces, each 120 μm wide, connect the bond pads near each detector with the bond pads near four positions where the MUX chips will be mounted at the outer edge of the waveguide plate. Note that this PCB is designed to accommodate only a subset of the potential 223 feedhorns due to design limitations and manufacturing costs. Since the initial MUSTANG-1.5 deployment will consist of at most 64 detectors the sparsely-populated PCB is adequate for now. Technical challenges for tightly packing narrow traces will need to be addressed for future upgrades to MUSTANG-1.5.

lenges for tightly packing narrow traces will need to be addressed in future upgrades of MUSTANG-1.5.

Each detector is housed within a brass module that contains two alignment pins and two clearance holes for the mounting hardware (see Figure 5.4). The module lid is tapered for convenient access to the bond pads with a wire bonder. Each

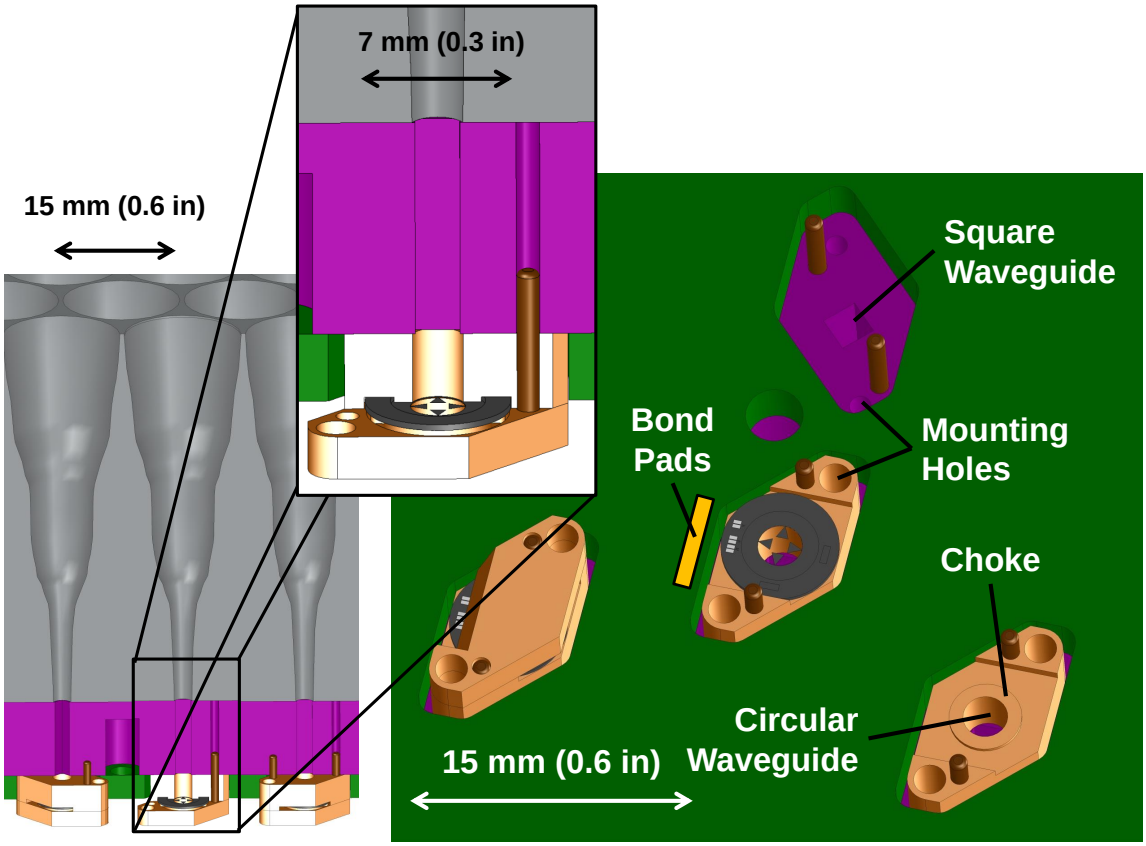

Figure 5.4: 3D model of the array assembly. **Left:** Cross-section view of the feedhorns (grey), the square waveguide plate (purple) and the detector PCB (green). The close-up view shows the detector module and the circular-square-circular waveguide transitions leading to the OMT. **Right:** Back view of the array. A fully installed detector module is shown near the left. The module lid is tapered near the bond pads to provide easier access for the wire-bonding machine. The central module is oriented so that the detector bond pads align with those on the PCB (represented as a yellow rectangle). The rightmost module has the detector removed to show the circular waveguide and RF choke.

module is screened with a dummy detector chip to ensure that there are no burrs or imperfections that could damage the real detectors when they are installed in the modules. The underside of each lid contains a moat filled with microwave absorber to prevent stray out-of-band radiation from being reflected onto the detector.

Figure 5.4 shows the 3D model of the detector modules installed in the square waveguide plate, which has been artificially painted purple for illustrative purposes. The left module shows the exposed bond pads in a completely assembled module. The matching bond pads in the detector PCB, which is shown in green, are not included in this model, but are represented by a yellow rectangle. The center module has the lid removed to show the detector pixel mounted underneath. The pixel is removed from the rightmost location to show the section of circular waveguide and the waveguide choke in the base of the module. In practice, fully assembled modules are guided along the alignment pins and then bolted onto the square waveguide plate. The detector PCB is then lowered into place and the wire bonds are installed between the detectors and the PCB. A dust lid is then secured over the back of the array to protect the wirebonds and detector chips.

5.2 Optics

With MUSTANG-1.5 we do not use any re-imaging optics, instead we couple the detectors to a monolithic array of feedhorns positioned so that the apertures are approximately at the Gregorian focus of the telescope. Since common mode subtraction attenuates astronomical signal on scales larger than the instantaneous FOV, we design the array to make full use of the focal plane available. We include a series of filters between the cryostat window and the array, which limits the usable focal plane diameter to approximately 30 cm, after accounting for the $f/1.92$ beam. A 30 cm center-center separation between outer pixels provides a maximum FOV of $\sim 5.5'$ diameter. This is an enormous improvement over the $42''$ diameter FOV

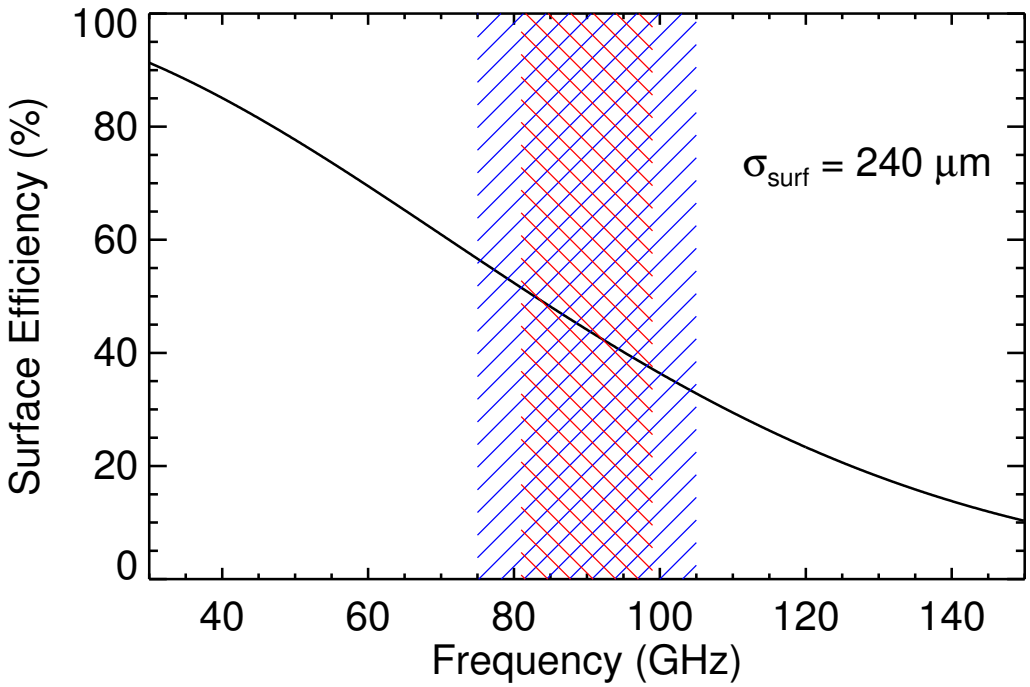

Figure 5.5: Surface efficiency as a function of frequency for the GBT primary with $\sigma_{\rm surf} = 240$ μm. The MUSTANG-1.5 75-105 GHz band is shown in blue and the 81-99 GHz MUSTANG band is shown in red.

provided by MUSTANG and will enable a wider range of science goals, as described in Chapter 7.

5.3 Bandpass

The target band of MUSTANG-1.5 is 75-105 GHz in order to optimize signal to noise ratio (SNR) based on expected weather conditions and detector characteristics. The SNR for an integration time t, assuming a background-limited single polarization

detector is given by [Dicker et al. 2014]

$$SNR = \frac{1}{2}\frac{\int d\nu A_{\rm eff}(\nu) S_\nu W(\nu) {\rm e}^{\tau(\nu)}}{\sqrt{\int d\nu (h\nu)^2 W_{\eta\epsilon}(W_{\eta\epsilon}+1)}}\sqrt{t}, \tag{5.1}$$

where $A_{eff}(\nu)$ is the telescope effective area, S_ν is the source flux, $W(\nu)$ is the bandpass, $W_{\eta\epsilon}$ is the optical efficiency of the receiver, and $\tau(\nu)$ is the atmospheric opacity along the line of sight. Dicker et al. [2014] calculate the SNR for a wide range of atmospheric opacities, bandpasses, and telescope elevations and the 75-105 GHz range was found to be optimal. At frequencies below 70 GHz the SNR drops off rapidly because the atmosphere contains a complex of O_2 emission lines at $\sim$ 60 GHz. Frequencies exceeding 105 GHz approach another O_2 line at $\sim$ 120 GHz and provide diminishing returns as the telescope efficiency becomes limited by the $> 240\mu$m surface accuracy of the primary mirror (see Figure 5.5).

5.3.1 Feedhorns

Many current generation radio and sub-millimeter receivers use corrugated feeds to couple incident radiation to the detectors. While corrugated feeds would provide low sidelobes and a frequency independent beam pattern, for our purposes they are prohibitively expensive to manufacture and could not be as closely packed as smooth-walled feedhorns. Conical feeds are the simplest design, but provide high sidelobes and an asymmetrical beam pattern. Instead we used mode-matching software, following Zeng et al. [2010], to optimize the design of a profiled horn, which has been shown to provide comparable performance to corrugated feeds in our 75-105 GHz band.

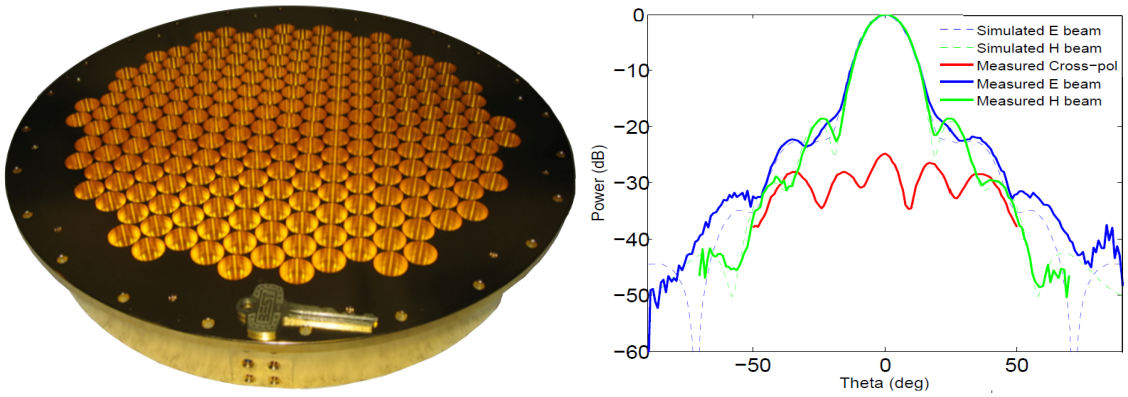

Figure 5.6: **Left:** Monolithic array of 223 feedhorns for MUSTANG-1.5. The array has been gold plated to improve thermal conductivity to the ^{3}He fridge. **Right:** Beam measurements at 90 GHz. The dashed lines show the beam profiles from simulations, which strongly agree with the measurements.

Measurements of the beam profile (see Figure 5.6) confirm that the optimized feed design produces the shape predicted by simulations.

The optimal smooth wall feedhorn profile for the MUSTANG-1.5 feeds can be seen in the left of Figure 5.4. The feed tapers down to circular waveguide 1.172 mm in diameter, which cuts off the dominant mode at $1.841c/(2\pi r) \approx 75$ GHz. A higher order mode can propagate in the circular waveguide at 98 GHz. In order to preserve the beam shape without sacrificing bandwidth we add a length of 2 mm wide square waveguide (shown in purple), which also cuts off at 75 GHz, but prevents higher order modes from propagating.

The feeds are machined in a single block of aluminum using a set of custom drill bits. A combination of rough bits and finishing bits precisely cut the optimized feed profile including a small length of circular waveguide at each end. A separate plate was machined that contains the square waveguide section for each feed and to which the detector modules and circuit board are mounted. The square waveguide plate

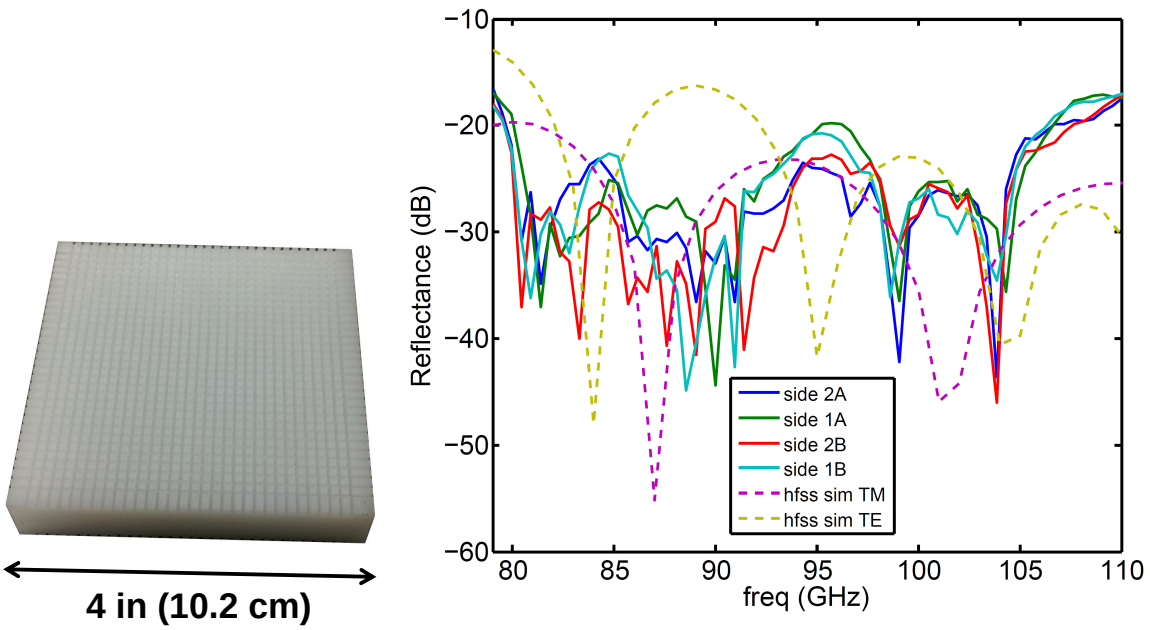

Figure 5.7: **Left:** A test block of HDPE patterned with grooves to provide AR coating. **Right:** Measurements of the reflectance of both sides (denoted A and B, respectively) of two AR-coated test pieces, carried out by collaborators at the University of Michigan. Dashed lines show the reflectance predicted by HFSS simulations. In general, the measurements agreed with the simulations across the MUSTANG-1.5 band.

also contains four platforms for conveniently mounting the μMUX modules next to the matching bond pads on the detector PCB.

5.3.2 Filters and IR Blockers

The aperture of the MUSTANG-1.5 cryostat is sealed by a 16 inch (41 cm) diameter, 0.375 inch (9.5 mm) thick, high-density polyethylene (HDPE) window. Based on results from a finite element analysis using the high frequency structural simulator (HFSS), we patterned the window with 0.017 inch (0.43 mm) wide, 0.027 mil (0.67 mm) deep grooves spaced by 0.059 inches (1.50 mm), to provide an

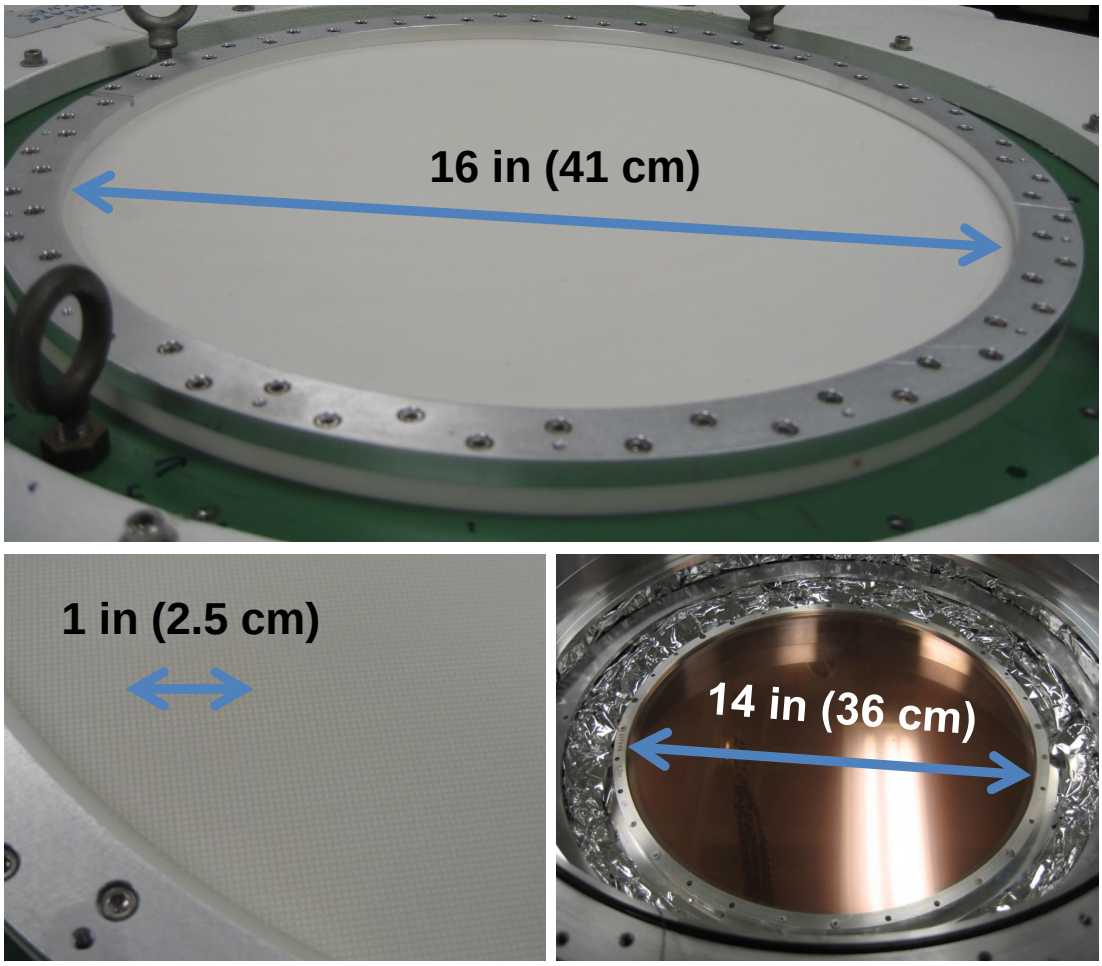

Figure 5.8: MUSTANG-1.5 HDPE window and IR blocking filters. **Top:** Window attached to top vacuum plate. **Bottom left:** Close-up of the window showing the grooves cut to provide an anti-reflective surface. **Bottom right:** An IR blocking filter at the top of the 3 K filter stack.

anti-reflective (AR) coating. Similar designs have been used recently for cryogenic lenses in ACTPol [Datta et al. 2013]. In order to verify the accuracy of the simulation we constructed a 2 inch (5.1 cm) square test piece and measured reflections at 15° incidence (see Figure 5.7).

In order to keep the array at 300 mK it is crucial to carefully control the thermal

loading within the cryostat. If there were only free space between the HDPE window and the 300 mK array, and taking the worst case scenario that all power emitted by the window is absorbed by the array, then the incident power from the window alone would be

$$P = \epsilon\sigma \left(T_h^4 - T_c^4\right) A \approx 60\text{W},$$

where σ is the Stefan-Boltzmann constant and we have assumed the window acts as a perfect blackbody ($\epsilon = 1$) at 300 K. A 60 W load is almost six orders of magnitude above the acceptable load at 300 mK so we use a series of reflective and absorbing filters mounted at 300, 40, 3, and 0.3 K. Figure 5.8 shows the HDPE window and the 4 K filter stack as viewed from above. The 3D model in Figure 5.9 shows the layout and order of the variety of filters used in MUSTANG-1.5. We use low pass filters at 3 K and 300 mK to define the upper 105 GHz edge of the band. The filters have high absorptivity at near-infrared (NIR) wavelengths and, coupled with poor thermal conductivity to the cryogenic fixtures at the filter edges, can heat up significantly and then re-emit at the higher temperature [Ade et al. 2006]. Some of this power will be in the observing band. In order to mitigate this effect, we mount thin, very fine metal mesh filters to reflect away most of the NIR radiation ($\lambda < 50$ μm) before it can be absorbed by the thick low-pass edge filters.

5.4 Cryogenics

In MUSTANG-1.5 a Cryomech PT410 Pulse Tube (PT) provides two independent cooling stages at $\sim$ 30 K (1$^{\text{st}}$ stage) and $\sim$ 2.5 K (2$^{\text{nd}}$ stage) with capacities of 35 W

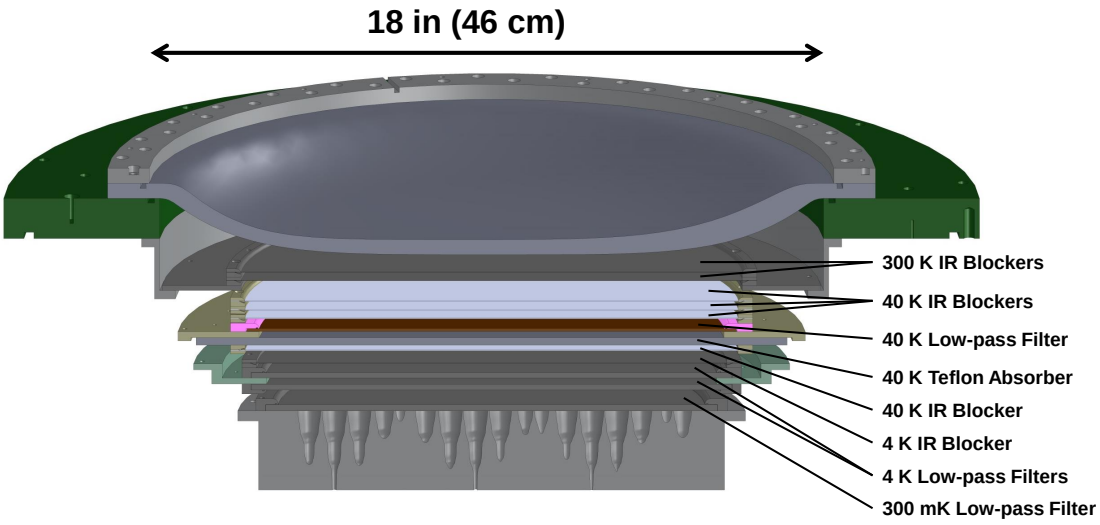

Figure 5.9: The optical path between MUSTANG-1.5 window and the feedhorn array. Thin metel mesh filters reflect thermal IR emission at 300 K, 40 K, and 3 K. Low pass quasi-optical filters define the upper edge of the band at 150 GHz and absorb out of band radiation transmitted through the IR blockers. At 40 K, an absorbing sheet of teflon removes significant excess loading that was discovered during the initial cryogenic characterization. The HDPE window was modeled to take into account the measured 1.6 inch depression at the center, in order to ensure enough space was kept between the window and the 300 K IR blockers. Recently, we added an absorbing Nylon filter at 4 K and found that it significantly reduced the optical load that had been heating the array all the way up to $\sim$ 370 mK.

at 45 K and 1 W at 4.2 K, respectively. The 1st stage is responsible for cooling the first layer of radiation shielding as well as the intermediate stack of reflecting and absorbing filters. The 2nd stage provides cooling to the helium adsorption fridges, High Electron Mobility Transistor (HEMT) amplifiers, electrical wiring, and an additional filter stack. As with MUSTANG we use a combination ^{3}He and ^{4}He fridge system to cool the array to 300 mK. We use an additional ^{4}He fridge to provide a separate 1 K buffer stage between the 3 K structure and the array.

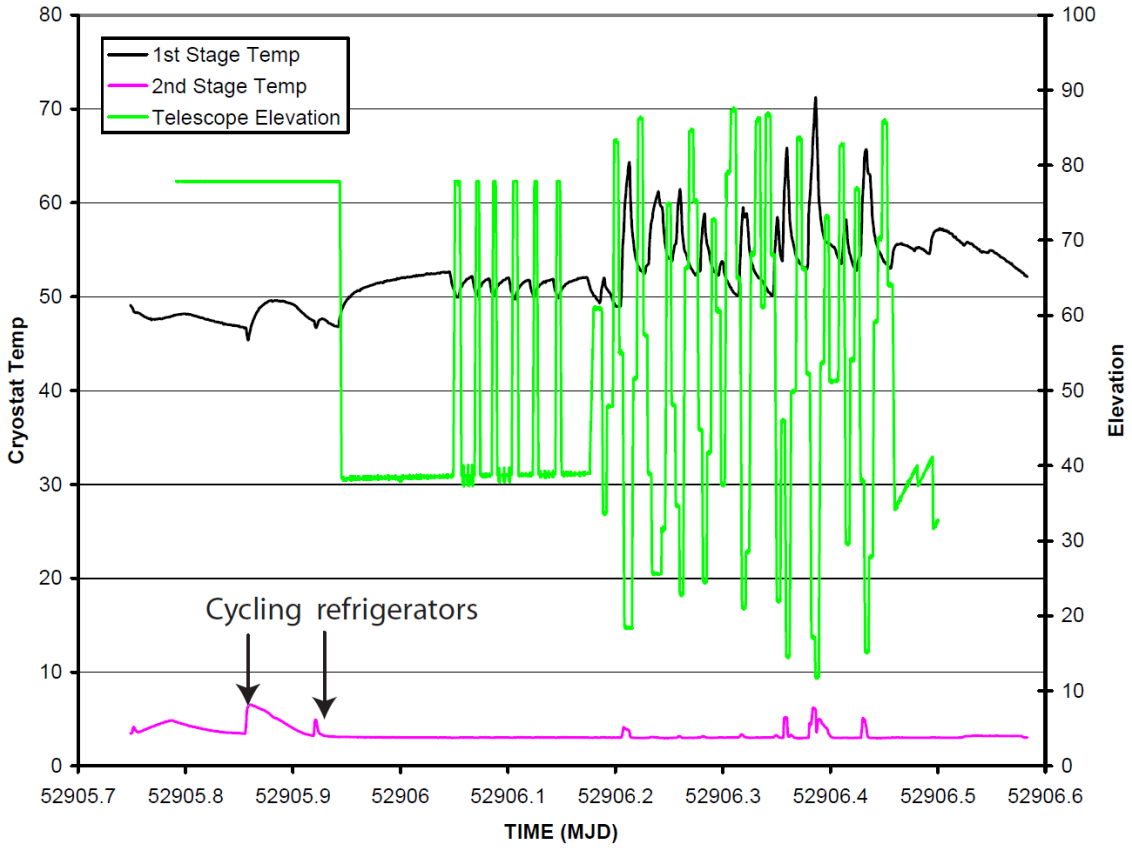

Figure 5.10: Pulse Tube response as the GBT tips in elevation. The temperature fluctuations at the beginning of the plot are expected during the daily cryogenic cycle procedure. Figure taken from Devlin et al. [2004].

5.4.1 Pulse Tube Tilt

The angle of the PT strongly impacts the base temperature achieved. The receiver cabin is angled such that the 5° lower elevation limit of the GBT corresponds to a pointing elevation of 18°. Since the PT is mounted vertically in the cryostat, this means it can tip as low as 18° depending on what science targets are being observed. Since the GBT is a user facility, we have no control over who observes before we do. If the GBT is tipped below $\sim 25°$ before our observing session then it takes almost an

Cryogenic Stage	Thermal Load	Capacities	Dominant Load Sources
40 K	10 W	35 W @ 45 K	G10 mount, radiation
3 K	172 mW	500 mW @ 3.5 K	G10 mount, Coax, radiation
1 K	123 μW	1 mW @ 1.1 K	Carbon fiber supports
300 mK	10μ W	100 μW @ 308 mK	Carbon fiber supports, wiring
Cryogenic Stage	Thermal Load	Cable Materials (Inner/Outer Conductors)	
40 K	252 mW	SS/BeCu	—
3 K	12 mW	SS/BeCu	—
1 K	20 μW	SS/BeCu, NbTi/NbTi	—
300 mK	1 μW	SS/BeCu, NbTi/NbTi	—

Table 5.3: Estimates for thermal loading on each of the cryogenic stages due to the mechanical assembly, radiation, and coaxial cables used by the four μMUX readout channels. In all cases, the load is well below the required limits. The components that contributed the most to the thermal loading are listed in the last column.

hour for the 300 mK stage to recover and stabilize. Figure 5.10 shows measurements of the PT 2nd stage as a function of GBT elevation.

In order to prevent the PT from being tipped to extreme angles it is installed at a 37° angle and the MUSTANG-1.5 cryostat is mounted in a rotating assembly. As the turret wheel rotates to put different receivers into the focus position, the MUSTANG-1.5 cryostat can be rotated such that the PT will tip by a maximum of 45° at all telescope pointings.

A summary of the expected thermal load on each of the cryogenic stages is given in Table 5.3. Independent calculations of the thermal load due to the coaxial cables from the readout electronics were used to determine the minimum cable lengths between separate thermal stages.

5.4.2 Radiation Shielding

MUSTANG-1.5 uses two layers of aluminum radiation shields (see Figure 5.11), tied to the 1st and 2nd stages of the PT, respectively. The 40 K radiation shield also serves as the thermal link between the PT and the 40 K filter stack so to maximize thermal conductivity we weld several ultra-high purity aluminum bars along the cylindrical face of the shield. Both radiation shields are wrapped many times over in Mylar super-insulation in order to reflect away much of the radiation that would otherwise be absorbed by the aluminum.

The PT cools the cryostat internals through two OFHC copper heat straps. The heat straps use flexible copper braid to minimize vibrations at the array. Figure 5.12 shows the interior of the 40 K cavity surrounding the PT. The 2nd stage heat strap is attached to a large copper bar leading to the 3 K structures that hold the helium fridges, HEMT amplifiers, and intermediate filter stack. The 3 K plate that holds the ^{3}He and ^{4}He fridges is shown to the right including the gas gap heat switches used to control the cooling of the charcoal during cryogenic cycling.

Figure 5.13 shows the interior of the cryostat with the heat shields removed. The 40 K and 3 K aluminum plates are separated from the 300 K top plate, as well as from each other, by cylindrical tubes of G10 wrapped in super-insulation. Holes are cut in the G10 to allow cables to pass underneath the 40 K plate to feedthroughs leading to to the cold electronics below 3 K. The HEMT amplifiers are mounted at the front of the 3 K fridge mount structure. In the back there are three cryogenic breakout boards (CBOBs), which heat sink the 50-wire twisted-pair cables and divide them into a series of smaller cables for each thermometer, heater, or MUX module.

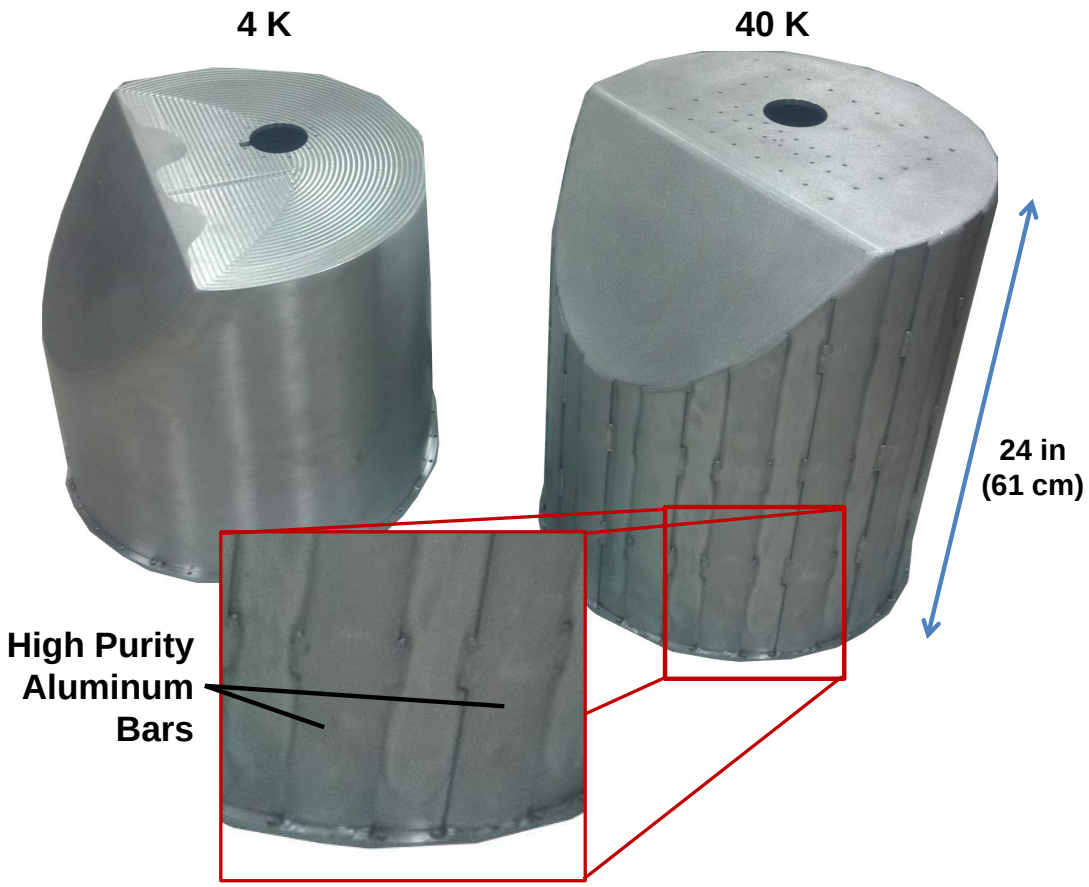

Figure 5.11: Thermal radiation shields for the 3 K (left) and 40 K (right) stages. The inset shows the high purity aluminum bars that improve the thermal link between the 40 K filter stack and the 1st stage of the PT. Both of these shields are wrapped in at least a dozen layers of Mylar super-insulation (not shown) to reflect away the incident radiation before it can be absorbed by the aluminum shield.

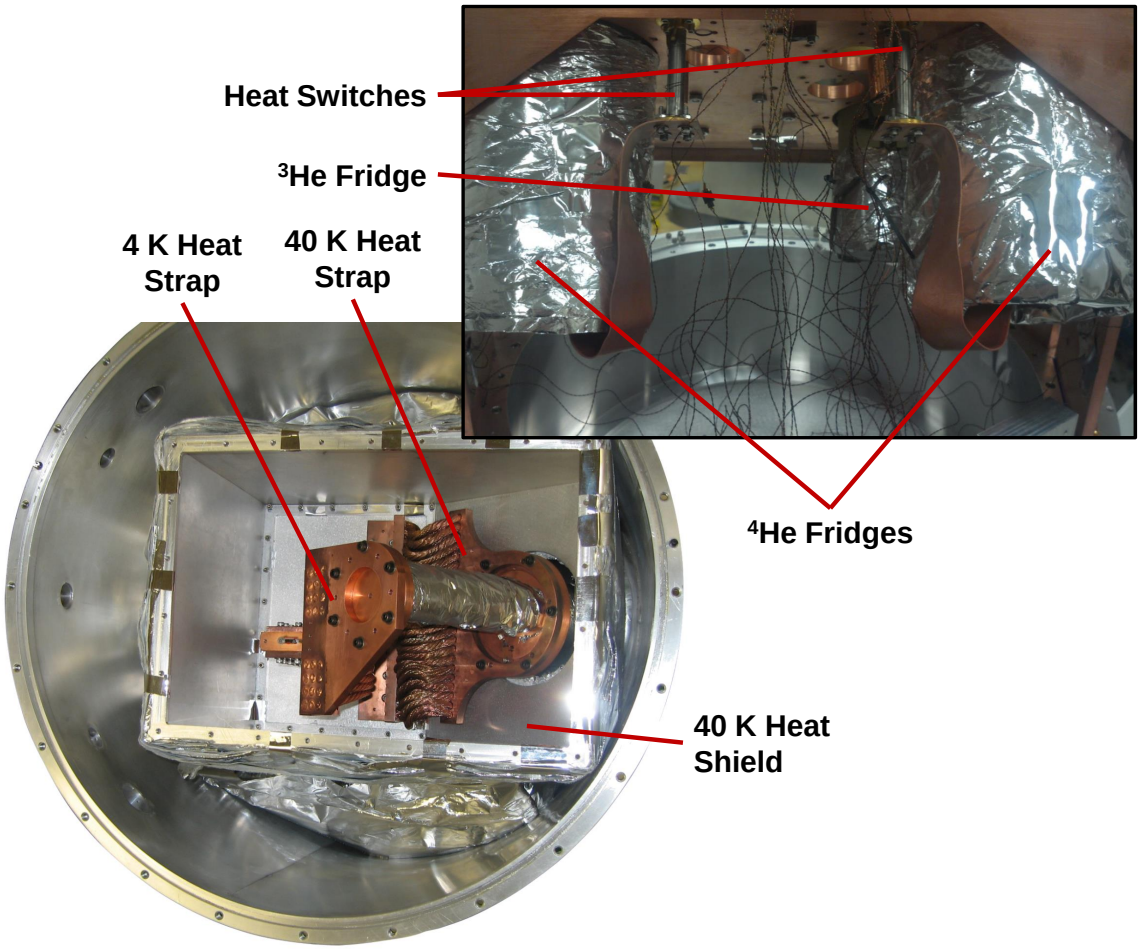

Figure 5.12: **Lower left:** The 40 K cavity surrounding the Pulse Tube. OFHC copper braid is used provide high thermal conductivity and low sensitivity to vibrations. **Upper right:** 3 K structure that holds the fridges, heat switches, and HEMT amplifiers (not pictured here). Thin annealed copper sheets connect the heat switches to the charcoal pots in each fridge.

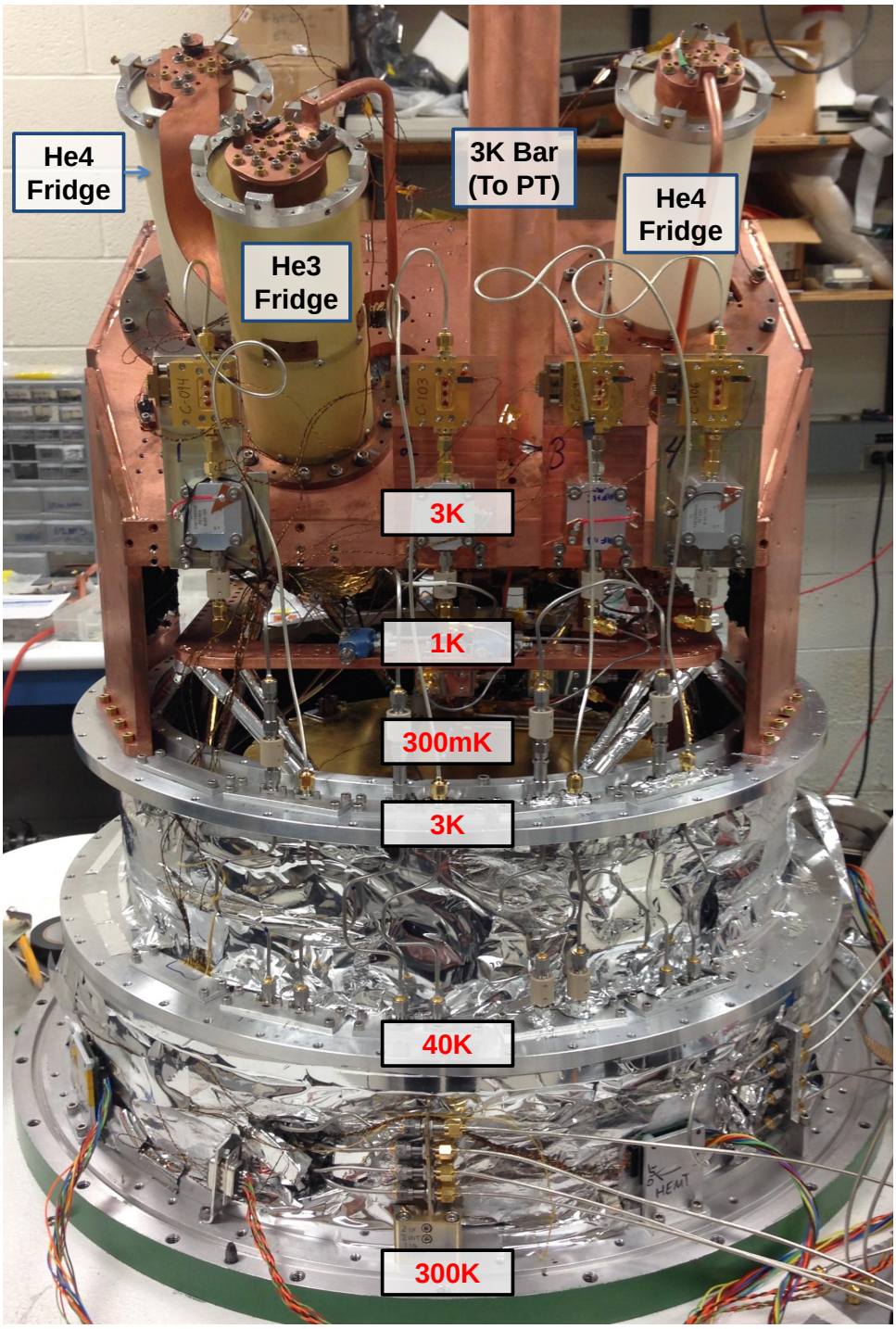

Figure 5.13: Photo of the MUSTANG-1.5internal components. The window is at the bottom of the frame so MUSTANG-1.5 is upside-down here.

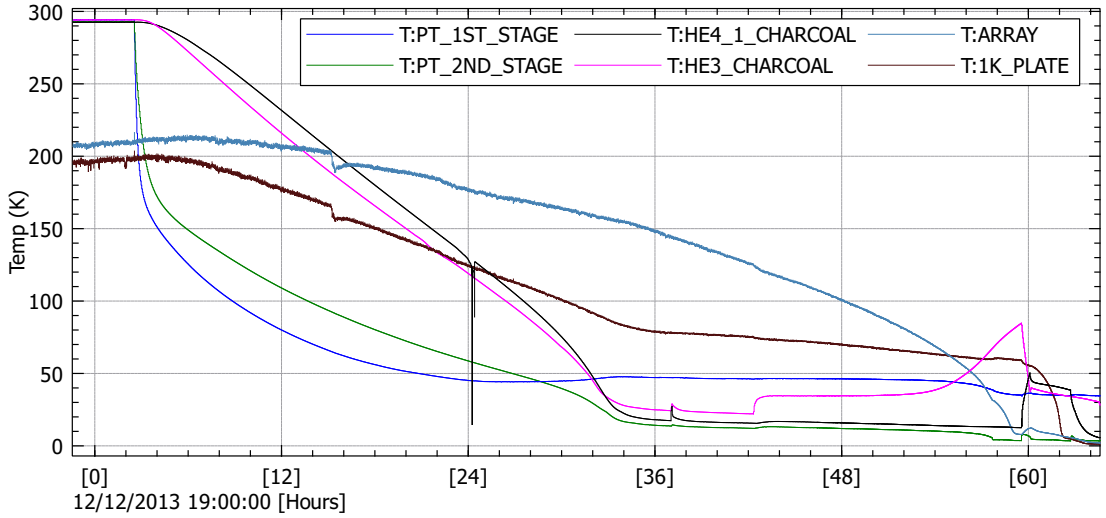

Figure 5.14: Representative MUSTANG-1.5 cooldown in the dark. The PT nears base temperature in just over a day, but the array takes almost three days days to reach base temperature. Given the long thermal path between the PT and the array, the lengthy cooling time is not surprising.

5.5 Cryogenic Characterization

The first tests of the cryogenic performance are carried out with the receiver aperture sealed by a metal plate and metal blanks placed at each of the filter stages. These so-called "dark tests" determine the baseline performance of the cryogenics, in which the minimum thermal radiation is absorbed by each component. This serves as a reference to track the performance of the instrument over its operational lifetime.

A typical cooldown takes approximately three to five days depending on the quality of the internal thermal links, the orienation the cryostat is left in while cooling, and whether or not the cryostat is open to the light. Figure 5.14 shows representative temperatures from an early cooldown in the dark. A passive heat switch connects the array to the 1 K stage and turns off automatically when the array is below 15 K and

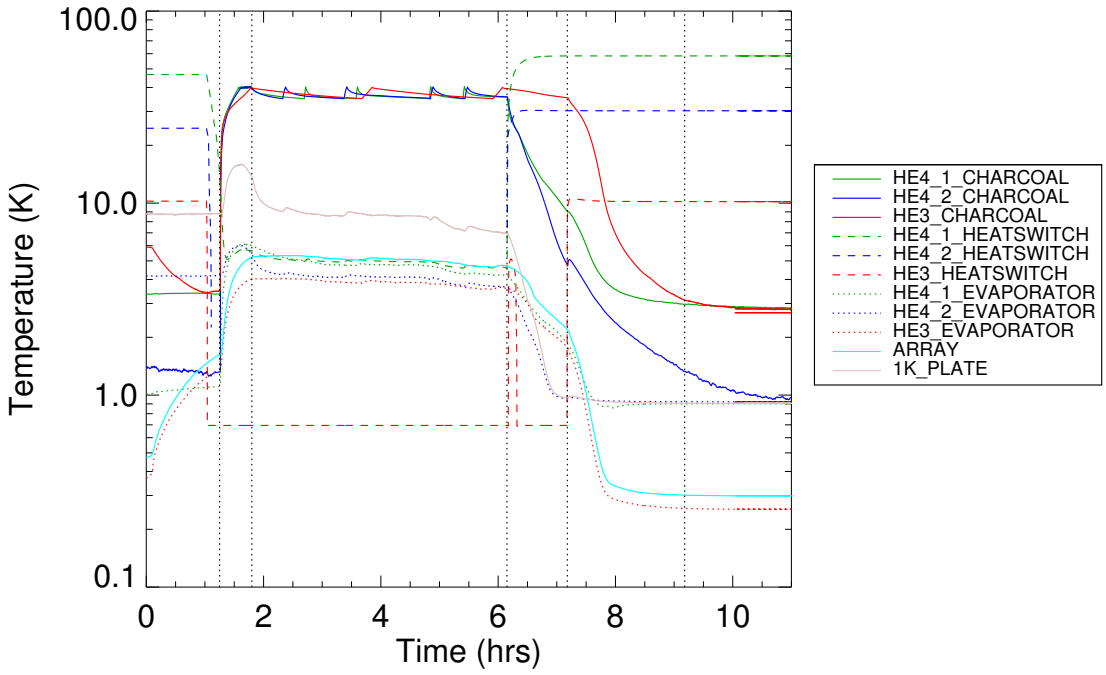

Figure 5.15: Temperatures during a typical cryogenic cycle. Dotted vertical lines indicate the end of each cycle stage beginning with stage 1. The cycle stages are described in detail in the text. The cycle is considered complete when the array reaches base temperature, which in this case was ~ 300 mK.

contributes minimal parasitic loading during normal operations. Without this heat switch the array cools primarily through the relatively inefficient thermal connection to the ^{3}He fridge, which increases the overall cooldown time dramatically.

Once the array reaches ~ 3 K we can begin cycling the helium fridges following the same five stage procedure as in MUSTANG. An example cycle is shown in Figure 5.15 with each of the following stages separated by vertical dotted lines:

- **Stage 1:** Turn all heaters off. Wait until heat switches reach an "off" state below ~ 12 K.

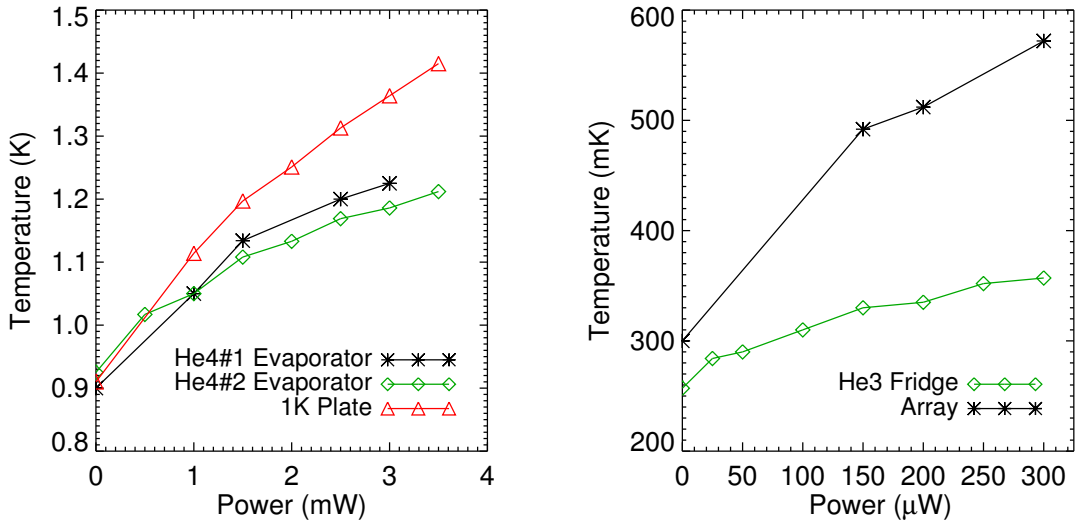

Figure 5.16: Measurements of applied power versus temperature for the low temperature components of MUSTANG-1.5.

- **Stage 2:** Turn on all charcoal heaters. Wait for charcoal to reach $T > 35$ K.
- **Stage 3:** Maintain charcoal temperature of 35 K $< T <$ 40 K. Wait for helium to condense and the ^{4}He evaporators to reach $T < 3.8$ K.
- **Stage 4:** Turn on ^{4}He heat switches to cool the ^{4}He charcoal and pump on the condensed helium. Wait for the ^{3}He evaporator to reach $T < 1.8$ K.
- **Stage 5:** Turn on the ^{3}He heat switch to pump on the condensed ^{3}He. Wait for the ^{3}He evaporator to cool to base temperature $T \sim 260$ mK. Cycle is now complete.

The key figures of merit used to characterize the cryogenics include the base temperature achieved by each component, the Joule capacity of each fridge, and the response of each fridge to an applied load (see Figure 5.16). Table 5.4 provides a comparison between base temperatures achieved in the dark and those achieved with

Location	Dark T(K)	Light (40 K Teflon) T(K)	Light (4 K Nylon) T(K)
PT 1st Stage	31.2	27.0	29.3
PT 2nd Stage	2.7	2.4	2.6
1K Plate	0.91	0.95	0.7
^{4}He #1 Evaporator	0.90	0.90	0.90
^{4}He #2 Evaporator	0.92	0.95	0.92
^{3}He Evaporator	0.25	0.30	0.26
Array	0.30	0.37	0.30

Table 5.4: Post-cycle temperatures reached with the cryostat cover removed and open, respectively. The third column shows the temperatures reached after installing a teflon absorbing filter at 40 K. The 70 mK increase in array base temperature corresponds to $\sim$ 80 μW additional load transmitted through the filters. The last column gives the temperatures after a nylon filter was added at 4 K. The nylon filter greatly reduced the excess optical loading and the target bath temperature of 300 mK has been achieved.

the cryostat window open. With a single absorbing Teflon filter at 40 K the array is approximately 70 mK warmer in the light than in the dark. While a bath temperature of 370 mK will still prevent the detectors from saturating ($T_b < T_c = 500$ mK), the phonon noise NEP_G will increase by $\sim$ 20%. Recently, we added a Nylon filter at 4 K and all of the excess radiation now appears to be absorbed before reaching the array.

Another important characteristic of the MUSTANG-1.5 cryogenic system is the duration each fridge remains at base temperature before the cryogenic cycling needs to be repeated. We characterize each fridge based on the total Joule capacity C following a cycle as well as the parasitic load $P_{\rm par}$, which accounts for all sources of extra power loading the evaporator. The capacity of a fridge with power $P_{\rm app}$ applied

Fridge	P_{app}	t_{app}	t_{hold}	P_{par}	C	Max Hold Time
	mW	s	s	mW	J	hr
^{4}He #1	3	14148	20628	1.9	82.0	12
—	5	11664	12348	—	—	—
^{4}He #2	3	9677	12960	0.3	32.3	30
—	5	6091	7355	—	—	—
	μW	s	s	μW	J	
^{3}He	100	38160	38160	18.9	4.5	66
—	40	77100	77100	—	—	—

Table 5.5: Measurements of the parasitic load and capacity for each fridge in MUSTANG-1.5.

for time $t_{\rm app}$ is given by

$$C = P_{\rm par} t_{\rm hold} + P_{\rm app} t_{\rm app} \tag{5.2}$$

where $t_{\rm hold}$ is the time it takes for all of the condensed helium to evaporated, marked by a sudden increase in evaporator temperature. We measure $t_{\rm hold}$ for at least two different applied powers in order to solve for the two unknown variables, $P_{\rm par}$ and C, in Equation 5.2. Measurements from these "hold tests" are summarized in Table 5.5. Given the measured fridge capacities and parasitic loads, we expect the hold time during observations to well exceed the required minimum of 12 hours.

5.6 Electronics

In order to prevent excessive radio frequency interference (RFI) from contaminating astronomical signals, the National Radio Quiet Zone (NRQZ)[2] was established

[2]www.gb.nrao.edu/nrqz/nrqz.html

in a $\sim 13,000$ square mile area surrounding the GBT. This area is divided into five zones with Zone 1 representing the region closest to the GBT. Any new instrument installed in the receiver cabin must first be measured in an anechoic chamber[3] and shown to comply with the Zone 1 ITU-R RA.769 RFI requirements.[4]

The MUSTANG-1.5 electronics are housed entirely within an RFI-tight (~ 40 dB attenuation) crate with feedthroughs for the AC electrical power, housekeeping cables, and the coaxial cables for the μMUX detector readout. A 3D model of the crate is shown in Figure 5.17. The interface between the DAQ computer, the readout electronics, and the cryostat is shown schematically in Figure 5.18. The readout electronics are described in more detail in Chapter 6 so I only give a brief overview here.

Up to four readout enclosures are powered by a single power supply box and connected to the cryostat with flexible coaxial cables. For laboratory testing we housed all electronics in a 19 inch rack (see Figure 5.19). A Stanford Research Systems DS345 Function Generator is controlled by the DAQ computer and generates the flux ramp signal. For convenience the flux ramp signal is carried by a coaxial cable to the housekeeping box, divided into four twisted pairs and sent to the cryostat on the 50-wire cable that carries the detector biases. In order to provide a uniform timebase and synchronize the electronics for accurate time-stamping, each readout enclosure receives both a 10 MHz frequency standard and a 1 pulse-per-second (PPS) reference for timestamping. On the telescope, the 1 PPS signal and the 10 MHz signals will be supplied by in-house electronics in the receiver cabin.

[3] An anechoic chamber is designed to absorb all EM radiation so that the emission from a device under test can be measured without contribution from reflections

[4] See the RFI limits at www.itu.int/rec/R-REC-RA.769/en

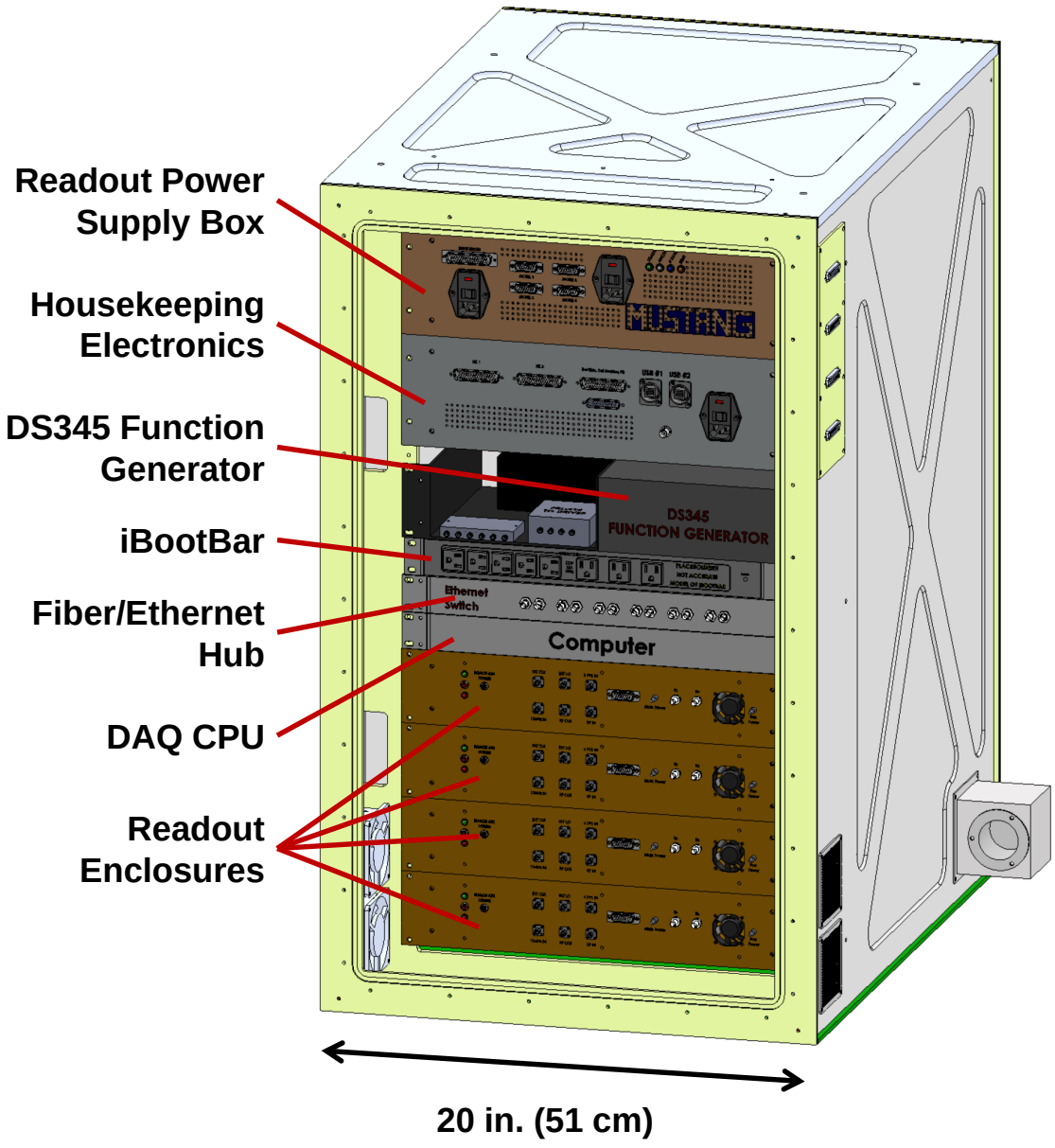

Figure 5.17: RFI-tight crate design for MUSTANG-1.5. The crate is a standard 19 inch rack and can accommodate up to four readout enclosures in addition to the other components. Standard AC power is provided by an 8-outlet iBootBar, which is essentially a power strip that can be controlled remotely. Four 50-pin feedthroughs carry housekeeping, detector biases, HEMT power, and flux ramp between the crate and the cryostat. On the left panel (not shown) there are 10 SMA feedthroughs for the μMUX signal lines and the synchronization signals described in the test. All connectors are capacitively filtered to preventing high frequency signals from propagating out into the receiver cabin.

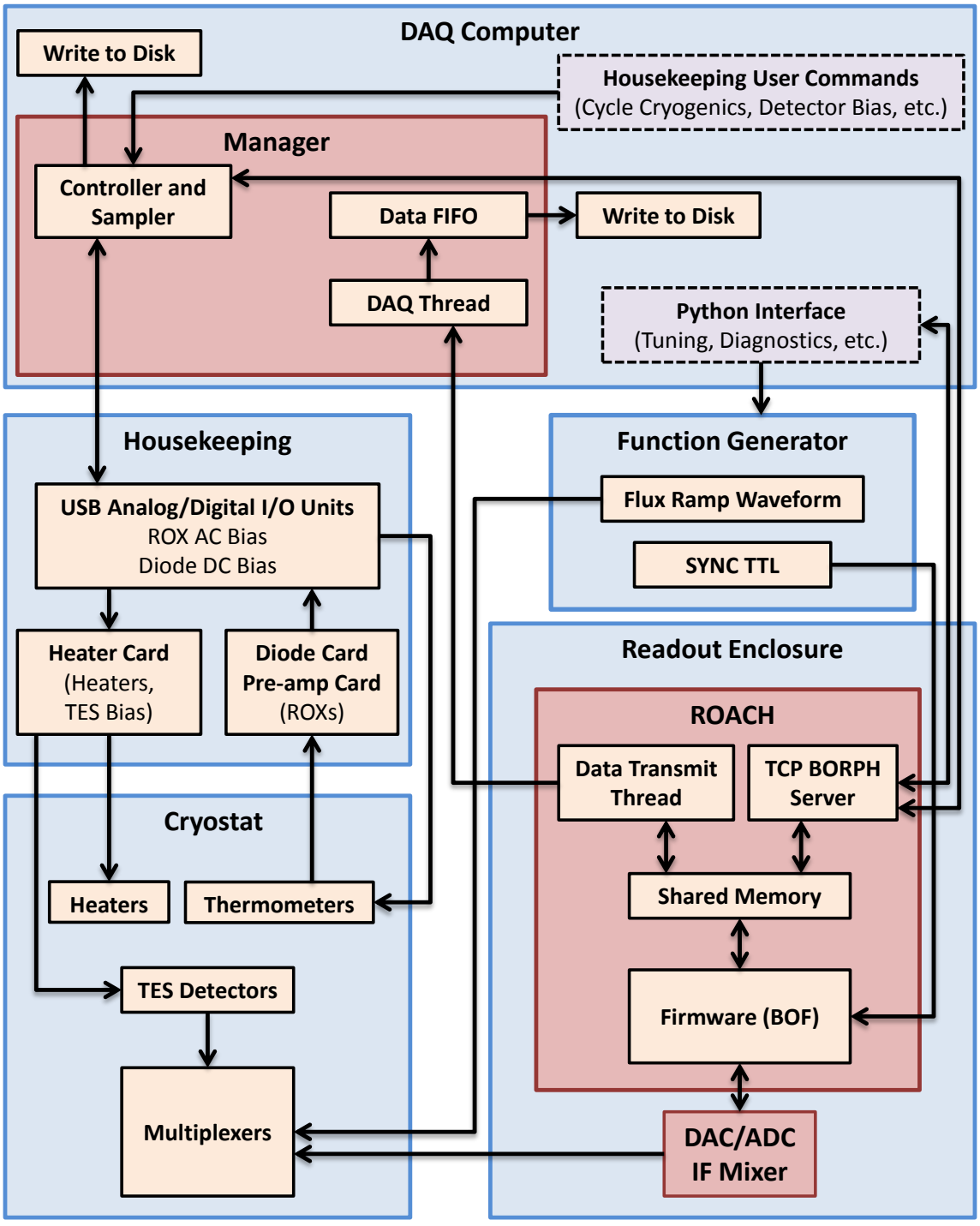

Figure 5.18: MUSTANG-1.5 system diagram.

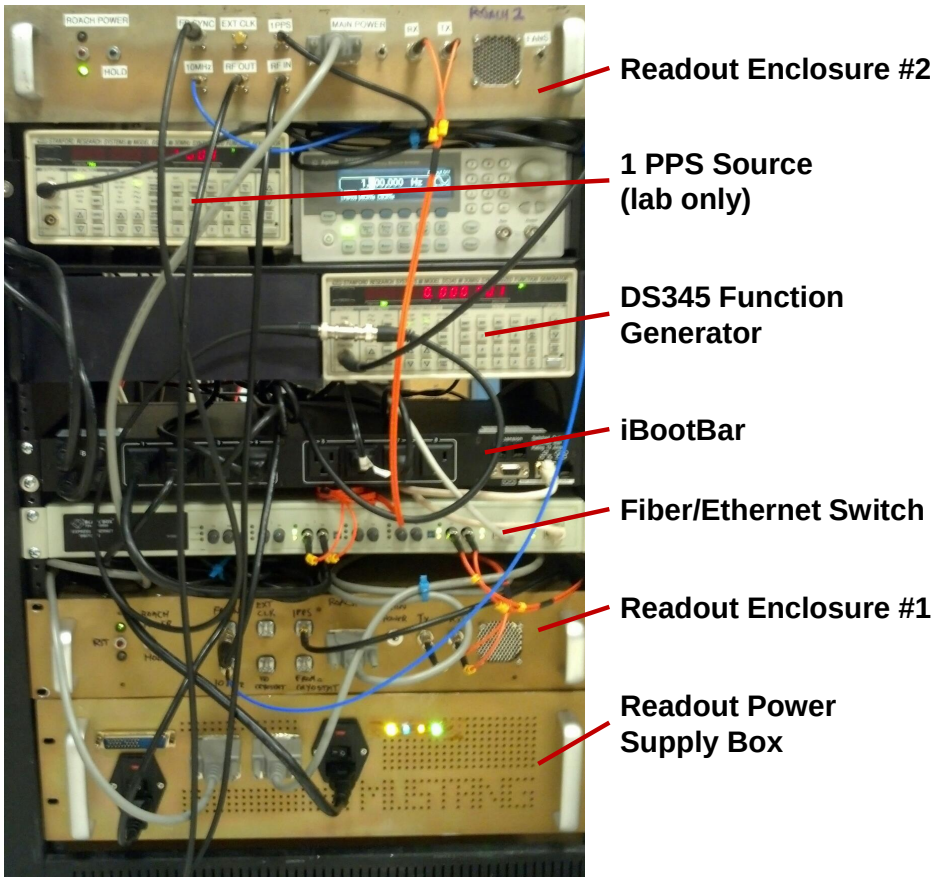

Figure 5.19: A 19 inch rack populated with the MUSTANG-1.5 electronics that will be installed in the electronics crate before deployment. On the telescope, the 1 PPS synchronization signal and the 10 MHz frequency standard will be supplied by in-house electronics in the receiver cabin. For laboratory testing we use the 10 MHz timebase output by the flux ramp DS345 as our frequency standard. For the 1 PPS synchronization we use a 1 Hz TTL signal generated at the SYNC output of a separate DS345, which has been configured to output a 1 Hz arbitrary waveform. Not visible are the 4-way active TTL driver that splits and amplifies the 1 PPS signal, as well as a passive 6-way splitter that divides up the 10 MHz timebase.

5.6.1 Housekeeping and Detector Bias

In MUSTANG-1.5, the cryogenic thermometers fall into two categories - silicon diodes and resistance temperature detectors (RTDs). When current-biased, the voltage across a silicon diode varies with temperature with a characteristic response curve.

Likewise, the resistance of an RTD changes characteristically with temperature. Figure 5.20 shows the response curves for typical diodes and RTDs.

The diode voltage increases linearly with temperature from 3 K $\lesssim T \lesssim$ 400 K. The excitation current is kept low $\sim$ 10 μA to prevent the thermometer from self-heating. At very low temperatures, $T \lesssim$ 3 K, RTDs such as Ruthenium Oxide (ROX) sensors provide better performance and lower power dissipation than diodes. We use an AC voltage bias and software lock-in to measure the resistance of the ROX. Many of the MUSTANG-1.5 diodes and ROXs have been calibrated against well-characterized devices in order to construct individual Voltage-Temperature or Resistance-Temperature calibration curves for each thermometer.

The analog and digital input/output channels for the housekeeping are provided by two ACCES I/O (AIO) multifunction USB units (DPK-AIO16). The associated Linux drivers for these devices already existed in the GBT control software architec-

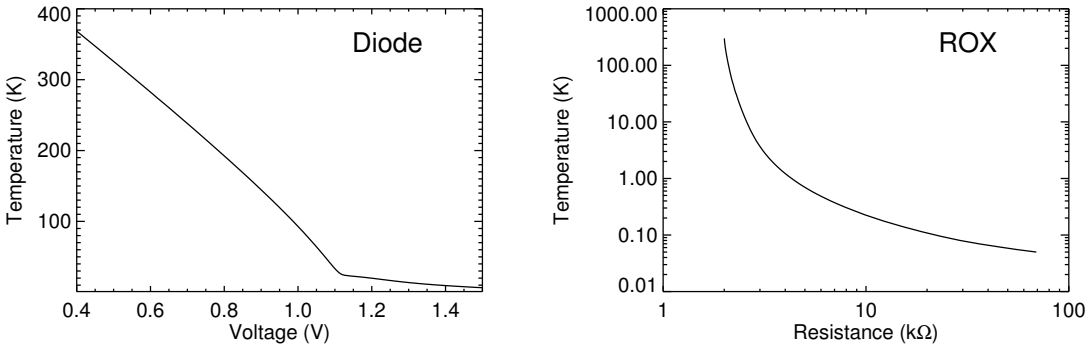

Figure 5.20: Typical calibration curves for the diodes (left) and ROXs (right) used in MUSTANG-1.5. For the diodes, the voltage is measured with a current bias of 10 μA. For the ROXs, resistance measurements are carried out using a software-defined lock-in with a $\pm$2 V or $\pm$0.2 V (depending on temperature range) AC bias of $\sim$ 27 Hz. The measured voltage can be converted to a resistance provided the bias voltage and bias reistances are known.

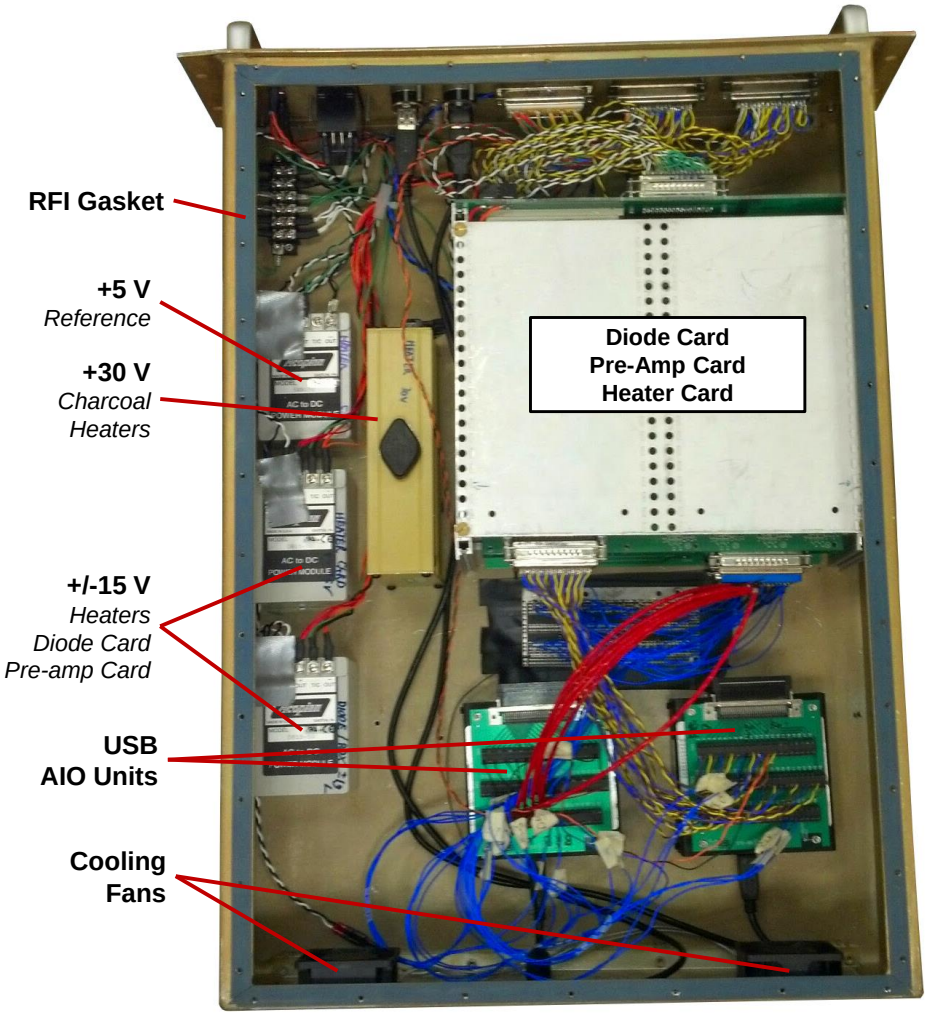

Figure 5.21: The RFI-tight enclosure for the housekeeping electronics. Three linear regulated power supplies provide the voltages necessary for operating the thermometery and heaters. The AIO units are powered by the DAQ through the USB interface. At the front panel there are two USB ports for the AIO units, two 50-position connectors for the housekeeping, and one BNC connector for the flux ramp. There is an additional 50-position connector for the detector bias and for carrying the flux ramp into the cryostat. In case we decide to expand the electronics during commissioning, there is an extra BNC connector and 25-position connector on the front panel.

ture and configuring them for telescope operations was expected to require minimal additional effort. Some firmware and hardware malfunctions made these devices diffi-

cult to initially implement, however after a firmware upgrade from the manufacturer and extensive laboratory characterization to calibrate out systematic errors in each channel, the devices were proven to meet the design specification for MUSTANG-1.5. The AIO units and power supplies are enclosed in an RFI tight box as shown in Figure 5.21.

In addition to thermometer and heater control, the AIO units provide the bias voltage for the TES detectors. The detectors are divided into four sections, each of which receives an independent bias voltage. Since the bias voltage is the same for all detectors within a section, it is important to group together detectors with similar T_c. Therefore, immediately after fabrication, the NIST detectors are screened to determine T_c and also to remove any pixels that are permanently unresponsive due to manufacturing defects.

5.6.2 Readout Electronics

The design and principles of operation for the MUSTANG-1.5 μMUX are described in Chapter 6. Here I discuss primarily the hardware associated with the readout electronics.

The outer RFI crate crate is designed to accommodate up to four readout enclosures, each of which can currently read out 32 TESs (16 dual-polarization spatial pixels). With the design of new MUX chips the number of detectors per readout is expected to increase by up to a factor of eight. All four readout enclosures are powered by a separate power supply box shown in Figure 5.22. A schematic for the internal wiring is shown in Figure 5.23. The ADC/DAC boards and IF Mixer boards

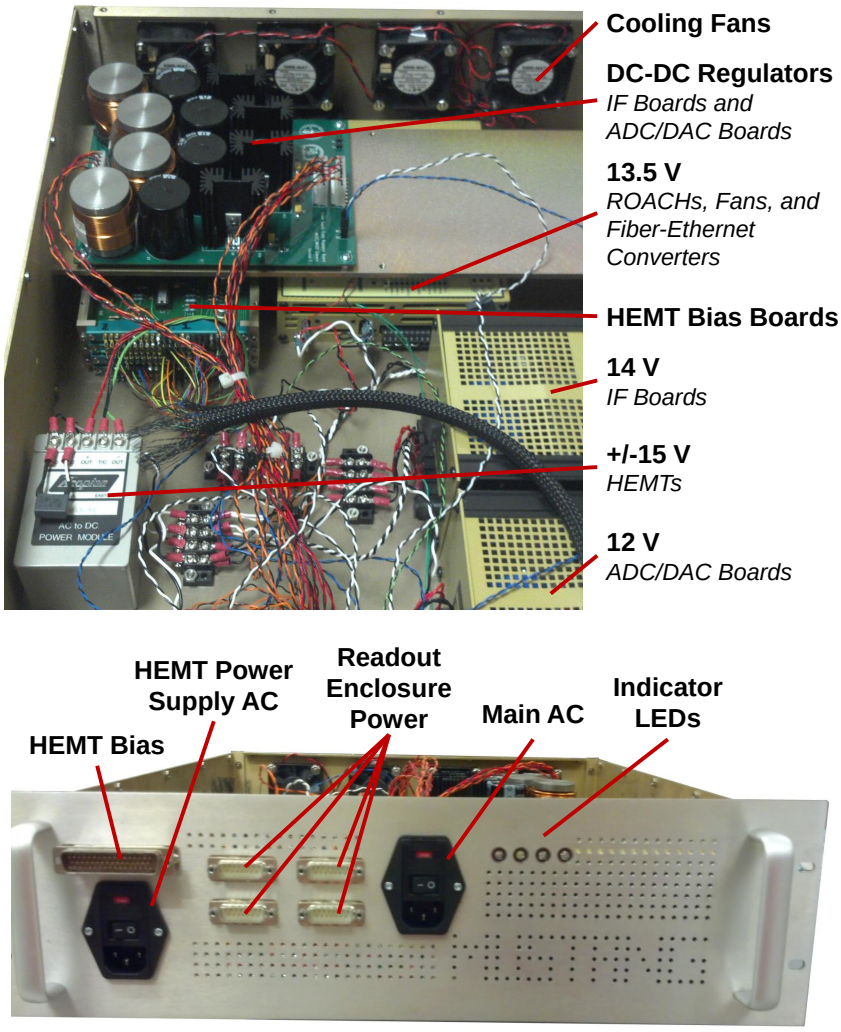

Figure 5.22: The MUSTANG-1.5 readout electronics power supply box.

are powered by a combination of unregulated AC-DC power supplies with custom DC-DC regulator boards, providing stable output voltages of 6.5 V and 10 V, respectively. The ROACH boards, cooling fans, and fiber-optic/RJ45 Ethernet converter modules are powered by a single 13 V switching power supply. The HEMT amplifiers are powered by a separate AC input (not shown in the schematic) leading to a linear ±15 V power supply. Using a single outlet for the HEMTs in the iBootBar allows us

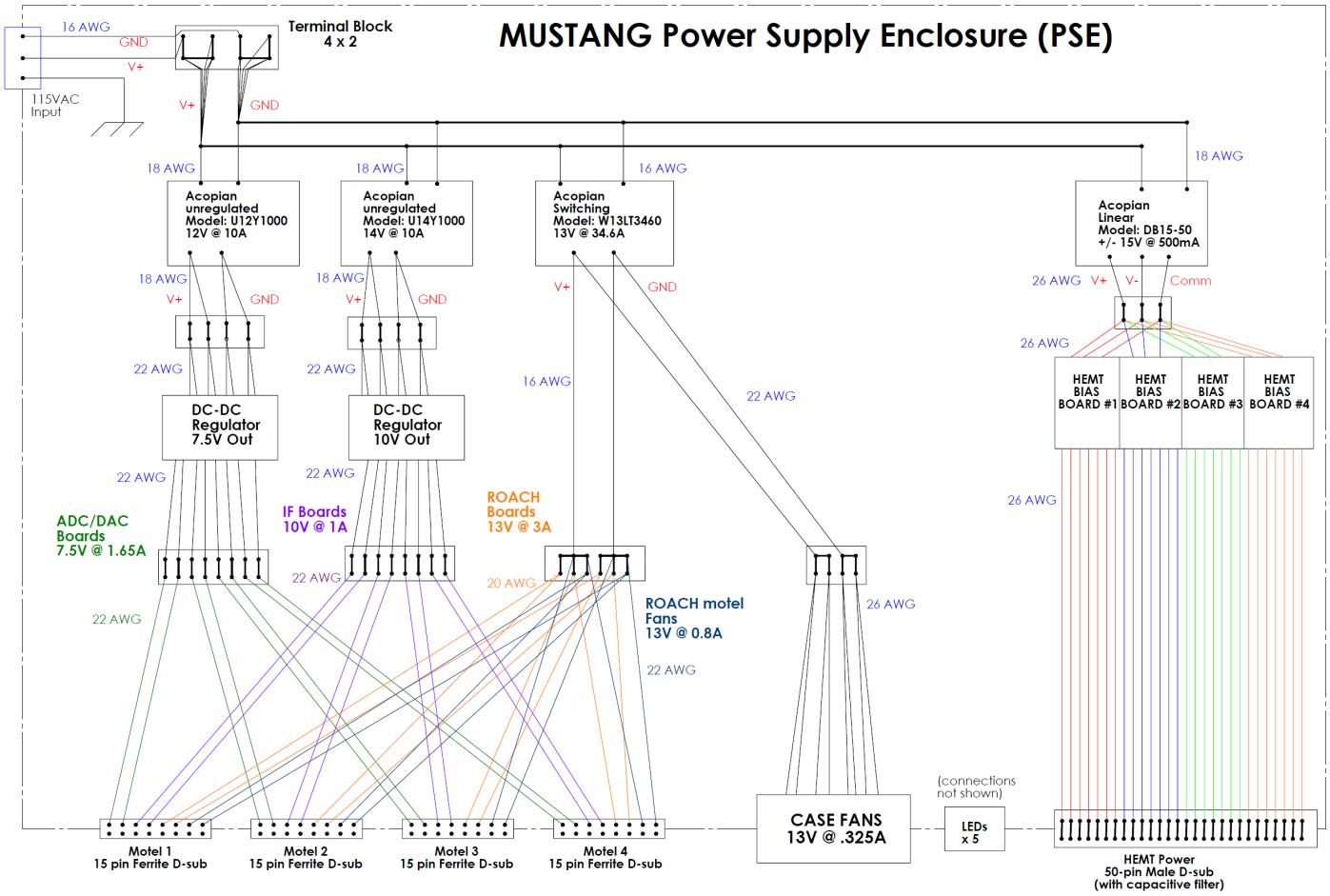

Figure 5.23: Schematic of the power supply box for MUSTANG-1.5.

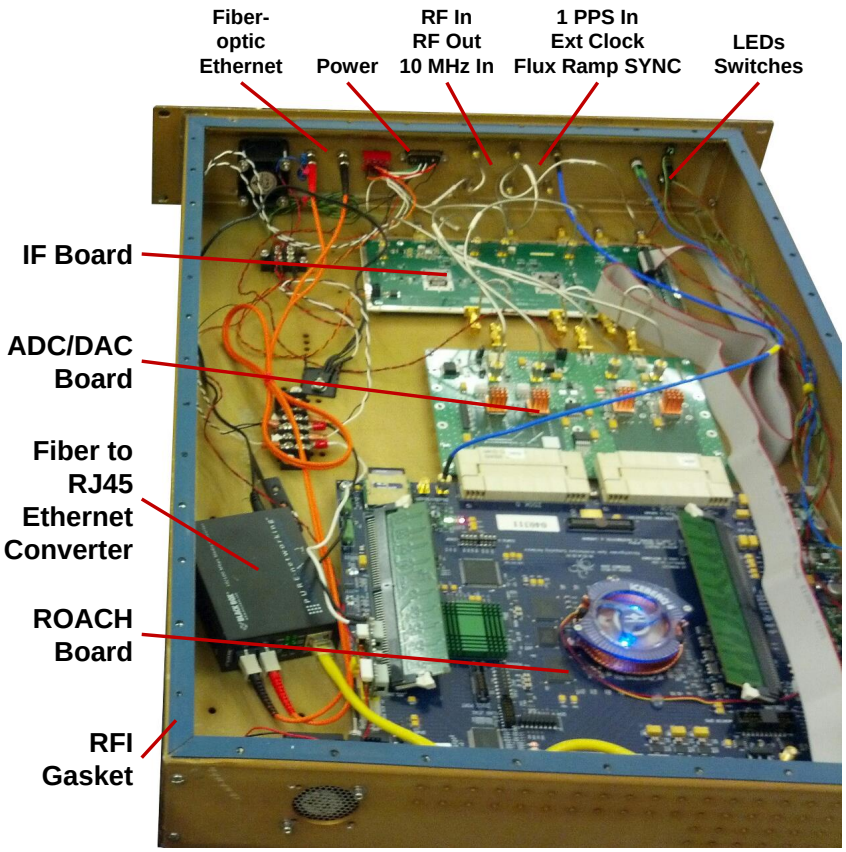

Figure 5.24: A MUSTANG-1.5 readout enclosure.

to turn them on and off remotely while leaving the rest of the readout components powered on. A set of custom bias boards provides the three stages of gate and drain voltages to each HEMT.

Figure 5.24 shows the inside of the readout electronics enclosures. The front panel has SMA ports for connections to the IF Mixer board as well as for the flux ramp sync signal from the DS345 function generator. Power enters on a 15-pin D-subminiature connector and supplies 7 V to the ADC/DAC and IF mixer board, 13 V to the ROACH and cooling fans, and 9 V to the Ethernet converter. While the main power to the enclosure can be toggled remotely, a switch on the front panel allows the

power to be manually cycled as well. The ROACH PowerPC is configured to boot automatically when the board is powered, enabling us to cycle the ROACH power remotely. A gasket is installed to attenuate the RFI emission from the electronics in order to meet the GBT facility requirements.

Chapter 6

The MUSTANG-1.5 Microwave SQUID Multiplexer

Within the past several years, TES detectors have been fabricated with photon-limited performance [e.g., Niemack et al. 2010; Appel et al. 2009; Austermann et al. 2009]. In the photon noise limit, the only way to achieve better sensitivity within a fixed integration time is to increase the number of detectors N_d (S/N $\propto \sqrt{N_d}$). Current generation CMB instruments typically read out thousands of detectors using time-division and frequency-division multiplexing architectures with tens of detectors per readout channel. These technologies often require expensive cold readout electronics and high wire counts, making them unfeasible for future $> 100,000$-pixel arrays.

A microwave SQUID multiplexer (μMUX) [Irwin et al. 2006; Mates et al. 2008; Mates 2011] has been developed at NIST with the potential to read out hundreds to thousands of detectors on a single coaxial line. MUSTANG-1.5 will be the first

astronomical instrument to field the μMUX. In this chapter, I discuss the design of the μMUX and present early characterization data from laboratory testing.

6.1 Principles of Operation

The μMUX combines the sensitivity of TES bolometers with the multiplexing capabilities of Magnetic Kinetic Inducatance Detectors (MKIDs). MKIDs are superconducting microresonators and experience a shift in resonant frequency with incident optical power. The MKIDs are interrogated with a comb of probe tones, each tuned to target individual resonances. A shift in the resonant frequencies of the MKIDs will modify the transmitted amplitude and phase of the probe signals (Figure 6.1), which can be measured in order to determine the photon energy incident on each detector.

The μMUX is very similar to an MKID array, except the resonators do not themselves function as the detectors. Instead, optical power is absorbed by TES bolometers coupled to rf-SQUIDs, which are in turn coupled to the individual resonators (Figure 6.2). In the context of the μMUX I refer to rf-SQUID simply as SQUIDs. The TES circuit is identical to that used in MUSTANG. The TES is voltage biased and inductively coupled to the SQUID. A change in the TES current induces a change in magnetic flux through the SQUID and shifts the resonance frequency of the resonator to which the SQUID is inductively coupled. As with MKIDs, the resonators are interrogated with a frequency comb and the transmitted phase and amplitude of the probe tones traces the incident power on the TES.

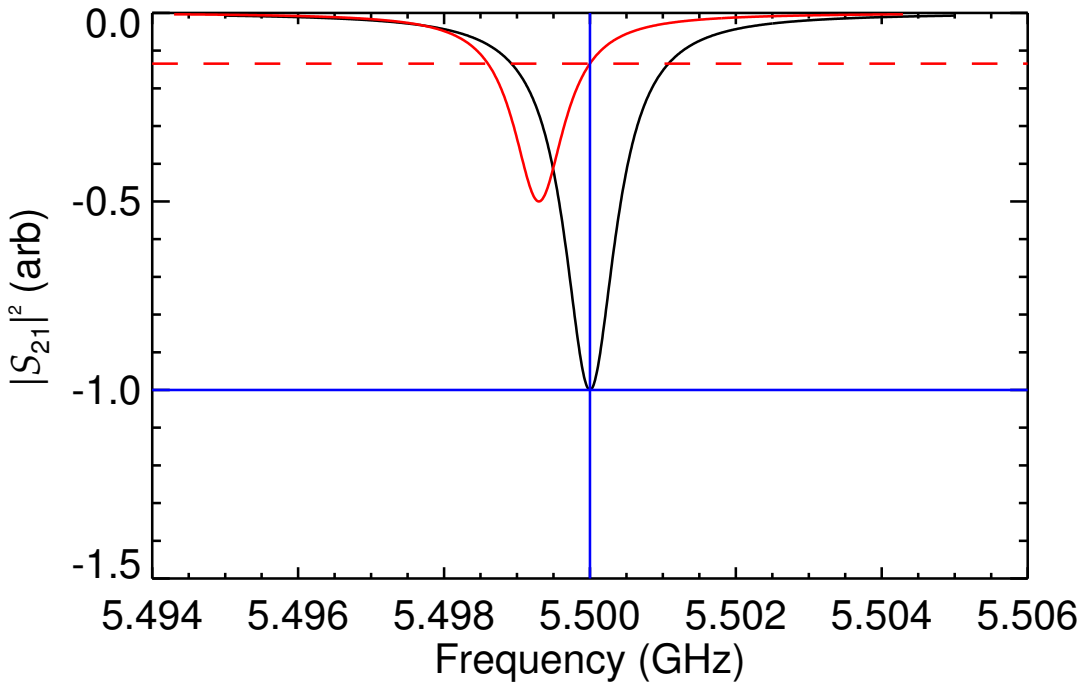

Figure 6.1: The change in resonance frequency due to absorbed incident power affects the amplitude and phase of the transmitted microwave probe tone. The black curve represents the trasmission for a probe tone on resonance, while the red curve shows the transmission for an off-resonance tone. The solid blue lines mark the amplitude and central frequency of the on-resonance tone. The dashed line shows the amplitude that would be measured after the resonance has shifted. As the resonance shifts, the phase of the probe tone is also affected, which is not shown here.

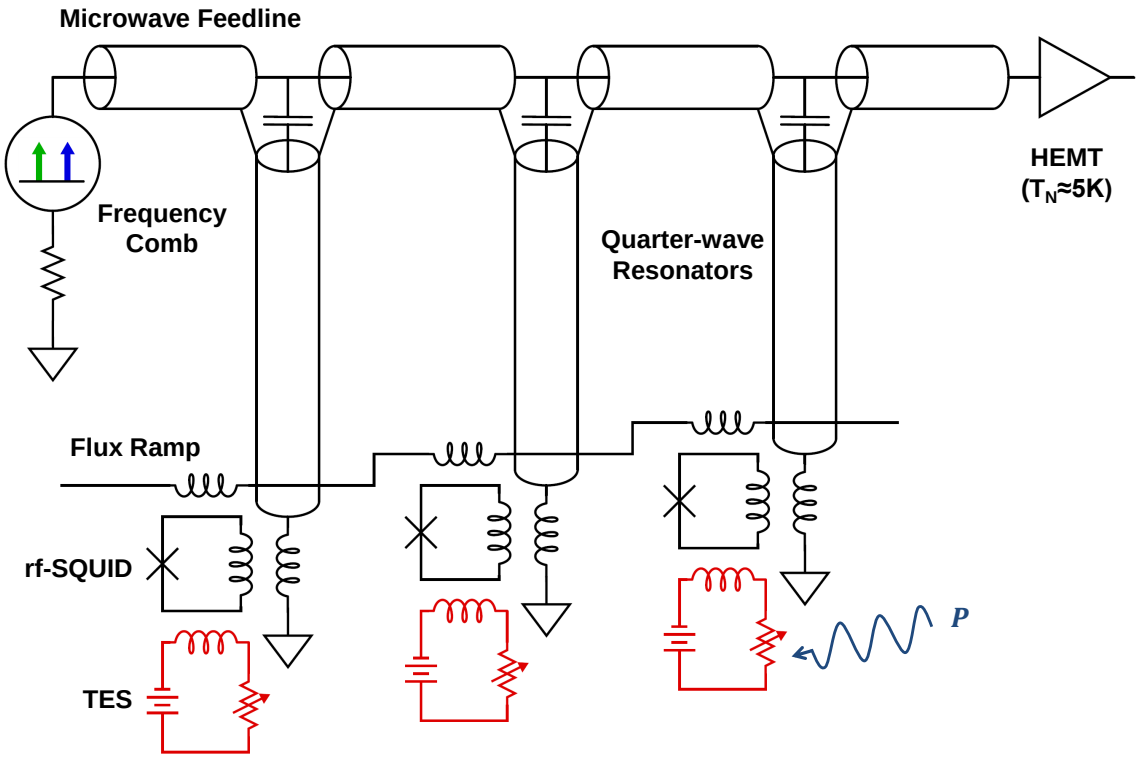

Figure 6.2: A schematic of a three-pixel μMUX setup. Optical power is absorbed by a TES (red) and induces a shift in the resonance frequency of the resonator, which in turn modifies the amplitude and phase of the transmitted microwave tone. Figure taken from Mates 2011.

6.1.1 Flux Ramp Modulation

SQUIDs are intrinsically non-linear and respond sinusoidally as a function of magnetic flux. In TDM systems such as MUSTANG a feedback flux is applied to keep SQUIDs in the linear region of their response, referred to as a flux-locked loop (FLL). The applied feedback flux then directly traces the signal flux from the detector. With the μMUX system, all SQUIDs are read out simultaneously so operating a FLL would require individual pairs of feedback wires for each SQUID, which would defeat the purpose of frequency domain multiplexing. Instead we employ a novel technique called flux ramp modulation (FRM) [Mates et al. 2012] to linearize the response of the SQUIDs. FRM has the added advantage of modulating the SQUID response to higher frequencies, avoiding the low frequency noise that enters the circuit after the SQUID.

In the μMUX each SQUID contains a second input coil through which the flux ramp is applied. The secondary input coils from all SQUIDs on a chip are connected in series so that the flux ramp can be sent down a single feedline and shared among many resonators. In the μMUX system we choose a sawtooth waveform with an amplitude spanning several flux quanta. For the MUSTANG-1.5 MUX chips with 24 pH mutual inductance $M_{\rm fr}$ and 1 kΩ bias resistance, a 0.5 Vpp ramp will drive ~ 6 flux quanta through the SQUIDs. The ramp rate is chosen to greatly exceed the expected input signal, so that the input signal will appear as a DC offset to the flux ramp. This will shift the phase of the SQUID response according to

$$\phi = 2\pi \frac{\Phi}{\Phi_0}. \tag{6.1}$$

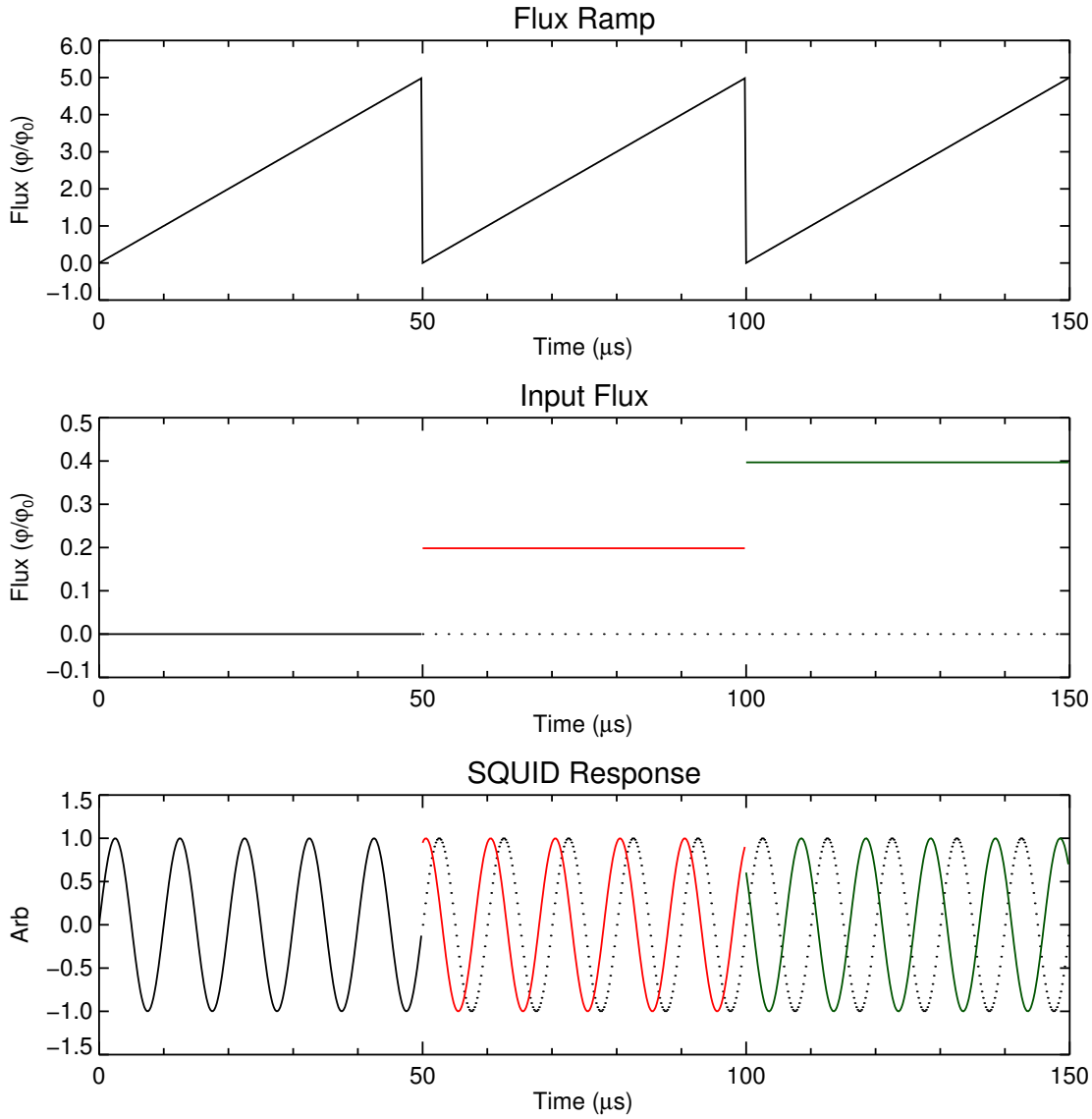

Figure 6.3: Simulated flux ramp modulation in the MUSTANG-1.5 μMUX. A sawtooth waveform (top) ramps through 5 flux quanta at a rate of 20 kHz. Provided the slew rate is much less than that ramp slope, input flux (middle) will appear as a DC offset to the ramp and induce a phase shift in the SQUID response (bottom). The dotted lines show the SQUID response in the absence of additional input flux. The difference in phase between the solid and dotted sinusoids directly traces the input flux.

An example of the flux ramp modulation is shown in Figure 6.3. The SQUID response within a flux ramp period can be represented as

$$x_i = A\sin(\omega_c t_i + \phi), \tag{6.2}$$

where ϕ is the phase shift due to input flux, as given by Equation 6.1. The carrier frequency ω_c is determined by the number of flux quanta per ramp N_{Φ_0} and the ramp rate $f_{\rm FRM}$ according to

$$\omega_c = 2\pi N_{\Phi_0} f_{FRM}. \tag{6.3}$$

In order to demodulate the signal and determine ϕ from Equation 6.2, we use a COordinate Rotation Digital Computer (CORDIC) [Volder 2000] arctan algorithm to solve

$$\phi = \arctan\left(\frac{\sum_{i=0}^{N_s-1} x_i \sin(\omega_c t_i)}{\sum_{i=0}^{N_s-1} x_i \cos(\omega_c t_i)}\right), \tag{6.4}$$

where $N_s = f_s/f_{\rm FRM}$ is the number of samples within a ramp period. I describe the details of the demodulation procedure in more detail in §6.4.2.

6.2 The MUSTANG-1.5 μMUX Design

The MUSTANG-1.5 μMUX is shown schematically, for one readout channel, in Figure 6.4. The frequency comb is generated by a DAC within the ROACH enclosure (see §6.3), mixed from baseband ($\sim$ 10-500 MHz) up to $\sim$ 5.3-5.8 GHz by a local oscillator (LO), and sent into the cryostat via a single coaxial cable. The signal

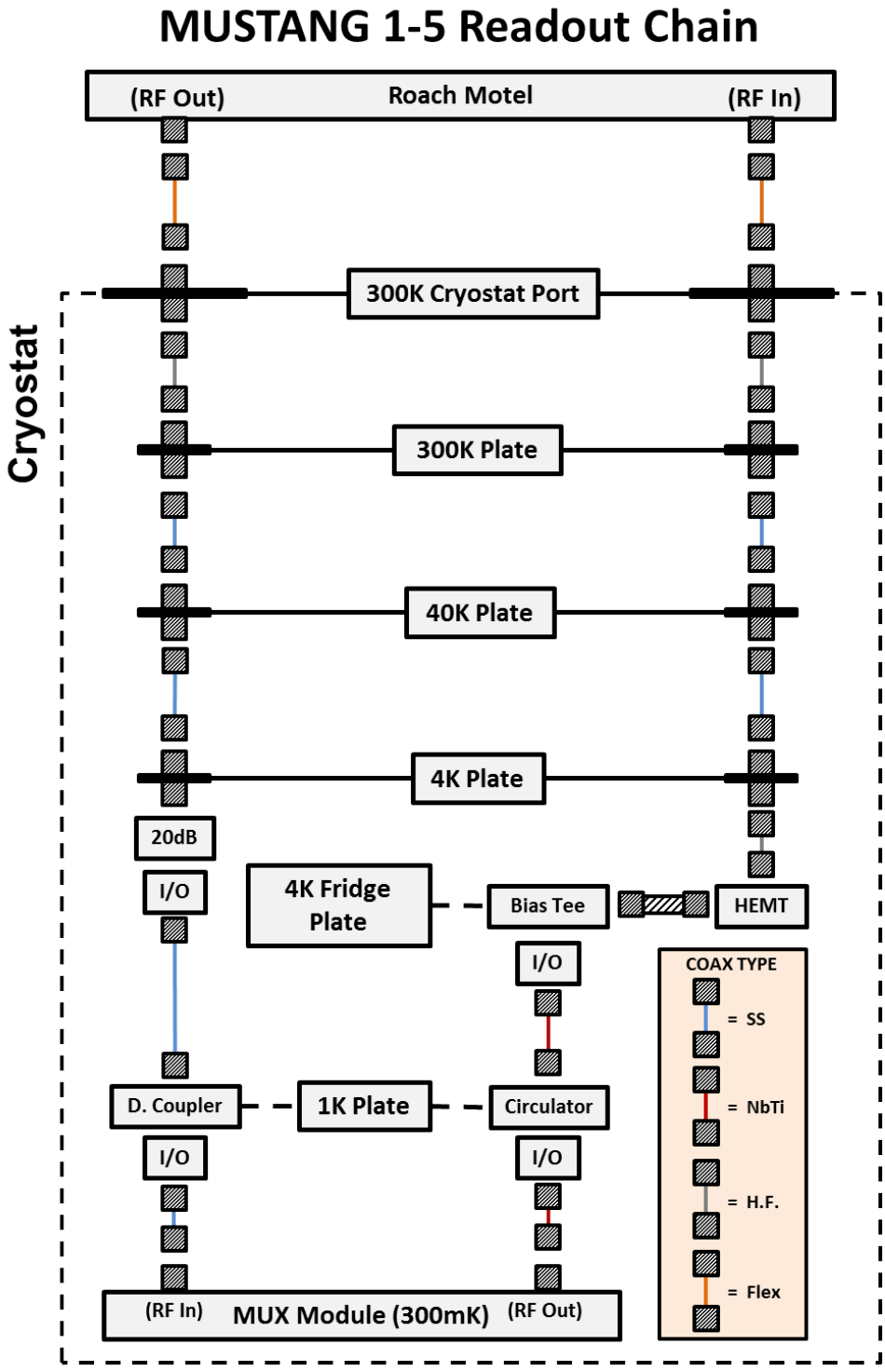

Figure 6.4: Schematic of the MUSTANG-1.5 readout components inside the cryostat.

passes through a 20 dB attenuator at 3 K followed by a 20 dB directional coupler at 1 K. This tunes the input microwave power at the MUX chip to the desired -70 dBm to -80 dBm range, and attenuates the room temperature noise below the noise temperature of the HEMT amplifier ($\sim$ 3 K). The directional coupler ensures that the power is dissipated at a cold termination that is isolated from the MUX module at 300 mK. The μMUX hardware is shown in Figure 6.5.

After interrogating the resonances at the MUX chip, the microwave signals are amplified $\sim$ 37 dB by the HEMT at 3 K. Between the MUX and the HEMT are a cryogenic circulator to prevent reflections from the HEMT from reaching the MUX. We use a bias tee to heat sink the center pin of the HEMT at 3 K. After the HEMT, the signals pass out of the cryostat and into the ROACH enclosure where they are mixed back down to baseband, amplified, and then digitized by the Analog-to-Digital Converter (ADC).

At various thermal stages we use inner/outer (I/O) DC blocks to break the Wiedemann-Franz conductivity and thereby provide thermal isolation along the coaxial cables. In instances where thermal isolation is unnecessary we use hand-formable copper coax. For most other connections we use coax cables with a SS outer conductor and BeCu inner conductor, providing low thermal conductivity with low electrical loss.[1] Between the MUX and the HEMT, where low signal loss is crucial, we use superconducting NbTi-NbTi coax.[2]

[1] www.rf-coax.com
[2] www.coax.co.jp

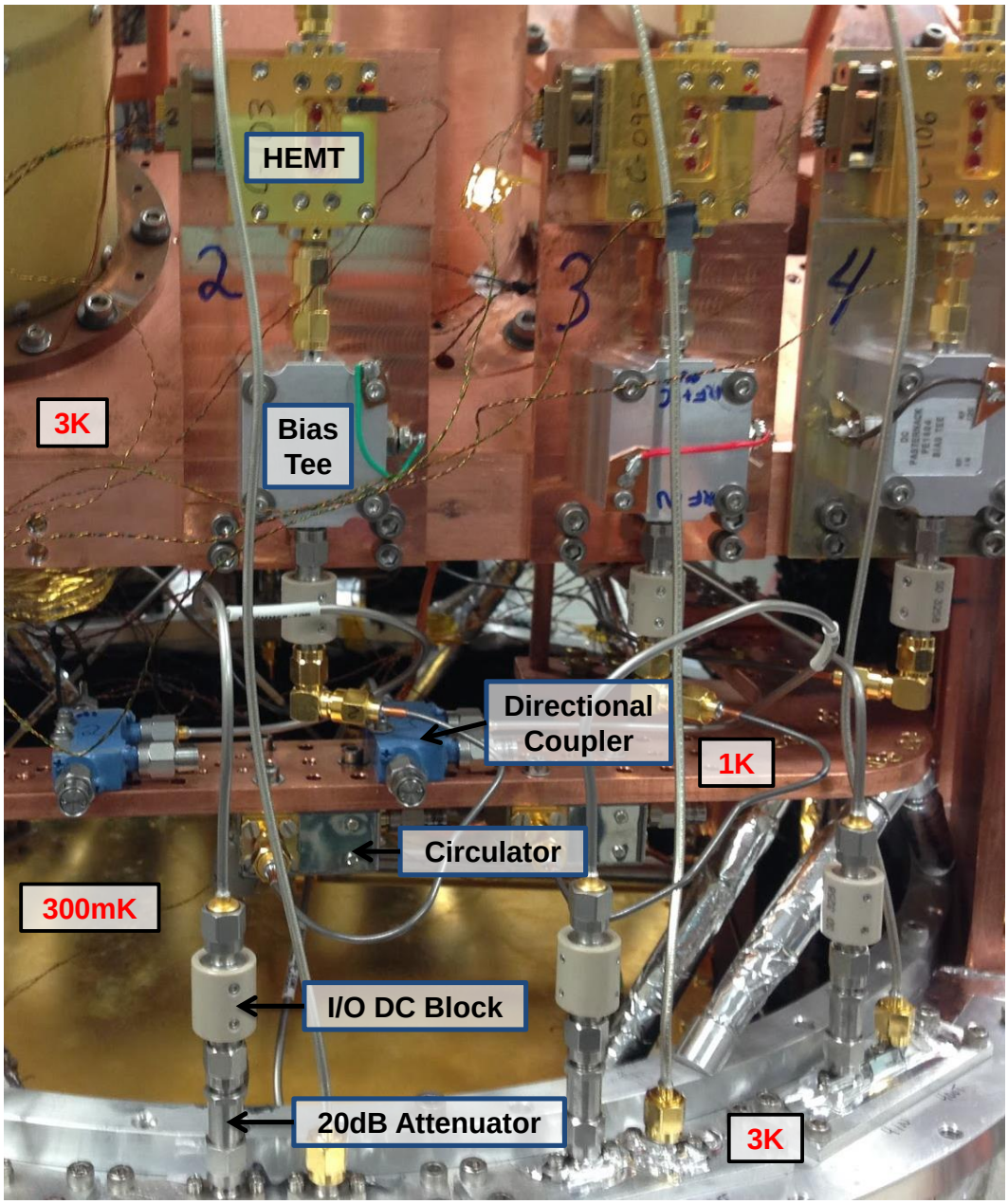

Figure 6.5: MUSTANG-1.5 cold readout electronics.

6.3 Back-end Electronics

The μMUX back-end electronics are comprised primarily of hardware and firmware developed by the UC Berkeley Collaboration for Astronomy Signal Processing and Electronics Research (CASPER) group. The primary goal of the CASPER group is to develop scalable, upgradeable, FPGA-based hardware with flexibility for use in a wide range of radio telescope signal processing applications [Parsons et al. 2009]. Usually, radio astronomy instrumentation employs specialized electronics for individual applications, which generally becomes outdated by the time the instrument is fielded. CASPER promotes streamlined modular development of open-source hardware and software that can be used in instruments with a variety of design requirements and is easy to upgrade as higher performance electronics become available.

The Reconfigurable Open Architecture Computing Hardware (ROACH)[3] board is a current generation CASPER processing board that has been used in a number of instruments including MUlitcolor Submillimeter Inductance Camera (MUSIC) [Golwala et al. 2012], ARray Camera for Optical to Near-infrared Spectrophotometry (ARCONS) [McHugh et al. 2012], and VErsatile GBT Astronomical Spectrometer (VEGAS)[4]. The next generation ROACH-2 processing boards have already passed prototyping stage and will soon replace ROACH-1 in a number of astronomical instruments.

[3] www.digicom.org
[4] www.gb.nrao.edu/vegas

6.3.1 ROACH Enclosures

The MUSTANG-1.5 μMUX readout is based on the Software-Defined Radio (SDR) system that is used by MUSIC and ARCONS as part of the open-source readout (OSR) program [Duan et al. 2010]. The individual readout enclosures, also referred to as ROACH enclosures, each contain a ROACH board for signal processing, a combined DAC and ADC board[5] to generate the frequency comb and digitize the input signals, and an Intermediate Frequency (IF) Mixer board to mix the frequency comb from baseband to the target $\sim 5.5 \pm 0.25$ GHz band of the resonators.

The ROACH is controlled by a PowerPC running Linux, which communicates with the Xilinx Virtex 5 SX95T FPGA. In addition to the block random-access memory (BRAM) on the FPGA, the ROACH contains two quad data rate (QDR) static random-access memorys (SRAMs) for high-speed memory operations. In practice, the BRAMs are used for diagnostic snapshots of small amounts of readout data, while the QDRs are used for full science data. The ADC/DAC board is connected to the ROACH through high-speed 40-pair Z-DOK+ connectors. The output analog signals are generated with a 16-bit 1 GS/s DAC (Texas Instruments DAC568). The input analog signals are digitized with a 12-bit 550 MS/s ADC (Texas Instruments ADS5463).

6.3.2 Electronics Crate

The ROACH readout enclosures are housed within an outer RFI-tight electronics crate, which is mounted to the bottom of the cryostat. A schematic of the electronics

[5] www.techneinstruments.com

rack and the connections pertaining to the μMUX is shown in Figure 6.6.

The flux ramp is generated using a Stanford Research Systems DS345 Function Generator, which is controlled by the DAQ computer through a serial interface. The flux ramp is shared across all the MUX chips, each of which contains a 1 kΩ resistor in series with the flux ramp wiring to prevent overloading the MUX circuit. A 10 MHz frequency standard and a 1 pulse per second (PPS) synchronization signal are supplied to the electronics from external shared resources in the receiver cabin. Communication between the DAQ and the outside world is carried out over fiber-optic Ethernet cables instead of the standard copper Ethernet cables, which are known to transmit unacceptable levels of RFI.

6.4 Firmware

Firmware for the ROACH FPGA is developed and compiled into a Berkeley Operating system for ReProgrammable Hardware (BORPH) executable (BOF) file using the Simulink package for MATLAB. BOF files are treated as individual firmware modules that run on the PowerPC and are responsible for setting up the software registers, memory buffers, and signal processing procedures on the FPGA.

6.4.1 Frequency Comb Generation

The generation of the frequency comb follows the ARCONS procedure outlined in McHugh et al. [2012]. Given an array of frequencies $[f_0, f_1, \ldots, f_n]$, a look-up table (LUT) is generated that contains the sum of waveforms at each frequency. The summed waveform is 2^{16} samples long, which provides 7.813 kHz frequency resolution

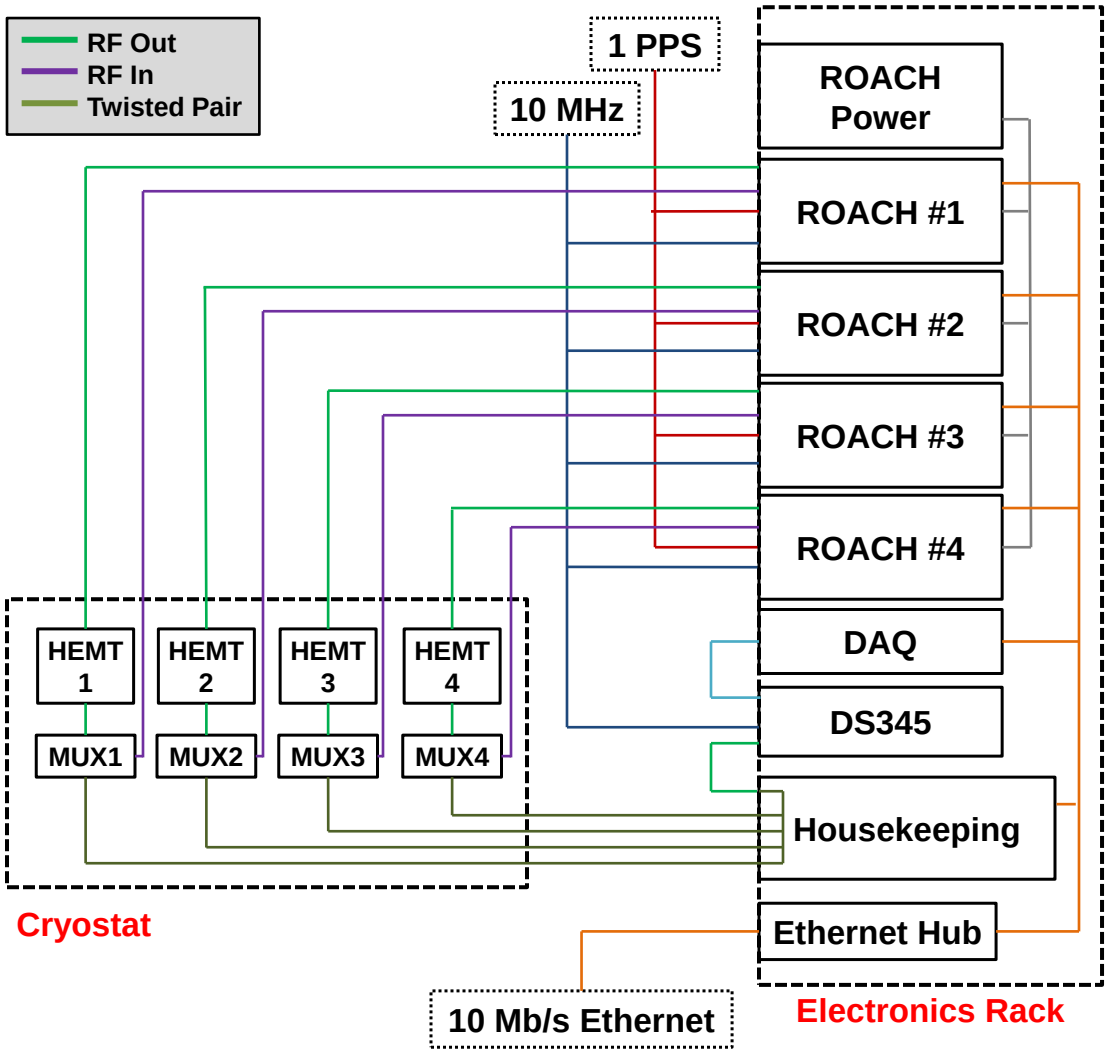

Figure 6.6: The MUSTANG-1.5 electronics rack, which contains a power supply box for four ROACH enclosures, the DS345 function generator for that generates the flux ramp, and the DAQ computer that controls both the DS345 and housekeeping electronics. An 8-port Fiber/Ethernet hub provides communication between the control room, the DAQ, and the ROACH enclosures.

at the 512 MHz clock rate, and is normalized so that the maximum amplitude does not exceed the limit of the DAC output, 2^{16} counts. The summed DAC waveform for $N_{\rm res}$ resonators is given by

$$D_s = \frac{2^{16}}{D_{max}} \sum_{n=0}^{N_{\rm res}} A_n \left(\cos\left(\frac{2\pi f_n s}{512\ \text{MHz}} + \theta_n \right) + i \sin\left(\frac{2\pi f_n s}{512\ \text{MHz}} + \theta_n \right) \right) \tag{6.5}$$

where $s = [0, 1, \ldots, 2^{16} - 1]$ and A_n is the relative amplitude for each probe tone, which is determined by the tuning algorithm. A random phase θ_n is applied to each probe tone in order to minimize $D_{\rm max}$ and maximize the dynamic range of the DAC.

6.4.2 Demodulation

By separately reading out the in-phase (I) and quadrature (Q) components, I and Q are sinusoids separated in phase by 90°, of the probe tones we can determine the phase of the transmitted signals within the full 550 MHz band provided by the dual 550 MS/s ADCs. Reading out 12 bits each of I and Q data for 256 channels at a 1 MHz sampling rate would require $(2 \times 12 \times 256 \times 10^6) \approx 2$ Gb/s, which far exceeds the 10 Mb/s data rate provided by the ROACH Ethernet interface[6]. Therefore, we must perform the demodulation algorithm on the FPGA prior to transmitting data to the DAQ. Assuming we choose a 10 kHz flux ramp rate, as long as we downsample or coadd the demodulated data by at least a factor of 3 we can stream at the full $(12 \times 256 \times 10^4)/3 \approx 10$ Mb/s data rate. During astronomical observing, we only require sampling up to ~ 100 Hz, which yields an even lower data rate.

[6]The ROACH does provide 10 GB/s transmission on each of four CX4 ports, but using them for MUSTANG-1.5 would require significant modification to the existing firmware. On-board demodulation is a much simpler approach.

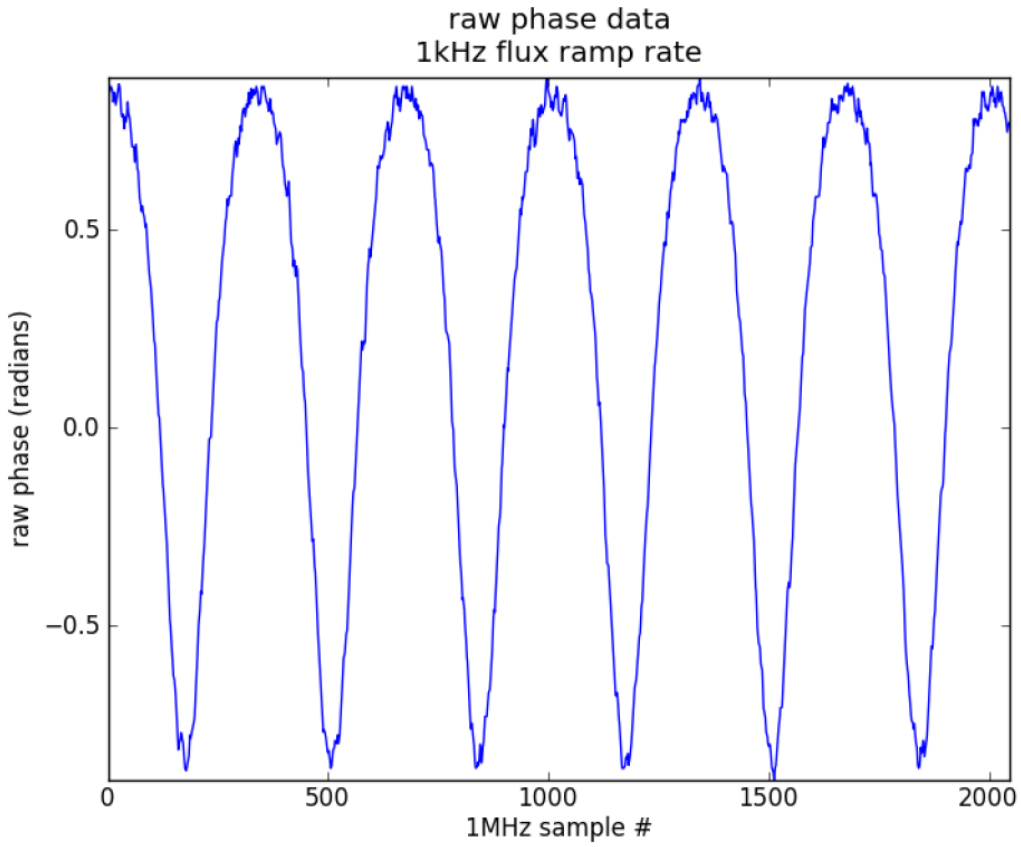

Figure 6.7: Raw phase timestream for a single resonator driven with a 1 kHz flux ramp. Figure courtesy of Justus Brevik.

The demodulation proceeds as follows. Let us assume that we are operating a 10 kHz flux ramp. For each readout channel, I and Q data are accumulated at a 1 MHz rate. We use a CORDIC algorithm to compute arctan(I/Q) and determine the phase for each sample. The flux ramp function generator provides a TTL signal at f_{FR} and allows the start of each flux ramp period to be tracked by the firmware. We refer to the data within a single flux ramp period for a single resonator channel as a "raw phase timestream". For a sawtooth flux ramp these timestreams will trace a sinusoid with frequency given by Equation 6.3. An example raw phase timestream

for a 1 kHz flux ramp is shown in Figure 6.7.

For each raw phase timestream the phase of the sinusoidal response is calculated according to Equation 6.4 using a second CORDIC algorithm. The product of x_t and $\sin(\omega_c t)$ or $\cos(\omega_c t)$ will yield higher-frequency $2\omega_c$ terms that must be filtered out for Equation 6.4 to hold true. Therefore, prior to running the second CORDIC arctan algorithm, we filter the timestreams use a finite impulse response (FIR) filter with a cutoff frequency set 50% higher than the mean carrier frequency and with a stop band that extends to the 500 kHz Nyquist frequency in order to minimize ringing in-band. We refer to the output of the second CORDIC algorithm $\phi_{\rm demod}$ as a "demodulated timestream".

The demodulated timestreams represent the phase shift within each period of the flux ramp response, which directly traces the input flux on the TES. To convert from phase to units of power

$$P_{\rm opt} = I_{\rm TES} V_{\rm bias} = \frac{\phi_{\rm demod} \Phi_0 V_{\rm bias}}{2\pi M_{\rm in}} \tag{6.6}$$

where $M_{\rm in} = 88$ pH for the MUSTANG-1.5 SQUIDs. The demodulated timestreams are time-stamped, packetized, and transmitted to the DAQ where they are written to a FITS file that includes peripheral information such as cryostat temperatures and telescope pointing centers. I present raw phase and demodulated timestreams in §6.6.

6.5 Software

The μMUX software is comprised of a primary Python[7] module called ***umuxlib***, which contains a number of routines for initializing the readout electronics, performing diagnostics, and starting the continuous demodulation algorithm. Commands are communicated to the ROACH FPGA with the *corr* Python package, which uses the Karoo Array Telescope Control Protocol (KATCP) developed by CASPER.

6.5.1 vVNA Sweep

In order to locate the resonant frequencies for each resonator we use a virtual VNA (vVNA) routine to sweep across a broad band of frequencies and measure the transmitted amplitude ($|S_{21}| = \sqrt{|\mathrm{I}|^2 + |\mathrm{Q}|^2}$). The precise resonant frequencies are determined during the tuning algorithm, so the requirement of the vVNA is simply to determine the rough resonant frequencies for each resonator.

For a given start and stop frequency, the DAC is programmed with a comb of evenly-spaced probe tones. The LO is then swept over the spacing of the tones in steps of 10 kHz. The output power varies across the DAC probe tones, which means that adjacent bins in the sweep will have arbitrary offsets. Additionally, the DAC has an intrinsic $\sin(x)/x$ roll-off in power, which attenuates the tones furthest from the LO frequency. The software stitches together the adjacent bins and then subtracts a low order polynomial to address these issues. However, since the data are heavily processed the range is rescaled to a 0-1 interval to prevent them from being interpreted as proper S_{21} magnitudes.

[7] www.python.org

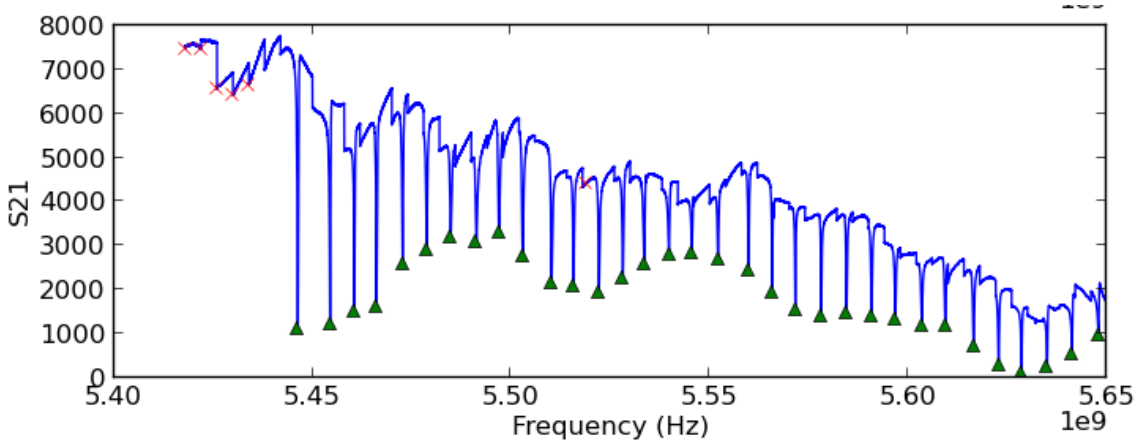

Figure 6.8: $|S_{21}|$ (in arbitrary units) versus frequency measured with the virtual VNA procedure. The green triangles indicate the resonances that were detected by the custom resonance-detection algorithm. The red crosses show candidate resonances that did not pass the selection criteria.

A custom resonance-detection algorithm is used to pick out the resonant frequencies. First, candidate resonances are selected from all local minima within 3 MHz bins in the sweep. Then a Lorentzian is fit to each of the candidates and calculate the standard deviation in amplitude and half-width half-maximum (HWHM). Any candidates that deviate by more than 3σ in either parameter are removed. The resonance detection algorithm is illustrated in Figure 6.8. The green triangles indicate the confirmed resonances and the crosses represent the candidates that were removed by the detection algorithm.

6.5.2 Tuning

Prior to demodulating the raw SQUID response, the power, initial phase, and frequency of the probe tones are optimized using an automated tuning algorithm (Figures 6.9 - 6.12).

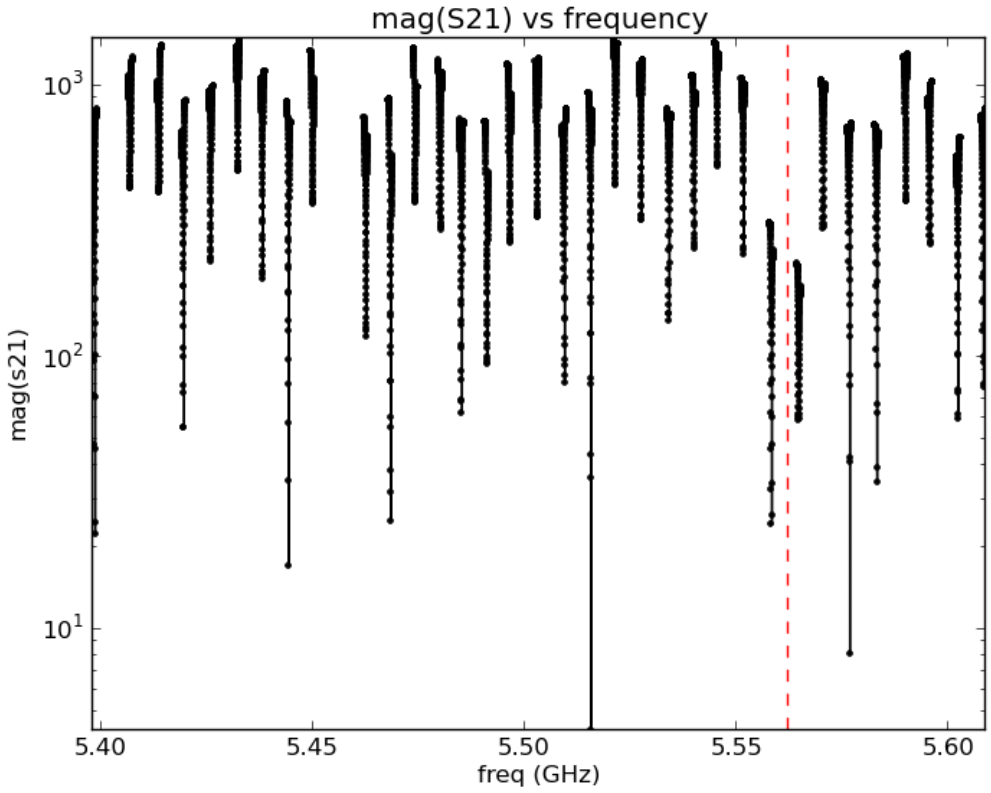

Figure 6.9: Plots associated with the tuning algorithm (continued below). Sweep of S_{21} versus frequency to verify the selected resonant frequency bins.

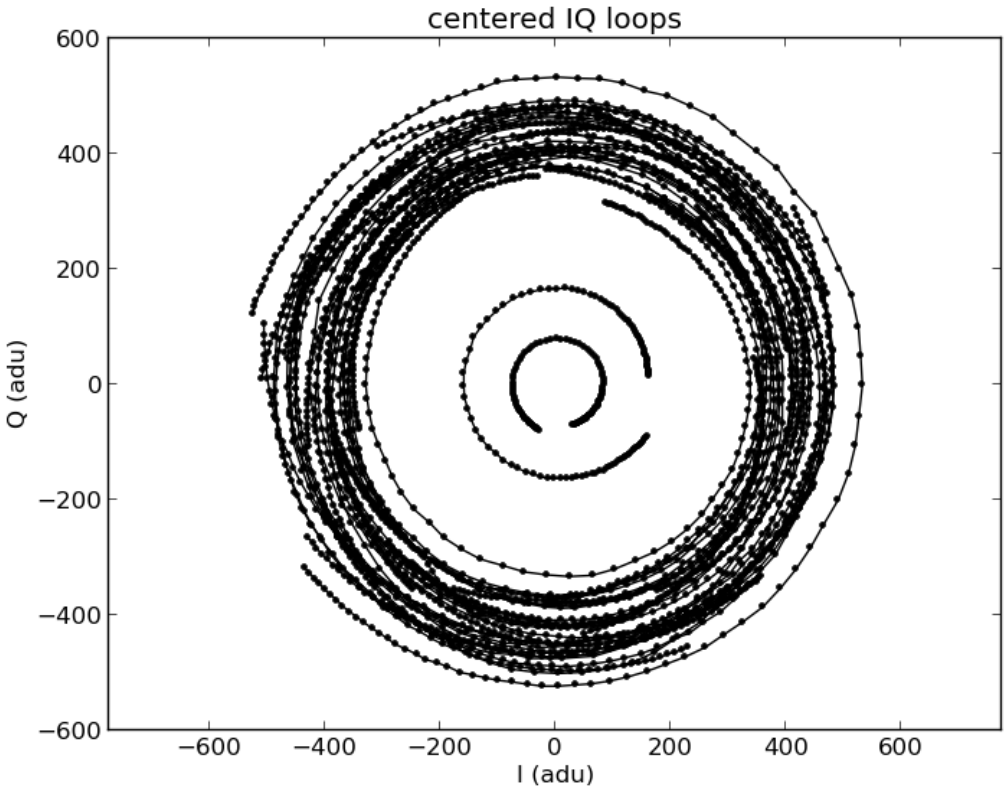

Figure 6.10: Tuning plots (continued). Q versus I, tracing out the resonance circles for each resonator. Arbitrary offsets have been subtracted to center each loop on the origin.

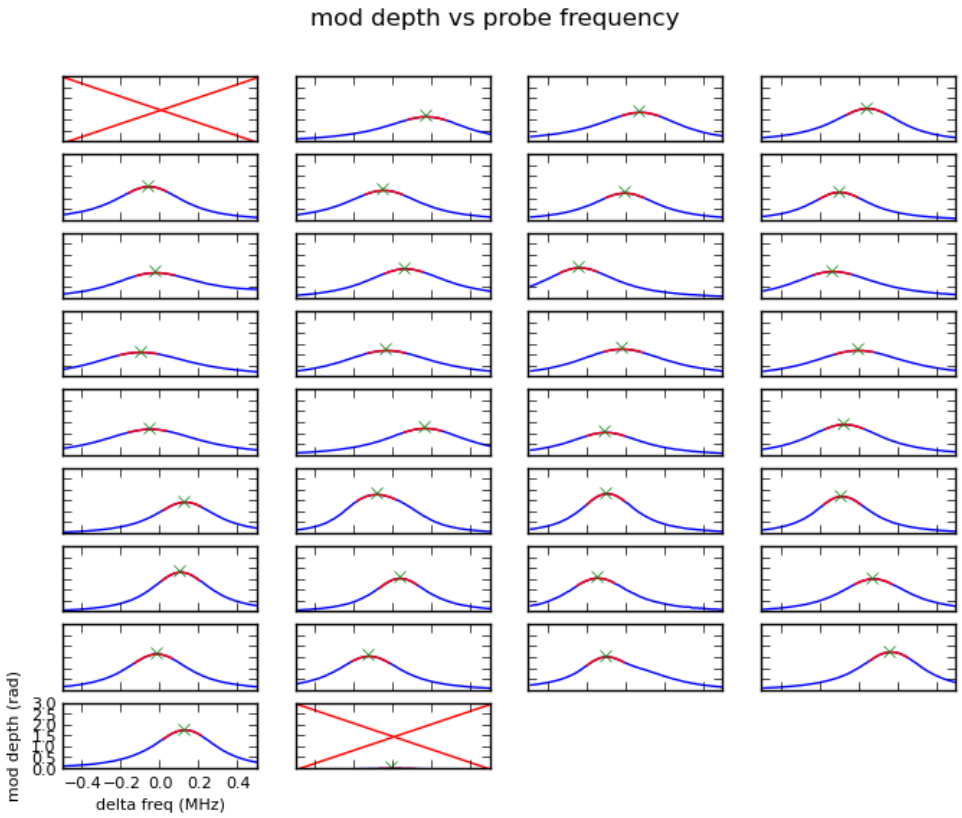

Figure 6.11: Tuning plots (continued). Modulation depth, which represents the maximum response as a function of probe tone frequency. The green crosses are displayed at the best-fit peak response for each resonator channel.

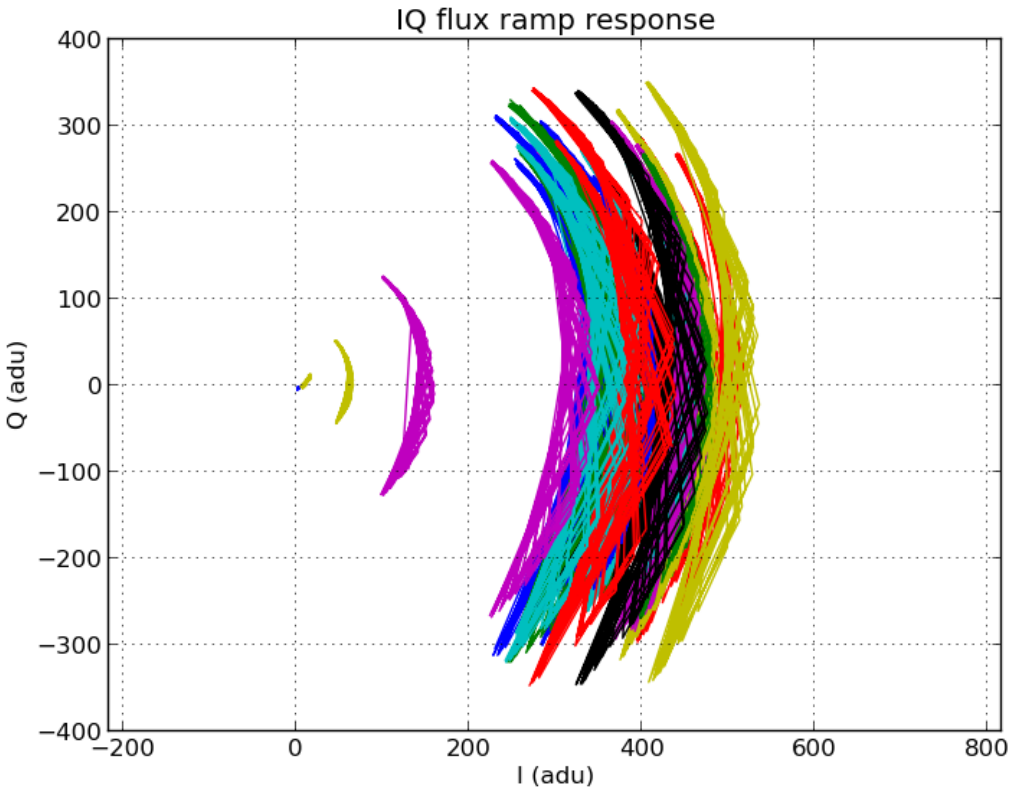

Figure 6.12: Tuning plots (continued). I-Q response to a flux ramp sweep through several flux quanta, after being rotated to center on the positive x-axis. This ensures that the flux ramp response during observing will not exceed the $\pm\pi/2$ boundaries of the CORDIC algorithm used to calculate arctan(I/Q).

First, the waveform for the frequency comb is sent to the DAC and the LO is programmed 10 MHz below the lowest resonant frequency. The LO is then swept ± 1 MHz and the S_{21} magnitudes are visually inspected to identify any problems with the setup. The centers of the resonance circles in the I-Q plane, revealed by the LO sweep, are recorded and subtracted from each channel. The LO is swept again to verify the correct centers have been programmed.

Next the flux ramp is set to step linearly in voltage and at each step the LO is swept ± 0.5 MHz. For each frequency sample within $f_c \pm 0.5$ MHz, the maximum phase shift, or modulation depth, is determined. Close to resonance, the modulation depth versus frequency will approximate a parabola, which we fit to precisely determine the optimal resonant frequency for each channel.

Finally, a 1 Hz sawtooth flux ramp is applied to sweep the SQUID response through several flux quanta. For each channel, the SQUID response forms an arc in the I-Q plane, which can be centered and rotated by adjusting the phase of each probe tones. We rotate these arcs such that the response in the I-Q plane does not exceed $\pm \pi/2$, which is the limit of the CORDIC arctan algorithm used to calculate the phase from the flux ramp response.

6.6 Early Characterization

Currently, four fully populated μMUX modules, designated MUXs 1 - 4, have been characterized in the MUSTANG-1.5 cryostat. S_{21} sweep data for each MUX are shown in Figure 6.13. MUXs 1 and 2 show the expected 35 resonances. MUX 3 has 34 resonances because one resonator is too close to another to be interrogated without

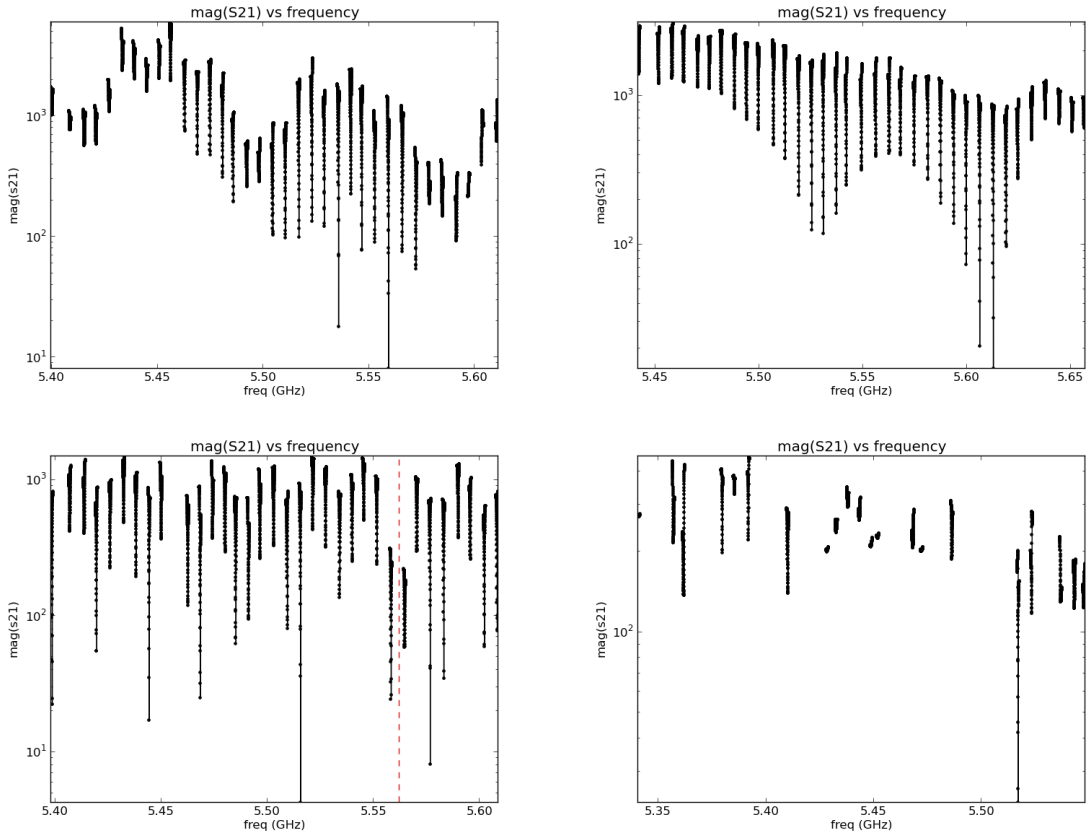

Figure 6.13: S_{21} measurements of the first four MUX chips tested in MUSTANG-1.5. Significant standing waves, due to impedence mismatches in the microwave launches, are seen in each sweep. MUX 4 (bottom right) shows only the small subset of resonances that passed the initial detection algorithm. Most likely the low resonator yield is due to a hardware problem inside the MUX module.

contributing crosstalk. MUX 4 shows ~ 20 resonances, only a few of which have high quality factors. This is most likely due to a hardware problem inside the MUX 4 module housing and will need to be fixed before it can be used in MUSTANG-1.5. Likely culprits include broken wire bonds and electrical shorts between the MUX chip and other components in the module.

During the initial testing we focused primarily on MUX 2, which showed the best combination of quality factor and resonator yield. Additionally, one of the resonator input coils in MUX 2 was wired to the cryostat feedthrough so that we can use an external power source to emulate a TES current signal. A 1 kΩ resistor was connected in series so that we do not inadvertently apply too much power to the resonator input coil.

After running a vVNA sweep and the tuning algorithm, we configure the firmware to run the demodulation. First, we record raw phase timestreams for each resonator channel. Then we stack adjacent flux ramp periods, average them, and fit a sinusoid to determine the carrier frequency. It is important at this stage that all external flux sources, aside from the flux ramp, are removed or else the averaged waveform will no longer be accurate. Examples of the stacked raw phase timestreams recorded from the NIST test setup as well as MUX 2 in MUSTANG-1.5 are shown in Figure 6.14. The NIST data show much better noise properties than the μMUX, but significant progress will be made to improve the MUSTANG-1.5 readout noise level prior to deployment.

The beginning of each ramp period can exhibit ringing due to the sudden change in output voltage from the sawtooth waveform. In MUSTANG-1.5 this is compounded

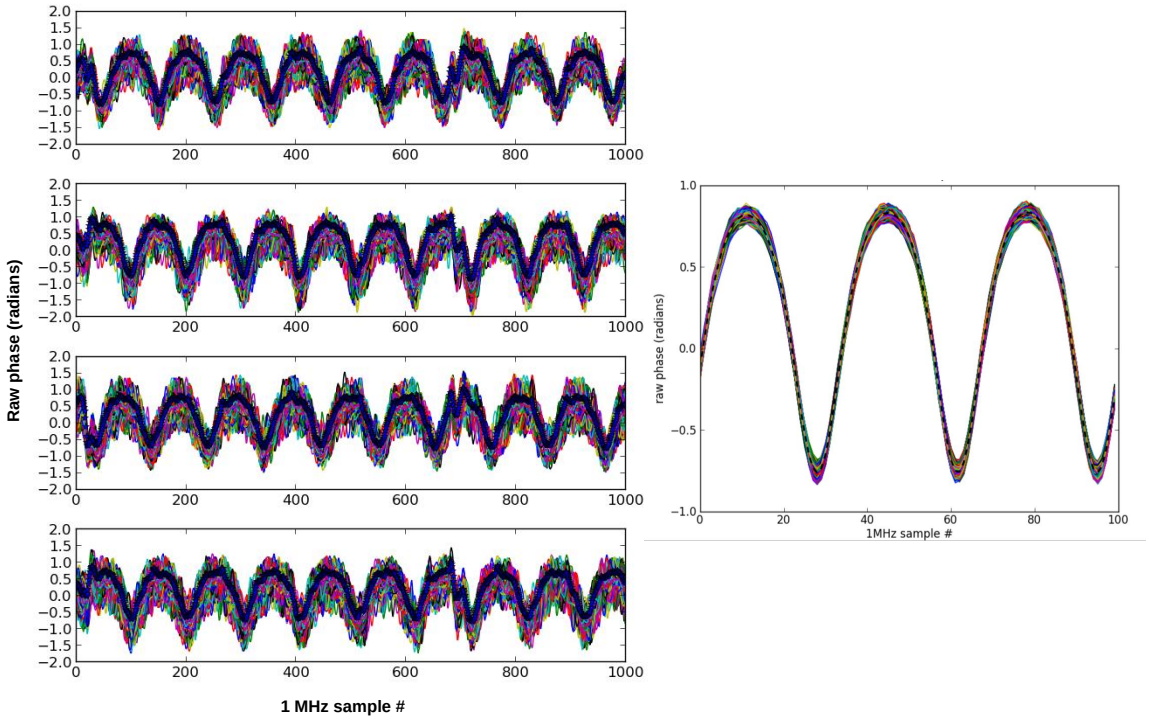

Figure 6.14: Plots of raw phase timestreams divided into bins by flux ramp period and stacked. The right panel shows the results from preliminary testing of a similar setup at NIST.

by the RFI filters installed on the flux ramp cabling, which amplify the ringing considerably. In order to mitigate the effects of the ringing on the demodulated data, we mask out a user-specified number of samples from the start of each flux ramp period.

Once the μMUX frequency comb is tuned, the flux ramp is started, and the carrier frequency is determined, we are ready to record demodulated timestreams. Figure 6.15 shows demodulated timestreams for several resonators. With a DC current applied to the input coil of one resonator the demodulated phases shifts as expected. As the system becomes fully integrated, we will be able to apply sinusoidal waveforms and ensure they return the expected amplitude and frequency following demodulation.

We analyzed both the raw phase timestreams and the demodulated timestreams to measure the readout noise and troubleshoot problems with the hardware. The raw phase timestreams in Figure 6.14 show excessive ringing at the start of each period and a frame-synchronous glitch near the end of the frame. This glitch appears in the same fraction of the frame for several flux ramp frequencies and across all resonators, even with a several day delay between measurements. Therefore, it is likely that there is a fault in the firmware or that the glitch is caused by a hardware component, such as the temporary 10 MHz frequency standard produced by the flux ramp function generator, that is synchronized with the flux ramp rate.

However, despite the excess noise in the raw phase timestreams, the demodulated timestreams exhibit noise that is only a factor of two higher than the detector noise limit. The bottom panel of Figure 6.15 shows a power spectrum for one of the demodulated timestreams using a 1 kHz flux ramp. We expect that after reducing the raw phase timestream noise and with minimal post-processing the readout noise

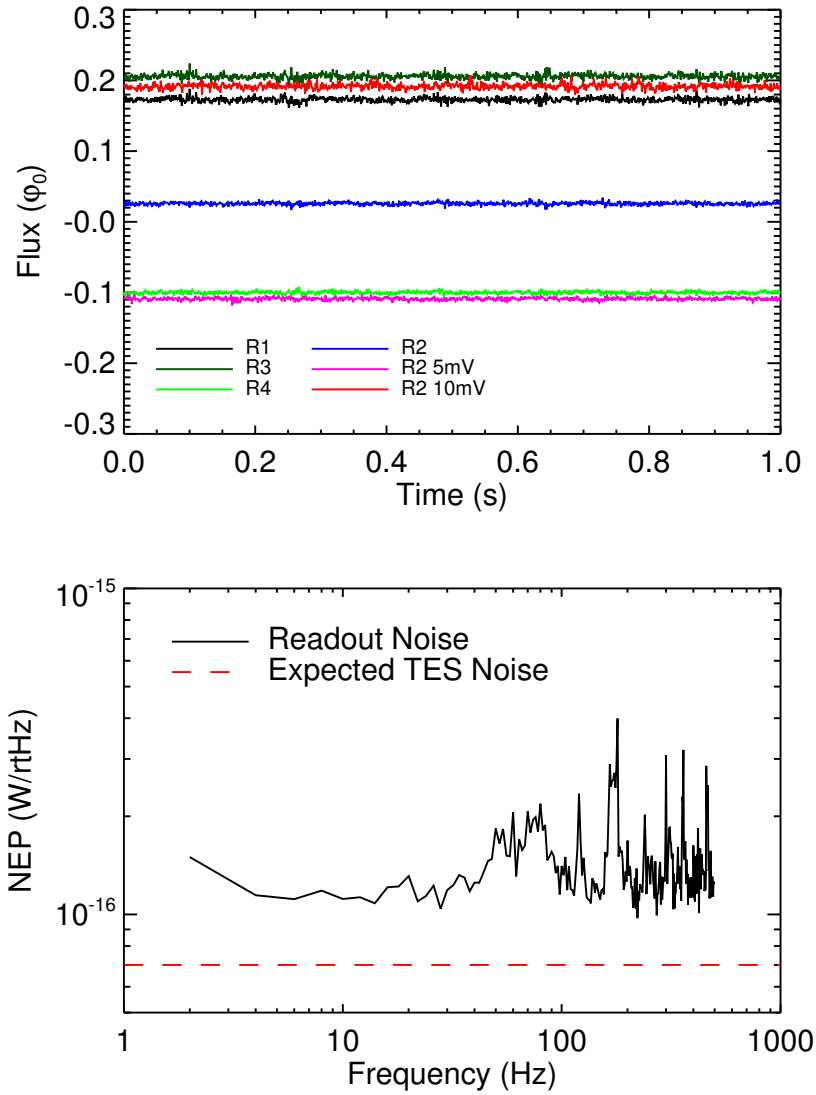

Figure 6.15: **Top:** Demodulated timestreams with a 1 kHz flux ramp for four of the resonators, designated R1-R4, in MUX 2. Also shown are two additional timestreams from R2 for which we applied DC voltages of 5 mV and 10 mV, respetively. The DC offsets in these demodulated timestreams reflect the change in input flux. **Bottom:** Power spectrum of a single timestream. Currently, the average noise level is approximately twice the detector noise level. The noise structures at the higher frequency end are beyond the anticipated astronomical sampling rate at ~ 20 Hz.

will be driven well below the detector noise limit.

6.7 Planned Upgrades

The MUX chips used for MUSTANG-1.5 were fabricated as a proof of concept by Mates [2011] and were not necessarily planned for use in a fielded instrument. As such, conservative choices were made for the MUX design that could be addressed for next generation chips. In particular, the total frequency coverage of the band on the chip could be increased by a factor of two and still meet the Nyquist sampling criterion set by the ADC. Production is currently underway for resonator chips which span a 250 MHz band offset from the existing band by ~ 10 MHz.

An additional improvement in MUX capacity can be gained by spacing the resonators closer together. The maximum crosstalk between adjacent resonators, spaced $N_{\rm BW}$ bandwidths apart, into the imaginary component of S_{21} is proportional to $(1/16)N_{\rm BW}^2$ [Mates 2011]. Given the $\sim$ 300 kHz bandwidth of the MUSTANG-1.5 resonators, a spacing of 3 MHz instead of the conservative 6 MHz could have been chosen and still yielded crosstalk below 1 part in 1000. As resonator fabrication improves and narrower bandwidths are achieved, resonances can be spaced even closer together.

Following the first MUSTANG-1.5 observing season, we expect to have a second generation of MUX chips. Assuming that the chips are designed to span the ~ 500 MHz bandwidth provided by the ADC, and the resonators are spaced instead by 3 MHz, which is well within current fabrication capabilities, then MUSTANG-1.5 will be able to read out ~ 83 polarization sensitive (2 TES/pixel) detectors in a single

readout channel. The entire 223-element array will be read out with three readout channels. Given modest improvements to resonator fabrication ($\leq$ 2.2 MHz spacing), or by dropping polarization sensitivity, the entire focal plane could be read out with only one or two readout enclosures.

Chapter 7

Early Science and Beyond

The MUSTANG-1.5 cryogenics development will be completed by the end of July 2014 at which time detector characterization will begin and carry through the end of the summer. The receiver will be deployed first with 64 detectors and the remainder of the 223-pixel focal plane will be populated with more detectors as we receive them. MUSTANG-1.5 will be installed on the GBT in September 2014 and carry out early science observations throughout the fall and winter. In this chapter, I summarize the technical capabilities of MUSTANG-1.5 and discuss the extensive science program enabled by the new instrument. I focus particularly on topics covered by the last two years of GBT proposals.

7.1 MUSTANG-1.5 Technical Specifications

Simulations of the current 64-pixel layout predict that MUSTANG-1.5 will map a $4' \times 4'$ region to $\sim 40\,\mu$Jy/beam in 1 hour of integration time, which is ~ 25 times

	MUSTANG-1.5	MUSTANG-1.5	MUSTANG
N_{det}	223	64	64
T_c (mK)	450		490
$T_{\rm bath}$ (mK)	280		300
$P_{\rm sat}$ (pW)	45		42
$P_{\rm opt}$ (pW)	20		12
$NEP_{\rm BLIP}$ (W/$\sqrt{\rm Hz}$)	1.6×10^{-16}		1.3×10^{-16}
NEP_G (W/$\sqrt{\rm Hz}$)	5.5×10^{-17}		1.6×10^{-16}
$NEP_{\rm Tot}$ (W/$\sqrt{\rm Hz}$)	1.7×10^{-16}		1.6×10^{-16}
Map RMS noise (μJy/beam$\sqrt{\rm hr}$)	21	40	201
Map RMS noise (Compton-$y\sqrt{\rm hr}$)	1.8×10^{-5}	3.5×10^{-5}	17.5×10^{-5}
Map RMS noise (μK/arcmin$^2\sqrt{\rm hr}$)	9.6	18.2	93.8

Table 7.1: Comparison between the technical capabilities of MUSTANG-1.5 and MUSTANG. P_{opt} is the optical loading with an observing angle of 45° and a sky opacity $\tau \approx 0.2$ representing decent weather conditions. The map RMS noise applies to a $4.25' \times 4.25'$ region.

the mapping speed of MUSTANG. With a fully populated array we expect to cover a $6.5' \times 6.5'$ region to ~ 21 μJy/beam in the same amount of time (~ 100 times the mapping speed of MUSTANG). A summary of the technical specifications for MUSTANG-1.5 is given in Table 7.1.

The primary advantages of MUSTANG-1.5 over MUSTANG come from the background-limited detector sensitivity and the dramatic increase in FOV. As discussed in Chapter 4, common mode subtraction of the atmospheric noise will remove signals of interest on scales larger than the FOV. Even with a partially populated array, MUSTANG-1.5 will provide a $\gtrsim 3.5'$ diameter FOV, which will enable most clusters to be mapped out to R_{500}. With the fully populated array we can measure beyond R_{200}. MUSTANG-1.5 is the only instrument with the combination of spatial dynamic range, sensitivity, and resolution to study both small- and large-scale features in high redshift clusters.

Semester	PI	Brief Description	Grade	Time (hr)
2013B	Simon Dicker	Early Cluster Science	A	48
2013B	Amanda Kepley	Measuring Ionized Gas in IC 342	B	17
2014A	Jonathan Williams	Survey of Disks in the λ Ori Cluster	A	27
2014A	Amanda Kepley	Star Formation in Nearby Galaxies	C	16
2014A	Adam Ginsburg	HCHIIs in Massive Proto-clusters	A	14
2014A	Alexander Young	High-resolution Cluster Astrophysics	B	45
2014A	Esra Bulbul	Multi-wavelength Study of Mergers	B	49
2014A	Simon Dicker	Observing the Edge of Galaxy Clusters	C	54
2014B	Simon Dicker	Mapping Cluster substructure	A	60
2014B	Charles Romero	Observing CLASH with MUSTANG-1.5	B	30
2014B	Devin Crichton	A complete SZE-selected sample	B	60

Table 7.2: Summary of the MUSTANG-1.5 shared-risk observing proposals that have been awarded telescope time since August 2013. The grades assigned by the TAC are explained in the text. Given the MUSTANG-1.5 commissioning schedule the 14B projects will likely be the first observations carried out. Several of these proposals are described in more detail in the text.

7.2 MUSTANG-1.5 Science Program

MUSTANG-1.5 is currently open to "shared risk" proposals, for which the Principal Investigator (PI) understands the receiver sensitivity estimates have not been astronomically verified. With a significant number of proposals submitted from the GBT-users community at large, MUSTANG-1.5 has been consistently awarded over one hundred observing hours each semester targeting a variety of science goals. Table 7.2 provides the proposal title, grade, and hours awarded for each semester. The designated "A" semester runs from February 1st to July 31st, while the "B" semester runs from August 1st to January 31st.

The letter grades correspond to rankings determined by a time allocation committee (TAC). Grade *A* projects have the highest priority and will carry over to the next semester if not completed during the first. Grade *B* projects are lower priority,

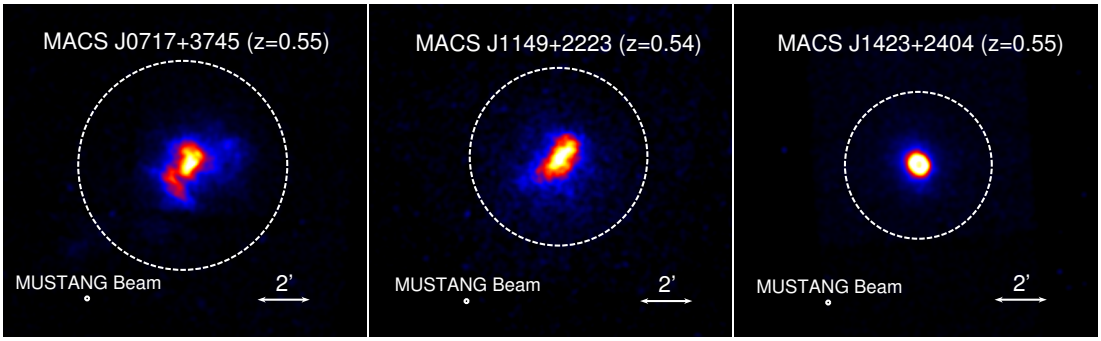

Figure 7.1: X-ray surface brightness images from *Chandra* of MACS J0717.5+3745 (left), MACS J1149+2223 (middle), and MACS J1423.8+2404 (right). From left to right, the white dashed circles correspond to regions with $R = R_{500} = [2.8', 3.4', 4.0']$. Assuming an initial complement of 64 detectors, MUSTANG-1.5 will be able map these regions to a target map RMS $\lesssim 30\,\mu$Jy/beam in 6.5 hours. With the full 223 detectors, these would require ~ 1.7 hours each.

but still likely to receive a majority of the requested observing time. They do not carry over to multiple semesters. Grade *C* proposals are considered filler time and are unlikely to receive all, if any, of the requested observing time. MUSTANG-1.5 has been consistently awarded approximately 50 hours of *A* time each semester, in addition to 100 hours of *B* time. Below we highlight some of the primary science goals of these proposals.

7.2.1 Cluster Astrophysics (*PIs: Simon Dicker, Charles Romero, Alexander Young*)

The large FOV and high angular resolution of MUSTANG-1.5 will enable detailed study of the ICM in intermediate redshift clusters. Figure 7.1 shows the X-ray surface brightness images of three clusters at $z \approx 0.55$ from the CLASH sample. These clusters have comparable masses, but are each in distinct hydrodynamical states:

"train-wreck", disturbed, and cool core, respectively. With MUSTANG-1.5 we can measure pressure profiles, detect shocks, and characterize substructure in the ICM in each of these complex systems.

With 64 detectors a 13 hour observation, which includes 50% time lost due to overhead, will reach noise level below 30 μJy/beam out to R_{500}. With 223 detectors we will only require $\sim$ 3 hours per cluster. By taking radial profiles in smaller wedges we can reach noise levels below 12 μJy/beam. This will allow us to systematically compare what are currently thought to be the most reliable estimates of cluster mass including strong lensing, weak lensing, hydrostatic, and a number of X-ray and SZE mass proxies. The combined analyses of MUSTANG-1.5 and archival *Chandra* data will reveal the detailed thermodynamic states of these clusters in an effort to quantify the effect that astrophysical phenomena have on the integrated SZE flux-mass scaling relations.

7.2.2 Cluster Outskirts (*PI: Simon Dicker*)

The SZE signal scales linearly with density and can therefore probe clusters out to larger radii than those accessible with current X-ray observations, which scale with the square of density. Pressure profiles measured via the SZE by *Planck* do not agree with those inferred from X-ray measurements beyond R_{500} [Planck Collaboration et al. 2013c]. The low pressure gas in cluster outskirts encompasses a large volume and is expected to contribute a significant fraction of the total integrated SZE flux. The models currently used to extrapolate pressure profiles to large radii are based primarily on X-ray measurements of nearby clusters in the later stages of evolution

when they are becoming more relaxed [Arnaud et al. 2010]. Measuring the SZE flux in cluster outskirts directly with MUSTANG-1.5, especially for higher redshift systems where mergers are more frequent, will determine the accuracy of these models and provide insight into the unexpectedly low normalization to the SZE power spectrum [Reichardt et al. 2012; Sievers et al. 2013].

7.2.3 AGN Feedback (*PI: Simon Dicker*)

In observations on the order of several hours per cluster MUSTANG-1.5 will be able to image bubbles in the ICM produced by AGN outbursts [e.g., Hlavacek-Larrondo et al. 2013]. These measurements will examine the role of AGN feedback in suppressing the cooling flow that feeds accretion. MUSTANG-1.5 is expected to provide the first ever detection of these bubbles via the SZE.

7.2.4 Cluster Substructure (*PIs: Esra Bulbul, Simon Dicker, Charles Romero, Alex Young*)

MUSTANG demonstrated the power of combining X-ray and high-resolution SZE imaging to detect and characterize merger shocks [Korngut et al. 2011]. MUSTANG-1.5 will have the spatial dynamic range and sensitivity to characterize shocks independently of the X-ray measurements. By simultaneously measuring bulk SZE flux and small-scale substructure, MUSTANG-1.5 will provide better insight into the dynamical states of merging sub-clusters. X-ray and radio observations are powerful tracers of merger activity, but often lack the sensitivity to detect or characterize shocks in the ICM, especially in high redshift clusters. However, MUSTANG-1.5 will follow up

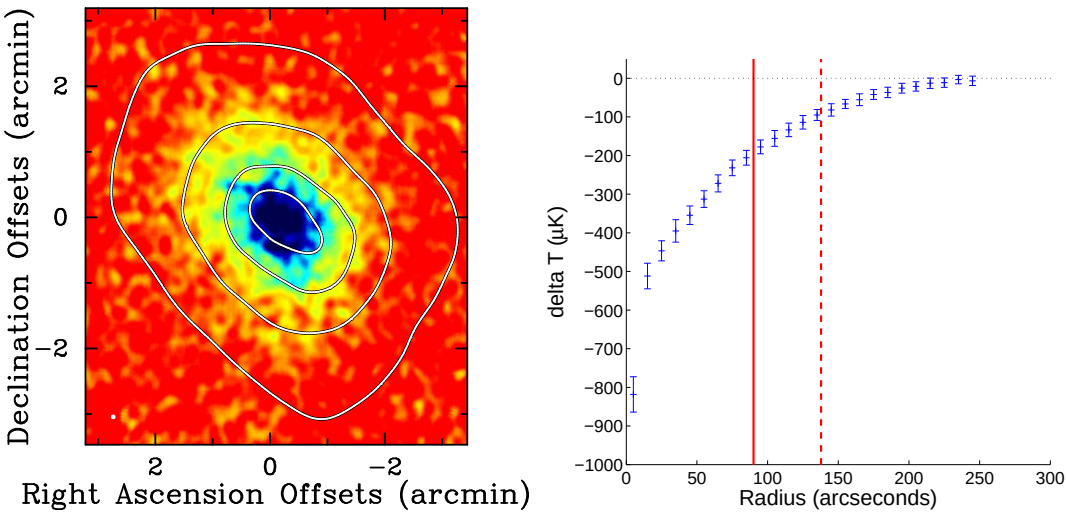

Figure 7.2: Simulated 2 hour MUSTANG-1.5 observation of a 4.5 $\times 10^{14}$ $M_{\odot}$ cluster at $z = 0.5$ from Battaglia et al. [2010]. The contours represent the input model and are shown in steps of 90 μJy/beam. MUSTANG-1.5 measures the integrated flux to $\sim$ 46-σ significance and accurately recovers the asymmetrical cluster morphology. The right panel shows the radial profile with vertical red lines marking R_{500} (solid) and R_{200} (dashed). MUSTANG-1.5 measures the radially averaged profile well beyond R_{200}.

X-ray or radio selected mergers and probe the shock regions to better constrain shock parameters such as Mach number.

7.2.5 Low Mass Clusters and Groups

Low mass ($M < 1.5 \times 10^{14}$ $M_{\odot}$) high-redshift ($z > .85$) clusters are expected to contribute $\sim$ 50% of the SZE power on angular scales of 3.5′ ($\ell \approx 3000$) [Trac et al. 2011]. The amplitude of the SZE power spectrum is a strong function of σ_8 ($A_{\rm SZ} \propto \sigma_8^{8.3}$) so accurate measurements of $A_{\rm SZ}$ can place tight constraints on σ_8 [e.g., Shaw et al. 2010]. However, for a given σ_8, the prediction for $A_{\rm SZ}$ varies dramatically depending on the modeling of cluster physics [Trac et al. 2011].

Current SZE surveys are limited to higher mass clusters and typically do not

resolve astrophysical phenomena on small scales. Low mass, low density systems tend to have ICM temperatures below $k_{\rm B}T_{\rm e} \sim 2$ keV, which (at $z \gtrsim 0.5$) would require hundreds of kiloseconds of *Chandra* data to measure in the X-ray. MUSTANG-1.5, however, will be able to rapidly measure pressure profiles on scales from the cluster cores out to R_{500} and thereby constrain astrophysical properties of low mass clusters and groups. Figure 7.2 shows a simulated 2 hour observation of a $4.5 \times 10^{14}\ M_{\odot}$ cluster with MUSTANG-1.5 and the radially averaged profile. The profile is well constrained even in the cluster outskirts beyond R_{200}.

7.2.6 Cluster Samples

The improved mapping speed of MUSTANG-1.5 will enable hundreds of clusters to be observed each year. In ~ 7 minutes the integrated SZE flux in a $\sim 4.5 \times 10^{14}\ M_{\odot}$ cluster can be measured at 5-σ significance. Since the integrated SZE flux scales roughly as $M^{5/3}$, a $10^{14}\ M_{\odot}$ cluster can therefore be measured in just a few hours.

CLASH (*PI:Charles Romero*)

Multi-wavelength observations are crucial for understanding the complicated processes within galaxy clusters, as shown by Mroczkowski et al. [2012] and discussed in Chapter 4. The CLASH collaboration brings together deep measurements of clusters across the EM spectrum. By targeting CLASH clusters with extensive X-ray, radio data, and lensing data available, MUSTANG-1.5 will be be able to accurately interpret substructures that are detected. Jointly modeling SZE and X-ray observations will provide tighter constraints on the ICM density and temperature profiles than is

possible with either data set alone. Finally, with accurate lensing masses for every cluster, we will be able to directly compare SZE flux and total cluster mass in morphologically distinct subsamples. This will tell us the degree to which measurements of the integrated SZE are biased by the dynamical states of clusters.

ACT (*PI: Devin Crichton*)

One of the primary challenges for interpreting cluster number counts from surveys is the intrinsic bias in the selection functions. For instance, clusters detected in a flux-limited X-ray survey tend to be relaxed, with cool, dense cores driving the X-ray luminosity into higher mass bins. Optically-selected clusters at high redshifts tend to be more disturbed and yield velocity dispersions that do not necessarily reflect the virial mass. Gravitational lensing surveys are sensitive to any mass along the line of sight and can overestimate cluster mass through projection effects. For clusters in a state of hydrostatic equilibrium, the SZE flux should be a low-scatter mass proxy (see McCarthy et al. [2003]). Therefore, SZE surveys may select clusters based on total mass better than surveys in other wavebands, provided one understands the thermodynamic state of the ICM.

An SZE survey of a 504 $\deg^2$ region with ACT detected 68 clusters, which were optically confirmed [Hasselfield et al. 2013]. Many of these clusters have deep optical data and follow-up imaging to obtain spectroscopic redshifts [Menanteau et al. 2013], which are crucial for determining the cluster member galaxy population and measuring velocity dispersions to infer cluster mass. There are also follow-up observations in the X-ray planned with *Chandra* and XMM-*Newton*. Combined analysis of

MUSTANG-1.5 and ACT data will enable the SZE to be measured on a wide range of angular scales and study how astrophysical processes such as mergers and AGN feedback contribute to the scatter in the SZE flux-mass scaling relations. As with MUSTANG, we will carry out a joint model-fitting procedure with the ACT and MUSTANG-1.5 data to constrain ICM profiles without suffering significantly from parameter degeneracy.

LOFAR

The Low Frequency Array (LOFAR) is a new interferometer that operates at 10-240 MHz in northern Europe. LOFAR is expected to detect hundreds of clusters, selected by the presence of radio relics and halos [Nuza et al. 2012]. Since radio relics are "smoking gun" tracers of cluster mergers, a radio-selected survey sample is particularly attractive for follow-up with MUSTANG-1.5, which can image potential shocks associated with the merger. By studying the cluster environment that hosts these radio sources, MUSTANG-1.5 will be able to investigate the conditions under which these relics and halos form. See van Haarlem et al. [2013] for a recent review of the LOFAR instrument and science capabilities.

eROSITA

The X-ray satellite *eRosita* will be launched in 2015 and carry out an all-sky survey at energies from 0.5 keV to 10 keV. *eRosita* is expected to detect $\sim 10^5$ clusters out to redshifts > 1 in order to constrain inflationary theory and enable tests of ΛCDM cosmology. However, due to relatively low resolution ($\sim 0.5'$) and lack of temperature information in the high-redshift clusters, *eRosita* will rely on accurate X-

ray scaling relations in a parameter space ($z > 1$) that has yet to be deeply explored. Additionally, the low angular resolution prevents the cluster cores from being excised from the luminosity measurement, which can introduce significant scatter to the mass estimates [Maughan et al. 2012]. MUSTANG-1.5 will follow up a number of clusters detected by *eRosita* and better constrain the cluster mass by directly comparing X-ray and SZE mass proxies.

7.2.7 Galactic Massive Proto-clusters (*PI: Adam Ginsburg*)

MUSTANG-1.5 observations will be able to detect young massive stars forming in dense globular clusters, where most star formation occurs. At early stages of their evolution, young massive stars ionize the surrounding gas and produce a hypercompact HII (HCHII) region. At 90 GHz, flux from the HCHII region will dominate over dust emission and diffuse HII components. At lower frequencies, the HCHIIs are too faint to be detected by existing surveys and at higher frequencies dust emission dominates the continuum flux. By detecting and studying HCHII regions, MUSTANG-1.5 will be able to investigate the population of young massive stars in dense proto-clusters. For more details on Galactic proto-clusters and the formation of massive stars see Ginsburg et al. [2012].

7.2.8 Extragalactic Star Forming Regions (*PI: Amanda Kepley*)

In regions of active star formation, radiation from massive young stars ionizes the surrounding hydrogen gas and produces Hα photons. Additionally, strong photospheric UV radiation is emitted directly by massive stars. Both of these signatures

serve as direct tracers of the star formation in galaxies, however up to $\sim 80\%$ of this emission is absorbed by dust and re-emitted in the IR [Leroy et al. 2012]. Complementary observations in the IR at 24 μm have been shown to provide good estimates of the flux obscured by dust in order to obtain more accurate star formation rates (SFRs) [Leroy et al. 2012].

These hybrid Hα+IR and UV+IR measurements rely strongly on empirical relationships between two SFR tracers with very different physics. Continuum observations at 90 GHz are unaffected by dust and trace the free-free emission from thermal electrons ionized by photons from these massive stars. At 90 GHz, the galactic continuum spectrum is strongly dominated by the free-free emission [Condon 1992] so the contribution from synchrotron and dust emission can be ignored. Therefore, MUSTANG-1.5 observations of star forming regions would help to develop a new dust-insensitive tracer of star formation rates and assess the accuracy of existing SFR tracers.

7.2.9 Circumstellar Disks and Planet Formation (*PI: Jonathan Williams*)

The leading model for planet formation is the core-accretion process in which planetary cores form from icy planetesimals and accrete matter from surrounding gaseous nebulae. The planetesimals grow from dust and ice particles that collide and merge to form micron-millimeter sized grains. Studying the mechanisms and timescales for grain growth in circumstellar disks will provide inside into models of planet formation and disk evolution.

The maximum observable grain size is $\sim 3\lambda$ [Draine 2006] so MUSTANG-1.5 observations will be sensitive to emission from grains up to $\sim$ 1 cm in size. By measuring a large number of circumstellar disks, MUSTANG-1.5 can determine the mass of millimeter-centimeter sized grains during the later stages of disk evolution when rocky planet formation may still be occurring [Alibert et al. 2010].

For a review on the evolution of proto-planetary disks see Williams & Cieza [2011].

7.3 Conclusion

MUSTANG-1.5 will provide a powerful combination of angular resolution and spatial dynamic range, enabling a wide range of science goals in addition to the SZE imaging highlighted in this dissertation. The new receiver is almost complete, with at least 64 detectors being integrated mid-Summer. The readout electronics are working and the problems with excessive noise levels will be addressed as the commissioning continues. The mechanical assemblies for all internal and external components are complete and the receiver will be ready for installation on the GBT in the early Fall.

Acronyms

ADC

Analog-to-Digital Converter.

ARCONS

ARray Camera for Optical to Near-infrared Spectrophotometry.

BORPH

Berkeley Operating system for ReProgrammable Hardware.

BRAM

block random-access memory.

CASPER

Collaboration for Astronomy Signal Processing and Electronics Research.

DAC

Digital-to-Analog Converter.

FITS

Flexible Image Transport System.

FRM

flux ramp modulation.

GBT

The Green Bank Telescope.

GSFC

NASA Goddard Space Flight Center.

HDPE

high-density polyethylene.

ICM

intra-cluster medium.

IF

Intermediate Frequency.

KATCP

Karoo Array Telescope Control Protocol.

MKID

Magnetic Kinetic Inducatance Detector.

MUSIC

MUlitcolor Submillimeter Inductance Camera.

MUSTANG

The MUltiplexed SQUID/TES Array at Ninety GHz.

NEP

Noise Equivalent Power.

NIR

near-infrared.

NIST

The National Institute of Standards and Technology.

NRAO

The National Radio Astronomy Observatory.

OOF

Out-Of-Focus Holography.

OSR

open source readout.

PSF

point spread function.

PT

Pulse Tube.

QDR

quad data rate.

ROACH

Reconfigurable Open Architecture Computing Hardware.

SDR

Software-Defined Radio.

SNR

signal to noise ratio.

SQUID

Superconducting QUantum Interference Device.

SRAM

static random-access memory.

TDM

Time-Division Multiplexing.

TES

Transition-Edge Sensor.

TOD

time-ordered data.

UPenn

The University of Pennsylvania.

VEGAS

VErsatile GBT Astronomical Spectrometer.

Bibliography

Ade, P. A. R., Aikin, R. W., Barkats, D., Benton, S. J., Bischoff, C. A., Bock, J. J., Brevik, J. A., Buder, I., Bullock, E., Dowell, C. D., Duband, L., Filippini, J. P., Fliescher, S., Golwala, S. R., Halpern, M., Hasselfield, M., Hildebrandt, S. R., Hilton, G. C., Hristov, V. V., Irwin, K. D., Karkare, K. S., Kaufman, J. P., Keating, B. G., Kernasovskiy, S. A., Kovac, J. M., Kuo, C. L., Leitch, E. M., Lueker, M., Mason, P., Netterfield, C. B., Nguyen, H. T., O'Brient, R., Ogburn, R. W., Orlando, A., Pryke, C., Reintsema, C. D., Richter, S., Schwarz, R., Sheehy, C. D., Staniszewski, Z. K., Sudiwala, R. V., Teply, G. P., Tolan, J. E., Turner, A. D., Vieregg, A. G., Wong, C. L., Yoon, K. W., & Bicep2 Collaboration. 2014, Physical Review Letters, 112, 241101

Ade, P. A. R., Pisano, G., Tucker, C., & Weaver, S. 2006, in Society of Photo-Optical Instrumentation Engineers (SPIE) Conference Series, Vol. 6275, Society of Photo-Optical Instrumentation Engineers (SPIE) Conference Series

Aghanim, N., Majumdar, S., & Silk, J. 2008, Reports on Progress in Physics, 71, 066902

Alibert, Y., Broeg, C., Benz, W., Wuchterl, G., Grasset, O., Sotin, C., Eiroa, C., Hen-

ning, T., Herbst, T., Kaltenegger, L., Léger, A., Liseau, R., Lammer, H., Beichman, C., Danchi, W., Fridlund, M., Lunine, J., Paresce, F., Penny, A., Quirrenbach, A., Röttgering, H., Selsis, F., Schneider, J., Stam, D., Tinetti, G., & White, G. J. 2010, Astrobiology, 10, 19

Allen, S. W., Evrard, A. E., & Mantz, A. B. 2011, ARA&A, 49, 409

Alpher, R. A. & Herman, R. C. 1948, Physical Review, 74, 1737

Appel, J. W., Austermann, J. E., Beall, J. A., Becker, D., Benson, B. A., Bleem, L. E., Britton, J., Chang, C. L., Carlstrom, J. E., Cho, H. M., Crites, A. T., Essinger-Hileman, T., Everett, W., Halverson, N. W., Henning, J. W., Hilton, G. C., Irwin, K. D., McMahon, J., Mehl, J., Meyer, S. S., Niemack, M. D., Parker, L. P., Simon, S. M., Staggs, S. T., Visnjic, C., Yoon, K. W., & Zhao, Y. 2009, in American Institute of Physics Conference Series, Vol. 1185, American Institute of Physics Conference Series, ed. B. Young, B. Cabrera, & A. Miller, 211–214

Arnaud, M., Pratt, G. W., Piffaretti, R., Böhringer, H., Croston, J. H., & Pointecouteau, E. 2010, A&A, 517, A92

Austermann, J. E., Niemack, M. D., Appel, J. W., Beall, J. A., Becker, D., Bennett, D. A., Benson, B. A., Bleem, L. E., Britton, J., Carlstrom, J. E., Chang, C. L., Cho, H. M., Crites, A. T., Essinger-Hileman, T., Everett, W., Halverson, N. W., Henning, J. W., Hilton, G. C., Irwin, K. D., McMahon, J., Mehl, J., Meyer, S. S., Parker, L. P., Simon, S. M., Staggs, S. T., Ullom, J. N., Visnjic, C., Yoon, K. W., & Zhao, Y. 2009, in American Institute of Physics Conference Series, Vol. 1185,

American Institute of Physics Conference Series, ed. B. Young, B. Cabrera, & A. Miller, 498–501

Battaglia, N., Bond, J. R., Pfrommer, C., & Sievers, J. L. 2012, ApJ, 758, 74

Battaglia, N., Bond, J. R., Pfrommer, C., Sievers, J. L., & Sijacki, D. 2010, ApJ, 725, 91

Benford, D. J., Allen, C. A., Kutyrev, A. S., Moseley, S. H., Shafer, R. A., Chervenak, J. A., Grossman, E. N., Irwin, K. D., Martinis, J. M., & Reintsema, C. D. 2000, in Eleventh International Symposium on Space Terahertz Technology, 187

Benford, D. J., Voellmer, G. M., Chervenak, J. A., Irwin, K. D., Moseley, H. S., Shafer, R. A., Staguhn, J. G., & Stacey, G. J. 2003, in Society of Photo-Optical Instrumentation Engineers (SPIE) Conference Series, Vol. 4855, Millimeter and Submillimeter Detectors for Astronomy, ed. T. G. Phillips & J. Zmuidzinas, 552–562

Biviano, A., Rosati, P., Balestra, I., Mercurio, A., Girardi, M., Nonino, M., Grillo, C., Scodeggio, M., Lemze, D., Kelson, D., Umetsu, K., Postman, M., Zitrin, A., Czoske, O., Ettori, S., Fritz, A., Lombardi, M., Maier, C., Medezinski, E., Mei, S., Presotto, V., Strazzullo, V., Tozzi, P., Ziegler, B., Annunziatella, M., Bartelmann, M., Benitez, N., Bradley, L., Brescia, M., Broadhurst, T., Coe, D., Demarco, R., Donahue, M., Ford, H., Gobat, R., Graves, G., Koekemoer, A., Kuchner, U., Melchior, P., Meneghetti, M., Merten, J., Moustakas, L., Munari, E., Regős, E., Sartoris, B., Seitz, S., & Zheng, W. 2013, A&A, 558, A1

Brown, M. L., Ade, P., Bock, J., Bowden, M., Cahill, G., Castro, P. G., Church, S., Culverhouse, T., Friedman, R. B., Ganga, K., Gear, W. K., Gupta, S., Hinderks, J., Kovac, J., Lange, A. E., Leitch, E., Melhuish, S. J., Memari, Y., Murphy, J. A., Orlando, A., O'Sullivan, C., Piccirillo, L., Pryke, C., Rajguru, N., Rusholme, B., Schwarz, R., Taylor, A. N., Thompson, K. L., Turner, A. H., Wu, E. Y. S., Zemcov, M., & QUa D Collaboration. 2009, ApJ, 705, 978

Brunetti, G., Setti, G., Feretti, L., & Giovannini, G. 2001, MNRAS, 320, 365

Carlstrom, J. E., Holder, G. P., & Reese, E. D. 2002, ARA&A, 40, 643

Cassano, R., Brunetti, G., Norris, R. P., Röttgering, H. J. A., Johnston-Hollitt, M., & Trasatti, M. 2012, A&A, 548, A100

Cavagnolo, K. W., Donahue, M., Voit, G. M., & Sun, M. 2009, ApJS, 182, 12

Condon, J. J. 1992, ARA&A, 30, 575

Cotton, W. D., Mason, B. S., Dicker, S. R., Korngut, P. M., Devlin, M. J., Aquirre, J., Benford, D. J., Moseley, S. H., Staguhn, J. G., Irwin, K. D., & Ade, P. 2009, ApJ, 701, 1872

Czakon, N. G., Sayers, J., Mantz, A., Golwala, S. R., Downes, T. P., Koch, P. M., Lin, K.-Y., Molnar, S. M., Moustakas, L. A., Mroczkowski, T., Pierpaoli, E., Shitanishi, J. A., Siegel, S., & Umetsu, K. 2014, ArXiv e-prints

Datta, R., Munson, C. D., Niemack, M. D., McMahon, J. J., Britton, J., Wollack, E. J., Beall, J., Devlin, M. J., Fowler, J., Gallardo, P., Hubmayr, J., Irwin, K.,

Newburgh, L., Nibarger, J. P., Page, L., Quijada, M. A., Schmitt, B. L., Staggs, S. T., Thornton, R., & Zhang, L. 2013, Appl. Opt., 52, 8747

Devlin, M. J., Dicker, S. R., Klein, J., & Supanich, M. P. 2004, Cryogenics, 44, 611

Dicker, S. & Devlin, M. 2005, Appl. Opt., 44, 5855

Dicker, S. R., Ade, P. A. R., Aguirre, J., Brevik, J. A., Cho, H. M., Datta, R., Devlin, M. J., Dober, B., Egan, D., Ford, J., Ford, P., Hilton, G., Irwin, K. D., Mason, B. S., Marganian, P., Mello, M., McMahon, J. J., Mroczkowski, T., Rosenman, M., Tucker, C., Vale, L., White, S., Whitehead, M., & Young, A. H. 2014, Journal of Low Temperature Physics

Dicker, S. R., Korngut, P. M., Mason, B. S., Ade, P. A. R., Aguirre, J., Ames, T. J., Benford, D. J., Chen, T. C., Chervenak, J. A., Cotton, W. D., Devlin, M. J., Figueroa-Feliciano, E., Irwin, K. D., Maher, S., Mello, M., Moseley, S. H., Tally, D. J., Tucker, C., & White, S. D. 2008, in Society of Photo-Optical Instrumentation Engineers (SPIE) Conference Series, Vol. 7020, Society of Photo-Optical Instrumentation Engineers (SPIE) Conference Series

Dicker, S. R., Mason, B. S., Korngut, P. M., Cotton, W. D., Compiègne, M., Devlin, M. J., Martin, P. G., Ade, P. A. R., Benford, D. J., Irwin, K. D., Maddalena, R. J., McMullin, J. P., Shepherd, D. S., Sievers, A., Staguhn, J. G., & Tucker, C. 2009, ApJ, 705, 226

Draine, B. T. 2006, ApJ, 636, 1114

Duan, R., McHugh, S., Serfass, B., Mazin, B. A., Merrill, A., Golwala, S. R., Downes, T. P., Czakon, N. G., Day, P. K., Gao, J., Glenn, J., Hollister, M. I., Leduc, H. G., Maloney, P. R., Noroozian, O., Nguyen, H. T., Sayers, J., Schlaerth, J. A., Siegel, S., Vaillancourt, J. E., Vayonakis, A., Wilson, P. R., & Zmuidzinas, J. 2010, in Society of Photo-Optical Instrumentation Engineers (SPIE) Conference Series, Vol. 7741, Society of Photo-Optical Instrumentation Engineers (SPIE) Conference Series

Ebeling, H., Edge, A. C., & Henry, J. P. 2001, ApJ, 553, 668

Ebeling, H., Ma, C. J., Kneib, J.-P., Jullo, E., Courtney, N. J. D., Barrett, E., Edge, A. C., & Le Borgne, J.-F. 2009, MNRAS, 395, 1213

Essinger-Hileman, T., Appel, J. W., Beall, J. A., Cho, H. M., Fowler, J., Halpern, M., Hasselfield, M., Irwin, K. D., Marriage, T. A., Niemack, M. D., Page, L., Parker, L. P., Pufu, S., Staggs, S. T., Stryzak, O., Visnjic, C., Yoon, K. W., & Zhao, Y. 2010, ArXiv e-prints

Fabian, A. C., Sanders, J. S., Taylor, G. B., Allen, S. W., Crawford, C. S., Johnstone, R. M., & Iwasawa, K. 2006, MNRAS, 366, 417

Feretti, L., Giovannini, G., Govoni, F., & Murgia, M. 2012, A&A Rev., 20, 54

Filippini, J. P., Ade, P. A. R., Amiri, M., Benton, S. J., Bihary, R., Bock, J. J., Bond, J. R., Bonetti, J. A., Bryan, S. A., Burger, B., Chiang, H. C., Contaldi, C. R., Crill, B. P., Doré, O., Farhang, M., Fissel, L. M., Gandilo, N. N., Golwala, S. R., Gudmundsson, J. E., Halpern, M., Hasselfield, M., Hilton, G., Holmes, W.,

Hristov, V. V., Irwin, K. D., Jones, W. C., Kuo, C. L., MacTavish, C. J., Mason, P. V., Montroy, T. E., Morford, T. A., Netterfield, C. B., O'Dea, D. T., Rahlin, A. S., Reintsema, C. D., Ruhl, J. E., Runyan, M. C., Schenker, M. A., Shariff, J. A., Soler, J. D., Trangsrud, A., Tucker, C., Tucker, R. S., & Turner, A. D. 2010, in Society of Photo-Optical Instrumentation Engineers (SPIE) Conference Series, Vol. 7741, Society of Photo-Optical Instrumentation Engineers (SPIE) Conference Series

Friedmann, A. 1922, Zeitschrift fur Physik, 10, 377

Gilmour, R., Best, P., & Almaini, O. 2009, MNRAS, 392, 1509

Ginsburg, A., Bressert, E., Bally, J., & Battersby, C. 2012, ApJ, 758, L29

Giodini, S., Lovisari, L., Pointecouteau, E., Ettori, S., Reiprich, T. H., & Hoekstra, H. 2013, Space Sci. Rev., 177, 247

Golwala, S. R., Bockstiegel, C., Brugger, S., Czakon, N. G., Day, P. K., Downes, T. P., Duan, R., Gao, J., Gill, A. K., Glenn, J., Hollister, M. I., LeDuc, H. G., Maloney, P. R., Mazin, B. A., McHugh, S. G., Miller, D., Noroozian, O., Nguyen, H. T., Sayers, J., Schlaerth, J. A., Siegel, S., Vayonakis, A. K., Wilson, P. R., & Zmuidzinas, J. 2012, in Society of Photo-Optical Instrumentation Engineers (SPIE) Conference Series, Vol. 8452, Society of Photo-Optical Instrumentation Engineers (SPIE) Conference Series

Gonzalez, A. H., Sivanandam, S., Zabludoff, A. I., & Zaritsky, D. 2013, ApJ, 778, 14

Grace, E. A., Beall, J., Cho, H. M., Devlin, M. J., Fox, A., Hilton, G., Hubmayr, J., Irwin, K., Klein, J., Li, D., Lungu, M., Newburgh, L. B., Nibarger, J., Niemack, M. D., McMahon, J., Page, L. A., Pappas, C., Schmitt, B. L., Staggs, S. T., Van Lanen, J., & Wollack, E. 2014, Journal of Low Temperature Physics

Gralla, M. B., Crichton, D., Marriage, T. A., Mo, W., Aguirre, P., Addison, G. E., Asboth, V., Battaglia, N., Bock, J., Bond, J. R., Devlin, M. J., Dunner, R., Hajian, A., Halpern, M., Hilton, M., Hincks, A. D., Hlozek, R. A., Huffenberger, K. M., Hughes, J. P., Ivison, R. J., Kosowsky, A., Lin, Y.-T., Marsden, D., Menanteau, F., Moodley, K., Morales, G., Niemack, M. D., Oliver, S., Page, L. A., Partridge, B., Reese, E. D., Rojas, F., Sehgal, N., Sievers, J., Sifon, C., Spergel, D. N., Staggs, S. T., Switzer, E. R., Viero, M. P., Wollack, E. J., & Zemcov, M. B. 2013, ArXiv e-prints

Guth, A. H. 1981, Phys. Rev. D, 23, 347

Haig, D. J., Ade, P. A. R., Aguirre, J. E., Bock, J. J., Edgington, S. F., Enoch, M. L., Glenn, J., Goldin, A., Golwala, S., Heng, K., Laurent, G., Maloney, P. R., Mauskopf, P. D., Rossinot, P., Sayers, J., Stover, P., & Tucker, C. 2004, in Society of Photo-Optical Instrumentation Engineers (SPIE) Conference Series, Vol. 5498, Society of Photo-Optical Instrumentation Engineers (SPIE) Conference Series, ed. C. M. Bradford, P. A. R. Ade, J. E. Aguirre, J. J. Bock, M. Dragovan, L. Duband, L. Earle, J. Glenn, H. Matsuhara, B. J. Naylor, H. T. Nguyen, M. Yun, & J. Zmuidzinas, 78–94

Hand, N., Addison, G. E., Aubourg, E., Battaglia, N., Battistelli, E. S., Bizyaev, D., Bond, J. R., Brewington, H., Brinkmann, J., Brown, B. R., Das, S., Dawson, K. S., Devlin, M. J., Dunkley, J., Dunner, R., Eisenstein, D. J., Fowler, J. W., Gralla, M. B., Hajian, A., Halpern, M., Hilton, M., Hincks, A. D., Hlozek, R., Hughes, J. P., Infante, L., Irwin, K. D., Kosowsky, A., Lin, Y.-T., Malanushenko, E., Malanushenko, V., Marriage, T. A., Marsden, D., Menanteau, F., Moodley, K., Niemack, M. D., Nolta, M. R., Oravetz, D., Page, L. A., Palanque-Delabrouille, N., Pan, K., Reese, E. D., Schlegel, D. J., Schneider, D. P., Sehgal, N., Shelden, A., Sievers, J., Sifón, C., Simmons, A., Snedden, S., Spergel, D. N., Staggs, S. T., Swetz, D. S., Switzer, E. R., Trac, H., Weaver, B. A., Wollack, E. J., Yeche, C., & Zunckel, C. 2012, Physical Review Letters, 109, 041101

Hasselfield, M., Hilton, M., Marriage, T. A., Addison, G. E., Barrientos, L. F., Battaglia, N., Battistelli, E. S., Bond, J. R., Crichton, D., Das, S., Devlin, M. J., Dicker, S. R., Dunkley, J., Dünner, R., Fowler, J. W., Gralla, M. B., Hajian, A., Halpern, M., Hincks, A. D., Hlozek, R., Hughes, J. P., Infante, L., Irwin, K. D., Kosowsky, A., Marsden, D., Menanteau, F., Moodley, K., Niemack, M. D., Nolta, M. R., Page, L. A., Partridge, B., Reese, E. D., Schmitt, B. L., Sehgal, N., Sherwin, B. D., Sievers, J., Sifón, C., Spergel, D. N., Staggs, S. T., Swetz, D. S., Switzer, E. R., Thornton, R., Trac, H., & Wollack, E. J. 2013, J. Cosmology Astropart. Phys., 7, 8

Hinshaw, G., Larson, D., Komatsu, E., Spergel, D. N., Bennett, C. L., Dunkley, J., Nolta, M. R., Halpern, M., Hill, R. S., Odegard, N., Page, L., Smith, K. M.,

Weiland, J. L., Gold, B., Jarosik, N., Kogut, A., Limon, M., Meyer, S. S., Tucker, G. S., Wollack, E., & Wright, E. L. 2013, ApJS, 208, 19

Hlavacek-Larrondo, J., Fabian, A. C., Edge, A. C., Ebeling, H., Allen, S. W., Sanders, J. S., & Taylor, G. B. 2013, MNRAS, 431, 1638

Hubble, E. 1929, Proceedings of the National Academy of Science, 15, 168

Irwin, K. D., Beall, J. A., Doriese, W. B., Duncan, W. D., Hilton, G. C., Mates, J. A. B., Reintsema, C. D., Schmidt, D. R., Ullom, J. N., Vale, L. R., Zink, B. L., & Lehnert, K. W. 2006, Nuclear Instruments and Methods in Physics Research A, 559, 802

Irwin, K. D. & Hilton, G. C. 2005, in Cryogenic Particle Detection, ed. C. Enss (Springer), 63

Itoh, N., Kohyama, Y., & Nozawa, S. 1998, ApJ, 502, 7

Itoh, N. & Nozawa, S. 2004, A&A, 417, 827

Kaiser, N. 1986, MNRAS, 222, 323

Keshet, U. 2010, ArXiv e-prints

Komatsu, E., Matsuo, H., Kitayama, T., Kawabe, R., Kuno, N., Schindler, S., & Yoshikawa, K. 2001, PASJ, 53, 57

Komatsu, E., Smith, K. M., Dunkley, J., Bennett, C. L., Gold, B., Hinshaw, G., Jarosik, N., Larson, D., Nolta, M. R., Page, L., Spergel, D. N., Halpern, M., Hill,

R. S., Kogut, A., Limon, M., Meyer, S. S., Odegard, N., Tucker, G. S., Weiland, J. L., Wollack, E., & Wright, E. L. 2011, ApJS, 192, 18

Korngut, P. M. 2011, PhD thesis, University of Pennsylvania

Korngut, P. M., Dicker, S. R., Reese, E. D., Mason, B. S., Devlin, M. J., Mroczkowski, T., Sarazin, C. L., Sun, M., & Sievers, J. 2011, ApJ, 734, 10

Krause, E., Pierpaoli, E., Dolag, K., & Borgani, S. 2012, MNRAS, 419, 1766

Kravtsov, A. V. & Borgani, S. 2012, ARA&A, 50, 353

Lemaître, G. 1931, MNRAS, 91, 483

Leroy, A. K., Bigiel, F., de Blok, W. J. G., Boissier, S., Bolatto, A., Brinks, E., Madore, B., Munoz-Mateos, J.-C., Murphy, E., Sandstrom, K., Schruba, A., & Walter, F. 2012, AJ, 144, 3

Lockman, F. J., Free, N. L., & Shields, J. C. 2012, AJ, 144, 52

Ma, C.-J., Ebeling, H., & Barrett, E. 2009, ApJ, 693, L56

Mann, A. W. & Ebeling, H. 2012, MNRAS, 420, 2120

Mantz, A., Allen, S. W., Ebeling, H., Rapetti, D., & Drlica-Wagner, A. 2010, MNRAS, 406, 1773

Markevitch, M. 2010, ArXiv e-prints

Markevitch, M., Gonzalez, A. H., David, L., Vikhlinin, A., Murray, S., Forman, W., Jones, C., & Tucker, W. 2002, ApJ, 567, L27

Markevitch, M. & Vikhlinin, A. 2007, Phys. Rep., 443, 1

Mason, B. S., Dicker, S. R., Korngut, P. M., Devlin, M. J., Cotton, W. D., Koch, P. M., Molnar, S. M., Sievers, J., Aguirre, J. E., Benford, D., Staguhn, J. G., Moseley, H., Irwin, K. D., & Ade, P. 2010, ApJ, 716, 739

Mates, J. A. B. 2011, PhD thesis, University of Colorado

Mates, J. A. B., Hilton, G. C., Irwin, K. D., Vale, L. R., & Lehnert, K. W. 2008, Applied Physics Letters, 92, 023514

Mates, J. A. B., Irwin, K. D., Vale, L. R., Hilton, G. C., Gao, J., & Lehnert, K. W. 2012, Journal of Low Temperature Physics, 167, 707

Mather, J. C. 1982, Appl. Opt., 21, 1125

Mather, J. C., Cheng, E. S., Eplee, Jr., R. E., Isaacman, R. B., Meyer, S. S., Shafer, R. A., Weiss, R., Wright, E. L., Bennett, C. L., Boggess, N. W., Dwek, E., Gulkis, S., Hauser, M. G., Janssen, M., Kelsall, T., Lubin, P. M., Moseley, Jr., S. H., Murdock, T. L., Silverberg, R. F., Smoot, G. F., & Wilkinson, D. T. 1990, ApJ, 354, L37

Maughan, B. J., Giles, P. A., Randall, S. W., Jones, C., & Forman, W. R. 2012, MNRAS, 421, 1583

McCarthy, I. G., Babul, A., Holder, G. P., & Balogh, M. L. 2003, ApJ, 591, 515

McHugh, S., Mazin, B. A., Serfass, B., Meeker, S., O'Brien, K., Duan, R., Raffanti, R., & Werthimer, D. 2012, Review of Scientific Instruments, 83, 044702

McMahon, J., Appel, J. W., Austermann, J. E., Beall, J. A., Becker, D., Benson, B. A., Bleem, L. E., Britton, J., Chang, C. L., Carlstrom, J. E., Cho, H. M., Crites, A. T., Essinger-Hileman, T., Everett, W., Halverson, N. W., Henning, J. W., Hilton, G. C., Irwin, K. D., Mehl, J., Meyer, S. S., Mossley, S., Niemack, M. D., Parker, L. P., Simon, S. M., Staggs, S. T., Visnjic, C., Wollack, E., U.-Yen, K., Yoon, K. W., & Zhao, Y. 2009, in American Institute of Physics Conference Series, Vol. 1185, American Institute of Physics Conference Series, ed. B. Young, B. Cabrera, & A. Miller, 490–493

McNamara, B. R. & Nulsen, P. E. J. 2007, ARA&A, 45, 117

Menanteau, F., Sifón, C., Barrientos, L. F., Battaglia, N., Bond, J. R., Crichton, D., Das, S., Devlin, M. J., Dicker, S., Dünner, R., Gralla, M., Hajian, A., Hasselfield, M., Hilton, M., Hincks, A. D., Hughes, J. P., Infante, L., Kosowsky, A., Marriage, T. A., Marsden, D., Moodley, K., Niemack, M. D., Nolta, M. R., Page, L. A., Partridge, B., Reese, E. D., Schmitt, B. L., Sievers, J., Spergel, D. N., Staggs, S. T., Switzer, E., & Wollack, E. J. 2013, ApJ, 765, 67

Mroczkowski, T. 2011, ApJ, 728, L35

Mroczkowski, T., Dicker, S., Sayers, J., Reese, E. D., Mason, B., Czakon, N., Romero, C., Young, A., Devlin, M., Golwala, S., Korngut, P., Sarazin, C., Bock, J., Koch, P. M., Lin, K.-Y., Molnar, S. M., Pierpaoli, E., Umetsu, K., & Zemcov, M. 2012, ApJ, 761, 47

Nagai, D., Kravtsov, A. V., & Vikhlinin, A. 2007, ApJ, 668, 1

Navarro, J. F., Frenk, C. S., & White, S. D. M. 1997, ApJ, 490, 493

Niemack, M. D., Ade, P. A. R., Aguirre, J., Barrientos, F., Beall, J. A., Bond, J. R., Britton, J., Cho, H. M., Das, S., Devlin, M. J., Dicker, S., Dunkley, J., Dünner, R., Fowler, J. W., Hajian, A., Halpern, M., Hasselfield, M., Hilton, G. C., Hilton, M., Hubmayr, J., Hughes, J. P., Infante, L., Irwin, K. D., Jarosik, N., Klein, J., Kosowsky, A., Marriage, T. A., McMahon, J., Menanteau, F., Moodley, K., Nibarger, J. P., Nolta, M. R., Page, L. A., Partridge, B., Reese, E. D., Sievers, J., Spergel, D. N., Staggs, S. T., Thornton, R., Tucker, C., Wollack, E., & Yoon, K. W. 2010, in Society of Photo-Optical Instrumentation Engineers (SPIE) Conference Series, Vol. 7741, Society of Photo-Optical Instrumentation Engineers (SPIE) Conference Series

Nikolic, B., Prestage, R. M., Balser, D. S., Chandler, C. J., & Hills, R. E. 2007, A&A, 465, 685

Nuza, S. E., Hoeft, M., van Weeren, R. J., Gottlöber, S., & Yepes, G. 2012, MNRAS, 420, 2006

Ogburn, IV, R. W., Ade, P. A. R., Aikin, R. W., Amiri, M., Benton, S. J., Bock, J. J., Bonetti, J. A., Brevik, J. A., Burger, B., Dowell, C. D., Duband, L., Filippini, J. P., Golwala, S. R., Halpern, M., Hasselfield, M., Hilton, G., Hristov, V. V., Irwin, K., Kaufman, J. P., Keating, B. G., Kovac, J. M., Kuo, C. L., Lange, A. E., Leitch, E. M., Netterfield, C. B., Nguyen, H. T., Orlando, A., Pryke, C. L., Reintsema, C., Richter, S., Ruhl, J. E., Runyan, M. C., Sheehy, C. D., Staniszewski, Z. K., Stokes, S. A., Sudiwala, R. V., Teply, G. P., Tolan, J. E., Turner, A. D., Wilson, P., &

Wong, C. L. 2010, in Society of Photo-Optical Instrumentation Engineers (SPIE) Conference Series, Vol. 7741, Society of Photo-Optical Instrumentation Engineers (SPIE) Conference Series

Parsons, A., Werthimer, D., Backer, D., Bastian, T., Bower, G., Brisken, W., Chen, H., Deller, A., Filiba, T., Gary, D., Greenhill, L., Hawkins, D., Jones, G., Langston, G., Lasio, J., Van Leeuwen, J., Mitchell, D., Manley, J., Siemion, A., So, H. K.-H., Whitney, A., Woody, D., Wright, M., & Zarb-Adami, K. 2009, in Astronomy, Vol. 2010, astro2010: The Astronomy and Astrophysics Decadal Survey, 21

Penzias, A. A. & Wilson, R. W. 1965, ApJ, 142, 419

Perlmutter, S., Aldering, G., Goldhaber, G., Knop, R. A., Nugent, P., Castro, P. G., Deustua, S., Fabbro, S., Goobar, A., Groom, D. E., Hook, I. M., Kim, A. G., Kim, M. Y., Lee, J. C., Nunes, N. J., Pain, R., Pennypacker, C. R., Quimby, R., Lidman, C., Ellis, R. S., Irwin, M., McMahon, R. G., Ruiz-Lapuente, P., Walton, N., Schaefer, B., Boyle, B. J., Filippenko, A. V., Matheson, T., Fruchter, A. S., Panagia, N., Newberg, H. J. M., Couch, W. J., & Project, T. S. C. 1999, ApJ, 517, 565

Planck Collaboration, Ade, P. A. R., Aghanim, N., Armitage-Caplan, C., Arnaud, M., Ashdown, M., Atrio-Barandela, F., Aumont, J., Baccigalupi, C., Banday, A. J., & et al. 2013a, ArXiv e-prints

—. 2013b, ArXiv e-prints

Planck Collaboration, Ade, P. A. R., Aghanim, N., Arnaud, M., Ashdown, M., Atrio-

Barandela, F., Aumont, J., Baccigalupi, C., Balbi, A., Banday, A. J., & et al. 2013c, A&A, 550, A131

Postman, M., Coe, D., Benítez, N., Bradley, L., Broadhurst, T., Donahue, M., Ford, H., Graur, O., Graves, G., Jouvel, S., Koekemoer, A., Lemze, D., Medezinski, E., Molino, A., Moustakas, L., Ogaz, S., Riess, A., Rodney, S., Rosati, P., Umetsu, K., Zheng, W., Zitrin, A., Bartelmann, M., Bouwens, R., Czakon, N., Golwala, S., Host, O., Infante, L., Jha, S., Jimenez-Teja, Y., Kelson, D., Lahav, O., Lazkoz, R., Maoz, D., McCully, C., Melchior, P., Meneghetti, M., Merten, J., Moustakas, J., Nonino, M., Patel, B., Regös, E., Sayers, J., Seitz, S., & Van der Wel, A. 2012, ApJS, 199, 25

Pratt, G. W., Croston, J. H., Arnaud, M., & Böhringer, H. 2009, A&A, 498, 361

Press, W. H. & Schechter, P. 1974, ApJ, 187, 425

Press, W. H., Teukolsky, S. A., Vetterling, W. T., & Flannery, B. P. 1992, Numerical Recipes in C. The Art of Scientific Computing (Cambridge: Cambridge University Press, 2nd ed.)

Randall, S. W., Sarazin, C. L., & Ricker, P. M. 2002, ApJ, 577, 579

Ransom, S. M., Stairs, I. H., Archibald, A. M., Hessels, J. W. T., Kaplan, D. L., van Kerkwijk, M. H., Boyles, J., Deller, A. T., Chatterjee, S., Schechtman-Rook, A., Berndsen, A., Lynch, R. S., Lorimer, D. R., Karako-Argaman, C., Kaspi, V. M., Kondratiev, V. I., McLaughlin, M. A., van Leeuwen, J., Rosen, R., Roberts, M. S. E., & Stovall, K. 2014, Nature, 505, 520

Reichardt, C. L., Shaw, L., Zahn, O., Aird, K. A., Benson, B. A., Bleem, L. E., Carlstrom, J. E., Chang, C. L., Cho, H. M., Crawford, T. M., Crites, A. T., de Haan, T., Dobbs, M. A., Dudley, J., George, E. M., Halverson, N. W., Holder, G. P., Holzapfel, W. L., Hoover, S., Hou, Z., Hrubes, J. D., Joy, M., Keisler, R., Knox, L., Lee, A. T., Leitch, E. M., Lueker, M., Luong-Van, D., McMahon, J. J., Mehl, J., Meyer, S. S., Millea, M., Mohr, J. J., Montroy, T. E., Natoli, T., Padin, S., Plagge, T., Pryke, C., Ruhl, J. E., Schaffer, K. K., Shirokoff, E., Spieler, H. G., Staniszewski, Z., Stark, A. A., Story, K., van Engelen, A., Vanderlinde, K., Vieira, J. D., & Williamson, R. 2012, ApJ, 755, 70

Reichardt, C. L., Stalder, B., Bleem, L. E., Montroy, T. E., Aird, K. A., Andersson, K., Armstrong, R., Ashby, M. L. N., Bautz, M., Bayliss, M., Bazin, G., Benson, B. A., Brodwin, M., Carlstrom, J. E., Chang, C. L., Cho, H. M., Clocchiatti, A., Crawford, T. M., Crites, A. T., de Haan, T., Desai, S., Dobbs, M. A., Dudley, J. P., Foley, R. J., Forman, W. R., George, E. M., Gladders, M. D., Gonzalez, A. H., Halverson, N. W., Harrington, N. L., High, F. W., Holder, G. P., Holzapfel, W. L., Hoover, S., Hrubes, J. D., Jones, C., Joy, M., Keisler, R., Knox, L., Lee, A. T., Leitch, E. M., Liu, J., Lueker, M., Luong-Van, D., Mantz, A., Marrone, D. P., McDonald, M., McMahon, J. J., Mehl, J., Meyer, S. S., Mocanu, L., Mohr, J. J., Murray, S. S., Natoli, T., Padin, S., Plagge, T., Pryke, C., Rest, A., Ruel, J., Ruhl, J. E., Saliwanchik, B. R., Saro, A., Sayre, J. T., Schaffer, K. K., Shaw, L., Shirokoff, E., Song, J., Spieler, H. G., Staniszewski, Z., Stark, A. A., Story, K., Stubbs, C. W., Šuhada, R., van Engelen, A., Vanderlinde, K., Vieira, J. D., Vikhlinin, A., Williamson, R., Zahn, O., & Zenteno, A. 2013, ApJ, 763, 127

Ruze, J. 1966, IEEE Proceedings, 54, 633

Sanders, J. S. 2006, MNRAS, 371, 829

Sarazin, C. L. 2002, in Astrophysics and Space Science Library, Vol. 272, Merging Processes in Galaxy Clusters, ed. L. Feretti, I. M. Gioia, & G. Giovannini, 1

Sayers, J. 2008, PhD thesis, California Institute of Technology

Sayers, J., Czakon, N. G., Mantz, A., Golwala, S. R., Ameglio, S., Downes, T. P., Koch, P. M., Lin, K.-Y., Maughan, B. J., Molnar, S. M., Moustakas, L., Mroczkowski, T., Pierpaoli, E., Shitanishi, J. A., Siegel, S., Umetsu, K., & Van der Pyl, N. 2013a, ApJ, 768, 177

Sayers, J., Golwala, S. R., Ameglio, S., & Pierpaoli, E. 2011, ApJ, 728, 39

Sayers, J., Mroczkowski, T., Zemcov, M., Korngut, P. M., Bock, J., Bulbul, E., Czakon, N. G., Egami, E., Golwala, S. R., Koch, P. M., Lin, K.-Y., Mantz, A., Molnar, S. M., Moustakas, L., Pierpaoli, E., Rawle, T. D., Reese, E. D., Rex, M., Shitanishi, J. A., Siegel, S., & Umetsu, K. 2013b, ApJ, 778, 52

Shaw, L. D., Nagai, D., Bhattacharya, S., & Lau, E. T. 2010, ApJ, 725, 1452

Sievers, J. L., Hlozek, R. A., Nolta, M. R., Acquaviva, V., Addison, G. E., Ade, P. A. R., Aguirre, P., Amiri, M., Appel, J. W., Barrientos, L. F., Battistelli, E. S., Battaglia, N., Bond, J. R., Brown, B., Burger, B., Calabrese, E., Chervenak, J., Crichton, D., Das, S., Devlin, M. J., Dicker, S. R., Bertrand Doriese, W., Dunkley, J., Dünner, R., Essinger-Hileman, T., Faber, D., Fisher, R. P., Fowler, J. W., Gallardo, P., Gordon, M. S., Gralla, M. B., Hajian, A., Halpern, M., Hasselfield,

M., Hernández-Monteagudo, C., Hill, J. C., Hilton, G. C., Hilton, M., Hincks, A. D., Holtz, D., Huffenberger, K. M., Hughes, D. H., Hughes, J. P., Infante, L., Irwin, K. D., Jacobson, D. R., Johnstone, B., Baptiste Juin, J., Kaul, M., Klein, J., Kosowsky, A., Lau, J. M., Limon, M., Lin, Y.-T., Louis, T., Lupton, R. H., Marriage, T. A., Marsden, D., Martocci, K., Mauskopf, P., McLaren, M., Menanteau, F., Moodley, K., Moseley, H., Netterfield, C. B., Niemack, M. D., Page, L. A., Page, W. A., Parker, L., Partridge, B., Plimpton, R., Quintana, H., Reese, E. D., Reid, B., Rojas, F., Sehgal, N., Sherwin, B. D., Schmitt, B. L., Spergel, D. N., Staggs, S. T., Stryzak, O., Swetz, D. S., Switzer, E. R., Thornton, R., Trac, H., Tucker, C., Uehara, M., Visnjic, K., Warne, R., Wilson, G., Wollack, E., Zhao, Y., & Zunckel, C. 2013, J. Cosmology Astropart. Phys., 10, 60

Smoot, G. F., Bennett, C. L., Kogut, A., Wright, E. L., Aymon, J., Boggess, N. W., Cheng, E. S., de Amici, G., Gulkis, S., Hauser, M. G., Hinshaw, G., Jackson, P. D., Janssen, M., Kaita, E., Kelsall, T., Keegstra, P., Lineweaver, C., Loewenstein, K., Lubin, P., Mather, J., Meyer, S. S., Moseley, S. H., Murdock, T., Rokke, L., Silverberg, R. F., Tenorio, L., Weiss, R., & Wilkinson, D. T. 1992, ApJ, 396, L1

Springel, V., White, S. D. M., Jenkins, A., Frenk, C. S., Yoshida, N., Gao, L., Navarro, J., Thacker, R., Croton, D., Helly, J., Peacock, J. A., Cole, S., Thomas, P., Couchman, H., Evrard, A., Colberg, J., & Pearce, F. 2005, Nature, 435, 629

Sunyaev, R. A. & Zel'dovich, Y. B. 1972, Comments Astrophys. Space Phys., 4, 173

Trac, H., Bode, P., & Ostriker, J. P. 2011, ApJ, 727, 94

Umetsu, K., Medezinski, E., Nonino, M., Merten, J., Zitrin, A., Molino, A., Grillo,

C., Carrasco, M., Donahue, M., Mahdavi, A., Coe, D., Postman, M., Koekemoer, A., Czakon, N., Sayers, J., Mroczkowski, T., Golwala, S., Koch, P. M., Lin, K.-Y., Molnar, S. M., Rosati, P., Balestra, I., Mercurio, A., Scodeggio, M., Biviano, A., Anguita, T., Infante, L., Seidel, G., Sendra, I., Jouvel, S., Host, O., Lemze, D., Broadhurst, T., Meneghetti, M., Moustakas, L., Bartelmann, M., Benítez, N., Bouwens, R., Bradley, L., Ford, H., Jiménez-Teja, Y., Kelson, D., Lahav, O., Melchior, P., Moustakas, J., Ogaz, S., Seitz, S., & Zheng, W. 2012, ApJ, 755, 56

van Haarlem, M. P., Wise, M. W., Gunst, A. W., Heald, G., McKean, J. P., Hessels, J. W. T., de Bruyn, A. G., Nijboer, R., Swinbank, J., Fallows, R., Brentjens, M., Nelles, A., Beck, R., Falcke, H., Fender, R., Hörandel, J., Koopmans, L. V. E., Mann, G., Miley, G., Röttgering, H., Stappers, B. W., Wijers, R. A. M. J., Zaroubi, S., van den Akker, M., Alexov, A., Anderson, J., Anderson, K., van Ardenne, A., Arts, M., Asgekar, A., Avruch, I. M., Batejat, F., Bähren, L., Bell, M. E., Bell, M. R., van Bemmel, I., Bennema, P., Bentum, M. J., Bernardi, G., Best, P., Bîrzan, L., Bonafede, A., Boonstra, A.-J., Braun, R., Bregman, J., Breitling, F., van de Brink, R. H., Broderick, J., Broekema, P. C., Brouw, W. N., Brüggen, M., Butcher, H. R., van Cappellen, W., Ciardi, B., Coenen, T., Conway, J., Coolen, A., Corstanje, A., Damstra, S., Davies, O., Deller, A. T., Dettmar, R.-J., van Diepen, G., Dijkstra, K., Donker, P., Doorduin, A., Dromer, J., Drost, M., van Duin, A., Eislöffel, J., van Enst, J., Ferrari, C., Frieswijk, W., Gankema, H., Garrett, M. A., de Gasperin, F., Gerbers, M., de Geus, E., Grießmeier, J.-M., Grit, T., Gruppen, P., Hamaker, J. P., Hassall, T., Hoeft, M., Holties, H. A., Horneffer, A., van der Horst, A., van Houwelingen, A., Huijgen, A., Iacobelli, M., Intema, H., Jackson, N.,

Jelic, V., de Jong, A., Juette, E., Kant, D., Karastergiou, A., Koers, A., Kollen, H., Kondratiev, V. I., Kooistra, E., Koopman, Y., Koster, A., Kuniyoshi, M., Kramer, M., Kuper, G., Lambropoulos, P., Law, C., van Leeuwen, J., Lemaitre, J., Loose, M., Maat, P., Macario, G., Markoff, S., Masters, J., McFadden, R. A., McKay-Bukowski, D., Meijering, H., Meulman, H., Mevius, M., Middelberg, E., Millenaar, R., Miller-Jones, J. C. A., Mohan, R. N., Mol, J. D., Morawietz, J., Morganti, R., Mulcahy, D. D., Mulder, E., Munk, H., Nieuwenhuis, L., van Nieuwpoort, R., Noordam, J. E., Norden, M., Noutsos, A., Offringa, A. R., Olofsson, H., Omar, A., Orrú, E., Overeem, R., Paas, H., Pandey-Pommier, M., Pandey, V. N., Pizzo, R., Polatidis, A., Rafferty, D., Rawlings, S., Reich, W., de Reijer, J.-P., Reitsma, J., Renting, G. A., Riemers, P., Rol, E., Romein, J. W., Roosjen, J., Ruiter, M., Scaife, A., van der Schaaf, K., Scheers, B., Schellart, P., Schoenmakers, A., Schoonderbeek, G., Serylak, M., Shulevski, A., Sluman, J., Smirnov, O., Sobey, C., Spreeuw, H., Steinmetz, M., Sterks, C. G. M., Stiepel, H.-J., Stuurwold, K., Tagger, M., Tang, Y., Tasse, C., Thomas, I., Thoudam, S., Toribio, M. C., van der Tol, B., Usov, O., van Veelen, M., van der Veen, A.-J., ter Veen, S., Verbiest, J. P. W., Vermeulen, R., Vermaas, N., Vocks, C., Vogt, C., de Vos, M., van der Wal, E., van Weeren, R., Weggemans, H., Weltevrede, P., White, S., Wijnholds, S. J., Wilhelmsson, T., Wucknitz, O., Yatawatta, S., Zarka, P., Zensus, A., & van Zwieten, J. 2013, A&A, 556, A2

van Weeren, R. J., Intema, H. T., Rottgering, H. J. A., Bruggen, M., & Hoeft, M. 2011, ArXiv e-prints

Vikhlinin, A., Kravtsov, A. V., Burenin, R. A., Ebeling, H., Forman, W. R., Horn-

strup, A., Jones, C., Murray, S. S., Nagai, D., Quintana, H., & Voevodkin, A. 2009, ApJ, 692, 1060

Volder, J. E. 2000, Journal of VLSI signal processing systems for signal, image and video technology, 25, 101

Vollmer, B. 2009, VizieR Online Data Catalog, 8085, 0

Vollmer, B., Gassmann, B., Derrière, S., Boch, T., Louys, M., Bonnarel, F., Dubois, P., Genova, F., & Ochsenbein, F. 2010, A&A, 511, A53

Weiland, J. L., Odegard, N., Hill, R. S., Wollack, E., Hinshaw, G., Greason, M. R., Jarosik, N., Page, L., Bennett, C. L., Dunkley, J., Gold, B., Halpern, M., Kogut, A., Komatsu, E., Larson, D., Limon, M., Meyer, S. S., Nolta, M. R., Smith, K. M., Spergel, D. N., Tucker, G. S., & Wright, E. L. 2011, ApJS, 192, 19

Wik, D. R., Sarazin, C. L., Ricker, P. M., & Randall, S. W. 2008, ApJ, 680, 17

Williams, J. P. & Cieza, L. A. 2011, ARA&A, 49, 67

Zeng, L., Bennett, C. L., Chuss, D. T., & Wollack, E. J. 2010, Antennas and Propagation, IEEE Transactions on, 58, 1383

Zitrin, A., Broadhurst, T., Barkana, R., Rephaeli, Y., & Benítez, N. 2011, MNRAS, 410, 1939

ZuHone, J. A., Markevitch, M., & Johnson, R. E. 2010, ApJ, 717, 908